Institute of Experimental Pharmacology and Toxicology
Center for Experimental Medicine
University Medical Center Hamburg-Eppendorf

Active contribution of transplanted induced pluripotent stem cell-derived cardiomyocytes to left ventricular function in a guinea pig model

---

Dissertation

submitted to the Department of Chemistry
Faculty of Mathematics, Informatics, and Natural Sciences
University of Hamburg

for the degree of
Doctor of Natural Sciences
(Dr. rer. nat.)

by

Tim Niklas Stüdemann

born in Bremen

Hamburg, 2021

First referee: Prof. Dr. Elke Oetjen

Second referee: Prof. Dr. Thomas Eschenhagen

Dr. Florian Weinberger practically supervised this work.

Disputation committee:

Prof. Dr. Elke Oetjen

Prof. Dr. Sebastian Wicha

Prof. Dr. Thomas Oertner

Date of disputation: 08.04.2022

Carried out in the Institute of Experimental Pharmacology and Toxicology from November 2018 to December 2021.

I. PUBLICATIONS AND CONGRESS PARTICIPATIONS

Publications

Querdel, E., Reinsch, M., Castro, L., Köse, D., Bähr, A., Reich, S., Geertz, B., Ulmer, B., Schulze, M., Lemoine, M. D., Krause, T., Lemme, M., Sani, J., Shibamiya, A., **Stüdemann, T.**, Köhne, M., von Bibra, C., Hornaschewitz, N., Pecha, S., … Weinberger, F. (2021). Human Engineered Heart Tissue Patches Remuscularize the Injured Heart in a Dose-Dependent Manner. Circulation, 143(20), 1991–2006. https://doi.org/10.1161/CIRCULATIONAHA.120.047904

von Bibra, C., Shibamiya, A., Geertz, B., Querdel, E., Köhne, M., **Stuedemann, T.**, Starbatty, J., Hansen, A., Hiebl, B., Eschenhagen, T., Weinberger, F. (2021). Human engineered heart tissue transplantation in a guinea pig chronic injury model. BioRxiv, https://doi.org/10.1101/2021.06.28.450176

Stüdemann T., Weinberger F. (2021). The guinea pig model in cardiac regeneration research; Current tissue engineering approaches and future directions. Advanced Technologies in Cardiovascular Bioengineering, Zhang J, Serpooshan V. (Editors), ISBN: 978-3-030-86139-1

Stuedemann T., Roessinger J., Manthey C., Geertz B., Srikantharajah R., von Bibra C., Shibamiya A., Koehne M, Wiehler A., Wiegert JS., Eschenhagen T., Weinberger F. (2021). Contractile force of transplanted cardiomyocytes contributes to heart function after injury. BioRxiv, https://doi.org/10.1101/2021.11.23.469715

Congress Participations

Stüdemann T., Pan B., Köhne M., von Bibra C., Shibamiya A., Stenzig J., Eschenhagen T., Weinberger F., Generation of human engineered heart tissue with light activated ion channels. Early Career Investigators Pre-Meeting Symposium at International Society for Heart Research-European Section, 2021.

Stüdemann T., Manthey C., Schulz C., Köhne M., Shibamiya A., Penalosa Ruiz G., Christ T., Eschenhagen T., Weinberger F., Generation and characterization of human engineered heart tissue with a pharmacological off-on switch. EMBO Workshop: Cardiomyocyte Biology, 2021.

II. TABLE OF CONTENTS

III. LIST OF ABBREVIATIONS

2D	Two-dimensional
3D	Three-dimensional
5HT3	Serotonin receptor 3a
A	
AAR	Area at risk
AAV	Adeno-associated virus
AAVS1	Adeno-associated virus integration site 1
ACEI	Angiotensin-converting enzyme inhibitor
AChR	Acetylcholine receptor
ACR	Anion-selective channelrhodopsin
ADP	Adenosine diphosphate
AGG	Aggregation coefficient
Akt	Protein kinase B
AMI	Acute myocardial infarction
AP	Action potential
APC	Allophycocyanin
APD	Action potential duration
ARB	Angiotensin II receptor blocker
ARNI	Angiotensin receptor neprilysin inhibitor
ATP	Adenosine triphosphate
AU	Arbitrary units
AV	Atrioventricular
α-SMA	α-smooth muscle actin
B	
Bcl-xL	B-cell lymphoma-extra large
bFGF	Basic fibroblast growth factor
BMI	Body mass index
B-mode	Brightness-mode
BMP-4	Bone morphogenetic protein 4
bp	Base pair
bpm	Beats per minute
BSA	Bovine serum albumin
BTS	N-benzyl-p-toluenesulfonamide
bw	Body weight
C	
$CaCl_2$	Calcium dichloride
cAMP	Cyclic adenosine monophosphate

Cas9	CRISPR associated protein 9
ChR	Channelrhodopsin
CICR	Calcium-induced calcium release
CRISPR	Clustered regularly interspaced short palindromic repeats
Cl^-	Chloride
c_{max}	Maximal concentration
CMV	Cytomegalovirus
c-Myc	Cellular myelocytomatosis
crRNA	crisprRNA
CsA	Cyclosporin A
CTMV	Consulting Team Machine Vision
cTnt	Cardiac troponin T
CTZ	Coelenterazine
CVD	Cardiovascular disease

D

d	Day
DAB	3,3'-Diaminobenzidin
DAPI	4',6-Diamidino-2-phenylindol
diH2O	Deionized water
DMEM	Dulbecco's Modified Eagle Medium
DMSO	Dimethyl sulfoxide
DNA	Deoxyribonucleic acid
dNTP	Deoxynucleoside triphosphate
DPBS	Dulbecco's phosphate buffered saline

E

E. coli	*Escherichia coli*
EB	Embryoid body
EC_{50}	Half maximal effective concentration
ECG	Electrocardiogram
EDTA	Ethylenediaminetetraacetic acid
EF1α	Eukaryotic translation elongation factor 1 alpha 1
EGFP	Enhanced green fluorescent protein
EHT	Engineered heart tissue
E_{rev}	Reversal potential
ESC	Embryonic stem cell
EYFP	Enhanced yellow fluorescent protein

F

F	Forward
FACS	Fluorescence-activated cell sorting
FBS	Fetal bovine serum
FITC	Fluorescein isothiocyanate

FSC	Forward scatter
FTDA	bFGF, TGF-β1, dorsomorphin and activin A-based hiPSC culture medium

G

g	Relative centrifugal force
G	Gauge
GLucM23	*Gaussia* Luciferase mutant 23
GlyR	Glycine receptor
GOI	Gene of interest
GtACR1	*Guillardia theta* anion channelrhodopsin-1

H

h	Hours
HA	Homology arm
HBSS	Hank's balanced salt solution
HCl	Hydrochloride
HCN4	hyperpolarization-activated cyclic nucleotide-gated channel 4
HDR	Homology-directed repair
HEPES	4-(2-hydroxyethyl)-1-piperazineethanesulfonic acid
hERG	Human E*ther-à-go-go*-related Gene
hESC	Human ESC
HF	Heart failure
hiPSC	Human iPSC
hrGFP	Humanized *Renilla reniformis* green fluorescent protein
HSA	Human serum albumin
Hz	Hertz

I

I_{CaL}	L-type calcium current
iChloC	Improved chloride-conducting channel
ICPT	Institute of Clinical Pharmacology and Toxicology
IEPT	Institute of Experimental Pharmacology and Toxicology
I_f	Pacemaker current (funny current)
IF	Immunofluorescence
IGF-1	Insulin-like growth factor-1
I_{K1}	Inward rectifier potassium current
I_{KaCh}	Muscarinergic-gated potassium current
I_{Kr}	Rapid delayed rectifier potassium current
I_{Ks}	Slow delayed rectifier potassium current
I_{Kur}	Ultra-rapid delayed rectifier potassium current
IL-10	Interleukin-10
iLMO	Inhibitory Luminopsin
I_{Na}	Sodium current

i.p.	Intraperitoneal
IPD	Ion pore domain
iPSC	Induced pluripotent stem cell
IRES	Internal ribosome entry site
I_{to}	Transient outward current
i.v.	Intravenous

K

kb	Kilobase
KCl	Potassium chloride
KH_2PO_4	Potassium dihydrogen phosphate
Klf4	Kruppel-like factor 4

L

LAD	Left anterior descending artery
LB	Lysogeny broth
LBD	Ligand binding domain
LDL	Low density lipoprotein
LMO	Luminopsin
LTCC	L-type Calcium channels
LV	Left ventricle
LVAD	Left ventricular assist device
LVDP	Left ventricular developed pressure
LVID;d	Left ventricular inner diameter diastolic
LVID;s	Left ventricular inner diameter systolic

M

M	Molar
mA	Milliampere
mAChR	Muscarinic acetylcholine receptor
Mb	Mega base
MD	Medical doctor
mesDa	Mesencephalic dopaminergic
$MgCl_2$	Magnesium chloride
MHC	Myosin heavy chain
min	Minute
MKH	Modified Krebs-Henseleit
MLC2a	Myosin regulatory light chain 2, atrial isoform
MLC2v	Myosin regulatory light chain 2, ventricular isoform
mM	Millimolar
mmHg	Millimeter mercury
M-mode	Motion-mode
mN	Millinewton
MOI	Multiplicity of infection

MRA	Mineralocorticoid receptor antagonist
mRNA	Messenger RNA
mW	Milliwatt
MYH	Myosin heavy chain

N

Na_2HPO_4	Di-sodium hydrogen phosphate
nAChR	Nicotinic AChR
NaCl	Sodium chloride
$NaHCO_3$	Sodium hydrogen carbonate
NE	Norepinephrine
NEAA	Non-essential amino acids
NHEJ	Non-homologous end joining
NIH	National institutes of health
NpHR	*Natronomonas* Halorhodopsin
NSC	Neural stem cells

O

Oct3/4	Octamer-binding transcription factor 3/4
OXPHOS	Oxidative phosphorylation system

P

p	Photon
PAM	Protospacer adjacent motif
PCI	Percutaneous coronary intervention
PCR	Polymerase chain reaction
PEI	Polyethylenimine
P_i	Inorganic phosphate
PKA	Proteinkinase A
pM	Picomolar
PPP1R12C	Protein Phosphatase 1 Regulatory Subunit 12C
PSAM	Pharmacologically selective actuator module
PSAX	Parasternal short axis
PSC	Pluripotent stem cell
PSEM	Pharmacologically selective effector molecule
PSLAX	Parasternal long axis

R

R	Reverse
RAS	Renin–angiotensin system
RH	Relative humidity
RNA	Ribonucleic acid
RNP	Ribonucleoprotein particle
ROS	Reactive oxygen species

rpm	Rounds per minute
RPMI	Roswell Park Memorial Institute
RT	Relaxation time
RyR	Ryanodine receptor

S

sc	Subcutaneous
SD	Standard deviation
sec	Second
SEM	Standard error of mean
SERCA	Sarco/endoplasmic reticulum Ca^{2+}-ATPase
SGLT2	Sodium/glucose cotransporter 2
sgRNA	Single guide RNA
SOC	Super optimal broth with Catabolite repression
Sox2	Sex-determining region Y-Box transcription factor 2
SR	Sarcoplasmic reticulum
Sr	Steradian
SSC	Sideward scatter
SSEA3	Stage-specific embryonic antigen 3
ssODN	Single-stranded oligodeoxynucleotide

T

T-tubule	Transversal tubule
TAE	Tris acetate EDTA
TALEN	Transcription activator-like effector nuclease
TBS	Tris-buffered saline
TGF-β1	Transforming growth factor β1
TnC	Troponin C
TnI	Troponin I
TnT	Troponin T
tracrRNA	Trans activating crRNA
TRIS	Tris(hydroxymethyl)aminomethane
TTP	Time to peak

U

U	Unit
µM	Micromolar

V

V	Volt
v/v	Volume percent
VChR1	*Volvox* Channelrhodopsin
V_{max}	Maximal upstroke velocity

W

W	Watt
w/v	Mass concentration
WGA	Wheat germ agglutinin
WNT	Wingless-related integration site

Y

YLL	Years of life lost

Z

ZFN	Zinc-finger nuclease
ZVAD-fmk	Z-Valine-Alanine-Asparagine-(OMe) fluoromethyl ketone

1 ZUSAMMENFASSUNG

Die Transplantation von stammzell-abgeleiteten Kardiomyozyten hat sich innerhalb der letzten zwanzig Jahre zu einer potentiell neuartigen Therapieform für Patient*innen mit Herzinsuffizienz entwickelt. Sowohl in Klein- als auch Großtiermodellen wurde die Wirksamkeit gezeigt. Aufgrund dieser erfolgsversprechenden Ergebnisse wurden erste klinische Studien im Jahr 2021 begonnen. Jedoch ist der Wirkmechanismus nicht vollständig geklärt. Es ist unbekannt, ob die transplantierten Kardiomyozyten zur Kraftentwicklung des linken Ventrikels beitragen. In dieser Arbeit habe ich untersucht ob die transplantierten Kardiomyozyten zur Herzfunktion beitragen. Die zugrunde liegende Hypothese lautet, dass das selektive und reversible Ausschalten der Kontraktion der transplantierten Kardiomyozyten zu einer Verringerung der linksventrikulären Funktion führen sollte. Nach Wiederanschalten sollte eine Vergrößerung der Funktion erfolgen. Dies würde zeigen, dass die transplantierten Kardiomyozyten zur Kraftentwicklung beigetragen haben.

Zu diesem Zweck habe ich vier neue induzierte pluripotente Stammzelllinien (iPSCs) mittels CRISPR/Cas9 hergestellt, die künstliche Ionenkanäle exprimieren. Die Aktivierung dieser Kanäle sollte dann zu einem elektrischen Stilllegen und damit zu einem Stoppen der Kontraktion dieser Zellen führen. Die vier Zelllinien können nach ihrer Art der Aktivierung der Ionenkanäle in zwei Gruppen unterteilt werden. Zwei Zelllinien exprimieren chemogenetische Kanäle: Der Kationenkanal (PSAM 5HT3) und der Anionenkanal (PSAM GlyR) können durch das Substrat $PSEM^{89S}$ aktiviert werden. Die anderen Zelllinien sind chemo- und optogenetisch und exprimieren eine Luciferase, gekoppelt and einen optogenetischen Kationenkanal (LMO4) oder Anionenkanal (iLMO4). Diese Kanäle können durch das Substrat der Luciferase Coelenterazin aktiviert werden. Coelenterazin wird durch LMO4/iLMO4 umgewandelt. Hierdurch entsteht Licht, welches den gekoppelten optogenetischen Kanal aktiviert. Alternativ kann direkt Licht zur Aktivierung der Ionenkanäle genutzt werden. Sowohl in iPSCs als auch daraus abgeleiteten Kardiomyozyten wurden die Transgene exprimiert und waren funktional.

Aus iPSC-Kardiomyozyten wurden EHTs hergestellt. PSAM GlyR EHTs konnten mit $PSEM^{89S}$ gestoppt werden, während PSAM 5HT3 EHTs nicht stoppten. In den optogenetischen Linien konnten iLMO4 EHTs mit Lichtpulsen gestoppt werden, während LMO4 EHTs weiter schlugen und der gegebenen Frequenz folgten. Coelenterazin hatte unerwartet nachteilige Effekte auf EHTs und wurde deshalb nicht weiterverwendet.

Aufgrund dieser Resultate wurden PSAM GlyR und iLMO4 für weitere Analysen ausgewählt. PSAM GlyR EHTs entwickelten sich ähnlich wie Kontroll-EHTs. Zugabe von $PSEM^{89S}$ stoppte die Kontraktion von PSAM GlyR EHTs. iLMO4 EHTs entwickelten geringere Kräfte und waren heterogener. Während Kontroll-EHTs durch elektrische Stimulation bis zu einer Frequenz von 4 Hz stimuliert werden konnten, folgten iLMO4 EHTs nur bis 2.75 Hz.

Nachdem ich zwei Zelllinien generiert hatte, die reversibel ausgeschaltet werden konnten, war es nun möglich meine Hypothese im Meerschweinchen-Modell testen. Zunächst wurde eine Pharmakokinetikstudie zu PSEM^{89S} durchgeführt um herauszufinden, ob ausreichende Serumkonzentrationen erreicht werden können. Hierbei zeigte sich, dass eine ausreichende PSEM^{89S} Konzentrationen nur schwer erreicht werden konnte. Deshalb habe ich ein Langendorff-System etabliert, um die Herzfunktion ex vivo zu analysieren. Zudem konnten so iLMO4-Kardiomyozyten eingesetzt werden, weil eine direkte Lichtapplikation in vivo nicht möglich wäre.

Im Meerschweinchenmodell wurde eine Kryoverletzung des linken Ventrikels verursacht. Eine Woche nach der Induktion der Verletzung wurden entweder PSAM GlyR, iLMO4 oder Kontroll-Kardiomyozyten ($20x10^6$) transplantiert. Alle Kardiomyozyten-Zelllinien überlebten die Transplantation und zeigten ähnliche Transplantatgrößen. Zudem stabilisierte die Kardiomyozytentransplantation die Herzfunktion. Unerwarteterweise hatte PSEM^{89S} einen negativ inotropen und negativ chronotropen Effekt auf Meerschweinchenherzen im Langendorff-Modell, unabhängig von der transplantierten Zelllinie. Aus diesem Grund konnte mit diesem Ansatz der Einfluss von transplantierten Kardiomyozyten auf die Herzfunktion nicht untersucht werden. Jedoch zeigte sich im Langendorff-System nach der Transplantation von iLMO4 Kardiomyozyten ein Abfall der linksventrikulären Funktion bei Lichtapplikation. Nach Ausschalten des Lichts erholte sich die Funktion. Dieser Effekt war frequenzabhängig: So zeigte sich kein signifikanter Effekt, wenn die Herzen elektrisch bei höherer Frequenz stimuliert wurden. Dieses Resultat passte zu den in vitro Resultaten die zeigten, dass iLMO4 EHTs nicht verlässlich über 2.75 Hz stimuliert werden konnten.

Abschließend lässt sich sagen, dass ich zum ersten Mal in dieser Arbeit zeigen konnte, dass transplantierte Kardiomyozyten aktiv an der Herzarbeit beteiligt sind. Dies ist ein erster Schritt um zu verstehen, wie die Kardiomyozytentransplantation Patient*innen in der Zukunft helfen kann.

2 SUMMARY

Induced pluripotent stem cell (iPSC)-derived cardiomyocyte transplantation has evolved into a potential novel therapeutic option for heart failure patients in the past twenty years. It has shown efficacy in both small and large animal models. Because of these promising results, the first clinical studies have started in 2021. However, the mechanism of action is not understood. It is still unknown if the transplanted cardiomyocytes contribute to force generation of the left ventricle. In this work, I aimed to investigate if transplanted cardiomyocytes contribute to left ventricular function after transplantation. I hypothesized that selectively and reversibly switching off cardiomyocyte contractility only in engrafted cardiomyocytes will result in a drop in left ventricular function. Switching cardiomyocytes back on should result in recovery of cardiac function. This could indicate that the engrafted cells contribute to left ventricular force.

For this, I created four novel iPSC lines using CRISPR/Cas9 expressing artificial ion channels, hypothesizing that their activation will lead to electrical silencing and thereby switching off contractility. The four approaches were divided into two groups by their mode of activation. Two cell lines expressed a chemogenetic construct, meaning that the artificial cation (PSAM 5HT3) or anion (PSAM GlyR) channels can be activated by the small molecular substrate PSEM^{89S}. The other two cell lines were chemo- and optogenetic cation (LMO4) and anion (iLMO4) channels, consisting of a luciferase coupled to an optogenetic channel. Coelenterazine, the luciferase substrate, is converted, producing light that activates the fused optogenetic channel. Alternatively, direct activation by light can be used. In iPSCs and differentiated cardiomyocytes, the four transgenes were expressed and functional. PSAM GlyR cardiomyocytes, cast into EHTs, could be stopped with PSEM^{89S}, while PSAM 5HT3 EHTs were not affected. In the optogenetic lines, iLMO4 EHTs could be stopped using light pulses while LMO4 EHTs continued to beat and followed the light pulse frequency. Coelenterazine had unexpected detrimental effects on EHTs and was therefore not further used.

Hence, PSAM GlyR and iLMO4 were chosen for further thorough analysis. PSAM GlyR EHTs developed similarly to control EHTs. PSAM GlyR EHTs stopped to contract immediately upon PSEM^{89S} application. iLMO4 EHTs showed lower force generation and were overall more heterogenous. iLMO4 EHTs could not be electrically paced reliably above 2.75 Hz compared to control EHTs which could be paced up to 4 Hz.

With two cell lines that could reversibly be switched off, we aimed to test our hypothesis in a guinea pig model. Beforehand, we conducted a pharmacokinetic study, which revealed that sufficient PSEM^{89S} concentrations were difficult to reach in guinea pigs. Therefore, I set out to assemble a Langendorff system to assess cardiac function ex vivo. This allowed us to use iLMO4 cardiomyocytes because in vivo light application would have been impossible.

We then transplanted PSAM GlyR, iLMO4, or control cardiomyocytes ($20x10^6$) in a cryoinjury guinea pig model. Cardiomyocytes from all cell lines engrafted and showed similar graft sizes.

Cardiomyocyte transplantation stabilized left ventricular function. Unexpectedly, PSEM^{89S} had a negative inotropic and chronotropic effect on guinea pig hearts in the Langendorff system, regardless of the transplanted cell line. Therefore, we could not assess the degree of contribution of the engrafted cells to left ventricular function with this approach. However, after transplantation of iLMO4 cardiomyocytes, we observed an immediate decline in left ventricular function upon light application in the Langendorff system. Upon the termination of light application, the left ventricular function recovered. Interestingly, this effect was frequency-dependent, i.e., the contribution was smaller under electrical pacing than at a higher frequency. This finding fits the in vitro results, where iLMO4 EHTs could not be paced reliably above 2.75 Hz.

In conclusion, I was able to show for the first time that transplanted cardiomyocytes can actively contribute to left ventricular function, which is the first step into understanding how cardiomyocyte transplantation can potentially benefit patients in the future.

3 INTRODUCTION

3.1 Cardiovascular Disease Is a Massive Health Burden

Cardiovascular disease (CVD) is a massive global health burden. A total of 523 million people are affected worldwide, and this number has doubled since 1990 (Roth et al. 2020). Risk factors for CVD can be categorized as non-modifiable and modifiable. Non-modifiable risk factors are genetic predisposition, sex, and age (Levy and Kannel 1988). In addition, it was recently discovered that age-related clonal hematopoiesis is an additional risk factor for CVD (Jaiswal et al. 2017; Burns and Kapur 2020). Modifiable risk factors include high blood pressure, high blood glucose (diabetes), high low-density lipoprotein (LDL) blood content (dyslipidemia), and a high body mass index (BMI). Hence, the risk for CVD is, to a certain degree, dependent on lifestyle choices such as smoking behavior, nutrition, and physical activity (Levy and Kannel 1988; Roth et al. 2020).

In Germany, atherosclerotic cardiovascular disease is the number one cause of death (73,459 people in 2019; Figure 1). On positions four and five following acute myocardial infarction (AMI; 44,282) and heart failure (35,297; Figure 1). If the overlap between these categories is excluded, all CVDs caused 194,197 deaths in 2019, making up 53.9% of total deaths (Statistisches Bundesamt 2021). This number highlights the importance of CVD research; however, CVD research is chronically underfunded. One study investigated disease burden as "years of life lost" (YLL) and connected this to the National Institutes of Health (NIH) funding. The results give an estimate of the funding allocated to a disease in relation to its morbidity. While breast cancer research receives around $900 per YLL (place 1), ischemic heart disease receives only $200 (place 7). The same holds when relating funding to mortality. While breast cancer research receives around $20,000 per death (place 1), ischemic heart disease receives only $2,600 (place 7) (Stockmann et al. 2014).

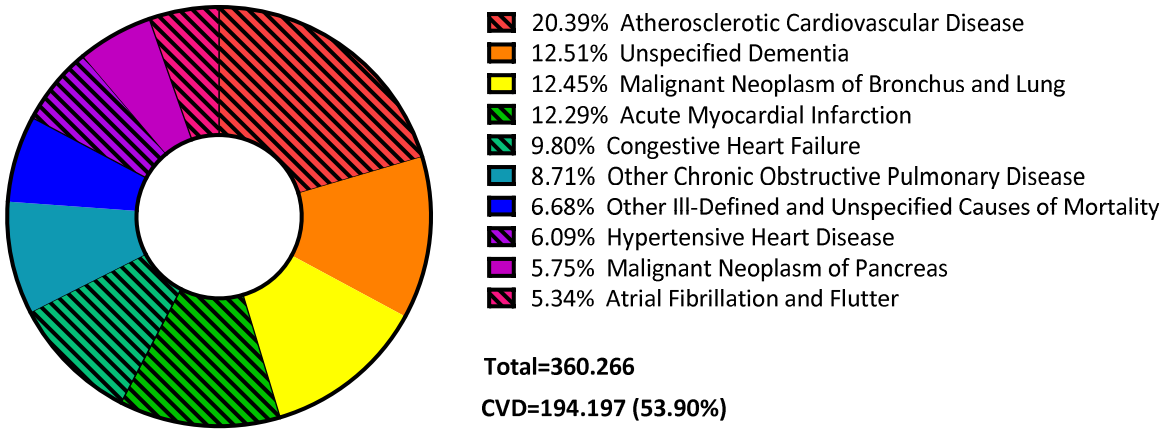

Figure 1: Causes of death in Germany, 2019, classified by ICD-10. Stripes highlight CVD-deaths, which make up 53.90% of all deaths. Data obtained from Statistisches Bundesamt 2021.

3.2 The Human Heart

The heart is a hollow muscular organ responsible for maintaining blood circulation in the body. The right heart, consisting of the right atrium and right ventricle, receives blood from the body circulation via the superior and inferior vena cava and pumps blood through the lungs via the arteria pulmonalis. The left heart is responsible for systemic blood circulation. It receives blood via the pulmonary veins and ejects blood into the aorta. Blood is then recirculated via the vena cava to the right atrium, thereby closing the circuit.

3.2.1 Heart Cycle

The repeating pump cycles of the heart to assert its function of supplying the body with oxygen and nutrients are divided into systole and diastole. Electrical activation and Ca^{2+} release trigger actin-myosin interactions and sarcomere shortening during systole. Hence, the left ventricle (LV) contracts, increasing pressure. When the LV pressure exceeds the atrial pressure, the mitral valve closes while the aortic valve is still closed, leading to the first phase of isovolumic contraction. LV pressure further increases, and when it exceeds aortic pressure, the aortic valve opens, and ejection starts.

During diastole, the sarcoplasmic reticulum (SR) takes up previously released Ca^{2+}, the actin-myosin interactions loosen, and relaxation starts. LV pressure decreases and drops below aortic pressure, the aortic valve closes, and ejection stops. The intraventricular pressure then drops below atrial pressure. The mitral valve opens, allowing blood to enter the LV. Once pressures in the atrium and LV equalize, filling ceases. This phase is followed by atrial systole that acts as a booster for LV filling. Diastole ends here, and the heart cycle starts over (Libby et al. 2008).

3.2.2 Contraction Mechanism and Ultrastructure

Although making up 75% of the heart's volume, cardiomyocytes make up only one-third of all cells in the heart. Hence, cardiomyocytes are large cells filled mainly with myofibrils, the functional unit of contraction, and mitochondria to supply the large amounts of adenosine tri-phosphate (ATP) needed to conduct contractions. The sarcolemma has many invaginations, the transversal (T)-tubules. These structures extend to the inside of the cell, harboring the L-type calcium channels (LTCC). An incoming action potential (AP) then triggers LTCC opening and Ca^{2+} release from the SR. This process is exerted by ryanodine receptors (RyR). During a contraction cycle, cytoplasmic Ca^{2+} increases 100-fold from 10^{-7} to 10^{-5} M (Libby et al. 2008).

The major proteins involved in cardiomyocyte contraction are actin, myosin, tropomyosin, titin, and the troponin (Tn) complex. These proteins are organized in the functional unit of all muscle cells called a sarcomere. Sarcomeres are serially organized within a cardiomyocyte. Each sarcomere spans from one Z-disc to the next. Connected to the Z-disc are filamentous actin molecules, spanning to roughly the middle of a sarcomere. Two actin filaments are intertwined with a tropomyosin molecule (thin filament). In regular intervals along the actin/ tropomyosin filament, the Tn complex, containing TnC, TnI, and TnT, is located.

In contrast to actin, myosin is not directly connected to the Z-disc but via the elastic spring-like protein titin. The myosin filament consists of several individual myosin heavy chain (MHC) molecules intertwined in their tail region (thick filament). The head part of each MHC acts as a motor protein. During a contraction, the head and neck parts flex while binding to actin, moving the two filaments alongside each other. This movement shortens the sarcomere (moving the Z-discs into closer proximity), performing a muscle contraction. For relaxation, titin plays an important role. Titin's extensible, spring-like part centers the thick filament between two Z-discs. This becomes especially important during relaxation where titin recoils, recentering the thick filaments. Additionally, titin serves as a strain-sensor, increasing Ca^{2+}-sensitivity upon sarcomere stretching (Libby et al. 2008; Linke 2018).

A sarcomere contraction is dependent on Ca^{2+} in the cytoplasm, released from or taken up by the SR. Under low Ca^{2+} conditions, the Tn/tropomyosin complex prevents actin from interacting with myosin. Upon Ca^{2+} release during depolarization, Ca^{2+} binds to TnC, leading to a conformational change that decreases the inhibitory effect of TnI on actin/ tropomyosin. Tropomyosin can now be repositioned, allowing the actin to form cross-bridges with myosin to exert a contraction. The myosin head has two essential domains: the actin-binding and ATPase domains. Upon ATP binding to the myosin head, it releases from actin. ATP is then hydrolyzed to adenosine diphosphate (ADP) and inorganic phosphate (P_i), which decreases the probability of actin-binding. Upon P_i release, myosin strongly binds to actin, and a power stroke of the head moves the actin and myosin filaments 10 nm along each other. ADP is then released from the myosin head, and another contraction cycle can begin when ATP binds to the myosin head. Contraction comes to a halt when Ca^{2+} decreases because of reuptake in the SR via sarcoplasmic reticulum calcium ATPase (SERCA). The subsequent depolarization then can induce another contraction (Libby et al. 2008).

The heart is innervated to adjust the force and frequency of contractions. Sympathetic norepinephrine (NE) release and β-receptor activation raises the influx of Ca^{2+}, thereby increasing contraction force (positive inotropic) in cardiomyocytes. In addition, phospholamban gets phosphorylated, which relieves its inhibitory effect on SERCA-mediated Ca^{2+} uptake into the SR. This process decreases the relaxation time (positive lusitropic) (Libby et al. 2008). In addition, NE activates cyclic adenosine monophosphate (cAMP) production in the sinus node, which increases heart rate (positive chronotropic) (Libby et al. 2008; Fenske et al. 2020).

3.2.3 Electric Conduction

Electrical signals trigger the contraction of cardiomyocytes. The sarcolemma of cardiomyocytes contains ion channels and ion transporters that translate the incoming electrical signal into a mechanical contraction. The totality of ion fluxes shapes the membrane potential over time, integrated by the cardiac AP, consisting of five phases (Figure 2).

Phase 4: Resting Membrane Potential

The resting membrane potential of cardiomyocytes is around -80 to -90 mV (Figure 2). That is due to an abundance of open K^+ channels with an equilibrium potential of -94 mV. Due to the constant activity of the Na^+ K^+ pump, which constantly moves Na^+ outwards and K^+ inwards (against the concentration gradient), intracellular Na^+ remains low, while K^+ is high.

Phase 0: Upstroke

The upstroke phase is characterized by a sudden depolarization of the cardiomyocyte within 1-2 ms. This depolarization is triggered in an "all-or-none" manner when a threshold potential of -70 mV is reached. Within 1-2 ms, the membrane potential rises around 110 mV to values of +30 mV (Figure 2). Voltage-gated sodium channels are responsible for the fast upstroke, leading to a rapid inward current (influx of Na^+, along their electrochemical gradient; I_{Na}; Figure 2). As the Na^+ channels are voltage-gated, they quickly become inactivated during depolarization. The voltage-gated LTCC opens as soon as the threshold of ~-50 mV is reached.

Phase 1: Early Rapid Depolarization

In this phase, the membrane potential drops from 30 mV to 0 mV because the inward sodium current is inactivated, while a short K^+ flux out of the cardiomyocyte leads to slight repolarization (I_{to} and I_{Kur}; Figure 2).

Phase 2: Plateau Phase

The plateau phase makes up the majority of time during an AP. The plateau occurs because there is an outward current of K^+ (I_{Ks} and I_{Kr}) and Cl^-, as opposed to an inward current from LTCCs. The

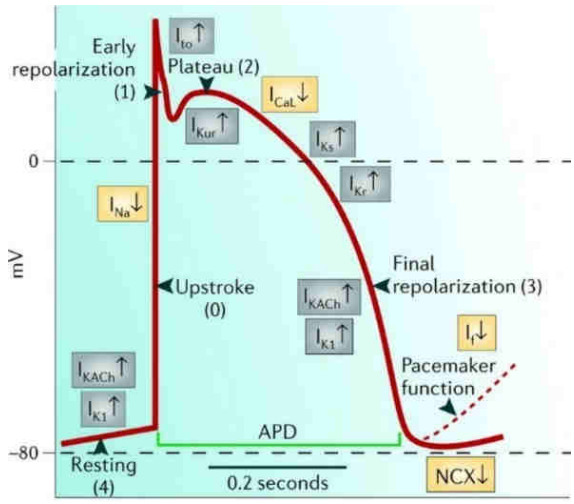

Figure 2: Action potential of cardiomyocytes. Phase 0, the upstroke, is characterized by sudden Na^+ inward flow, leading to depolarization. Early depolarization (1) occurs due to K^+ efflux. The plateau (2) is maintained because of I_{CaL} opposing I_{Ks} and I_{Kr}. Next, repolarization (3) is caused by repolarizing K^+ flow. Then the resting membrane potential (4) is reached and maintained until the next action potential reaches the cardiomyocyte. Reprinted from "Cardiac Ion Channels" by Grant, Circulation: Arrhythmia and Electrophysiology. Volume 2, pages 185–194 (2009).

open LTCCs lead to calcium-induced calcium release (CICR) and contraction of the sarcomeres (I_{CaL}; Figure 2).

Phase 3: Final Rapid Repolarization

The activation of repolarizing K^+ currents (I_{KACh}, I_{K1}) characterizes the rapid repolarization. The whole AP of a human cardiomyocyte lasts 200-300 ms (Libby et al. 2008; Grant 2009).

The electrical signal that triggers cardiomyocyte contraction originates from the sinus node between the superior vena cava and the right atrium. The pacemaker cells of the sinus node are characterized by spontaneous depolarization. This unique feature arises from the presence of I_f, the hyperpolarization-activated current. In contrast to ventricular cardiomyocytes, pacemaker cells have no stable resting potential. Whenever repolarization occurs after an AP, the I_f current immediately depolarizes the cell again, leading to a spontaneous contraction rhythm, the sinus rhythm. Neuronal signals regulate this rhythm. Postganglionic innervation occurs from sympathetic (adrenergic) and parasympathetic (cholinergic) terminals. NE, the adrenergic messenger molecule, binds to β-adrenergic receptors in pacemaker cells, causing a positive chronotropic effect mainly mediated by the activation of I_f and calcium channels. M2-muscarinergic activation (parasympathetic) leads to opposing effects. Activation leads to hyperpolarization of cells by activation of I_{KACh} and inhibition of I_f; hence, reducing the rate of depolarization causes a negative chronotropic effect. Electrical signals generated by the sinus node are conducted via the atria to the atrioventricular (AV) node and from there to the bundle of His, ultimately to the Purkinje fibers and ventricular cardiomyocytes (Libby et al. 2008).

3.2.4 Acute Myocardial Infarction and Heart Failure

Acute myocardial infarction (AMI) is characterized by acute myocardial injury detected by cardiac Tn elevation in the blood and through evidence of acute myocardial ischemia such as typical electrocardiogram (ECG) changes, loss of viable myocardium observed with imaging techniques, or thrombus detection (Thygesen et al. 2019).

Myocardial ischemia describes the lack of coronary blood flow having immediate consequences for the myocardium and coronary vessels (Heusch 2019). In most cases, this is the consequence of coronary vessel occlusion through an atherosclerotic plaque (DeWood et al. 1980). The rupture or erosion of such an atherosclerotic plaque in a coronary artery sets free its thrombogenic contents leading to platelet activation and induction of coagulation. A thrombus forms and plaque debris can occlude the vessel (Reed et al. 2017). The myocardium previously supplied by this vessel is quickly affected and is considered the area at risk (AAR). Contractility of the AAR can reduce within 60 seconds of ischemia onset (Jennings 2013). With increasing ischemic time, the infarct spreads from subendocardial to subepicardial regions like a wave front and can become a transmural infarct (Reimer et al. 1977; Reimer and Jennings 1979).

Upon coronary occlusion, the oxygen-underserved AAR switches from aerobic to anaerobic glycolysis (Jennings 2013). The switch to anaerobic glycolysis leads to a decline in ATP concentrations because of the inefficient ATP production. In addition, lactate and H^+ accumulate, leading to acidosis. A further consequence of acidosis is disturbed ion balance which can be the source of arrhythmia when electrical activity persists (Buja 2005; Jennings 2013). Ion imbalance and acidosis lead to mitochondria and SR swelling and alterations in myofibrils, reducing contractility. The metabolic changes caused by mitochondria swelling and acidosis lead to reactive oxygen species (ROS) accumulation. This accumulation quickly induces irreversible cardiomyocyte injury via sarcolemma disruption (Buja 2005; Jennings 2013). Therefore, released cellular components such as cardiac Tn can be used as a diagnostic tool, currently the primary method for detecting AMI (Thygesen et al. 2019). Ultimately, coronary occlusion results in cardiomyocyte necrosis and apoptotic cell death in the AAR as fast as 20 minutes after AMI (Buja 2005; Burke and Virmani 2007; Libby et al. 2008; Heusch 2019). Therefore, it is not surprising that the infarct size is determined by the duration of ischemia (Reimer et al. 1977; Reimer and Jennings 1979) and the number of collateral arteries (Miura et al. 1987).

However, ischemic cardiomyocytes can be salvaged when reperfused, reducing the potential infarct size (Ginks et al. 1972; Jennings 2013). Hence, the most critical intervention is reperfusion by reopening occluded vessels via percutaneous coronary intervention (PCI). Reperfusion therapy should be initiated as soon as possible after diagnosing AMI (Van De Werf 2014; Ibanez et al. 2018; Collet et al. 2020). However, reperfusion comes with its own consequences. The sudden increase in blood supply in the infarcted region leads to an activation of the inflammatory cascade and ROS accumulation leading to further functional impairment of the myocardium and more cell death (Buja 2005; Jennings 2013). Nevertheless, the benefit of reperfusion, the salvaging of cardiomyocytes at risk, outweighs the reperfusion-inflicted myocardial injury if performed quickly enough (Buja 2005). Experimentally, preconditioning, postconditioning, and pharmacological interventions can reduce reperfusion injury, but these approaches have not reached the clinic yet or were unsuccessful (Ibáñez et al. 2015).

After these immediate consequences of myocardial ischemia, the AAR will undergo several cellular and molecular changes, eventually leading to a healed infarct. The ischemic area appears red when reperfusion occurs, and hemorrhaging and broken vessels can be observed histologically (Burke and Virmani 2007). After AMI, this first phase is the inflammatory phase lasting up to four days. Due to the extensive cell death, cytokines and chemokines are set free or secreted, and neutrophils infiltrate the AAR (Liehn et al. 2011). Neutrophil infiltration at first glance seems harmful because of their extensive ROS production (Dobaczewski et al. 2010; Liehn et al. 2011). Indeed, in experimental settings abolishing neutrophils from the infarct resulted in reduced infarct size (Jolly et al. 1986; Liehn et al. 2008). However, neutrophils are also crucial for monocyte recruiting, which clears the AAR of cardiomyocyte debris. Cleared of debris, the AAR is now mainly made up of fibrin, a provisional matrix prone to cardiac rupture. The proliferative

phase follows the inflammatory phase. Secretion of chemokines and cytokines, in particular transforming growth factor β1 (TGF-β1) and interleukin 10 (IL-10), induces angiogenesis and modulates immune cell function (Liehn et al. 2011), leading to the proliferative phase, which takes up to four weeks. Histologically, newly formed vessels can be observed and lymphocytic and plasma cell infiltration. Fibroblast numbers in the infarcted area increase due to the proliferation of fibroblasts in the border zone, migrating into the injured area (Burke and Virmani 2007; Fu et al. 2018). These fibroblasts adopt a myofibroblast phenotype, expressing α-smooth muscle actin (α-SMA) and periostin (Fu et al. 2018). The proliferative phase is characterized by angiogenesis and collagen synthesis, stabilizing the infarcted region. A healing phase follows it. During this phase (up to two months), the scar matures. Scar maturation includes extracellular matrix stabilization via cross-linking of collagen (Liehn et al. 2011) and (myo)fibroblast apoptosis (Dobaczewski et al. 2010). However, a recent study challenged this classical textbook knowledge and reported that the myofibroblasts do not die but adopt an α-SMA-negative, non-proliferative phenotype in the mature scar (Fu et al. 2018). Macroscopically, the infarct becomes white from scarring, and the ventricular wall is thinning (Burke and Virmani 2007). This remodeling process has several consequences. It leads to myocardial hypertrophy in the remaining myocardium (Rockey et al. 2015; Nakamura and Sadoshima 2018). The scar is also the source of arrhythmia, as myofibroblasts alter conduction velocity (Miragoli et al. 2006), and fibrosis correlates with arrhythmia/ sudden cardiac death (Wu et al. 2008). It is also important to note that cardiomyocytes do not repopulate the scar as these cells do not proliferate significantly, rendering the scar cardiomyocyte-scarce (Bergmann et al. 2015). Together these events can, over the years, result in heart failure (HF).

HF is a broad definition of a clinical syndrome that describes the progressive decline of heart function. This decline often starts with an index event such as AMI but can also be caused by chronic hypertension, myocarditis, or valvular heart disease. The decline in LV function leads to compensatory neurohormonal activation, including activation of the adrenergic nervous system, the renin-angiotensin system (RAS), and cytokines (Mann and Felker 1999; Libby et al. 2008). This perpetual neurohormonal activation leads to LV remodeling, further LV damage, and eventually cardiac decompensation (Mann and Felker 1999). 1-2% of the adult population is suffering from HF. In the elderly population (>70 years of age), the number is even higher, and about 10% are suffering from HF, making it a disease of the elderly (Ponikowski et al. 2016). Worldwide, about 23 million adults are suffering from the consequences of HF (Bui et al. 2011). After hospitalization, 17-45% of HF patients die within one year. In Germany, 0.5% of the population is hospitalized because of HF each year (Vogel 2020). Albeit improvements in evidence-based medicine and patient management have prolonged the life expectancy, the survival of HF patients is still low (Levy et al. 2006; Velagaleti et al. 2008; Ponikowski et al. 2014). However, a decline in mortality is observed during the last decade, attributed to improved treatment and guideline adherence (Vogel 2020). As previously mentioned, HF prevalence is increasing with age. An aging population plus improved patient care causes more HF cases leading to a worldwide economic, social, and

personal burden (Ponikowski et al. 2014). The costs for HF patient care are predicted to double by 2030 in the US (Heidenreich et al. 2013).

3.2.5 Heart Failure Therapy

Although HF exerts an increasing burden on the health care system, there are no therapeutical options that tackle the major underlying cause of HF, which is the loss of cardiomyocytes. Instead, pharmacological therapy aims to improve the clinical status, hospitalization ratio, and quality of life by acting on the remaining functional myocardium (Ponikowski et al. 2016). Therefore, drugs that antagonize the overshooting neurohumoral activation are used. Current guidelines recommend using angiotensin-converting enzyme (ACE) inhibitors (ACEI) which reduce RAS activity. ACEIs act on cardiac remodeling and were the first class of drugs that reduced mortality in heart failure patients (Ponikowski et al. 2016). β-blockers reduce mortality and morbidity in HF patients by lowering heart rate and contractility. Although these characteristics appear counter-intuitive, at first sight, the reduction of heart rate and contractility reduces O_2 consumption, therefore enhancing O_2 supply, improving cardiomyocyte survival, and substantially prolonging life expectancy (Aktories et al. 2013). ACEIs can be combined with β-blockers. In addition, Mineralocorticoid/aldosterone receptor antagonists (MRA) can be used, acting as diuretics that reduce blood pressure but are also thought to reduce cardiac remodeling (Aktories et al. 2013).

The combination of the angiotensin receptor blocker (ARB) valsartan with a Neprilysin inhibitor (sacubitril) showed a further reduction in morbidity and mortality compared to the ACEI enalapril (Docherty et al. 2020). Most recently, sodium-glucose cotransporter (SGLT2) inhibitors were introduced in heart failure therapy, further reducing hospitalization and mortality in HF patients (Packer et al. 2020; Zannad et al. 2020).

In many cases, though, pharmacological treatment is not enough. Therefore, two surgical options remain for advanced heart failure patients as a last measure. The first option is to implant a left ventricular assist device (LVAD). These mechanical circulatory support systems unload the failing LV and support end-organ perfusion (Ponikowski et al. 2016). However, LVAD therapy is associated with severe complications (Morgan et al. 2014; Mishra et al. 2017; Fuchs et al. 2019). Hence, LVADs are mainly an intermediate measure as a bridge to donor heart transplantation. Only when patients are ineligible for transplantation can an LVAD become a destination therapy which is becoming more common (Ponikowski et al. 2016; Fuchs et al. 2019).

The second option is heart transplantation. However, the availability of donor hearts is limited. 4477 heart transplantations were performed in 2013 worldwide as opposed to 23 million total HF patients (Bui et al. 2011; Lund et al. 2015). In Germany 2020, there were 913 post-mortem organ donors, but numbers have been slightly decreasing over the past two years. In 2020, 1120 people were on the donor organ waiting list. While 339 (30%) received a heart in Germany, 90 (8%) died while on the waiting list, and 420 (38%) patients were ineligible for transplantation (Deutsche Stiftung Organtransplantation 2021). These numbers are also in stark contrast to ~35.000 people

dying from HF in Germany per year (Statistisches Bundesamt 2021). Heart transplantation patients have a median survival of 11 years. 86% of transplanted patients survive the first year, which is the most critical period. After the one-year period, mortality decreases strongly (Lund et al. 2015). The downside of heart transplantation is the ongoing immunosuppression. Under-immunosuppression can lead to graft rejection. In the case of over-immunosuppression, patients have a high risk for infection, malignancy, or renal failure. Hence, patients need to be monitored regularly (Söderlund and Rådegran 2015).

In conclusion, the transplantation of donor hearts is the only curative option for HF. However, its use is limited by a lack of sufficient donor hearts and comes with immunological problems. Hence, novel therapy options are urgently needed.

3.3 Human Induced Pluripotent Stem Cells

Researchers have had a long-anticipated goal: To replace irreparable tissues or even whole organs such as the failing heart with patient-specific engineered cells or organs. The exploration of induced pluripotent stem cells got researchers one step closer to this goal.

Eukaryotic cells can have the potency to differentiate into more specialized cells. The degree of potency is organized in a hierarchy derived from embryonic development (Figure 3). The fertilized oocyte (zygote) is totipotent, meaning it can differentiate into all embryonic and extra-embryonic tissues (Figure 3). After several cell divisions, the zygote enters the blastocyst stage. One part, the so-called inner cell mass, will form the embryo later. These cells are defined as pluripotent: they can differentiate into all tissues of the three germ layers and, therefore, all embryonic tissues but not the extra-embryonic tissue placenta and yolk sac (Figure 3). The process of forming the three germ layers is called gastrulation. During gastrulation, the three germ layers, namely endoderm, mesoderm, and ectoderm, are formed (Figure 3). Cells of the germ layers are multipotent; they can give rise to many different cells and tissues but are limited to one germ layer. The mesoderm, one of the germ layers, will differentiate terminally via several intermediate steps into cardiomyocytes or endothelial cells. These terminally differentiated cells are defined as nullipotent (Figure 3) (Takahashi and Yamanaka 2016; Tewary et al. 2018).

One obvious source of pluripotent cells is the embryo itself. Embryonic stem cells (ESC) can be obtained from the blastocyst; however, the blastocyst is destroyed in the process. The destruction of the blastocyst makes the procedure ethically problematic for human ESCs (Thomson et al. 1998).

Fortunately, in 2007 researchers came up with another source of human pluripotent cells. By introducing four transcription factors (c-Myc, Oct3/4, Sox2, and Klf4) retrovirally to somatic cells, they could reprogram these cells into a pluripotent state. These cells could then be differentiated into all three germ layers (Takahashi et al. 2007). Subsequently, instead of retrovirus, the four factors could be delivered via a Sendai virus. The advantage of the Sendai virus is that it does not integrate into the host genome, enhancing safety for patient application (Fusaki et al. 2009).

To use induced pluripotent stem cells (iPSC) for regenerative medicine, efficient ways to generate large and pure target cell populations had to be developed. Differentiation protocols that mimic embryonic development were developed for a plethora of different cell types. Today, 14 years after their discovery, there is a protocol for almost every cell type. The search terms "iPSC", "differentiation", and "protocol" resulted in 2,073 results on PubMed with a steady increase since iPSC discovery in 2007, highlighting the interest in hiPSCs and their progeny (as of 10.11.2021) (NIH 2021).

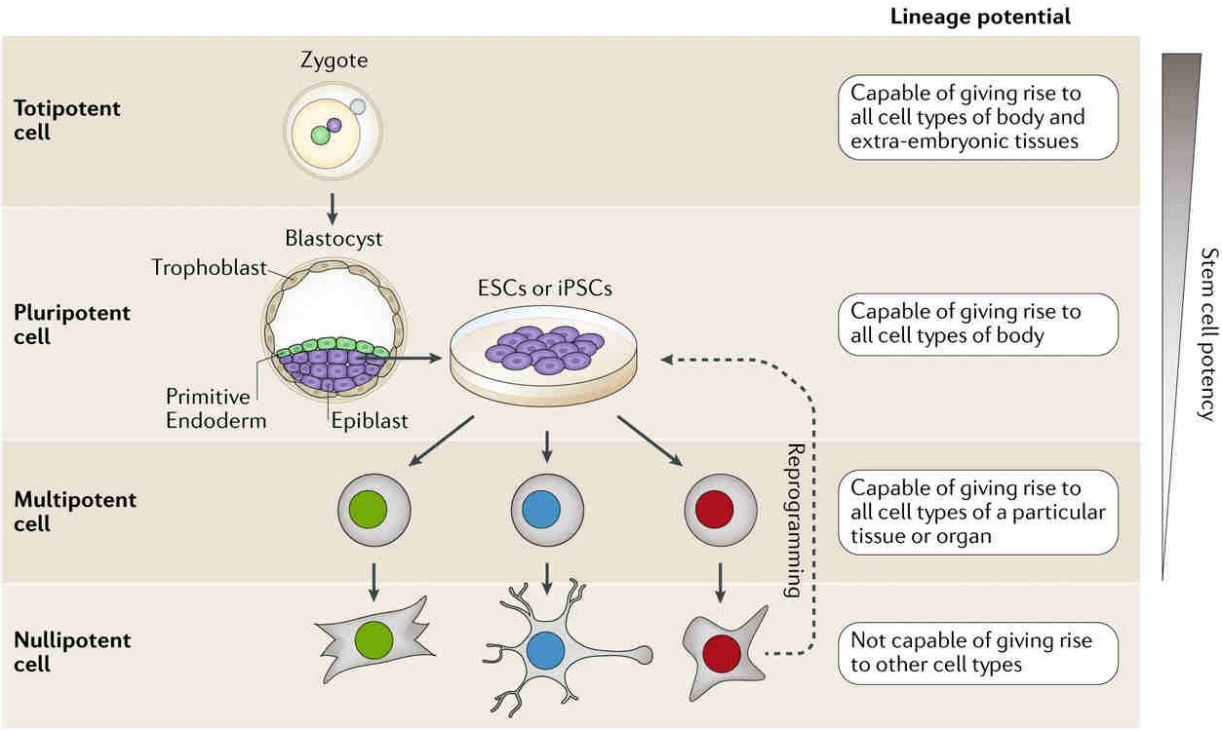

Figure 3: The stem cell hierarchy. Lineage potential of different cell types. Reprinted from "Stem cell bioengineering: building from stem cell biology" by Tewary et al., Nature Reviews Genetics, volume 19, pages 595–614 (2018).

3.3.1 Genetic Editing in hiPSCs

With the possibility of working with PSCs, it became essential to edit the genome of these cells to study genetic disorders or knock-in reporter genes such as fluorescing proteins or alter cell behavior, e.g., with optogenetic ion channels. For genome editing, precise cutting of genomic DNA is crucial to either knock-in or knock-out genes at a desired location in the genome. The CRISPR/Cas9 system virtually replaced all its predecessors in the last couple of years, such as transcription activator-like effector nucleases (TALEN) and Zinc-finger nucleases (ZFN). These proteins need to be engineered to recognize a specific DNA sequence, limiting their applications. In addition, synthesis and target validation remained a problem. The Cas9 enzyme as a dual-RNA-guided DNA endonuclease offers the advantage of RNA target recognition and avoids protein design for each target sequence. Cas9 requires a transactivating crisprRNA:crisprRNA (tracrRNA:crRNA) duplex to direct DNA cleavage. The tracrRNA:crRNA duplex, called single guide

RNA (sgRNA), possesses a 20 base pair (bp) sequence at the 5' end homologous to the targeted genomic sequence.

Additionally, a genomic protospacer adjacent motif (PAM) sequence, typically homologous to NGG, adjacent to the 20 bp sequence, is required to allow recognition. The sequence that follows downstream binds to the Cas9 enzyme. sgRNAs can be designed according to the researchers' wishes to recognize any target sequence (Doudna and Charpentier 2014).

There are physical and viral options to either deliver Cas9 enzyme or Cas9 mRNA. Viruses are rarely used because they are limited in packaging capacity, come with safety concerns, and are expensive. On the other hand, they are very efficient. For iPSCs, electroporation/ nucleofection is frequently used as a physical method to deliver Cas9. Cell death is a problem here, but there is no packaging capacity issue as with viruses, and the transfection efficiency is high (Liu et al. 2017). Typically, a direct enzyme delivery is preferred over Cas9 plasmids in iPSCs. This is because the preformed sgRNA-Cas9 ribonucleoprotein complex (RNP), unlike Cas9 plasmids, cannot integrate into the genome. In addition, with Cas9, plasmids expression is maintained for days, leading to more off-target effects. Hence RNP or mRNA delivery is preferred, although rapid degradation potentially occurs (Kim et al. 2014; Liang et al. 2015).

The genomic location is important not to alter pluripotency or disrupt other genes for the knock-in of additional genes. It was shown that disruption of the Protein Phosphatase 1 Regulatory Subunit 12C (PPP1R12C) gene has no adverse effect on the targeted cells and is therefore considered a "safe harbor" for gene integration (Smith et al. 2008). PPP1R12C is located on chromosome 19. A region in intron 1 is called adeno-associated virus integration site 1 (AAVS1) because it was shown that adeno-associated virus 2 (AAV2) could integrate into the genome here (Kotin et al. 1992). Transgene integration is not subject to silencing since the locus maintains an open chromatin structure (Ogata et al. 2003). In hESC, transgenes were consistently expressed when integrated into AAVS1. This expression was maintained after differentiation into the three germ layers (Smith et al. 2008). Similarly, transgene expression (in this case enhanced green fluorescent protein [EGFP]) was stable after differentiation and transplantation of hiPSC-derived cardiomyocytes (Luo et al. 2014).

Once the Cas9 enzyme enters the nucleus, it will introduce a double-strand break upstream of the PAM sequence. The DNA repair machinery of the cell will subsequently recognize the damage and begin the repair. The repair can happen either via non-homologous end joining (NHEJ) or homology-directed repair (HDR). NHEJ describes the re-ligation of the two separated DNA strands when no other DNA template is present. However, the process often creates small insertion/deletions, so-called Indels, leading to frameshift mutations and premature stop codons. This can be desired in the case of knock-out approaches. Alternatively, supplying a DNA template in the form of a plasmid or single-stranded oligodeoxynucleotide (ssODN), the HDR machinery can precisely edit the genome with the help of a template (Ran et al. 2013) (Figure 4). Diploid cells

such as human iPSCs can also perform HDR without an exogenous template using the sister chromatid or homologous chromosome. However, this means the machinery is only available in S and G2 phase when two sister chromatids are present (Musunuru et al. 2018). Hence it is not surprising that NHEJ dominates, and editing ratios of only 2-4% are reported for knock-in strategies (Mali et al. 2013). To enhance the HDR/ NHEJ ratio, different strategies have been employed. For example, a cold shock of 32 °C for up to 48 hours was shown to increase HDR events in iPSCs (Guo et al. 2018). Alternatively, cell cycle synchronization and timely delivery of Cas9 can enhance HDR (Lin et al. 2014; Yang et al. 2016; Zhang et al. 2017; Yiangou et al. 2019), or in the case of plasmid approaches, the linearization of the plasmid can be of help (Zhang et al. 2017). However, in the case of cell cycle synchronization, pluripotency might be disturbed (Kallas et al. 2011).

HDR-based integration relies heavily on the chosen 20 bp target sequence of the sgRNA. Mali et al. described an almost doubling editing efficiency (2.3 vs. 3.9%) when testing two different sgRNAs (Mali et al. 2013). Editing success is also dependent on the donor template design. Homologous DNA sequences up- and downstream of the transgene enhance editing success (Smithies et al. 1985). These so-called homology arms can be more than 1 kb each (Deng and Capecchi 1992). In hiPSCs, homology arms of 800 bp each are sufficient and regularly used (Oceguera-Yanez et al. 2016; Hong et al. 2017; Yao et al. 2017), although other results show that for circular plasmids, 1 kb each is best (Byrne et al. 2015; Zhang et al. 2017). The plasmids for this study employ homology arms of 804 and 837 bp (Figure 4) (Qian et al. 2014).

In all studies, the donor plasmid for expressing a transgene in the AAVS1 locus of hiPSCs typically has the same basic structure. In-between the 5' and 3' homology arm, a puromycin cassette is usually used for antibiotic-resistance selection followed by a CAG promoter (Figure 4). This promoter demonstrated stronger resistance to silencing than elongation factor 1-alpha (EF1α) and cytomegalovirus (CMV) promoters in hiPSCs (Luo et al. 2014). The transgene is followed by a poly-Adenine tail (Hockemeyer et al. 2011; Oceguera-Yanez et al. 2016).

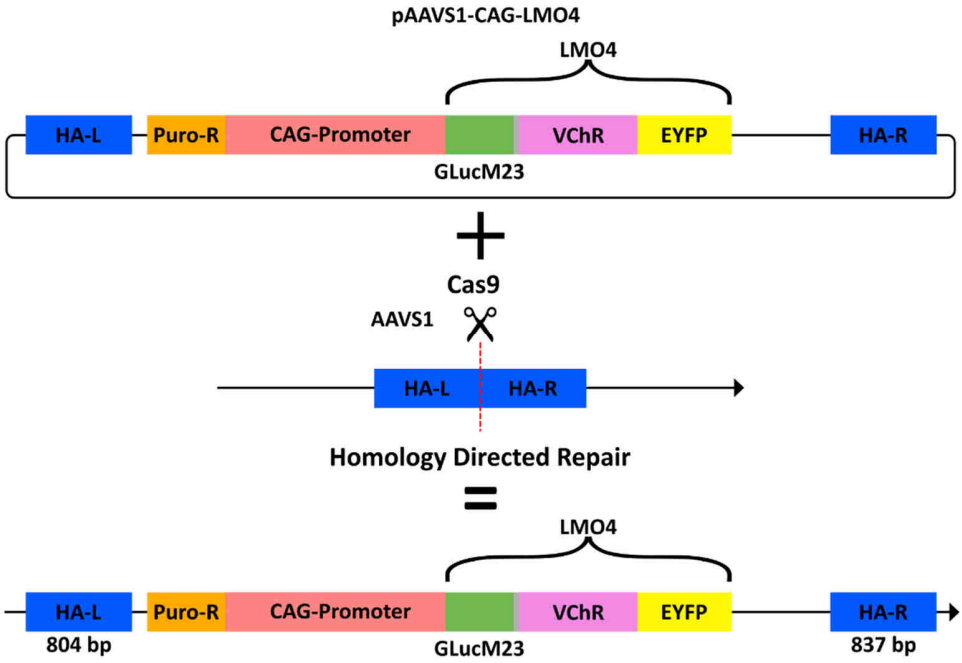

Figure 4: CRISPR strategy employed in this project. pAAVS1-CAG-LMO4 was generated and is transferred to the nucleus via nucleofection. The homology arms (HA-L and HA-R) are homologous to the targeted locus of the AAVS1 locus in the human genome. A Cas9-mediated double strand break activates the HDR machinery to use the supplied plasmid as template for repair. The result will be the transgene, knocked into the AAVS1 locus at the desired location.

3.3.2 Cardiac Differentiation

iPSCs and ESCs can be differentiated into cardiomyocytes. Over the last ten years, several protocols have been established (Kehat et al. 2001; Mummery et al. 2003) and improved for reliability and scale (Denning et al. 2016; Breckwoldt et al. 2017). In principle, these protocols rely on a two step-strategy. The cardiac specification follows mesoderm induction. For the first step, activation of transforming growth factor beta or nodal signaling (TGF-β1; including bone morphogenetic protein [BMP] and activin A) or basic fibroblast growth factor (bFGF; FGF2) is crucial. This step is followed by inhibiting the wingless-related integration site (WNT) pathway, leading to cardiac specification. Pathway-respective recombinant proteins or small molecules can induce activation/inhibition. These differentiation protocols commonly result in cardiomyocytes with a purity of >80% (Burridge et al. 2012; Denning et al. 2016).

3.3.3 Maturation of hiPSC-Derived Cardiomyocytes

The following sub-chapter has been published by me and Dr. Florian Weinberger elsewhere in a similar form (Stüdemann and Weinberger 2021). hiPSC-derived cardiomyocytes display an immature phenotype and, in many aspects, more closely resemble fetal cardiomyocytes. Several morphological and physiological characteristics differentiate adult from hPSC cardiomyocytes. Adult mature cardiomyocytes typically have a surface area of 12,000 µm^2, compared to 4,000 µm^2 in fetal cardiomyocytes and 1,000 µm^2 in PSC-cardiomyocytes (Li et al. 1996; Ribeiro et al. 2015; Dai et al. 2017). The increase in size is mainly attributed to the rise in highly organized myofibrils during maturation. An increased expression of sarcomeric proteins causes this higher

organization. Maturation increases the β-MHC (MYH7; mature) to α-MHC (MYH6; fetal) ratio (Snir et al. 2003; Siedner et al. 2003; Zhang et al. 2009; Mollova et al. 2013; Lundy et al. 2013; Weber et al. 2016; Iorga et al. 2018). Similarly, a switch from MLC2a to MLC2v occurs and is often used to assess maturity (Siedner et al. 2003; Iorga et al. 2018). In addition, the slow skeletal TnI is replaced by cTnI during maturation (Bedada et al. 2014; Iorga et al. 2018). These protein composition changes and the arrangement of longer longitudinal myofibrils increase cardiomyocyte contractility (McCain and Parker 2011; Ribeiro et al. 2015).

A further hallmark of cardiomyocyte maturation is the cell cycle exit. Human fetal and neonatal cardiomyocytes are still in the cell cycle. The number of cardiomyocytes increases dramatically in neonatal and fetal stages, but this comes to a halt shortly after birth. However, cell cycle activity is retained, resulting in multinucleated or polyploid cardiomyocytes (Mollova et al. 2013). Multinucleated cardiomyocytes result from nucleus division without cell division (karyokinesis without cytokinesis). Polyploid cardiomyocytes occur when karyokinesis lacks despite ongoing DNA synthesis, resulting in cardiomyocyte nuclei containing more than two complete sets of chromosomes (Alkass et al. 2015). Hence multinucleation/polyploidy is a sign of cardiomyocyte maturation. Therefore, it is no surprise that the percentage of multinucleated ESC/PSC-derived cardiomyocytes increases during prolonged culture (Lundy et al. 2013).

During maturation, cardiomyocytes switch from glycolysis (Lopaschuk et al. 1991) to fatty acid oxidation (Harris and Das 1991; Lopaschuk and Jaswal 2010). Mitochondria increase in number and mature structurally and functionally, enhancing OXPHOS activity (Dai et al. 2017). In adult cardiomyocytes, the mitochondria make up about 30% of the cellular volume (Piquereau et al. 2013), while in PSC-cardiomyocytes, it is less than 5% (Dai et al. 2017). Since most cell culture media only contain glucose, PSC-cardiomyocytes mainly rely on glycolysis for ATP generation. Still, they can be adapted to new energy substrates for increased fatty acid oxidation, resulting in maturation (Karbassi et al. 2020).

PSC-cardiomyocytes express the hyperpolarization-activated cyclic nucleotide-gated channel 4 (HCN4) and show differences in calcium handling. This results in one of their main characteristics – automaticity (Satin et al. 2004; Ma et al. 2011; Yechikov et al. 2016). Ca^{2+} handling matures (increase in Ca^{2+}storage capacity) with culture time (Satin et al. 2008; Louch et al. 2015; Hwang et al. 2015). The AP of PSC-cardiomyocytes is short and has a shortened plateau phase due to lower LTCC expression in fetal/ immature cardiomyocytes. Connexin 43 and N-cadherin as markers of cellular connections are expressed over the whole cell membrane; polarization (as a sign of maturation) occurs only during maturation (Salameh et al. 2010; Vreeker et al. 2014; Scuderi and Butcher 2017).

Cardiomyocyte maturation is a central aspect for many applications, e.g., disease modeling or cardiotoxicity studies. Therefore, it is of no surprise that countless studies have evaluated strategies to enhance maturation. These include i) long term culture (Kamakura et al. 2013), ii)

tissue engineering (Schaaf et al. 2011; Tiburcy et al. 2017; Lemoine et al. 2017; Ulmer et al. 2018; Ronaldson-Bouchard et al. 2018). iii) hormonal supplementation, e.g., with triiodothyronine (Yang et al. 2014) or iv) optimization of extracellular matrix combinations during cell culture (Herron et al. 2016). Additionally, fatty acid supplementation can mature PSC-cardiomyocytes (Horikoshi et al. 2019; Yang et al. 2019).

3.3.4 Engineered Heart Tissues

Efforts were made to develop three-dimensional tissue constructs to study cardiomyocytes in a more natural environment. This development was significant because access to native tissue is limited. The first three-dimensional tissues (so-called engineered heart tissues, EHTs) were developed from embryonic chick cardiomyocytes in a collagen matrix (Eschenhagen et al. 1997). Later on, neonatal rat cardiomyocytes were used (Eschenhagen et al. 2002; Zimmermann et al. 2002b). Nowadays, fibrin replaced collagen, and EHTs are cast in a 24-well format for automated analysis (Hansen et al. 2010; Schaaf et al. 2014). Instead of animal-cardiomyocytes, hiPSC-cardiomyocytes are now employed (Mannhardt et al. 2016; Breckwoldt et al. 2017). EHTs have especially proven helpful for in vitro drug testing (Saleem et al. 2020; Mannhardt et al. 2020) and disease modeling (Prondzynski et al. 2019). Moreover, transplantation of preformed cardiac tissues emerged as a regenerative strategy (Zimmermann et al. 2006).

3.4 Cardiac Regenerative Medicine

The adult human heart has a very limited potential to regenerate after injury. As previously described, cardiomyocytes are lost in the damaged myocardium during the events of an AMI. Cardiomyocyte debris is cleared, and a provisional fibrin matrix is assembled but quickly replaced by a cell-scarce collagen matrix. Hence, the mature scar contains only a small number of remnant cardiomyocytes. However, the lost cardiomyocytes are not replaced by newly formed cardiomyocytes (Eschenhagen et al. 2017).

Unlike the adult mammalian heart, the fetal and neonatal heart can regenerate to a certain degree. For example, mice regenerate their hearts when injured one day after birth but lose this ability seven days after birth (Porrello et al. 2011). Similar results were obtained in pigs that lose their regenerative potential two days after birth (Ye et al. 2018). Interestingly, a case report of a child who suffered a severe myocardial infarction at birth reported complete recovery, indicating that even human hearts have the potential to regenerate directly after birth (Haubner et al. 2016).

Nowadays, it is widely accepted that there is no cardiac stem cell or progenitor population that considerably contributes to cardiac regeneration in the adult mammalian heart (Van Berlo et al. 2014; He et al. 2019). cardiomyocyte turnover, estimated at around 0.5-2% per year, is not enough to functionally repair the heart after injury (Soonpaa and Field 1997; Bergmann et al. 2009, 2015). Only little mitosis of cardiomyocytes is found in adult mammals (Senyo et al. 2013; Mollova et al. 2013; Kimura et al. 2015). Other studies did not find any evidence for ongoing mitosis at all (Alkass et al. 2015). An AMI can kill up to 25% of the cardiomyocytes in the left

ventricle, which can be up to one billion cardiomyocytes in a human heart (Page et al. 1971). Since cardiomyocyte turnover is so low, regeneration cannot occur. Therefore, regeneration has to be enhanced by other means. True regeneration would be replacing the one billion cardiomyocytes, which is impossible with current technologies. But efforts are made to (partially) regenerate the heart nonetheless. These strategies can be divided into three categories: i) Activation of endogenous signaling cascades to reactivate cell cycle activity in resident cardiomyocytes, ii) direct reprogramming of non-cardiomyocytes to cardiomyocytes, or iii) replenishing the heart with exogenous cardiomyocytes derived from ESCs or iPSCs (Figure 5).

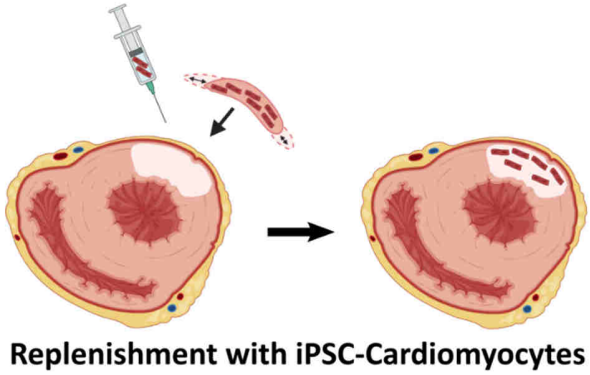

Figure 5: Basic principle of cardiac regenerative medicine. The scarred area (pale) is supplied with either an iPSC-cardiomyocyte suspension or a contractile construct such as an EHT. The result is a replenished LV with improved LV function. Reprinted from "The guinea pig model in cardiac regeneration research; Current tissue engineering approaches and future directions." Stüdemann and Weinberger, in Advanced Technologies in Cardiovascular Bioengineering, by Zhang and Serpooshan (Editors) (2021).

3.4.1 Cardiomyocyte Transplantation

The most intuitive approach of supplying new cardiomyocytes to an injured heart is the direct injection into the injured ventricle. The simplicity of this approach was first shown in 1978 when minced newt hearts were transplanted, and cells were able to graft (Bader and Oberpriller 1978). The same holds in mammals where syngeneic neonatal mouse cardiomyocyte transplantation led to grafting and formation of intercalated disks between the graft and host myocytes (Soonpaa et al. 1994). Additionally, EHTs can be grafted, resulting in grafted cells' survival and functional improvements (Zimmermann et al. 2006). Thus, two methods of cardiomyocyte delivery dominate the field of cardiac regenerative medicine—the direct injection of cardiomyocytes into the injured myocardium and the transplantation of preformed cardiac constructs. ESC/hiPSC cardiomyocyte transplantation consistently resulted in functional improvement, and grafted cells survived, regardless of the delivery route (Shiba et al. 2012, 2016; Chong et al. 2014; Riegler et al. 2015; Querdel et al. 2021).

3.4.2 Cell Injections for Cardiac Regeneration

Almost 30 years of research followed, and cardiomyocyte injection studies currently employ ESC- or iPSC-derived cardiomyocytes. A crucial factor for transplantation success after cell suspension injection is retention and survival. Graft size was significantly increased when cardiomyocytes were heat-shocked before transplantation at 43 °C for 30 minutes (Laflamme et al. 2005). Several

cellular pathways were targeted to prevent anoikis and mitochondria-mediated cell death in a second step. Additional factors were included to mimic ischemic preconditioning, activate protein kinase B (Akt) pathways, and inhibit caspases. This cocktail was termed pro-survival cocktail. It originally included Matrigel to target anoikis, Bcl-xL, and cyclosporin A, both targeting mitochondria-mediated cell death, pinacidil for ischemic preconditioning, IGF-1 for Akt activation, and ZVAD-fmk a caspase inhibitor (Laflamme et al. 2007). Modified versions of this PSC are used in most transplantation studies (Shiba et al. 2012, 2014, 2016; Chong et al. 2014; Liu et al. 2018; Romagnuolo et al. 2019). The beneficial effect of ESC-/iPSC-derived cardiomyocyte injection has been shown consistently in guinea pigs (Shiba et al. 2012, 2014), pigs (Romagnuolo et al. 2019), and primates (Chong et al. 2014; Shiba et al. 2016; Liu et al. 2018), demonstrating that the field has moved into a late preclinical stage. First clinical trials with cell injections are underway, such as the HEAL-CHF (NCT03763136) and LAPiS study (NCT04945018).

Injected cells reach deep scar areas and can even come into contact with the host myocardium, which might improve the likelihood of desired electrical coupling. However, the electrical coupling of immature cardiomyocytes could also increase the risk of arrhythmia. Yet, guinea pig studies not only demonstrated safety but imply a reduced arrhythmogenic risk after cardiomyocyte transplantation (Shiba et al. 2012; Pecha et al. 2019). However, large animal studies discovered cardiomyocyte transplantation to induce dangerous or even deadly ventricular tachycardia (Chong et al. 2014; Shiba et al. 2016; Romagnuolo et al. 2019). This was not observed in small animal models, most likely due to the small heart size and high heart frequency, urging for caution of results obtained from small animal models.

3.4.3 Engineered Heart Tissue for Cardiac Regeneration

Instead of injecting cardiomyocytes directly into the myocardium, an alternative approach uses preformed artificial tissues applied epicardially to the heart. EHTs from neonatal rat heart cells were the first successfully transplanted tissue constructs. Over 20 years, follow-up studies led to the first clinical trials with contractile constructs (BioVAT-HF, NCT04396899). Epicardial transplantation of collagen-based EHTs resulted in graft formation in the healthy (Zimmermann et al. 2002a) and injured heart (Zimmermann et al. 2006). Transplantation after myocardial injury enhanced left-ventricular function and provided the first evidence of electrical coupling of grafted cells and host myocardium in rats (Zimmermann et al. 2006). Similar results were obtained when transplanting human EHTs in a cryoinjury guinea pig model. These studies employed iPSC-cardiomyocytes that grafted and improved cardiac function (Weinberger et al. 2016).

Further improvements followed, including the optimization of EHT geometry. In guinea pigs, EHT patches remuscularized the injured heart in a dose-dependent manner (Querdel et al. 2021). Transplantation of high-dose EHTs improved left-ventricular function, whereas EHTs with lower cell numbers showed no beneficial effect (Querdel et al. 2021). Notably, the novel geometry allowed upscaling to human size. An EHT for pig/ human application was created with a size of 5x7cm containing ~$450x10^6$ cardiomyocytes (Querdel et al. 2021). EHTs are epicardially sutured

to the heart and mostly remain separated from the host myocardium by a fibrotic layer, making electrical coupling unlikely.

Nevertheless, a proof-of-concept study showed that even these cells could electrically couple to the host myocardium (Weinberger et al. 2016). However, two other studies did not find evidence for electrical coupling after epicardial transplantation (Gerbin et al. 2015; Shadrin et al. 2017). Thus, electrical coupling of spontaneously beating iPSC-cardiomyocytes to the host myocardium intuitively seems necessary, but it likely comes with the price of arrhythmogenicity.

Next to the maturation of the cells in the construct, the transplantation of a preformed tissue has another advantage. Engineered contractile constructs can be loaded with small molecular substances released over time to exert a prolonged effect after transplantation. This approach has successfully been applied to target Notch-signaling (Gerbin et al. 2020), the Wnt pathway (Fan et al. 2020), and stimulate angiogenesis (Munarin et al. 2020), and the cell cycle (Zhao et al. 2020). Especially reactivation of the cell cycle in the grafted cells can be crucial as proliferation participates in the final graft development (Weinberger et al. 2016; Liu et al. 2018; Romagnuolo et al. 2019). Attempts to genetically modify PSCs to stimulate cardiomyocyte proliferation were successful (Zhu et al. 2018; Fan et al. 2019).

3.4.4 The Guinea Pig Model in Cardiac Regeneration

The following sub-chapter has been published by me and Dr. Florian Weinberger elsewhere in a similar form (Stüdemann and Weinberger 2021). Next to classical animal models of preclinical research, guinea pigs are often used for transplantations studies with hiPSC or hESC-derived cardiomyocytes (Shiba et al. 2012, 2014; Weinberger et al. 2016). The reason is that they have a more similar cardiac (electro)physiology to humans than any other small animal model. For example, while mice and rats show heart rates of ~600 bpm and ~400 bpm, respectively (Heatley 2009), the guinea pig has a heart rate of 200-270 bpm in a conscious state (Table 1) (Shiotani et al. 2007; De Silva et al. 2020) that is closer to the basal human heart frequency of ~80 bpm and within the range of human cardiomyocytes that can be paced up to 5 Hz (300 bpm) (Weinberger et al. 2016).

Additionally, the electrophysiological properties of guinea pig and human cardiomyocytes resemble each other more closely. For example, AP shape and duration in guinea pigs are similar to human APs, while rats and mice differ significantly (Hume and Ueharat 1985; Kääb and Näbauer 2001; Schotten et al. 2011; Clauss et al. 2019). Ca^{2+}-handling in guinea pig cardiomyocytes is similar to human cardiomyocytes (Rajamohan et al. 2013; Clauss et al. 2019) than in mice and rats. These characteristics make the guinea pig a valuable model for predictive pharmacology studies (Table 1) (Kågström et al. 2007; Takahara et al. 2009; Himmel et al. 2012; Marks et al. 2012).

However, there are also disadvantages to the guinea pig as an animal model in cardiac research. Ligation (temporary or permanent) of the left ascending coronary artery (LAD) is the standard method to induce cardiac injury in mice and rats and has been described in guinea pigs (Table 1) (Dasagrandhi et al. 2018). However, the guinea pigs' extensive coronary collateralization hinders reproducibly creating myocardial injuries of similar size (Table 1) (Maxwell et al. 1987). Hence, we (and other research groups) use a cryoinjury model. Here, a liquid nitrogen cooled metal stamp is used to injure the left ventricle (Shiba et al. 2014; Weinberger et al. 2016; Castro et al. 2019). An essential advantage of this model is the reproducibility of injury size. Coronary artery anatomy has intraspecies differences. Hence, ligation will result in (slightly) different injury sizes in each animal. The stamp, however, has a consistent size and creates injuries of similar sizes. Therefore, this allows a better standardization and a more straightforward comparison of remodeling, repair, and regeneration (Van Den Bos et al. 2005; Lindsey et al. 2018). A further limitation of the cryoinjury model is the unphysiological mode of injury. Cryoinjury propagates from the epicardium to the subendocardial layers. In contrast, ischemic injuries predominantly affect the inner layers first (Reimer et al. 1977; Reimer and Jennings 1979). Ischemic injuries do not consistently kill all cardiomyocytes in the injured area, but myocardial islands in the core zone are spared. In contrast, cryoinjury usually results in uniform damage of the ventricular wall. Surviving myocardium is located mainly endocardially. This consistent damage can be advantageous because it simplifies the detection of newly transplanted cardiomyocytes but is unfavorable for functional coupling.

Nevertheless, of all small animal models, the guinea pig exerts significant advantages over other rodent models. The close-to-human electrophysiology balances the necessity of a cryoinjury model and makes it a valuable tool in regenerative medicine research.

Table 1: Species characteristics of electrophysiological parameters, coronary artery anatomy and heart rate. Reprinted from "The guinea pig model in cardiac regeneration research; Current tissue engineering approaches and future directions." Stüdemann and Weinberger, in Advanced Technologies in Cardiovascular Bioengineering, by Zhang and Serpooshan (Editors) (2021).

Species	**Mouse** (Heatley 2009; Schotten et al. 2011; Clauss et al. 2019)	**Rat** (Maxwell et al. 1987; Varró et al. 1993; Kääb and Näbauer 2001; Heatley 2009; Schotten et al. 2011; Clauss et al. 2019)	**Guinea Pig** (Hume and Ueharat 1985; Varró et al. 1993; Shiotani et al. 2007; Heatley 2009; Clauss et al. 2019; De Silva et al. 2020)
AP Shape	No plateau phase	No plateau phase	Similar but no notch
AP duration (ventricular)	< 100 ms	< 100 ms	~200 ms
LAD collateralization	LAD diverse	Variety between strains but LAD is present Little collateralization	Extensive
Heart Rate	600-800 bpm	400 bpm	250 bpm

3.5 Mechanism of Action of Transplanted Cardiomyocytes

A recent consensus statement stated that the transplanted cardiomyocytes "[…] may contribute to systolic force generation, although the extent of this contribution has not been precisely determined." (Eschenhagen et al. 2017) In addition, the statement declares that "Although direct force generation deriving from the injected myocytes may explain some of the functional improvement, it is not clear whether the degree of the emergence of new myocardium entirely accounts for the degree of contractile improvement; paracrine signaling events may contribute as well." (Eschenhagen et al. 2017). Hence, the two main contrasting hypotheses are paracrine signaling and the active contribution of the transplanted cardiomyocytes.

It seems intuitive that the replenishment of cardiomyocytes directly affects the ventricular performance by contributing new iPSC-cardiomyocytes to force generation. However, as stated above, this has never been formally demonstrated, and so the alternative hypothesis of paracrine signaling that originates from the iPSC-cardiomyocytes might also hold. Here, enhanced vascularization, antifibrotic effects, and reduction of cardiomyocyte apoptosis in the border zone could play a role. A third hypothesis is the mechanical stabilization of the scar by the transplanted cardiomyocytes that might improve heart function.

There is only indirect evidence that the beneficial effect of iPSC-cardiomyocyte transplantation depends on an active contribution. Some studies showed that only the transplantation of contractile EHTs (containing cardiomyocytes) improved left-ventricular function, whereas EHTs that included no or only non-contractile cells did not improve left ventricular function (Shiba et al. 2012; Weinberger et al. 2016). Additional support originates from studies in which larger grafts correlated to a more extensive improvement of left ventricular function (Bargehr et al. 2019; Sun et al. 2020). Also, the improved wall thickening at the transplantation location of contractile EHTs on infarcted rat hearts can be taken as indirect evidence for introducing new contractile myocardium (Zimmermann et al. 2006).

The paracrine mechanism hypothesis is supported by studies showing improved left ventricular function without or only minimal cell engraftment (Tachibana et al. 2017; Lancaster et al. 2019). The third hypothesis of mechanical stabilization is supported only by a few studies. Due to the variety of animal models used in these studies and only one clinical study, there is no strong evidence supporting mechanical stabilization as the main mode of action (Christman et al. 2004; Sabbah et al. 2013; Anker et al. 2015). Hence, a better understanding of the mode of action is desirable from an academic and patient perspective as the first clinical trials are underway. Furthermore, elucidating the mechanism of action could direct future studies to enhance further left ventricular function by PSC-cardiomyocyte transplantation.

3.5.1 Lessons from Neuroscience: Cardiac Optogenetics and Chemogenetics

At the start of the work for this thesis, we hypothesized that a possible strategy to dissect the mode of action was to switch off cardiomyocytes' contractility. By switching off the transplanted

cardiomyocytes selectively while assessing cardiac function, the degree of the contribution should be quantifiable. After switching off the transplanted cardiomyocytes, a decline of left ventricular function would show that they previously contributed to cardiac function. This process would ideally occur in a matter of seconds or minutes and should be reversible (high temporal response). Hence, the electrical inactivation of cardiomyocytes would be an ideal tool to study the mode of action.

The neuroscience field has developed various tools to activate or deactivate neuronal activity. These tools are ion channels activated either by light (optogenetics) or by selective chemical substances (chemogenetics). For example, activation of artificial cation channels resulted in neuronal depolarization and increased firing; on the other hand, activating of artificial anion channels resulted in shunting and neuronal silencing (Nagel et al. 2005; Magnus et al. 2011, 2019; Berglund et al. 2013; Park et al. 2017).

For optogenetic approaches, channelrhodopsins (ChR) are frequently used. These microbial opsin-related proteins were found in algae and are involved in phototaxis (Nagel et al. 2002). Additional variants were found in various species that differ in channel conductance, ion selectivity, kinetics, desensitization/ recovery, light sensitivity, spectral response, and membrane trafficking/ expression (Lin 2011). As all ChRs are cation specific, it was desirable to engineer an anion conducting ChR. This was achieved by replacing amino acids in the central gate of ChR2, which resulted in ChloC, an anion-selective channelrhodopsin (ACR) conducting chloride. Activation of ChloC allowed to silence rather than activate neurons with light (Wietek et al. 2014).

Further modifications improved ChloC (iChloC), showing reduced baseline membrane depolarization and improved neuronal silencing (Wietek et al. 2015). ChloC and iChloC work by shunting depolarizing currents. The equilibrium potential of Cl^- and the resting membrane potential are highly similar (around -70 mV) in neurons; the opening of iChloC at baseline conditions thus leads to no ion flux and, therefore, only minimal potential shifts. However, when a depolarizing current occurs (arising from an incoming AP), the activated iChloC will allow immediate Cl^- influx, preventing it to reach the threshold potential and leading to neuronal silencing (Wietek et al. 2014). Additionally to engineered ACRs, naturally occurring ACRs have been identified (Govorunova et al. 2015), complementing the toolbox of ACRs. ChR2 and its modified variant iChloC are maximally excited by 470 nm light. ChR2 has a rapid on-rate and moderate channel closing rate, but its high level of desensitization can be problematic (Nagel et al. 2003; Ishizuka et al. 2006; Lin 2011). Complete recovery occurs only after 25 seconds (Lin et al. 2009). The mutations in iChloC led to a reduced light intensity needed for activation compared to ChR2 (Wietek et al. 2015). The application of light in vivo is challenging. Thus, it would be desirable to be independent of an external light source and target the artificial ion channels with a small molecule. Combining optogenetic with chemogenetic approaches led to the development of luminopsins (LMO). These hybrid proteins consist of a light-sensitive ion channel fused to a light-producing enzyme. For this purpose, a ChR was fused to a Luciferase. Upon application of the

substrate of luciferase, light is generated and activates the ion channel (Berglund et al. 2013). Several combinations of different luciferases and ChRs have resulted in LMO4 and iLMO4, which show a coupling efficiency of emission and excitation wavelength of 26% and 36%, respectively. LMO4 consists of *Gaussia* Luciferase mutant 23 (GLucM23) and VChR1, while iLMO4 consists of GLucM23 but iChloC as a photosensitive channel (Figure 6). Application of the substrate coelenterazine (CTZ) results in increased neuronal activity or neuronal silencing, respectively. Both channels were successfully used in vitro and in vivo, making LMOs a helpful tool for optogenetic studies that cannot work with an external light source (Park et al. 2017).

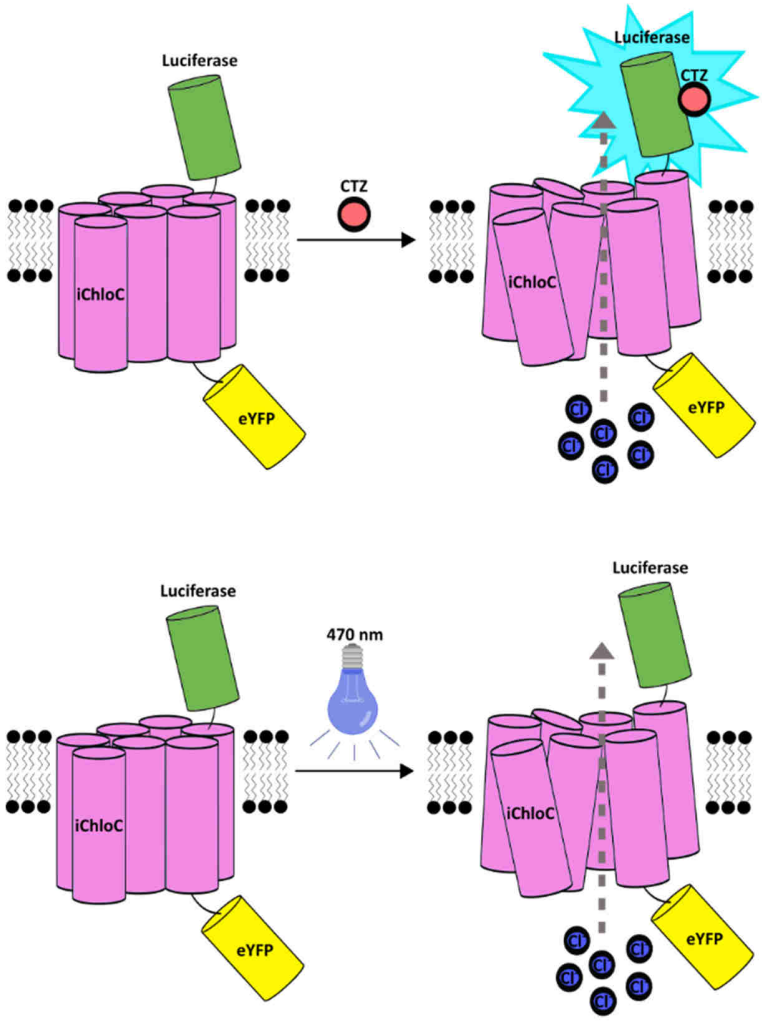

Figure 6: Schematic mechanism of iLMO4 activation. Upper panel: Upon CTZ application the Luciferase emits light that activates iChloC. Cl^- ions can now flow through the channel. Lower panel: Activation of iChloC can also occur via 470 nm light, causing the same ion flow. Adapted from "Light-Emitting Channelrhodopsins for Combined Optogenetic and Chemical-Genetic Control of Neurons" by Berglund et al., PLoS One, volume 8 pages e59759 (2013).

Purely chemogenetic approaches don't require light but instead rely on the specificity of a chemical compound to the engineered ion channel. In principle, these channels work in the same way: Activation of chemogenetic cation channels results in increased neuronal activity while activation of anion channels results in shunting and neuronal silencing (Magnus et al. 2011).

Magnus and colleagues created a toolbox of ligand-gated ion channels that can achieve these neuronal effects. They employed the ligand-binding domain (LBD) of the α7 nicotinic acetylcholine receptor (nAChR) and transplanted it onto the ion pore domain (IPD) of the serotonin receptor 3a or the glycine receptor (a7-5HT3 or a7-GlyR). By introducing several amino acid changes in the LBD, they created a pharmacologically selective actuator module (PSAM)^{L141F,Y115F}-5HT3, and PSAM^{L141F,Y115F}-GlyR. These amino acid changes rendered the LBD irresponsive to its natural ligand acetylcholine (half-maximal effective concentration [EC_{50}] increased from 26 µM to 170/570 µM, respectively) but instead created a high affinity to a pharmacologically selective effector molecule (PSEM) PSEM^{89S} (EC_{50} 4 µM), an artificially derived compound (Figure 7). With these PSAM/PSEM combinations, neuronal activation and silencing were achieved in vitro and in vivo (Magnus et al. 2011).

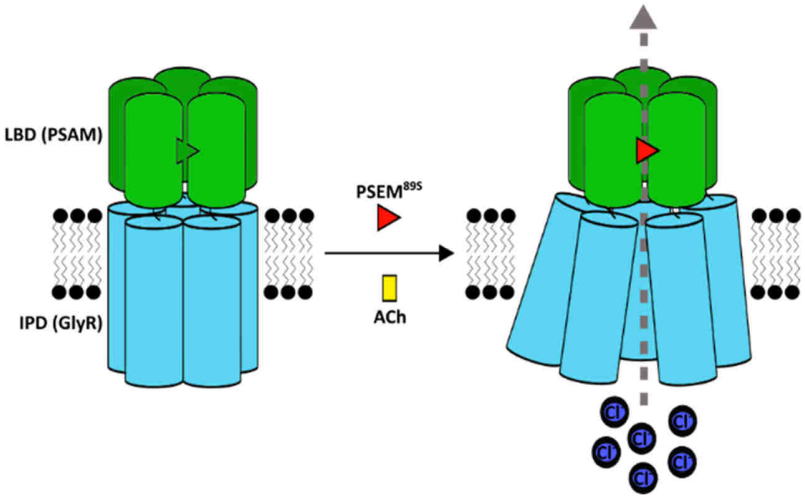

Figure 7: Schematic mechanism of PSAM GlyR activation. The LBD of nAChR is mutated so it can only be activated by PSEM^{89S}. The LBD is transplanted on the IPD of the glycin receptor. PSEM^{89S} activates PSAM GlyR, allowing Cl^- flow. The mutations diminished ACh affinity of the LBD. Adapted from "Chemical and genetic engineering of selective ion channel-ligand interactions" by Magnus et al., Science, volume 333 pages 1292-1296 (2011).

Further mutations in the LBD were introduced in the next step, and α7^{L131G,Q139L,Y217F}-GlyR was created and termed PSAM^4-GlyR. This procedure produced a PSAM with an EC_{50} of 1.6 nM to the respective activating compound varenicline and increased the EC_{50} of ACh to 83 µM (Magnus et al. 2019). Neuronal silencing was again achieved. The choice of PSAM channels depends on the planned experiment. Varenicline has a half-life of 1.4 hours in mice, in contrast to PSEM^{89S,} which has a half-life of ~15 minutes (Magnus et al. 2011, 2019). Hence, the previous generation of PSAM/PSEM^{89S} might be preferred for temporally sensitive experiments to PSAM^4-GlyR/varenicline.

With a toolbox of chemogenetic and optogenetic channels at hand, the question arose if cardiomyocyte behavior can be controlled similarly to neurons. By expressing ChR2 or *Natronomonas* Halorhodopsin (NpHR) in zebrafish, Arrenberg and colleagues simulated tachycardia and bradycardia, atrioventricular blocks, and cardiac arrest using light in zebrafish (Arrenberg et al. 2010). ChR2 was also used to control ESC-cardiomyocyte and mouse hearts using

light (Bruegmann et al. 2010). Moreover, ChR2 was used to pace EHTs optically (Lemme et al. 2020).

In concordance with results from neurons, activation of GtACR1 in neonatal rat cardiomyocytes resulted in AP silencing (Govorunova et al. 2016). Depolarization has been proposed in cardiomyocytes as an alternative mechanism to shunting-mediated silencing found in neurons. In cardiomyocytes, the reversal potential (E_{rev}) of Cl^- has been estimated between −40 and −33 mV (Clemo et al. 1999; Baumgarten et al. 2005). Therefore, the opening of additional Cl^--conducting channels results in membrane depolarization and stop of contraction. Only two studies investigated the effects of prolonged ACR activation in cardiomyocytes. Here, membrane depolarization and stop of contractility were observed (Figure 8) (Govorunova et al. 2016; Kopton et al. 2018).

Chemogenetic approaches to control contractility have not been tested in the heart. Only induction of oxidative stress has been investigated by chemogenetic means so far (Steinhorn et al. 2018; Sorrentino et al. 2019).

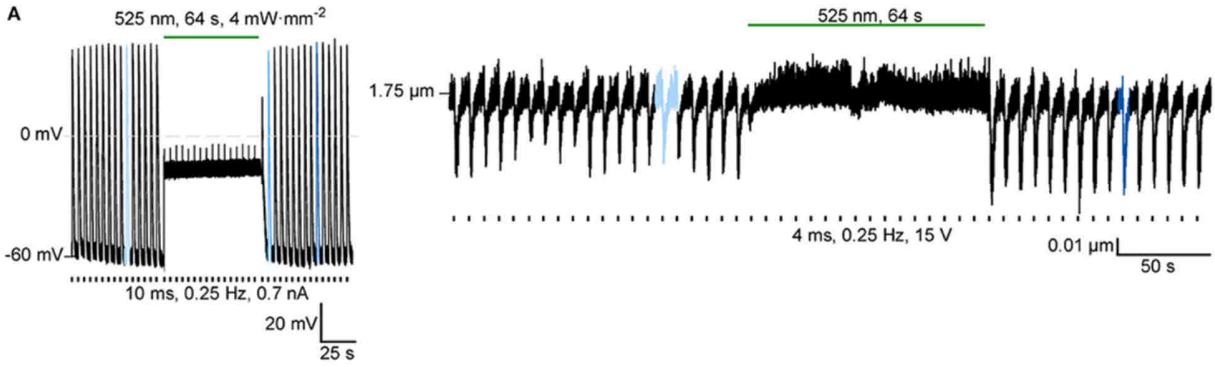

Figure 8: Optogenetic stop of contractility in rabbit cardiomyocytes. Left: GtACR activation with 525 nm light at 4mW*mm^{-2} for 64 seconds reversibly depolarizes cardiomyocytes regardless of electrical pacing (10 ms, 0.25 Hz, 0.7 nA). Right: Optogenetic inactivation for 64s with 525 nm light reversibly stops cardiomyocyte contractility regardless of electrical pacing (4 ms, 0.25 Hz, 15V). Adapted from "Cardiac Electrophysiological Effects of Light-Activated Chloride Channels" by Kopton et al., Frontiers in Physiology, volume 9, pages 1806 (2018).

3.5.2 Employing Opto-/Chemogenetic Approaches for Transplantation Studies

Only a handful of studies have employed cells for transplantation that had distinct functions, such as controlling graft cell function by optogenetic or chemogenetic tools. These studies stem mainly from neuroscience. For example, functional integration of optogenetic activatable dopamine neurons from stem cells transplanted into striatum was achieved (Tønnesen et al. 2011), and grafted neural progenitors could be controlled optogenetically (Ceto et al. 2020). Furthermore, stimulation of optogenetic neuronal stem cells (NSC) could improve recovery from stroke (Daadi et al. 2016) and silencing mesencephalic dopaminergic (mesDA) neurons derived from hESCs by optogenetic means reversed their beneficial effects in a model of Parkinson's disease (Steinbeck et al. 2015).

A chemogenetic approach decreased cerebral blood flow in areas where iPSC-neurons projected, showing functional integration of the grafted cells (Ji et al. 2016). Another study demonstrated that dopamine neurons could be controlled chemogenetically after transplantation and their beneficial effect depended on the chemogenetic activation (Dell'Anno et al. 2014).

Employing luminopsins, iPSC-derived neural progenitors (expressing LMO3) improved neural parameters and functional recovery from injury (Yu et al. 2019). In addition, in a Parkinson's disease model, LMO expressing neuronal precursor cells improved neuronal function more when activated with CTZ (Zenchak et al. 2020).

These studies show that opto- and chemogenetic tools are valuable to study the mode of action of cell transplantation studies successfully but have not been used in the field of cardiac regeneration.

4 AIM OF THIS WORK

Pluripotent stem cell cardiomyocyte transplantation is a novel therapeutic option for heart failure. Small animal and large animal studies consistently improve heart function after injury, and the first clinical studies are underway. However, the underlying mechanism of the beneficial effect of PSC-cardiomyocyte transplantations is still unknown. This study aimed to characterize one potential mechanism in detail – the active contribution of transplanted PSC-cardiomyocytes to heart function (Figure 9).

To investigate this question, we looked for technologies to quickly, selectively, and reversibly switch off transplanted PSC-cardiomyocyte contractility without affecting the host cardiomyocytes. Two options were tested in this study: Chemogenetic PSAMs and optogenetic LMOs. We used CRISPR/Cas9 to knock-in these constructs in hiPSCs, after which we differentiated these iPSCs into cardiomyocytes. We then characterized the cell lines in an EHT model and investigated the ability of the constructs to switch off contractility reversibly. Two successful approaches were PSAM GlyR and iLMO4. The compound PSEM^{89S} stopped PSAM GlyR expressing EHT contractility while 470 nm light stopped iLMO4 EHT contractility. These two cell lines were chosen for a transplantation study in guinea pigs, and eventually, heart function was analyzed ex vivo in a Langendorff model.

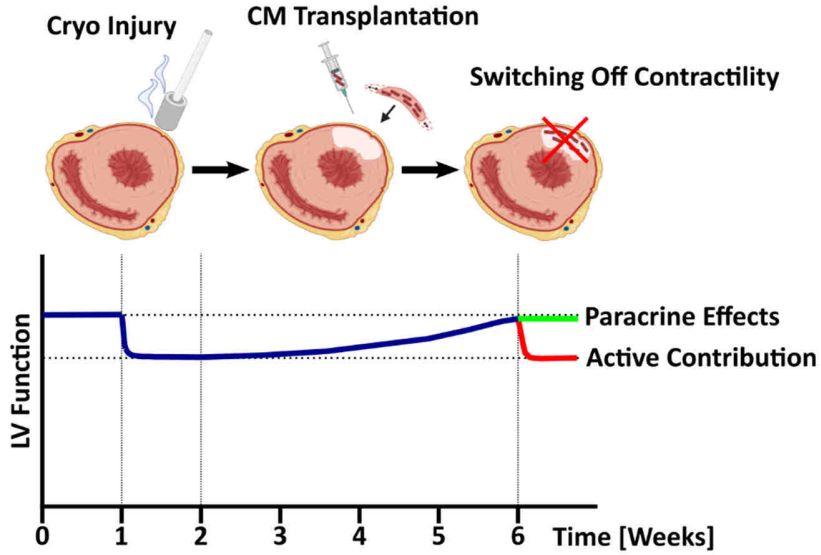

Figure 9: Investigation of the mechanism of action. After injury LV function drops (week 1). iPSC-derived cardiomyocyte transplantation gradually improves LV-function over the course of four weeks. Switching off contractility of only the engrafted cells could have two results. 1) A drop of function, showing active contribution to LV function (red). 2) No drop of LV function, demonstrating that paracrine effects are at work (green).

5 METHODS

A comprehensive list of devices, materials, and substances can be found in the supplement.

5.1 Custom Made Media Compositions

Table 2: Custom made media and buffers

Medium Type	Composition
FTDA (bFGF, TGF-β1, Dorsomorphin, Activin-α based hiPSC Culture Medium)	DMEM/F-12 without glutamine 2 mM L-glutamine 5 mg/L Transferrin 6.6 µg/L Sodium selenite 1% (v/v) Human serum albumin (HSA) (10% solution) 0.1% (v/v) Lipid mix 5 mg/L Human recombinant insulin 50 nM Dorsomorphin 2.5 µg/L Activin A 0.5 µg/L Transforming growth factor-β 1 (TGF-β1) The medium was sterile filtered and stored at 4 °C for up to one week. 30 µg/L bFGF was supplemented immediately before usage. For splitting, 10 µM Y-27632 was added.
Stage 0 medium (EB- Formation medium)	FTDA 4 g/L Polyvinyl alcohol in 1x DPBS 10 µM Y-27632 30 µg/L bFGF was supplemented immediately before usage.
Stage 1 medium (EB-Mesoderm Induction medium)	RPMI 1640 4 g/L Polyvinyl alcohol 10 mM HEPES (pH 7.4) 0.05% (v/v) Human serum albumin 5 mg/L Transferrin 6.6 µg/L Sodium selenite 0.1% (v/v) Lipid mix 10 µM Y-27632 250 µM Phosphoascorbate

	The medium was filter-sterilized (0.2 µm filter) and stored at 4°C for up to 1 week without growth factors. 5 µg/L bFGF, 3 µg/L Activin-A, and 10 µg/L BMP-4 were supplemented immediately before usage.
Stage 1 EB Wash Medium	RPMI 1640 4 g/L Polyvinyl alcohol 10 mM HEPES (pH 7.4)
FDM Medium (EB Cardiac Specification Medium)	RPMI 1640 0.5% (v/v) Penicillin/streptomycin 10 mM HEPES (pH 7.4) 0,5% (v/v) HSA 5 mg/L Transferrin 6.6 µg/L Sodium selenite 0.1% (v/v) Lipid mix 1 µM Y-27632 250 µM Phosphoascorbate The medium was filter-sterilized (0.2 µm filter) and stored at 4 °C for up to 1 week. 1 µM XAV-939 was added directly before usage.
Stage 2 Medium (EB Cardiac Specification Medium 2)	RPMI 1640 0.5% (v/v) Penicillin/streptomycin 10 mM HEPES (pH 7.4) 1 µM Y-27632 500 µM 1-Thioglycerol The medium was filter-sterilized (0.2 µm filter) and stored at 4 °C for up to 1 week. 2% (v/v) B27 with insulin and 1 µM XAV-939 were added freshly before usage.
RDM Medium (EB Cardiac Specification Medium 3)	RPMI 1640 0.5% (v/v) Penicillin/streptomycin 10 mM HEPES (pH 7.4) 1 µM Y-27632 500 µM 1-Thioglycerol The medium was filter-sterilized (0.2 µm filter) and stored at 4 °C for up to 1 week. 2% (v/v) B27 with insulin was added freshly before usage.

Stage 0 Medium (2D Differentiation)	StemPro-34™ SFM + Supplement 1 µg/l BMP4 2 mM GlutaMAX™ 1% (v/v) Matrigel High Growth Factor
Stage 1 Medium (2D Differentiation)	StemPro-34™ SFM + Supplement 8 µg/L Activin A 10 µg/l BMP-4 2 mM GlutaMAX™
Stage 2.1 Medium (2D Differentiation)	RPMI 1640 2% (v/v) B27 minus Insulin 10 µM KY021111 10 µM XAV939
Stage 2.2 Medium (2D Differentiation)	RPMI 1640 2% (v/v) B27 10 µM KY021111 10 µM XAV939 25 µM Insulin
RDM Medium (2D Differentiation)	RPMI 1640 2% (v/v) B27 25 µM Insulin
Basis Medium (Dissociation)	RPMI 1640 1% (v/v) Penicillin/streptomycin
Blocking Buffer (Dissociation)	RPMI 1640 6 ml/L DNase II Type V 1% (v/v) Penicillin/streptomycin
Cardiomyocyte Thawing medium	RPMI 1640 10% B27 + Insulin
NKM Medium	DMEM 1% (v/v) Penicillin/streptomycin 10% (v/v) FBS 1% (v/v) L-glutamine (2mM)
hEHT Medium	DMEM 1% (v/v) Penicillin/streptomycin 10% (v/v) Horse serum inactivated 10 mg/L Insulin 33 mg/L Aprotinin
Modified Krebs-Henseleit Buffer (MKH)	118 mM NaCl 4.7 mM KCl 0.8 mM $MgSO_4$

	25 mM $NaHCO_3$ 1.2 mM KH_2PO_4 5 mM Glucose 2 mM Na-Pyruvate 2.5 mM $CaCl_2$
Blocking Solution	10% goat serum 1% BSA 0.5% Triton-X100 In TBS
Immunofluorescence buffer (IF buffer)	0.25% BSA 0.5% Triton-X100 In TBS
Tyrode's solution	127 mM NaCl 4.5 mM KCl 1.5 mM $MgCl_2$ 1.8 mM $CaCl_2$ 10 mM Glucose 22 mM $NaHCO_3$ 0.42 mM Na_2HPO_4
TAE Buffer	0.4 M TRIS acetate 0.01 M EDTA pH 8.3
LB Medium	1000 ml diH_2O 1% Peptone 10mM NaCl 0.5% Yeast extract The medium was sterilized by autoclaving. For LB-plates, 40 g Luria-agar was boiled in 1 L diH_2O to dissolve and then autoclaved and filled in Petri dishes.
SOC Medium	1000 ml diH_2O 2% Peptone 10 mM NaCl 0.5% Yeast extract 2.5 mM KCl 10 mM $MgCl_2$ 10 mM $MgSO_4$

	20 mM Glucose pH 7.0 The medium was sterilized by autoclaving.

5.2 Cell culture of human induced pluripotent stem cells

5.2.1 Stem Cell Culture and Cell Expansion

hiPSCs used in this study were obtained from skin biopsies of donors. Reprogramming with Sendai virus was previously performed by the HEXT Facility, UKE. Studies were approved by the Ethics Committee of the UKE (Az. PV4798/28.10.2014). All experiments were carried out with the cell line UKEi001-A (https://hpscreg.eu/cell-line/UKEi001-A), which was characterized as *Mycoplasma* negative and with a normal karyotype at the start of the experiments. All cell culture was performed under sterile conditions. No antibiotics were employed during iPSC culture. Hence, hygienic precautions were taken. A facial mask, plastic arm covers, and gloves were worn during all cell culture work. Arms and hands were regularly disinfected with 70% Ethanol. Early passage hiPSCs or CRISPR-edited hiPSCs were expanded in FTDA medium on Geltrex® coated vessels. Cells were cultivated under hypoxic conditions (5% CO_2, 5% O_2) in incubators providing a temperature of 37 °C, with 98% relative humidity (RH). $4x10^4$ to $8.6x10^4/cm^2$ were seeded and cultivated for 3-5 days with daily FTDA medium change. When cells were 100% confluent, cells were washed once with DPBS and incubated with 0.1 ml/cm^2 Accutase + Y-27632 (10 µM) for 5-10 minutes. Accutase was neutralized with the same amount of FTDA + Y-27632, and the cell suspension was centrifuged at 200 g for 2 minutes. Cells were resuspended in FTDA + Y-27632, and cell viability, -number, and -aggregation was determined with a CASY cell counter. Viability of >85% and an aggregation coefficient (AGG) of <2 were considered sufficient for further cultivation. Alternatively, cells were manually counted using Trypan Blue and a Neubauer counting chamber. $4x10^4$ to $8.6x10^4/cm^2$ cells were seeded for expansion in FTDA supplemented with Y-27632. Y-27632 supplementation was discontinued after 24 hours. Cells were fed daily and twice daily when close to confluency.

5.2.2 Plate Coating

Cell culture vessel coating volumes can be found in table 3. Standard cell culture vessels were coated for 24h at room temperature with Geltrex, diluted 1:100 in RPMI 1640. Matrigel was used for CRISPR experiments and subsequent media change to mTeSR™ Plus. Matrigel was diluted at 1:60 in RPMI 1640 and coated for 24 hours at room temperature.

Table 3: Cell culture vessels and corresponding volumes used for coating.

Vessel	Geltrex Coating (1:100)	Matrigel Coating (1:60)
T-175 flask	16 ml	n/a
T-75 Flask	7 ml	n/a
6-well Plate	1 ml/well	1 ml/well
12-well Plate	n/a	500 µl/well
24-well Plate	500 µl/well	500 µl/well
48-well Plate	n/a	400 µl/well
96-well Plate	n/a	200 µl/well

5.2.3 Freezing and Thawing of hiPSCs

Confluent cells were washed and detached as previously described in the last subchapter. After cell counting $1x10^6$ iPSCs were frozen in 1 ml fetal bovine serum (FBS) + Dimethylsulfoxide (DMSO; 10:1). An isopropanol container ("Mr. Frosty") was used for the freezing process and placed at -80 °C for 24 hours. Alternatively, an Asymptote EF 600 automated cell freezer (GE Healthcare) was used. Cells were then transferred to -150 °C for long-term storage.

For thawing hiPSCs, cryovials were thawed in a water bath (37 °C) until one small ice clump (~5 mm diameter) was left. The vial was then transferred to a sterile hood and filled up with 1 ml appropriate medium. The cell suspension was transferred to a 15 ml Falcon tube, filled with 2 mL medium, and centrifuged at 200 g for 2 minutes. The supernatant was discarded, and cells were resuspended in an appropriate volume of FTDA + Y-27632/ mTeSR™ Plus + Y-27632 (10 µM) and seeded on Geltrex/ Matrigel-coated cell culture vessels.

5.2.4 *Mycoplasma* Test

One passage after thawing and regularly during regular cell culture, cell culture medium (0.2 ml to 1 ml) was collected and incubated for 10 min at 100 °C and briefly centrifuged. 2 µl of the supernatant was added to PCR Master Mix (Table 4) and ran with the recommended program (Table 4). Positive and negative control was included for each run. PCR products were analyzed by gel electrophoresis on 1% (w/v) agarose gel with TAE buffer.

Table 4: PCR reaction mix for *Mycoplasma* tests

Substance	1x
10x Buffer	5 µl
Q-Solution	10 µl
$MgCl_2$ (25 mM)	4 µl
Primer pool Myco-F (10 pM)	1 µl
Primer pool Myco-R (10 pM)	1 µl
dNTPs	1 µl
Taq-DNA Polymerase	0.25 µl
DNA sample	2 µl
Nuclease free water	25.75 µl
Total	50 µl

Table 5: PCR program for *Mycoplasma* test

Temperature	Time	Cycles
95 °C	15 min	
94 °C	30 sec	40x
56 °C	30 sec	
72 °C	1 min	
72 °C	10 min	

*Mycoplasm*a tests were kindly performed by June Uebeler, IEPT, UKE.

5.2.5 DNA Extraction

Genomic DNA was extracted from cells with the Blood & Tissue Kit (Qiagen) according to the manufacturer's protocol. DNA concentration was subsequently assessed with Nanodrop™.

5.2.6 Karyotyping

For karyotyping, gDNA was isolated as previously described. Next, 250 µg DNA was enzymatically digested. These processes were verified by agarose gel electrophoresis. gDNA was then hybridized with probes overnight at 65 °C. Hybridized DNA was then loaded in the nCounter cartridge (Nanostring), and probe detection was carried out with nCounter$^{SPRINT™}$ Profiler (Nanostring). Probes were selected to cover the whole genome and indicate chromosomal aberrations. nCounter CNV Collector Tool (Nanostring) was used for analysis. Karyotyping was kindly performed by Elisabeth Krämer, IEPT, UKE, and data were analyzed by Dr. Giulia Mearini, IEPT, UKE.

5.2.7 Pluripotency Test via Flow Cytometry

Regularly we employed SSEA3 staining and flow cytometry to assess the pluripotency of hiPSCs. First, $0.5x10^6$ to $1x10^6$ fresh hiPSCs were blocked in 1 ml FBS for at least 15 minutes. Next, cells were put into fluorescence-activated cell sorting (FACS) tubes, washed with 1 ml DPBS + 5% FBS, and centrifuged for 2 minutes at 200 g. Cells were then resuspended in 100 µl antibody solution and incubated for 45 minutes. Cells were then washed and centrifuged twice as described to wash out unbound antibodies. Finally, cells were resuspended in 250 µl for analysis. A Canto II (BD Biosciences) was used, and gates were set to identify single cells. Unstained control cells were used to set the fluorescence threshold so that <0.5% cells were counted as $SSEA3^+$. In genetically edited lines, endogenous EGFP and EYFP expression was assessed. Unedited cells were used to set gates so that <0.5% of cells were counted as $EGFP^+$ / $EYFP^+$. Acquired data were analyzed with FlowJo V10 or FACS Diva. All flow cytometry analysis was performed in the FACS Core Facility, UKE.

5.2.8 Nocodazole treatment

Nocodazole in DMSO was added to iPSCs for 16 hours in the cell culture medium. Cells were harvested with Accutase and analyzed via DAPI staining for DNA content by FACS with Canto II (BD). Data were analyzed with FACS Diva (BD).

5.3 Molecular Cloning

5.3.1 CRISPR/Cas9 Experimental Design PSAMs and Luminopsins

Plasmids for this study were obtained as kind gifts from Scott Sternson (CAG::PSAML141F,Y115F:GlyR-IRES-GFP, Addgene plasmid #32480 and CAG::PSAML141F,Y115F:5HT3HC-IRES-GFP Addgene plasmid #32476) and Su-Chun Zhang (AAVS1-CAG-hrGFP, Addgene plasmid # 52344). The EGFP-2A containing plasmid was constructed by the Vector Facility of the UKE. LMO constructs were kindly provided by Prof. Ute Hochgeschwender, M.D. Plasmid pAAV-hSyn-LMO4 and pcDNA-CAG-iLMO4 were used as templates. Our strategy with homology arms flanking the gene of interest (GOI) aimed for homology-directed repair (HDR) to insert the genes of interest into the AAVS1 locus of hiPSCs (Figure 10). To do so, a plasmid containing homology arms for the AAVS1 Locus ("safe harbor") and a CAG promoter were used as a starting point (pAAVS1-CAG-hrGFP, #52344). We cloned the LMOs and PSAMs into this plasmid using In-Fusion® cloning and used CRISPR/Cas9 to insert these constructs into the genome of hiPSCs. Plasmid maps can be found in the supplement.

The crRNA targeting the AAVS1 was designed using CRISPOR (http://crispor.tefor.net/) and selected by highest precision and lowest off-target values. Details on crRNA design can be found in the appendix. All cloning steps were performed in cooperation with the Vector Facility, UKE Hamburg. All cloning designs were carried out with Snapgene 3.3.4.

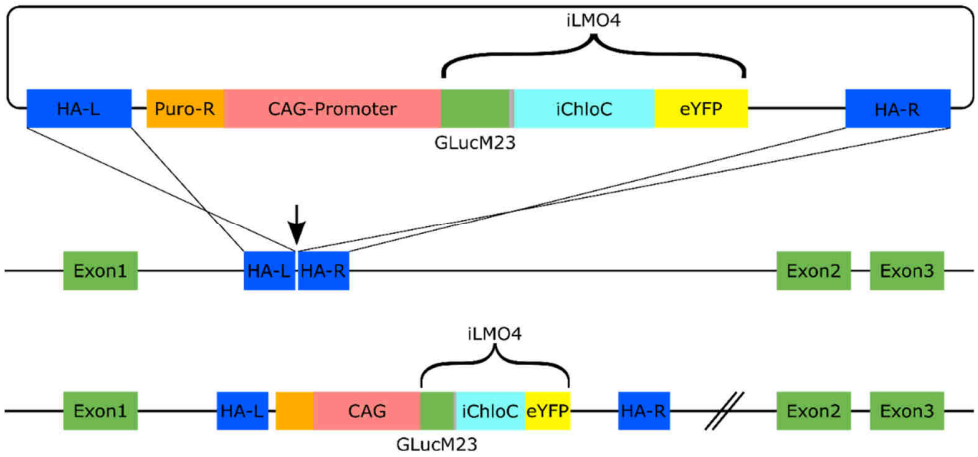

Figure 10: Illustration of the knock-in of iLMO4. A plasmid containing the CAG promoter and iLMO4 was created. The transgene is flanked by homology arms (HA). Cas9 targets the AAVS1 between Exon1 and 2 and when successful HDR occurs, the transgene is inserted. Previously published in "Contractile force of transplanted cardiomyocytes contributes to heart function after injury" by Stüdemann et al., BioRxiv, pages 2021.11.23.469715 (2021).

5.3.2 Amplification of PSAMs and LMOs with In-Fusion Overhangs

PSAMs were amplified from the aforementioned plasmids with 15 bp overhangs for In-Fusion cloning. In addition, however, we amplified EGFP and a T2A linker from a different plasmid (pFBGR-CMV-2A-LMNA) kindly provided by Vector Facility, UKE, Hamburg. Therefore, we amplified two In-Fusion fragments, subsequently cloned in the donor plasmid (#52344). Both LMO constructs were similarly used as the template for a PCR to amplify the gene of interest with 15 bp overhangs. Primer sequences can be found in the appendix.

Table 6: PCR mix for creating the GOI with In-Fusion overhangs

Substance	1x
5x PrimeSTAR® GXL Buffer	10 µl
dNTP Mix 2.5 mM	4 µl
Prime STAR® GXL DNA Polymerase (1 U)	0.8 µl
Primer F (10 pM)	0.5 µl
Primer R (10 pM)	0.5 µl
Template	10 ng
Nuclease free water	To 50 µl

Table 7: PCR program to create the GOI plus In-Fusion overhangs

Temperature	Time	Cycles
94 °C	5 min	
98 °C	15 sec	40x
57 °C	15 sec	
68 °C	2:30 min	
72 °C	5 min	

PCR reaction was confirmed by electrophoresis on 1% (w/v) agarose gel with TAE buffer (120 V, 100 mA, 11 W, 30-45 minutes).

5.3.3 Donor Plasmid Linearization

pAAVS1-CAG-hrGFP (Addgene, #52344) was digested with EcoRV and SalI to allow insertion of amplified GOIs with 15 bp overhangs.

Table 8: Plasmid linearization reaction

Substance	1x
FastDigest Green Buffer (10x)	4 µl
Plasmid Template	20 µl
FastDigest EcoRV	1 µl
FastDigest SalI	1 µl
Nuclease free water	To 40 µl
• **Incubate at 37 °C for 15 minutes**	

In case of incomplete digestion, the incubation time was increased to 30 minutes. Digestion was confirmed by electrophoresis on 1% (w/v) agarose gel (120 V, 100 mA, 11 W, 30-45 minutes).

5.3.4 PCR Product and Vector Clean-Up

PCR products and vectors were cleaned with a GeneJET PCR purification kit according to the manufacturer's protocol. All DNA concentrations were measured with Nanodrop™ ND-1000.

5.3.5 In-Fusion Reaction

For cloning fragments into the pAAVS1-CAG vector, the following mix was used. Linearized vector and PCR fragments were used in a 1:1 weight ratio.

Table 9: In-Fusion reaction

Substance	1x	
5x In-Fusion® HD Enzyme Premix	1 µl	
Linearized vector	1-2 µl	Vector and fragments were mixed in a 1:1 weight ratio
In-Fusion Fragment 1	1-2 µl	
(In-Fusion Fragment 2, for PSAMs)	1-2 µl	
Nuclease free water	To 5 µl	
• **Incubate at 50 °C for 15 minutes**		

5.3.6 Transformation of *E. coli*

Escherichia coli (*E. coli*) strain DB3.1 containing the gyrA462 allele was used for all experiments. This mutation makes the bacteria resistant to ccdB toxin included in the homology arm plasmids. Heat shock was used to transform *E. coli* with the PSAM and LMO plasmids.

Table 10: Transformation of *E. coli*

Substance	1x
In Fusion Reaction Mix	0.5 µl
***E. coli* suspension**	25 µl
Incubate mix 30 minutes on ice	
• **Heat shock reaction at 42 °C for 30 seconds**	
• **Place on ice for 2 minutes**	
• **Add 200 µl warm SOC medium and incubate at 37 °C for 45 minutes**	
• **Spread mix on Ampicillin^{+} LB plate and incubate at 37 °C overnight**	

5.3.7 Colony Picking and Colony PCR

Up to seven colonies were picked from each plate with a pipette tip by hand and suspended in 90 µl water. PCR was run to confirm insertion into plasmid directly from *E. coli*. A negative control without *E. coli* was added, and the PCR product was used as a positive control. PCR was run according to the manufacturer's protocol. Products were checked on 1% agarose (w/v) gels (120 V, 100 mA, 11 W, 30-45 minutes).

Table 11: PCR mix for screening of *E. coli*

Substance	1x
SapphireAmp® Fast PCR 2X Master Mix	5 µl
Primer F	0.1 µl
Primer R	0.1 µl
***E. coli* suspension**	0.5 µl
Nuclease free water	To 10 µl

Table 12: PCR program for *E. coli* screening

Temperature	Time	Cycles
94 °C	1 min	
98 °C	5 sec	30x
55 °C	5 sec	
72 °C	10sec/kb	

5.3.8 Verifying Cloning with Restriction Digestion

PCR positive *E. coli* clones were cultured overnight at 37 °C with 200 rpm shaking in 4 ml LB Ampicillin medium. NucleoSpin Plasmid® Kit (Macherey-Nagel) was used to isolate plasmids from cultures according to the manufacturer's protocol. PstI was used to digest the plasmid, and the mix was run on 1% (w/v) agarose gel. Bands were compared to in silico predicted band sizes.

Table 13: Restriction digestion with PstI

Substance	1x
FastDigest Green Buffer (10x)	2 µl
FastDigest PstI	0.5 µl
Plasmid DNA	750 ng
Nuclease free water	To 20 µl
• **Incubate at 37 °C for 30 minutes**	

5.3.9 Sequencing of Clones

One PCR and restriction digestion verified *E. coli* clone per plasmid was chosen for sequencing. Isolated plasmid DNA was used as a template for sequencing. 200 pg DNA and 1.5 pg primer (10 µM) per reaction were mixed, and nuclease-free water was added to 15 µl. Samples were dropped in an overnight Dropbox by Eurofins genomics, and results were obtained from the Eurofins webpage and aligned to hypothesized plasmids with Snapgene 3.4.4 (GSL Biotech LLC).

5.3.10 Plasmid Isolation (Maxipreparation)

One successfully sequenced *E. coli* clone per plasmid was cultured in 400 ml LB Ampicillin medium overnight. NucleoBond® Xtra Maxi kit (Macherey-Nagel) was used to isolate plasmids. DNA concentration was subsequently measured with Nanodrop™.

5.3.11 HEK 293 Cell Culture and Transfection

HEK293 cells were cultured in DMEM, 10% FBS, and 1% Penicillin/Streptomycin at normoxia conditions in 12-well plates. Transfection was performed using polyethylenimine (PEI). Plasmid DNA and PEI were mixed in a 1:2 ratio and directly added to the cell culture medium.

5.4 CRISPR/Cas9 Mediated Knock-In

5.4.1 Ribonucleoprotein Complex Formation

Custom crRNA and tracrRNA obtained from IDT were dissolved in IDTE buffer to a final concentration of 100 µM. Sequences can be found in the supplement. crRNA and tracrRNA were mixed in a 1:1 ratio and annealed at 95 °C for 5 minutes resulting in a 50 µM gRNA solution. Next, the mixture was cooled down for 1 hour, and 2 µl were mixed with 1.6 µl Cas9 protein (62 µM), resulting in an equimolar solution. Finally, the mixture was incubated for one hour at room temperature.

5.4.2 Nucleofection

For nucleofection of RNP complex and plasmid, early passage hiPSCs plated in 6-well format (FTDA and Geltrex) were switched to mTeSR™ Plus medium for increased nucleofection efficiency. One hour before nucleofection, the medium was supplemented with Y-27632 for increased cell survival during nucleofection. Cells were washed with DPBS, detached with Accutase and counted as mentioned before, and $8x10^5$ cells were resuspended in 100 µl nucleofector solution (82 µl P3 + 18 µl Supplement I) per reaction in a nucleofection cuvette. 4 µl plasmid solution (1 µg/µl), 1 µl Cas9 Electroporation Enhancer and the 3.6 µl µl RNP complex were added, and the nucleofection carried out with program CA137 in the 4D-Nucleofector (Lonza). Cells were subsequently incubated for 10 minutes at 37 °C under hypoxia for recovery before resuspension in 1 ml mTeSR™ Plus + CloneR Supplement. Finally, the cells were plated in 12-well format on Matrigel coating. mTeSR™ Plus feeding occurred daily until confluent.

5.4.3 Fluorescence-Activated Cell Sorting of Edited Cells

To enrich positively edited cells, FACS was employed. Cells were washed and detached as previously mentioned and resuspended in mTeSR™ Plus + Y. Sorting was carried out in the FACS Core Facility UKE by trained staff under sterile conditions in an Aria Fusion (BD). As hiPSCs are large cells, the 130 µm nozzle was employed, and the flow rate was kept to a minimum to reduce cell stress. Laser voltage intensities were adjusted to unedited cells, and the Fluorescein isothiocyanate (FITC) gate was set to include 0.0% of control cells. $EYFP^+$ or $EGFP^+$ ratios ranged from 0.94% to 3.13%. Up to 3,000 cells were sorted into a well of a 96-well plate supplied with mTeSR™ Plus + Y. Cell were subsequently cultivated under normal hiPSC culture conditions.

5.4.4 Clone Seeding and Picking

Cells were cultivated in 96-well format until confluency. Next, cells were washed and detached as previously described and seeded in low density for clonal expansion in mTeSR™ Plus + CloneR. Typically, 100-400 cells were seeded in a 6-well plate. After five to nine days, round-shaped $EYFP^+$ or $EGFP^+$ colonies were picked with a pipette and cultivated in 48-well format until confluent. Next, cells were detached and seeded into two 48-wells. Upon confluency, cells from one well were frozen, and cells from the copy well were used for genomic DNA isolation.

5.4.5 DNA Isolation from CRISPR Clones

DNeasy® Blood & Tissue Kit (Qiagen) was used to isolate genomic DNA from clones grown in 48-well format according to the manufacturer's protocol.

5.4.6 Knock-In Validation with Short PCR

Three PCR reactions were employed as a first screen for successful knock-In. Reaction one amplified a region spanning from native genomic DNA upstream of the insert, confirming the insertion of plasmid DNA. Reaction two amplified a region of native genomic DNA solely without insertion, detecting unedited alleles and possibly heterozygosity or mosaic cultures. Reaction three spanned a region from inside the plasmid DNA to native genomic DNA downstream of the

insert. Primer sequences can be found in the supplement. Product sizes were confirmed by gel electrophoresis on 1% (w/v) agarose gel (120 V, 100 mA, 11 W, 30-45 minutes).

Table 14: PCR mix for screening of gDNA for knock-in

Substance	1x
5X MyTaq Reaction Buffer	5 µl
Primer F 20 µM	0.5 µl
Primer R 20 µM	0.5 µl
Template	100 ng
MyTaq DNA Polymerase	0.5 µl
H_2O	To 25 µl

Table 15: PCR program for screening of knock-in

Temperature	Time	Cycles
95 °C	2 min	
95 °C	15 sec	10x
68 °C-1 °C/cycle	15 sec	
72 °C	30 sec/kb	
95 °C	15 sec	25x
58 °C	15 sec	
72 °C	30 sec/kb	
72 °C	2 min	

5.4.7 Knock-In Validation with Long-range PCR

Preselected clones were further confirmed with long-range PCR. Primer sequences can be found in the supplement. Product sizes were confirmed on 1% (w/v) agarose gel (120 V, 100 mA, 11 W, 30-45 minutes).

Table 16: PCR mix for long-range PCR

Substance	1x
NEBNext® High-Fidelity 2X PCR Master Mix	12.5 µl
Primer F 10 µM	1.25 µl
Primer R 10 µM	1.25 µl
Template	500 ng
H_2O	To 25 µl

Table 17: PCR program for long-range PCR

Temperature	Time	Cycles
98 °C	30 sec	
98 °C	10 sec	35x
60 °C	30 sec	
72 °C	30sec/kb	
72 °C	2 min	

5.4.8 Knock-In Validation with Sanger Sequencing

Successful long-range PCR products were used as sequencing templates. PCR products were purified using QIAquick PCR Purification Kit according to the manufacturer's protocol. Mix2Seq Kit (Eurofins genomics) was used for sequencing. 150 ng PCR products were mixed with 2 µl primer (10 µM) and filled up to 17 µl with nuclease-free water. Samples were dropped in an Overnight DropBox by Eurofins genomics, and results were obtained from the Eurofins webpage and aligned with Snapgene 3.4.4.

5.4.9 Knock-In Validation with Southern Blotting

Southern blotting was kindly performed by Dr. Irm Hermans- Borgmeyer, ZMNH, UKE. In brief, genomic DNA was digested with EcoRI. Next, DNA fragments were subjected to gel electrophoresis, followed by blotting to a membrane. Finally, detection of bands was conducted with self-designed radio-labeled probes.

5.5 Cardiac Differentiation

Confluent hiPSC cultures were subjected to differentiation by detaching cells, cultivating them for 24 hours in a spinner flask for embryoid body (EB) formation before subjecting EBs to mesoderm induction and cardiac differentiation. This is the so-called three-dimensional (3D) protocol. Alternatively, differentiation was conducted in 6-well plates, referred to as two-dimensional (2D) differentiation.

5.5.1 Cell Detachment and Embryoid Body Formation

Confluent hiPSC cultures in T75 flasks were washed with 10 ml DPBS. 0.1 ml/cm^2 Accutase + Y-27632 (10 µM) was added and cells were incubated for up to 15 minutes. The same amount of FTDA + Y-27632 was added for neutralization of Accutase. Cells were collected, centrifuged at 200 g for 2 minutes, and resuspended in Stage 0 medium at 3x10^4 cells per ml. Cell suspensions were filled into spinner flasks placed on a magnetic stirrer inside an incubator, cultured under hypoxic conditions for 24 hours at 40 rpm to form EBs.

5.5.2 3D Mesoderm Induction

On day 1, EBs were collected in T175 suspension culture flasks, placed in a V-rack to allow EBs to settle in one of the corners. These T175 were coated 24 hours prior with 1% Pluronic-F127 in DPBS and washed with DPBS twice. Stage 0 medium was aspirated, and EBs washed with Stage 1

wash medium. EB total volume was assessed by putting 10 ml EB suspension into a falcon tube (15 ml) and judging the settled EB volume. Total volume was then calculated as follows: $EB_{total} = EB_{10ml} \times V_{total}/10$ ml. Next, the washing medium was aspirated and replaced by new Stage 1 medium. 200-250 µl EBs in 46 ml were then put into one T175 flask and placed in a hypoxia incubator. Over the following two days (day 2 and 3), half of the medium was replaced per day, i.e., aspiration of 23 ml before the addition of 23 ml fresh medium.

5.5.3 3D Cardiac Differentiation

On day 4, EBs were collected in the corner of the T175. EBs were washed with FDM medium. Total EB volume was assessed as stated above as EB number tends to decrease during Stage 1. EBs were then distributed to new T175 flasks at 200 µl/ flask and placed in a normoxia incubator (21% O_2, 5% CO_2). Each day half of the medium was replaced until day 6. On day 7, FDM medium was aspirated and replaced by Stage 2 medium. Half of the medium was replaced each day until day 11. EBs usually started to show contractions on day 8 (24 hours after Stage 2 medium was added). On day 12, the medium was aspirated and replaced by RDM medium, which was continued until day 18.

5.5.4 Dissociation of EBs

For dissociation of EBs, the medium was aspirated from EBs, settled in a V-rack. EBs were washed twice with HBSS before adding 20 ml/ T175 Collagenase II solution (200 U/ml in HEPES) supplemented with 30 µM N-benzyl-p-toluene sulfonamide (BTS) and 10 µM Y-27632. Flasks were placed in an incubator for two to four hours and regularly checked for dispersing EBs under the microscope. Next, EBs were further dispersed by rapid pipetting before adding 20 ml/ T175 blocking buffer. Eventually, cells were centrifuged at 100 g for 10 minutes, resuspended in basis medium, and counted with a Neubauer chamber. As an alternative route of differentiation, a two-dimensional protocol was used.

5.5.5 Seeding, Preconditioning and Mesoderm Induction for 2D Differentiation

hiPSCs were seeded at 40-60x10^4/cm^2 in 6-well plates, coated with 1:100 Matrigel. Cells were fed daily with 3 ml FTDA until 70% confluency was reached. At this point, FTDA was replaced with 1.5 ml Stg0 medium for preconditioning. 16 hours later, the medium was replaced by 2 ml Stg 1 for 48 hours.

5.5.6 Cardiac Differentiation and Feeding of 2D Differentiation

Next, Stg 1 medium was aspirated and replaced with RPMI 1640 to wash out the remaining medium. Then 3 ml Stg 2.1 medium was added for 48 hours. After that, 3 ml Stg 2.2 replaced the old medium for another 48 hours. 3 ml RDM was used to maintain cells until heat shock and dissociation.

5.5.7 Dissociation of 2D Cardiomyocytes

All RDM medium was aspirated for dissociation, and cells were washed twice with HBSS before adding 1 ml/ well Collagenase II solution (200 U/ml in HEPES) supplemented with 30 µM BTS and

10 µM Y-27632. Plates were placed in an incubator for two to four hours and were regularly checked under the microscope for dispersing cells. Next, EBs were further dispersed by rapid pipetting before adding 1 ml/well blocking buffer. Cells were centrifuged at 100 g for 10 minutes, resuspended in basis medium, and counted with a Neubauer chamber.

5.6 Cardiomyocyte Preparation

5.6.1 Heat Shock

Regardless of the method used for cardiac differentiation, 24 hours before dissociation, cells that were to be used for cardiac transplantation underwent a heat shock. The medium was aspirated and mixed with fresh RDM. This medium mix was warmed to 43 °C in a water bath. After taking the medium out, cyclosporin A at 2 µM and IGF-1 at 100 ng/ml were added, and the medium was quickly distributed to the wells and cells put back into the incubator. Dissociation occurred in the same way as described above.

5.6.2 Cardiomyocyte Cryopreservation

Cardiomyocytes that were not immediately used for EHT casting were cryopreserved. Here, the cells were centrifuged again at 100 g for 10 minutes and resuspended in heat-inactivated FBS and DMSO (10:1) at up to $3x10^7$ cells per cryovial. Freezing was performed as previously described for hiPSCs. Cells were then transferred to -150 °C for long-term storage.

5.6.3 Cardiomyocyte Thawing

Cryovials were transferred from -150 °C to a water bath of 37 °C until only a small ice clump remained. The cell suspension was then transferred to a bigger tube before drop-wise adding of 9 ml prewarmed cardiomyocyte thawing medium. Cells were counted and used for EHT casting or transplantation.

5.6.4 Cardiomyocyte Preparation for Injection

Cardiomyocytes for injections were resuspended in a modified pro-survival cocktail (Laflamme et al. 2007). The cell suspension was then filled in a 29 G syringe for injection.

Table 18: Pro-survival cocktail mix

Substance	1 Injection
Cardiomyocytes	$20x10^6$
Matrigel	75 µl
Bcl-xL BH4 4-23	50 nM
Cyclosporin A	2 µM
IGF-1	100 ng/ml
Pinacidil	50 µM
RPMI 1640	To 150 µl

5.6.5 Cardiomyocyte 2D Culture

Cardiomyocytes were seeded at 3-10x10^5 cells/cm^2 on Geltrex or Matrigel-coated plates in RPMI 1640 supplemented with 10% B27 + Insulin. The medium was exchanged every two to three days for two weeks.

5.7 EHTs

EHT work was carried out by Christoph Manthey and Judith Rössinger under my supervision or by me.

5.7.1 EHT Casting

To cast EHTs, sterile 60 °C warm 2% agarose solution (1.6 ml/ well) was filled into 24-well plates. Teflon spacers were immediately placed in the liquid agarose to form casting molds. EHT master mix was prepared on ice.

Table 19: EHT casting mix

Substance	1 EHT (including + 10%)
Cardiomyocytes	1x10^6
2x DMEM	6.125 µl
Y-27632 10 mM	0.11 µl
Fibrinogen 200 mg/ml	2.78 µl
NKM medium	To 110 µl

Next, spacers were removed, and silicon racks placed in the mold. Then, 100 µl master mix were added to 3 µl Thrombin (100 U/ml) and swiftly pipetted into the casting mold. EHT casting plates were then incubated in a normoxia incubator for 1-2 h. Next, 500 µl EHT medium was added and incubated for 30 minutes before gently taking silicone racks with the cast EHTs to an EHT medium filled 24-well plates (1.5 ml/ well). EHTs were cultured under hyperoxic conditions (37 °C, 7% CO_2, 40% O_2, 98% RH) and fed with 1.5 ml per EHT every other day.

5.7.2 EHT Measurements

EHTs in 24-well format were measured with a video-optical platform at 37 °C with CO_2 and O_2 supplementation as previously described (Hansen et al. 2010). CTMV-Software (Consulting Team Machine Vision, Pforzheim) was used to analyze functional parameters such as force and frequency. Pharmacological studies were performed in either DMEM + HEPES or hEHT medium.

5.7.3 Sharp Microelectrode Action Potential Recording

AP recordings were conducted by Christoph Manthey and Judith Rössinger. A detailed description of the method is found in the dissertation of Tobias Krause (Krause 2021). First, EHTs were transferred into a bath containing Tyrode's solution at 36.5±0.5 °C. Then, EHTs were impaled by a standard sharp microelectrode, and data were acquired using Chart™5 (ADInstruments).

5.7.4 Light Pacing/ Stopping

A white box was darkened with black curtains for optogenetic experiments to reduce light exposure. Instead of the default LED plate (white LEDs), a custom-made plate with blue (470 nm) and red (700 nm) LEDs was used (Lemme et al. 2020).

5.8 Animal Procedures

All experiments were carried out on Dunkin Hartley guinea pigs bred at Envigo, Germany. This study was approved by the Amt für Verbraucherschutz, Freie und Hansestadt Hamburg (N098/2019). All procedures were performed by trained staff, legitimated by passing FELASA-B course and exemptions granted under § 16 Abs. 1 Satz 5 Verordnung zum Schutz von zu Versuchszwecken oder zu anderen wissenschaftlichen verwendeten Tieren. A study overview is depicted in Figure 11.

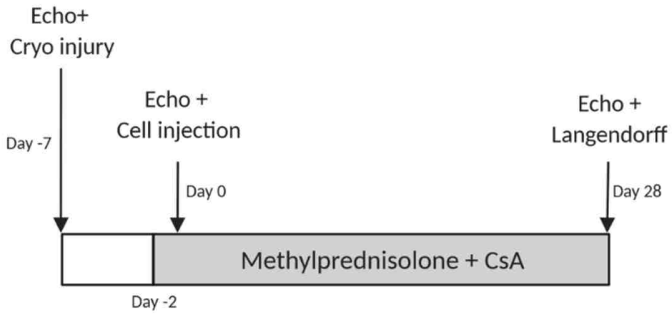

Figure 11: Study overview. On day -7 the basal echocardiography was performed, followed by cryoinjury. Two days prior to the second surgery, immunosuppression regime is started (day -2). On day 0, seven days after cryoinjury a second echocardiography was performed and cells were injected into the myocardium. After 4 weeks (day 28) a final echocardiography concludes the experiment, followed by Langendorff measurements. Created with BioRender.com.

5.8.1 First Echocardiography and Cryoinjury of Guinea Pig Hearts

300 to 400 g guinea pigs were weighed, and enrofloxacin (5-10 mg/kg body weight (bw) subcutaneously (sc)), buprenorphine (0.05 mg/kg bw, sc), carprofen (5 mg/kg bw, sc) and atropine (0.05 mg/kg bw, sc) administered. Animals were then placed in an anesthesia induction chamber and given 5% isoflurane + 95% clinical air. The animal was then placed on a heating pad and hair on the chest removed with a razor and depilatory cream. Paws were taped to ECG electrodes after applying electrode gel and ultrasound transmission gel to the chest. Routine echocardiography was then performed using the MS-250 transducer on a Vevo3100 (VisualSonics). Standard echocardiography included a parasternal long axis (PSLAX) and a parasternal short axis (PSAX) view in motion (M) and brightness (B)-mode to evaluate cardiac function.

The animals were then transferred to the surgery warming pad (37 °C), a tube for isoflurane delivery placed on the nose, and the paws were taped to the warming pad. The operation field was disinfected, and a tracheotomy was performed. After a skin incision, the thymus remnants and adipose tissue were bluntly dissected to expose the trachea. Next, a cannula (20 G) was used

to puncture the trachea, and a tracheal cannula (20 G) was placed and connected to a small animal respirator.

When stable ventilation was secured, a skin incision of two centimeters length was made on the edge of the musculus cutaneous trunci. M. cutaneous trunci and m. latissimus dorsi were moved aside and fixed to expose the thoracic wall. Mm. intercostales were dissected between the fourth and fifth rib, and a retractor was placed to open the thoracic cavity further. The pericardium was then carefully removed, and a liquid nitrogen-cooled stamp pressed on the left myocardial wall thrice for 30 seconds. It was released by inserting a modified smoldering bolt into the hollow stamp. Next, the lung was recruited, and the thorax closed tightly but carefully with three to four double surgeon's knots. M. cutaneous trunci and m. latissimus dorsi were then reconnected, and the skin closed with a continuous suture. Next, isoflurane anesthesia was reduced, and the tracheal cannula was removed after spontaneous inspiration was observed. Lastly, the trachea and skin were closed, and 6-8 ml Sterofundin® was administered to substitute fluid loss during surgery. Another dose of atropine (0.05 mg/kg bw, sc) was administered to ease breathing, and animals were placed under infrared light to compensate for the loss of body heat. Animals were closely monitored and, when nibbling and explorative behavior were seen, placed in a prewarmed cage (23 °C) with water and food ad libitum. For the following five days, buprenorphine (0.05 mg/kg bw, sc) was administered thrice, and carprofen (5 mg/kg bw, sc) was administered once daily to ensure continuous analgesia.

5.8.2 Transplantation of Cardiomyocytes

Seven days post cryoinjury, cardiomyocytes were transplanted. Procedures were similar to induction of cryoinjury, starting with routine echocardiography to ensure reduced cardiac function. After tracheotomy and thoracotomy, $20x10^6$ cardiomyocytes resuspended in a total of 150 µl pro-survival cocktail were injected with an insulin needle (29 G) in three to five locations of the infarcted area and its surroundings. Closing of the thorax, thoracotomy wake-up procedure, and perioperative medication remained the same as stated above. To avoid graft rejection, cyclosporin A (5 mg/kg bw, sc) and methylprednisolone (2 mg/kg bw, sc) were administered daily from 48 hours pre-transplantation until the end of the experiment.

5.8.3 Echocardiography

For analysis of left ventricular (LV) function, fractional shortening (FS) and fractional area change (FAC) were used. FS was assessed from an M-mode acquisition in a PSAX view. FS was calculated as the percental change of diameter between systole and diastole.

FS = (LVID;d-LVID;s)/ LVID;d

LVIDd: Left ventricular inner diameter diastolic
LVIDs: Left ventricular inner diamater systolic

FAC was assessed from a B-mode acquisition in the PSAX view. FAC was calculated as the percental change of endocardial area during systole compared to diastole.

FAC=(ENDOarea;d-ENDOarea;s)/ENDOarea:d

ENDOarea;d: Endocardial area diastolic
ENDOarea;s: Endocardial area systolic

Calculations were performed using the in-built tools of VevoLab (VisualSonics). Data were analyzed by Birgit Geertz, IEPT, UKE.

5.8.4 Pharmacokinetic Study for PSEM^{89S}

For evaluation of pharmacokinetics of the substrate PSEM^{89S} healthy guinea pigs were administered buprenorphine (0.05 mg/kg bw, sc), carprofen (5 mg/kg bw, sc), and heparin (500 µL). Anesthesia was induced with isoflurane. Animals were placed on a warming pad under continuous isoflurane anesthesia and the vena saphena or vena jugularis exposed. PSEM^{89S} was administered at 50 mg/kg body weight intravenously into either of these two veins, and blood was drawn at different time points from veins on the three other legs to avoid contamination. Alternatively, the injection was conducted intraperitoneally. After the experiment, the animals were euthanized by cervical dislocation. Blood samples were centrifuged for 20 minutes at 5,000 g. The supernatant (serum) was stored at -20 °C until use. Measurements of PSEM^{89S} were kindly performed by Prof. Edzard Schwedhelm, ICPT, UKE. Half-life time was determined using the formula $N(t) = N_0(\frac{1}{2})^{\frac{t}{t_{\frac{1}{2}}}}$.

5.9 Langendorff Experiments

To assess cardiac function ex vivo, a Langendorff apparatus was used. A self-built platform was used to create hydrostatic pressure of 70 cm (=51 mmHg). Hence, heart function was assessed in Langendorff mode. A big tank (2 L) was used as a reservoir. The reservoir was connected via silicone tubing to a bubble trap built from a 15 ml tube. A syringe was connected at the top of the bubble trap to eliminate air in the system. Below the bubble trap, a vertical condenser connected to a water bath was used to warm the buffer to 37 °C. A clipped and blunted 2.0 mm steel needle was used for cannulation of the aorta. Intraventricular developed pressure was measured using a pressure transducer connected via tubing to a self-built balloon catheter. This allowed isovolumetric pressure development. The catheter was assembled using cling film, 6-0 sutures, and blunted 21 G needles (AD Instruments 2003; Sutherland et al. 2003a). The pressure transducer was calibrated with a water column using two-point calibration in Chart™5 Pro. Two hooks (electrodes) made from stainless steel wire were placed in the right atrium for pacing experiments. Hearts were paced at baseline frequency plus an additional 15%. Pacing settings are depicted in table 20. Substrates such as PSEM^{89S} were administered via a syringe pump connected right above the blunted needle at a three-way valve. During optimization of the system, Lidocaine

170 µM was added to the system, effectively abolishing arrhythmic events (Vandecasteele et al. 1999).

Table 20: Langendorff heart pacing settings

Pacing Settings	
Start Mode	Free Run
Frequency	Variable
Delay	0.10 ms
Width	1.00 ms
Instrument Setup	Normal Run
F-Set	1
Polarity	POS
Amplitude	4-8 V

5.9.1 Modified Krebs-Henseleit Buffer Preparation

NaCl, KCl, $MgSO_4$, $NaHCO_3$, KH_2PO_4, glucose, and Na-pyruvate were weighed, placed in a beaker, and the appropriate volume of diH_2O was added. The buffer was then gassed with carbogen (5% CO_2, 95% O_2) for 15 minutes. Next, pH was adjusted to 7.4, and $CaCl_2$ was added. Eventually, the buffer was filtered through a 0.2 µm filter to remove calcium crystals. MKH buffer was then warmed and gassed with Carbogen until use.

5.9.2 Heart Preparation

Animals for Langendorff preparation were given buprenorphine (0.05 mg/kg bw, sc) at least 30 minutes prior to the start of the experiment. Heparin (500 µL) was given at least 10 minutes before starting the experiments to prevent blood coagulation while excising the heart. To induce anesthesia, fentanyl (0.025 mg/kg bw), midazolam (1.0 mg/kg bw) and medetomidine (0.2 mg/kg bw) were injected intramuscularly. The animal was euthanized by cervical dislocation. The four paws were fixed to the underlying surface and the thorax was opened. The aorta was localized and deducted. Next, the remaining attachments of the heart were removed, and the heart was washed in cold MKH buffer. The heart was then placed in a petri dish filled with cold MKH buffer, and the aorta cannulated with the previously mentioned 2.0 mm blunt needle using forceps. To fixate the heart, a suture and a clip were used. The cannulated heart was then quickly connected to the Langendorff apparatus and the MKH flow continuously increased. During this process, a hole was cut into the left atrium, and the balloon catheter was inserted into the left ventricle via the mitral valve. The balloon was then inflated using a 1 ml syringe until a baseline pressure of 5-10 mmHg was reached. The pacing electrodes (hooks) were attached to the right atrium. Upon full increase of the flow into the heart, the organ was left for equilibration of 15 minutes. During this time, a stable contraction pattern was reached. Then the experiment was conducted by either applying blue (470 nm)/ red (660 nm) light on the hearts with a PE4000 (coolLED) or administering

PSEM^{89S} via a syringe pump. After the experiment, hearts were flushed with KCl solution to arrest hearts in diastole before fixation in Roti®-Histofix. Blood was drawn for cyclosporin A level assessment, and organ samples for cryopreservation were taken from the lung, liver, kidney, and spleen.

5.9.3 Bioluminescence Images

At the end of an experiment, CTZ was infused as a bolus prior to arresting hearts with KCl. A digital single-lens reflex camera on a tripod with a magnification lens was used to take pictures. Exposure times of one minute were used.

5.9.4 Langendorff Data Analysis

Contraction data was analyzed with Chart™5 Pro. The in-built peak analysis tool was used. Settings can be seen in figure 12. Raw recordings were digitally filtered with a low-pass filter at 45 Hz, with auto-adjustment. Heart rate was determined using the cyclic measurements tool, which derived the heart rate from each contraction. Software-derived data tables were exported to Excel (Microsoft) for analysis. For PSAM GlyR studies, values of ten contractions were averaged and used for subsequent data plotting and calculations. To determine the LVDP prior, during, and after PSEM^{89S} application, the last value before PSEM^{89S} application, the last value during PSEM^{89S} application, and the value 120 seconds after PSEM^{89S} application were used.

For the iLMO4 study, individual contractions were plotted due to the quick response of hearts to light application. Therefore, ten contractions prior and thirty contractions during light exposure were plotted. For analysis of the recovery, the last ten contractions of light exposure and thirty subsequent contractions were plotted. Calculations were performed by averaging the first five and the last five contractions.

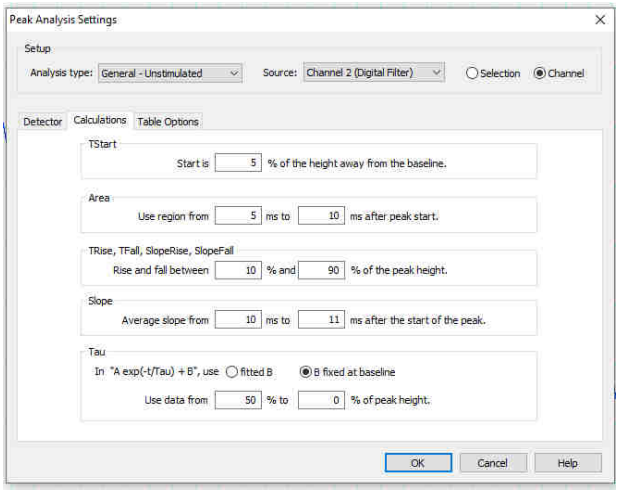

Figure 12: Peak analysis settings in Chart5™ Pro.

5.10 Histology and Stainings

5.10.1 Heart Processing

Hearts were fixed for 48 hours in Roti®-Histofix. Next, the organs were sectioned into four equally thick short-axis rings with a scalpel (Sections A to D). Photographs were taken from the whole heart and each section. Hearts were then placed in PBS until histological preparation.

5.10.2 Heart Sectioning and Staining

Further processing of tissue samples was performed by Kristin Hartmann, Mouse Pathology Facility, UKE. In brief, heart sections were dehydrated, embedded in paraffin, and sectioned. 4 µm sections were placed on glass object slides. One section per ring was stained for Dystrophin and scanned. Dystrophin was visualized with the multimer-technology-based UltraView Universal DAB Detection kit (Ventana® BenchMark® XT; Roche). Slides were then scanned with a NanoZoomer (Hamamatsu).

5.10.3 Antibody Stainings of Heart Sections.

Paraffin sections were rehydrated by submerging object slides in the following liquids:

Table 21: Rehydration of paraffin sections

Chemical	Time
Xylene	2x 5 min
Ethanol 99%	2x 2 min
Ethanol 96%	A few quick dips
Ethanol 70%	1x1 min
PBS	1x5 min

Next, slides were treated with Proteinase K for antigen retrieval. Slides were submerged in Tris-HCl (pH 7.6, 10 mM) with Proteinase K for 15 minutes at 37 °C Celsius. Alternatively, heat-induced antigen retrieval was used. Here, sections were boiled in sodium citrate (pH 6.0 10 mM) for twenty minutes, followed by permeabilization in 0.1% Triton X-100 in PBS. Regardless of the antigen retrieval, slides were blocked with blocking solution for 30 minutes and stained with primary antibodies overnight at 4 °C. On the next day, the primary antibody was washed thrice, and the secondary antibody was applied at 1:100 in IF-buffer for up to 2 hours. DAPI was added to the staining solution at 1:1000. After washing off excess antibodies, a coverslip was attached with Mowiol and slides left to dry at room temperature overnight.

5.10.4 2D Cardiomyocyte Stainings

Cells were fixed in Roti®-Histofix for 20 minutes. Antibodies for immunofluorescence stainings were diluted in 3% milk powder, 0.1% Triton X-100 in PBS, and incubated overnight at 4 °C under light agitation. Secondary antibodies were incubated for 1-2 hours at room temperature in 3%

milk powder 0.1% Triton X-100 in PBS. After washing with PBS, cells were incubated with DAPI (1:1000) to counterstain nuclei. Cells were stored at 4 °C until further use.

5.10.5 EHT processing

EHTs for microscopy were fixed in PFA for 12 hours. Fixed EHTs were removed from the silicon posts and stored in PBS at 4 °C. EHTs were then embedded in 4% agarose and sectioned at 100 µm with a vibratome. Sections were blocked with 1% BSA + 0.3% Triton X-100 in PBS for up to 90 minutes at room temperature. Primary antibody incubation followed in IF-buffer overnight at 4 °C. Sections were washed thrice in PBS before secondary antibody and DAPI (1:1000) incubation at room temperature for 90 minutes. Three times washing followed before sections were placed on microscope slides and covered with Mowiol and a coverslip.

5.10.6 Scar and Graft Quantification

NDP.view2 (Hamamatsu Photonics) was used to image dystrophin stained sections to analyze infarct and LV circumference and scar and LV area. Infarct percentage was calculated by dividing infarct circumference by LV circumference (length-based). Scar percentage was calculated by dividing scar area by LV area (area-based). For each heart, the average was calculated as the mean of one dystrophin staining per ring (A to D). An annotated example is shown in Figure 13.

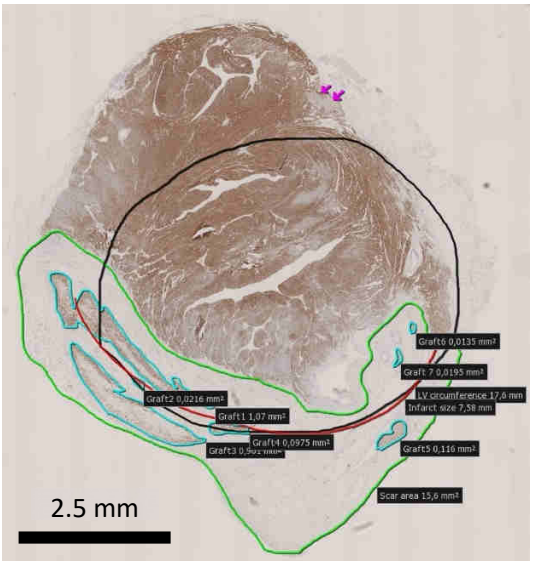

Figure 13: Scar, infarct and graft size calculation. Dystrophin stained section of an injured guinea pig heart. Red line indicates scar length which is divided by LV circumference (black) to result in infarct percentage (length-based). Scar area (green) is divided by total LV area (not indicated for better visibility) to result in scar percentage (area-based). Graft area (turquoise) is divided by the scar area (green) to result in the graft percentage.

6 RESULTS

6.1 Cloning of Plasmids

In this study, we selected four opto-/chemogenetic channels to be knocked into the genome of hiPSCs. To do so, we used a plasmid-based approach. The In-Fusion cloning method was chosen to produce the plasmids for our CRISPR approach. First, the gene of interest was amplified via PCR with primers that added a 15 bp sequence complementary to the last 15 bp of the linearized vector. The In-Fusion enzyme then recognized these complementary sequences and fused the gene of interest and vector. This was followed by bacterial transformation (Figure 14). The number of fragments cloned into the vector can be increased. We cloned one or two fragments into the vector, depending on the cell line.

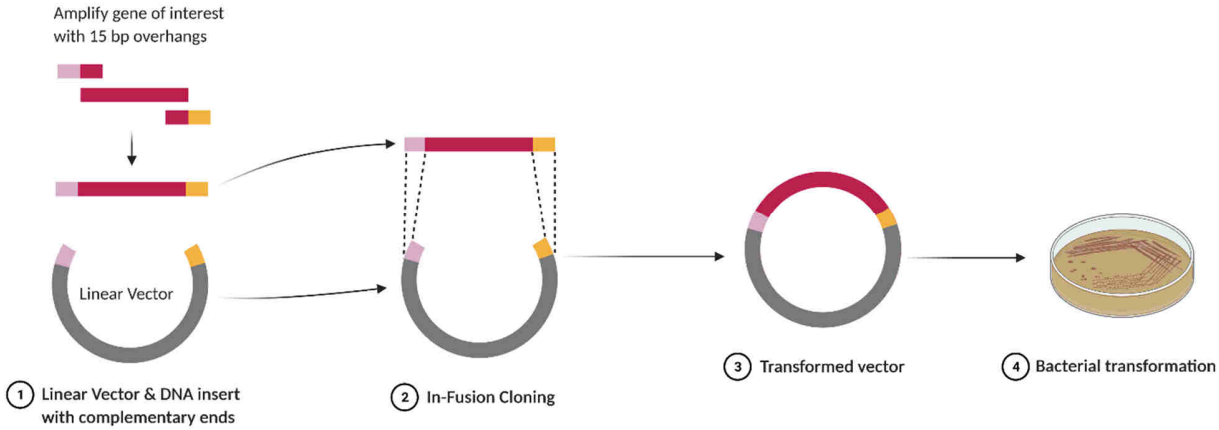

Figure 14: Principle of In-Fusion cloning. The gene of interest (red) is amplified with primers that add a 15 bp sequence (yellow and purple) to the PCR product. The chosen vector is linearized by restriction digestion. The In-Fusion enzyme then clones the gene of interest into the vector. Adapted from https://www.takarabio.com/learning-centers/cloning/in-fusion-cloning-faqs, created with BioRender.com.

6.1.1 Cloning of pAAVS1-EGFP-2A-PSAM 5HT3 and pAAVS1-EGFP-2A-PSAM GlyR

PSAM 5HT3 and PSAM GlyR plasmids were obtained from Addgene. To generate plasmids for the AAVS1 safe harbor locus integration, PSAM 5HT3 and PSAM GlyR genes were amplified by PCR with 15 bp In-Fusion overhangs. Direct cloning of PSAM 5HT3-IRES-GFP and PSAM-IRES-GFP from the original plasmids was unsuccessful (data not shown). Hence, to not lose the visual control of a fluorescent protein, EGFP-2A was amplified from a plasmid supplied by the vector facility of the UKE. Successful PCR with In-Fusion overhangs of PSAM 5HT3, PSAM GlyR (both 1.4 kb), and EGFP-2A (0.8 kb) was confirmed via gel electrophoresis (Figure 15, left). pAAVS1-CAG-hrGFP was used as a vector and digested with SalI and EcoRV. Gel electrophoresis confirmed digestion (9.1 kb and 0.8 kb; Figure 17, left). After clean-up, an In-Fusion reaction with the two fragments and the digested vector was conducted. Transformed *E. coli* clones were picked, plasmids isolated, and PstI digested. Bands were expected at 4.4 kb, 4.3 kb, 1.8 kb, 0.6 kb, 0.1 kb. Gel electrophoresis confirmed correct band size in all pAAVS1-EGFP-2A-PSAM 5HT3 and pAAVS1-EGFP-2A-PSAM GlyR clones (Figure 15, right). One clone of each approach was Sanger sequenced, which confirmed

the correct sequence (Figure 15, bottom). We found a silent mutation in PSAM 5HT3 TTC → TTT, at bp 423, amino acid 141 (Phenylalanine).

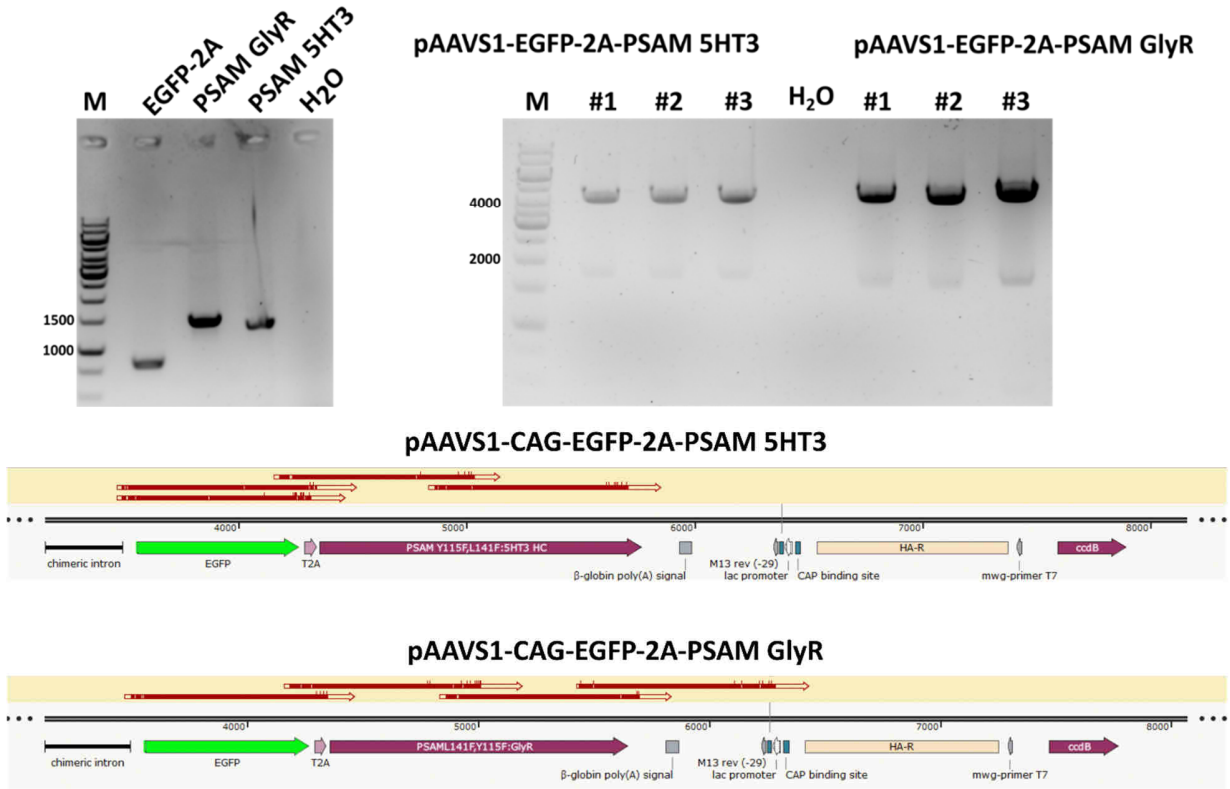

Figure 15: PSAM plasmid cloning. Left: EGFP-2A, PSAM GlyR and PSAM 5HT3 were amplified with 15 bp overhangs for In-Fusion reaction. Correct band size was confirmed (1.4 kb and 0.8 kb). Middle: pAAVS1-EGFP-2A-PSAM 5HT3 was isolated from three *E. coli* clones. One out of three clones was selected for further analysis. Right: pAAVS1-EGFP-2A-PSAM GlyR was isolated from three *E. coli* clones. One clone was selected for further analysis. Bottom: Sequencing of selected plasmid. Red areas indicate aligned bases along the plasmid DNA. Four sequencing reactions were performed to cover the region of EGFP-2A and the respective PSAM variant.

HEK293 cells were transfected with PSAM GlyR and PSAM 5HT3 plasmids, and EGFP expression was observed with both plasmids, confirming functionality (Figure 16). Large plasmid isolation (maxipreparation) was conducted to produce a sufficient amount of plasmid for nucleofection in hiPSCs. Large plasmid isolation resulted in 350 ng/µl in 100 µl for pAAVS1-EGFP-2A-PSAM 5HT3 and 950 ng/µl in 100 µl total volume for pAAVS1-EGFP-2A-PSAM GlyR respectively.

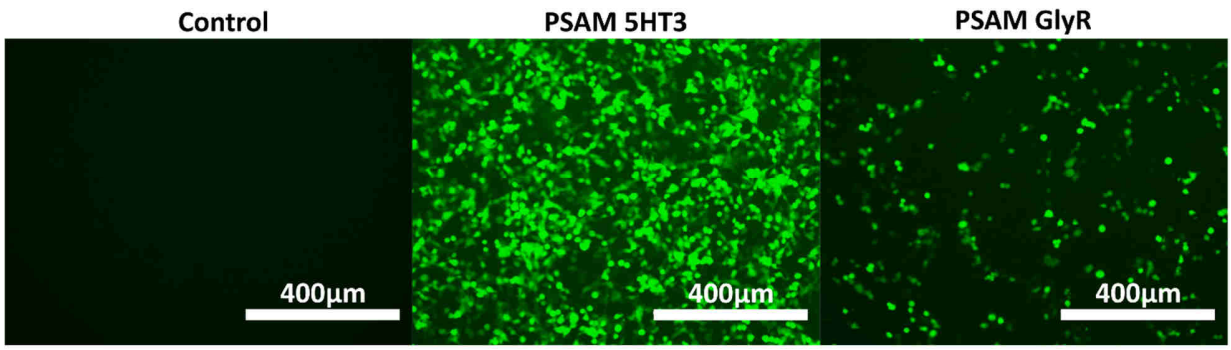

Figure 16: EGFP expression in HEK293 cells. Cells were transfected with the plasmids to confirm functionality. PSAM 5HT3 and PSAM GlyR transfected cells expressed EGFP.

6.1.2 Cloning of pAAVS1-LMO4 or pAAVS1-iLMO4

Plasmids for this study were obtained from Ute Hochgeschwender (pc DNA CAG-iLMO4 and pAAV-hSyn-LMO4 constructs). LMO4 and iLMO4 genes were amplified with 15 bp overhang primers for In-Fusion reaction. PCR success was confirmed with gel electrophoresis (2.3 kb; Figure 17, left). Vector backbone digestion with SalI and EcoRV was confirmed by gel electrophoresis with expected band sizes at 9.1 kb and 0.8 kb (Figure 17, left). After clean-up, In-Fusion reaction, and transformation, *E. coli* clones were picked, plasmids isolated, and PstI digested. Bands were expected at 5.2 kb, 4.4 kb, 1.1 kb, and 0.6 kb. Gel electrophoresis confirmed correct band size in one out of six pAAVS1-CAG-LMO4 clones and four out of five pAAVS1-CAG-iLMO4 clones (Figure 17, middle and right).

Plasmid DNA from one PCR positive clone was Sanger sequenced. Both plasmids aligned to the expected reference sequence, and no mutations were found (Figure 17, bottom).

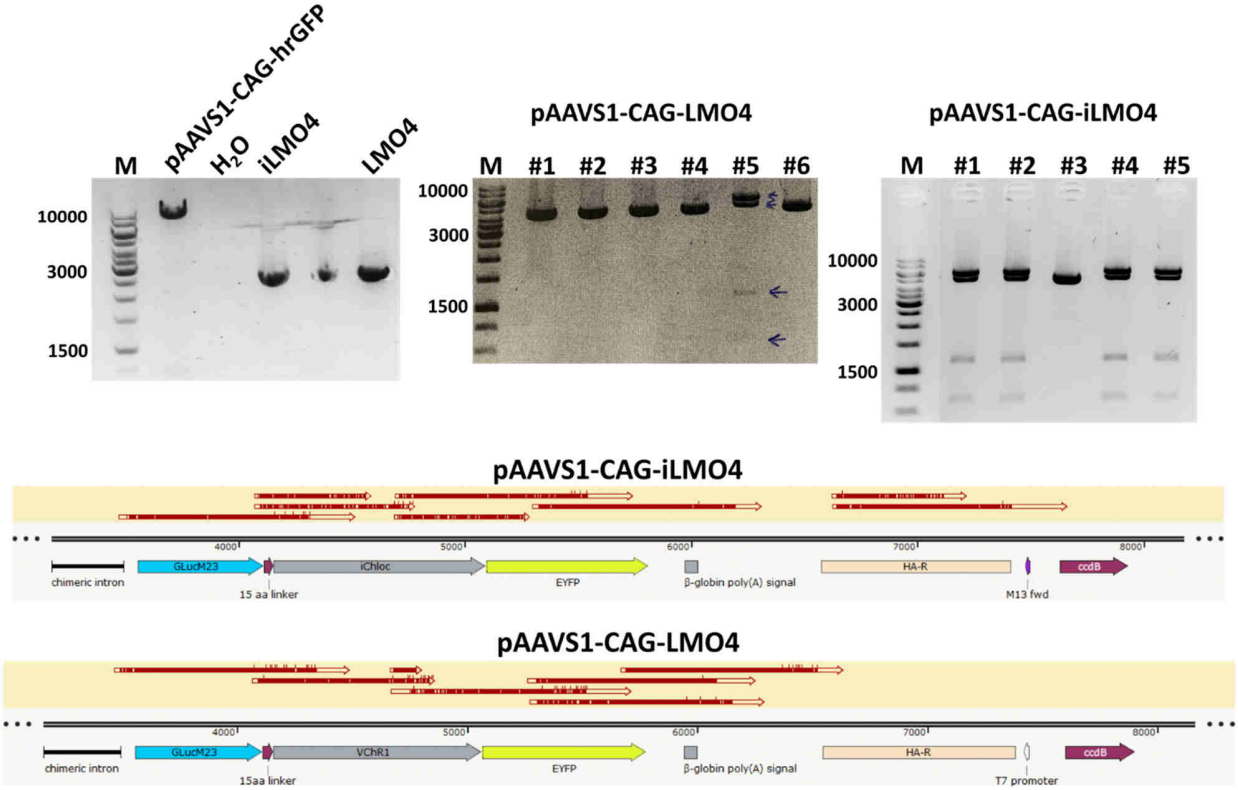

Figure 17: LMO plasmid cloning. Left: pAAVS1-CAG-hrGFP was digested with EcoRV and SalI. Two bands are visible, at 9 kb and 0.7 kb. iLMO4 and LMO4 were amplified with In-Fusion overhangs (2.3 kb). Middle: pAAVS1-CAG-LMO4 was isolated from six *E. coli* clones. One clone (#5) was selected for further analysis as it was the only one exhibiting the right bands after PstI digestion. Right: pAAVS1-CAG-iLMO4 was isolated from five *E. coli* clones. Four clones (#1, #2, #4 and #5) were selected for further analysis. Bottom: Sequencing of selected plasmid. Red areas indicate align bases along the plasmid DNA. Six and eight sequencing reactions were performed to cover the region of GLucM23 to EYFP.

HEK 293 cells were then transfected with pAAVS1-CAG-LMO4 or pAAVS1-CAG-iLMO4, and EYFP expression was observed (Figure 18).

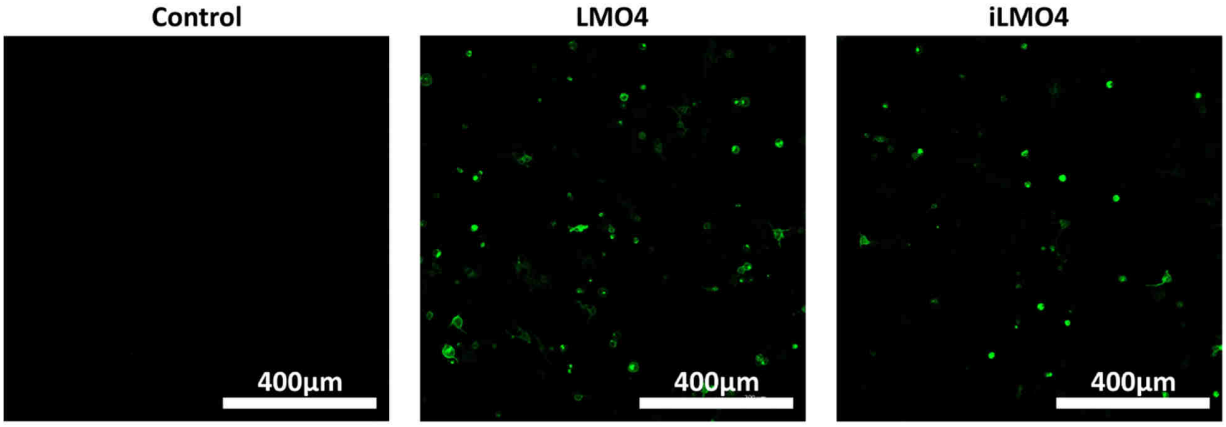

Figure 18: HEK293 cells were transfected with pAAVS1-CAG-LMO4 and pAAVS1-CAG-iLMO4. Transgene expression was confirmed by EYFP.

CTZ application on transfected HEK 293 cells confirmed luciferase functionality. While control cells exhibited a bioluminescence signal of $7.42x10^5$ AU, LMO4 showed $1.14x10^7$ AU and iLMO4 cells $1.22x10^7$ AU (Figure 19). As the last step, large plasmid isolation was conducted to produce sufficient plasmid for nucleofection in hiPSCs. For pAAVS1-CAG-LMO4, this resulted in 682 ng/µl and pAAVS1-CAG-iLMO4 in 772 ng/µl in 300 µl total volume, respectively.

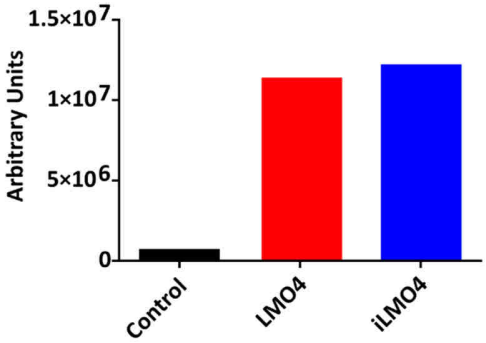

Figure 19: Bioluminescence signal of pAAVS1-CAG LMO4 and pAAVS1-CAG iLMO4 transfected HEK293 cells.

6.2 CRISPR/ Cas9 in iPSCs

To knock-in the transgenes from plasmids, the CRISPR/Cas9 system was employed. The in-house generated hiPSC line UKEi001-A (https://hpscreg.eu/cell-line/UKEi001-A) was used and served as a negative parental control for all experiments.

6.2.1 Protocol Optimization for the Knock-In of Plasmids

In the process of establishing CRISPR/Cas9 mediated knock-in, several modifications to an existing protocol that had been used for knock-out approaches or to edit single nucleotides were necessary. As a starting point, iPSCs were cultured in mouse endothelial fibroblast conditioned medium + Y-27632. Nucleofection was performed using an HDR enhancer and 1 µg of the plasmid. However, these approaches only resulted in a very low percentage of $EYFP^+$ cells (Table 22). During the optimization process, conditioned medium and Y-27632 were replaced by mTeSR Plus with CloneR. The plasmid quantity was gradually increased to 4 µg. Two different crRNA designs

were tested. Both sequences and their respective characteristics can be found in the appendix. Even though this test was not performed systematically, crRNA1 turned out superior and was used for all further experiments.

As HDR efficiency was low, we tested nocodazole treatment (10 to 100 ng/ml) to synchronize the iPSC cell cycle prior to nucleofection to enhance HDR events. In control cells, we found 44% of cells in the G1 phase while 2% were in S and 52% in the G2/M phase. Upon treatment with nocodazole, the G2/M percentage increased to a maximum of 93% when 100 ng/ml nocodazole was applied (Figure 20). Unfortunately, although cell cycle synchronization was successful, the treatment resulted in significant cell death. The viability of control cells was 95% and steadily declined with increasing nocodazole concentration to 75% (Figure 20). Hence, nocodazole treatment was discontinued.

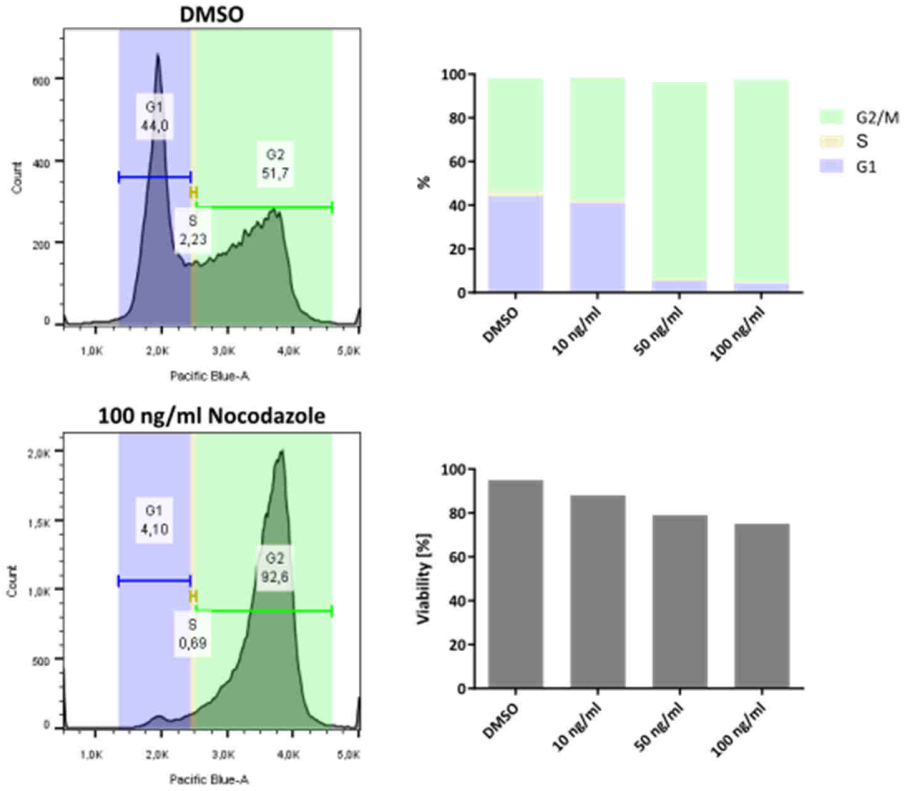

Figure 20: Nocodazole-mediated cell cycle synchronization of hiPSCs. Left panels: DNA content of hiPSCs measured with FACS. Upper right panel: 16 hours of treatment synchronized cells in G2/M phase, measured by their DNA content. Lower right panel: Viability of hiPSCs decreased with increasing concentrations of nocodazole.

With the optimized protocol, single EGFP$^+$/ EYFP$^+$ cells could be observed after nucleofection, sometimes growing in colonies (Figure 21, left). These were enriched by FACS (Figure 21, middle and right). The aforementioned optimizations resulted in up to 3% EYFP$^+$/ EGFP$^+$ cells (Table 22, Figure 22).

In summary, I improved the CRISPR/Cas9-mediated knock-in strategy. Although nocodazole treatment did not result in the expected result, the increase in plasmid concentration, mTeSR and CloneR instead of conditioned medium and the use of a superior crRNA improved the knock-in efficiency to a degree I could continue the experiments.

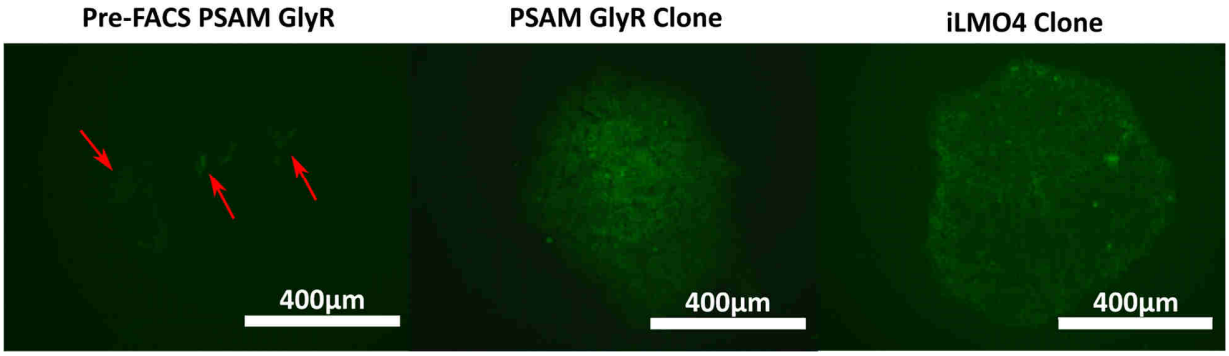

Figure 21: EGFP⁺/EYFP⁺ cells after nucleofection and FACS. Left: Colonies or single edited cells can be observed 48 hours after nucleofection. Middle and right: After FACS sorting clonal expansion leads to pure EGFP⁺/EYFP⁺ colonies.

Table 22: Nucleofection success prior and after optimization.

Cell Line	Prior to Optimization	Optimized Protocol
PSAM 5HT3	0.1% EGFP⁺	0.94% EGFP⁺
PSAM GlyR	1.3% EGFP⁺	2.87% EGFP⁺
LMO4	0% EYFP⁺	2.34% EYFP⁺
iLMO4	0% EYFP⁺	3.13% EYFP⁺

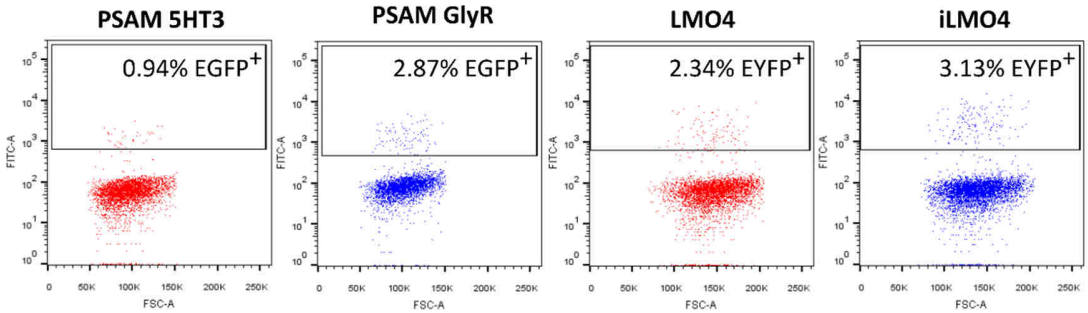

Figure 22: FACS results of the four knock-in cell lines. EGFP⁺/EYFP⁺ positive cell percentage ranged from 0.94% to 3.13%. Previously published in "Contractile force of transplanted cardiomyocytes contributes to heart function after injury" by Stüdemann et al., BioRxiv, pages 2021.11.23.469715 (2021).

6.2.2 Clonal Expansion and Characterization

After a recovery period of one passage, taking between one and four days, sorted iPSCs were seeded as single cells and clonally expanded in mTeSR Plus + CloneR (Figure 21). Several clones were picked for each cell line, and genomic DNA was used for genotype screening. For this strategy, three PCR reactions were prepared for each genomic DNA sample. One reaction covered the 5' insertion site (red + green primer, Figure 23), while a second reaction covered the 3'

insertion site (yellow + red primer, Figure 23). Finally, a third reaction covered the 5' and 3' insertion sites, but this reaction could only work if an unedited allele were present (red + red primer, Figure 23).

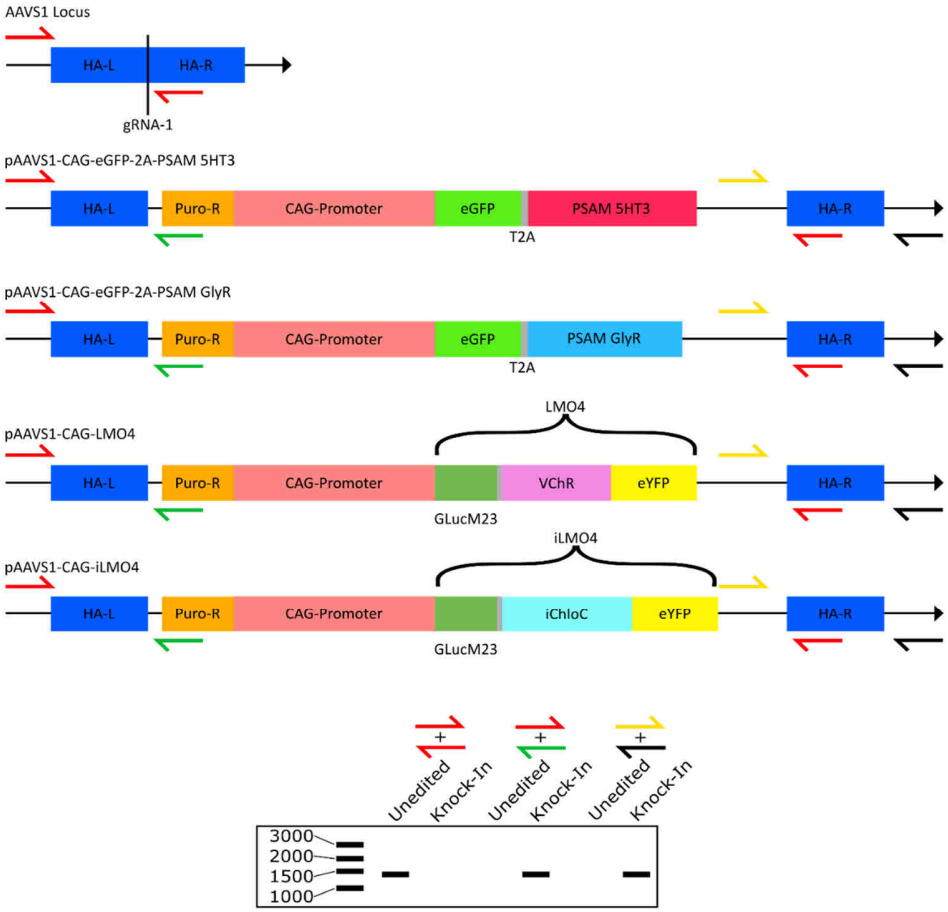

Figure 23: Genotype screening strategy for all four knock-in iPSC lines. Three PCR reactions were performed. 5’ reaction (green + red primers) confirmed genomic knock-in as well as the 3’ reaction (yellow + black primers). A third reaction (red + red primers) was only positive when the unedited allele was still present.

This screening method allowed to pre-select clones. Clones were categorized as homozygous, heterozygous, unclear, or aberrant (Table 23). The category "unclear" included all clones in which the 5' and 3' reactions showed opposing results, meaning the genotype could not be identified. All clones that showed an unusual and unexplainable combination of positive/ negative PCR reactions or unexpected bands at different sizes than expected were categorized as aberrant. Corresponding gel pictures can be found in the appendix.

Table 23: Genotype screening strategy. Three PCR reactions were performed per clone. Depending on the result of each reaction, a genotype was concluded.

Genotype Category	5’ Reaction	3’ Reaction	Unedited Reaction
Homozygous	+	+	-
Heterozygous	+	+	+
Unclear	5’ + while 3’- or 5’- while 3’ +		+/-
Aberrant	Unexpected bands		+/-

By this screening method, I characterized 65 clones across all four cell lines, of which 19 (29%) were homozygous, 24 (37%) were heterozygous, five (8%) were aberrant, and 17 (26%) had an unclear genotype (Figure 24).

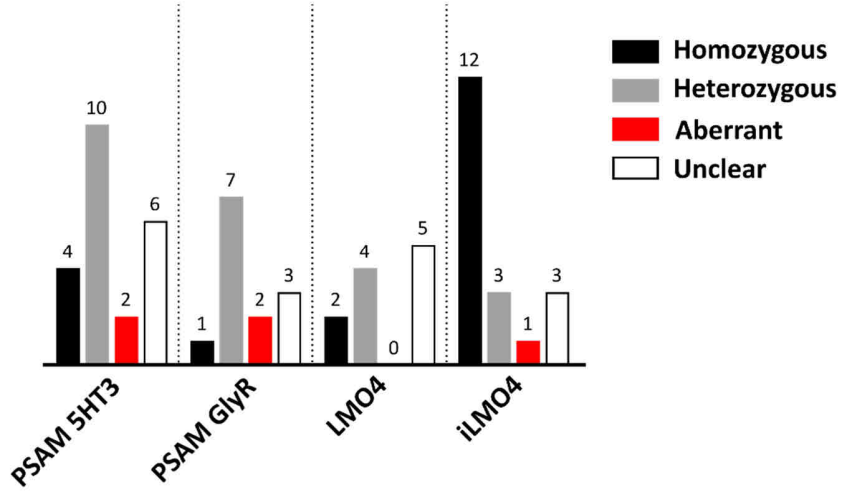

Figure 24: PCR genotype screening results. 11 to 22 clones were picked per knock-in approach.

Three homozygous or heterozygous clones were selected from each cell line, and correct transgene integration was further validated by PCR transgene amplification followed by Sanger sequencing. The correct sequence was found in two to three clones per cell line (Figure 25). In PSAM 5HT3, all clones were successfully sequenced. In PSAM GlyR, BF6 showed insufficient sequencing coverage and was excluded from further analysis.

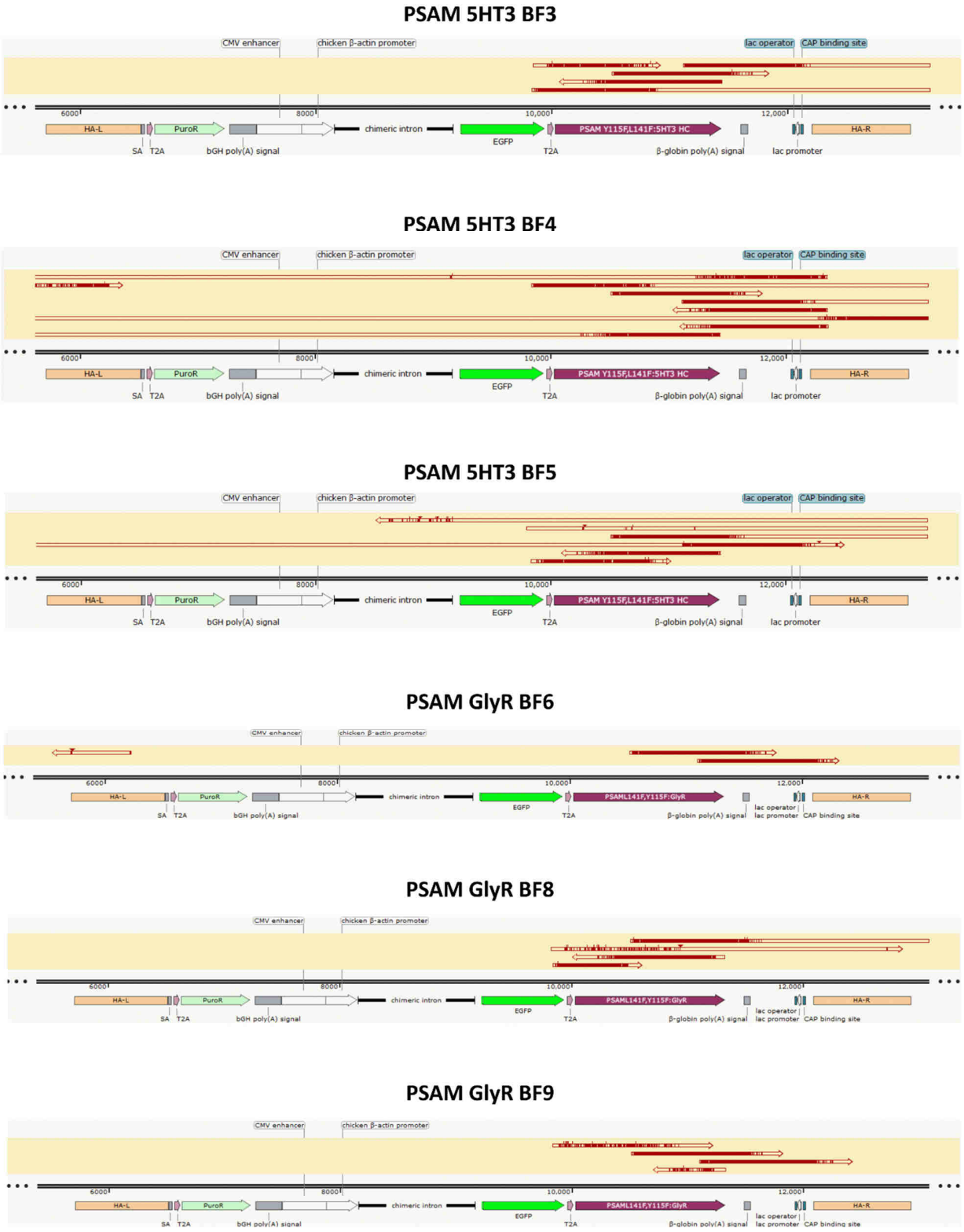

Figure 25: Sequencing of PSAM 5HT3 and PSAM GlyR. Red areas above the sequence indicate aligned base pairs from sequencing. In PSAM 5HT3 all three clones sequenced showed the correct sequence. In PSAM GlyR clones only BF8 and BF9 showed the correct sequence while BF6 was excluded due to insufficient coverage.

In LMO4 and iLMO4, all clones showed the correct sequence (Figure 26). However, a third clone (LMO AP5) was excluded at an earlier step because the transgene-covering PCR was unsuccessful.

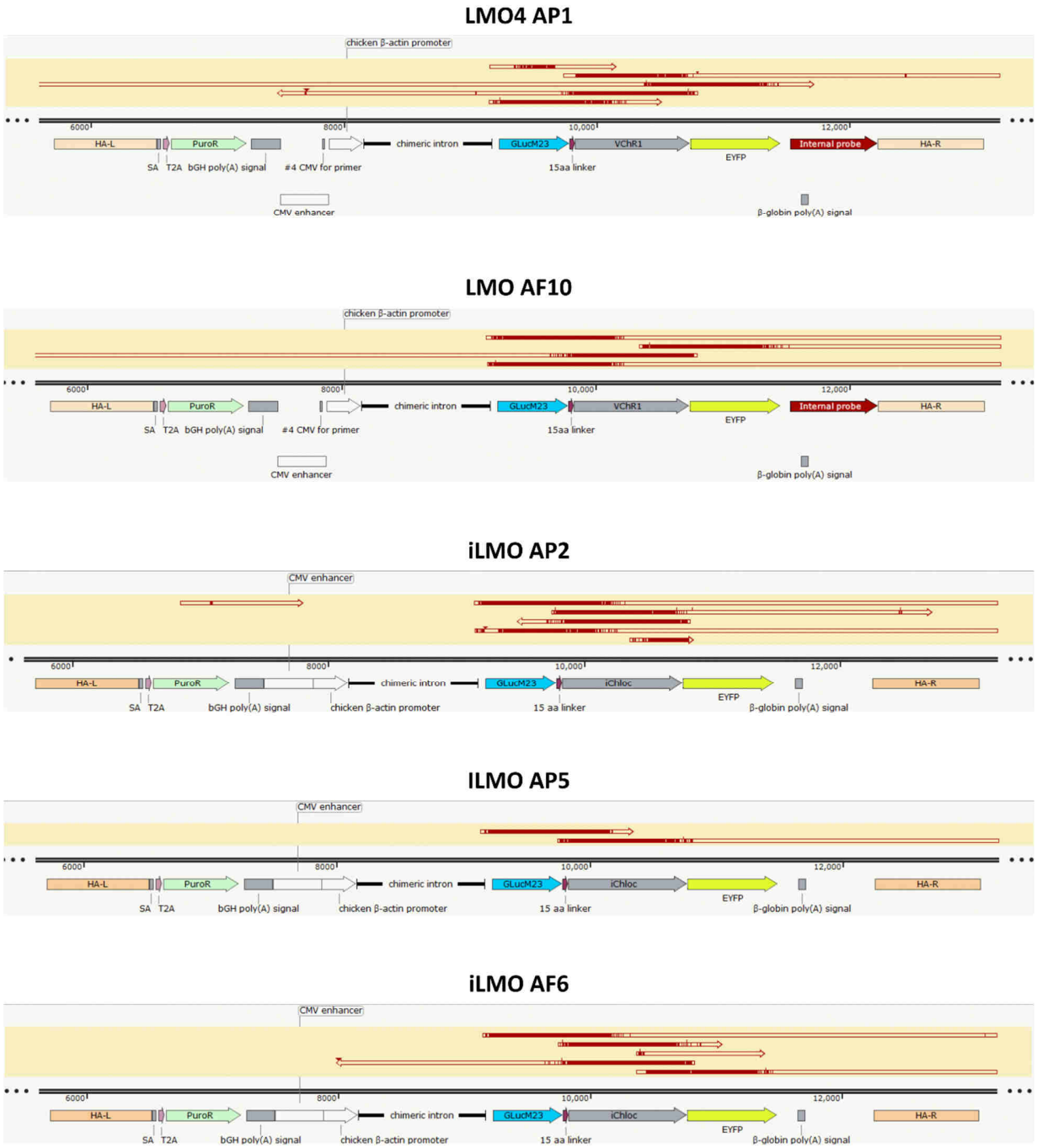

Figure 26: Sequencing of LMO4 and iLMO4 iPSCs. Red areas above the sequence indicate aligned base pairs from sequencing. In LMO4 both clones sequenced showed the correct sequence. In iLMO4 all three clones showed the correct sequence.

In addition to sequencing, Southern blotting confirmed the correct knock-in and homozygosity. For this, genomic DNA was digested with EcoRI and incubated with two DNA probes (Figure 27). Sequences of the probes can be found in the Appendix. The detection of the internal band (Int) confirmed knock-in in all eight cell lines (Figure 27). The 5' probe was used to confirm the genotype. In the case of correct integration, a 4917 bp band and not the 8252 bp band was detected. This method additionally confirmed that selected cells were homozygous. All

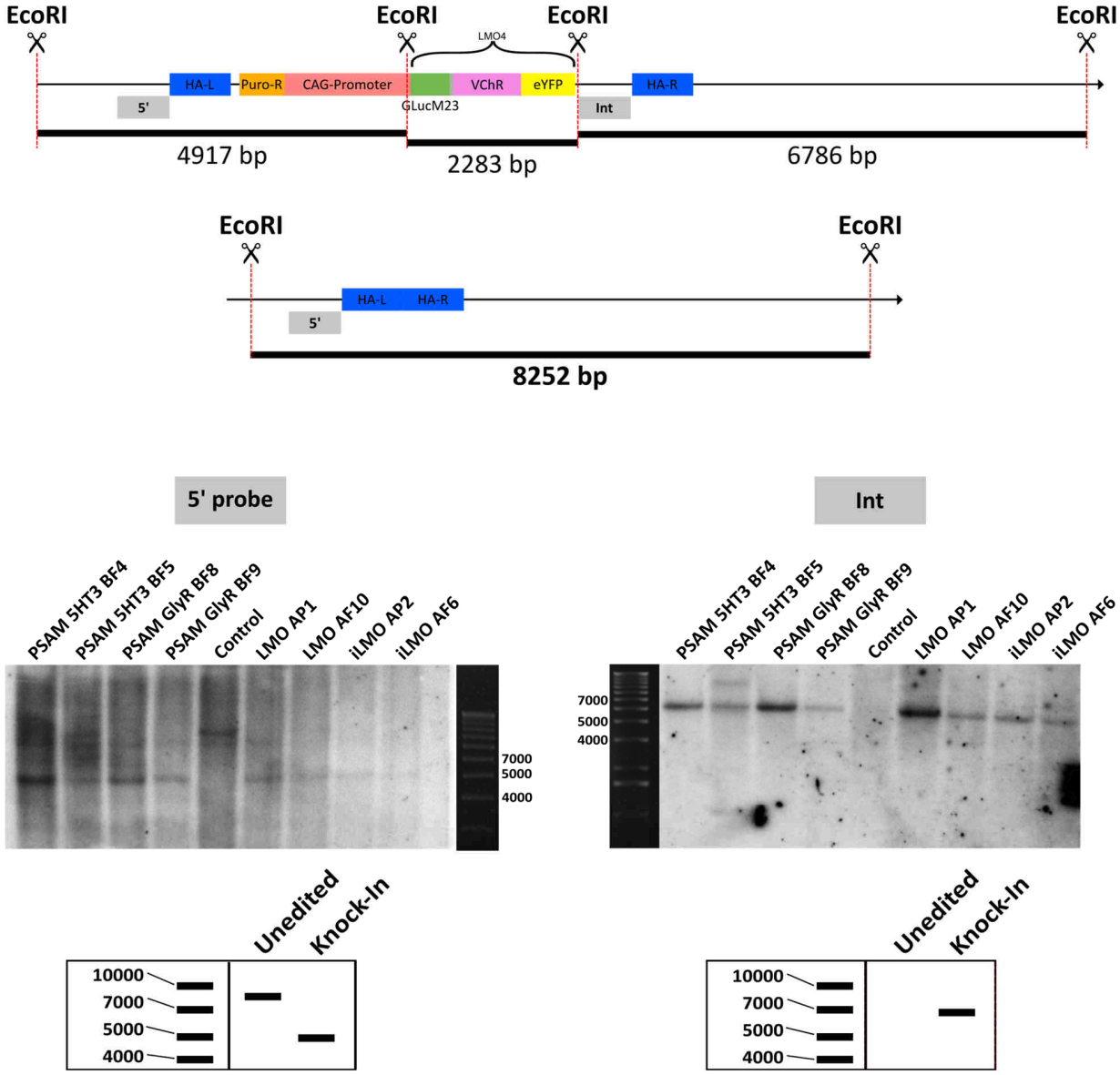

Figure 27: Southern Blotting strategy and results. Upper panel: Two probes were used to distinguish the genotype. A 5' probe (grey rectangle "5' ") detected a fragment that was either 8252 bp or 4917 bp large. The knock-in created an additional restriction site for EcoRI which created a different size depending on the genotype. An internal probe (grey rectangle, "Int") was used to detect a sequence just downstream of the transgene. This strategy allowed to detect the same band sizes in all four cell lines irrespective of their individual sequences as the 3' site of the transgene is homologous in all four lines. Lower left panel: The 5' probe is detected either at 8252 or 4917 bp. Detection of the 4917 bp band confirms homozygosity in all 8 clones. Lower right panel: The internal band is detected whenever the transgene is present, which is the case in all eight clones. Previously published in "Contractile force of transplanted cardiomyocytes contributes to heart function after injury" by Stüdemann et al., BioRxiv, pages 2021.11.23.469715 (2021).

genotyped cell lines showed correct integration and homozygosity (Figure 27). In PSAM 5HT3 BF5, we detected a second aberrant internal band which is why this clone was excluded from further analysis.

Next, master and working cell banks were created to ensure the continuously high quality of iPSCs (Shibamiya et al. 2020). For this, a quality control containing analysis of pluripotency markers, karyotyping, clonality, and sterility were performed. Cells were analyzed for the expression of

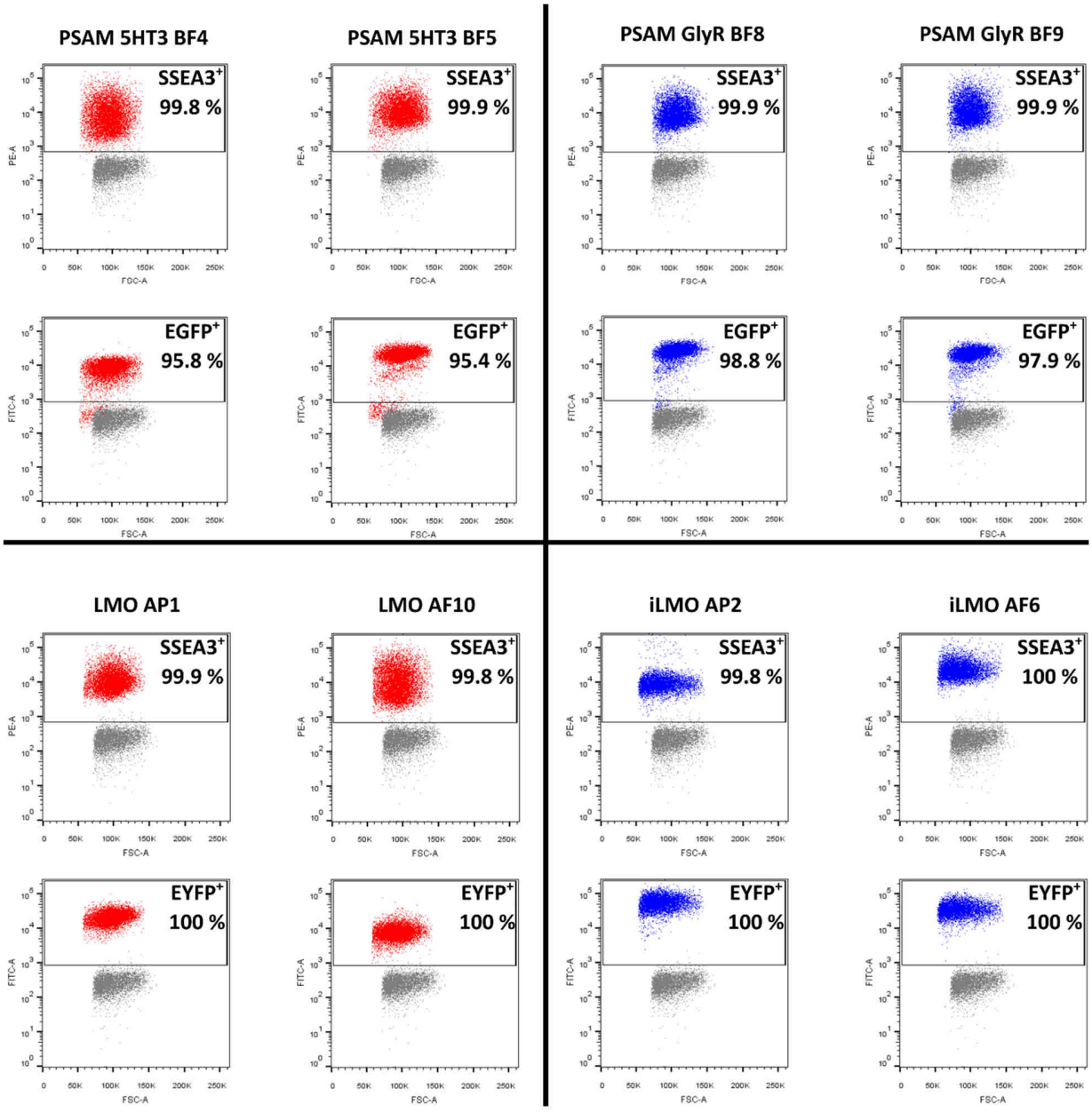

Figure 28: Transgene expression and pluripotency analysis by FACS of WCB stocks. For each clone (two per cell line approach) transgene expression was quantified by measuring EGFP/EYFP positive cells. All cell lines showed >95% expression. Pluripotency was assessed by SSEA3 staining. All WCB stocks exhibited a high level of pluripotency. Previously published in "Contractile force of transplanted cardiomyocytes contributes to heart function after injury" by Stüdemann et al., BioRxiv, pages 2021.11.23.469715 (2021).

SSEA3 as a marker of pluripotency and EGFP/EYFP expression. FACS confirmed pluripotency (>99% SSEA3$^+$) and purity of the selected clones (>95% EYFP$^+$/EGFP$^+$; Figure 28). All cells were *Mycoplasma* negative and assessed by Nanostring analysis showed a normal karyotype (Figure 29).

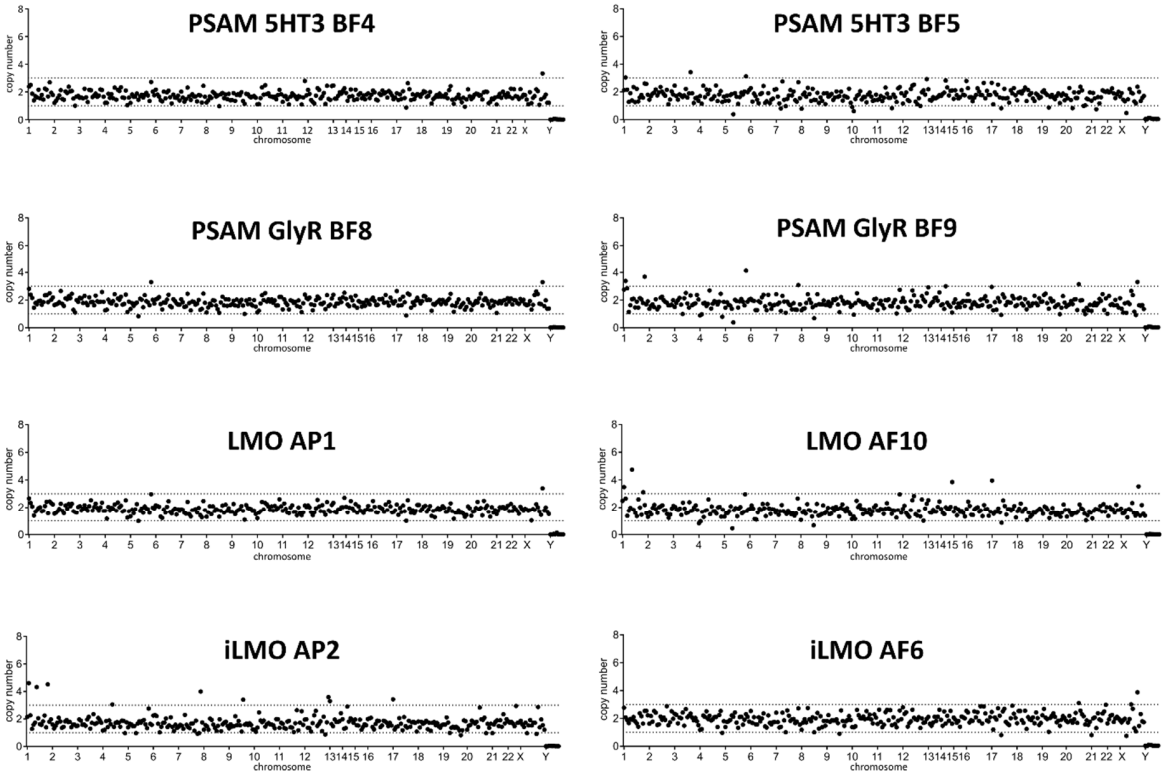

Figure 29: Karyotype analysis by Nanostring. No karyotypic abnormalities were found in any cell line.

To test if LMO iPSCs contained functional luciferase, we treated iPSCs with CTZ and measured the bioluminescence signal. We found that LMO4 iPSCs had a radiance of $3.0x10^{12}$ and iLMO4 iPSCs $5.4x10^{12}$ p/sec/cm^2/sr. This was roughly 100-fold higher than in control iPSCs ($3.7x10^{10}$ p/sec/cm^2/sr; Figure 30).

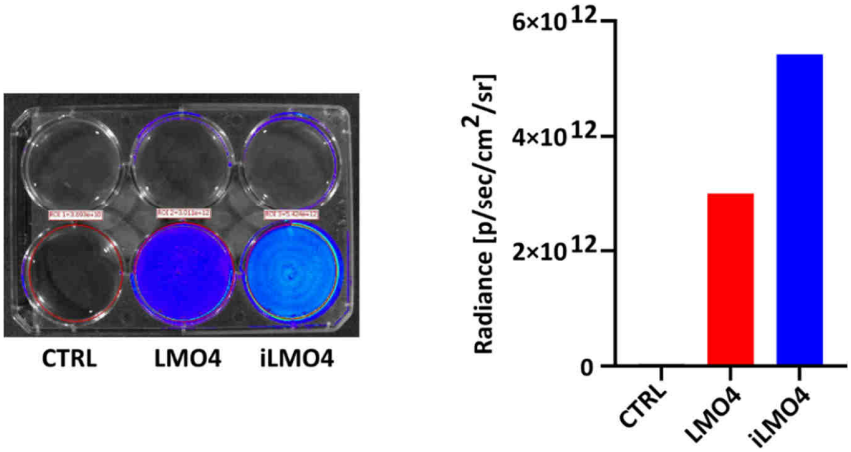

Figure 30: Bioluminescence of LMO and iLMO4. CTZ was added directly into cell culture medium and plates imaged immediately. Previously published in "Contractile force of transplanted cardiomyocytes contributes to heart function after injury" by Stüdemann et al., BioRxiv, pages 2021.11.23.469715 (2021).

To sum up, I created and characterized four novel hiPSC lines that expressed their respective transgene ubiquitously. Moreover, all cell lines were homozygous, showed an intact karyotype, and retained pluripotency.

6.3 Characterization of PSAM 5HT3 and PSAM GlyR Cardiomyocytes

The aim of this project was to produce iPSC-cardiomyocytes in which contractility could reversibly be switched off promptly. In addition, the necessary substrate concentration needed to be suitable for in vivo application. Hence, requirements for the cell line were a stop of contractility in a matter of minutes (preferably even within seconds) and that PSEM^{89S} in the micromolar range would be sufficient to stop contractility.

In a first trial, EHTs as a 3D cardiac in vitro model were cast from PSAM GlyR and PSAM 5HT3 hiPSC-cardiomyocytes. PSEM^{89S} was applied in increasing doses (based on data from neuroscience (Magnus et al. 2011)), and the force and frequency were analyzed. Increasing PSEM^{89S} concentrations of 1 µM up to 100 µM had little effect on the frequency and force of PSAM 5HT3 EHTs (Figure 31, left). In contrast, in PSAM GlyR EHTs, a tendency for an increase in beating frequency was observed up to a concentration of 30 µM while the force decreased. Furthermore, at 30 µM PSAM GlyR EHTs showed a stop of contractility after 15 minutes, while a concentration of 100 µM stopped contractility instantaneously (Figure 31, right). Hence, PSAM GlyR cardiomyocytes were chosen for thorough analysis and in vivo transplantation studies.

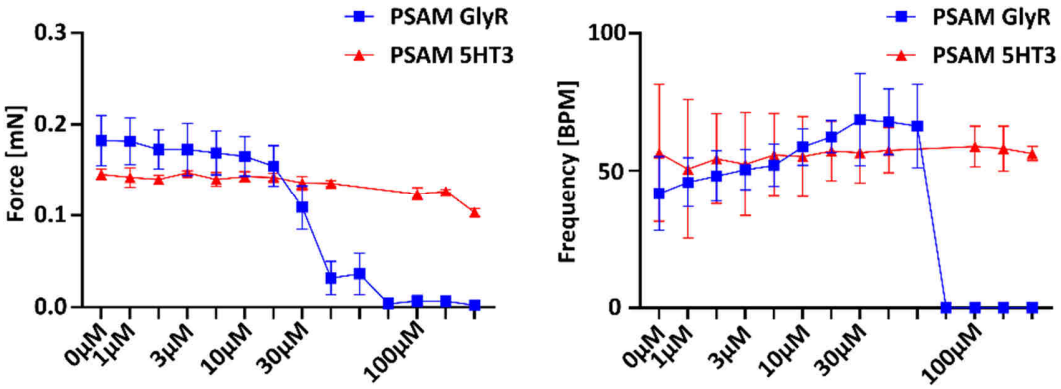

Figure 31: Force and frequency assessment of PSAM GlyR and PSAM 5HT3 EHTs upon PSEM^{89S} application. In PSAM GlyR EHTs contractility decreased and stopped at 30 to 100 µM. In PSAM 5HT3 EHTs no major effect was observed. n=3 for PSAM GlyR and n=2 for PSAM 5HT3 EHTs, mean±SD.

A total of 2.239x10^9 PSAM GlyR cells was generated for this work by 2D and 3D differentiation methods. Mean cTnt$^+$ was 70.94%. PSAM GlyR (Figure 32) cardiomyocytes were morphologically indistinguishable from control cardiomyocytes, e.g., showed comparable α-actinin structure in 2D but expressed EGFP. Additionally, the nicotinergic IBD could be visualized with α-Bungarotoxin in the cell membrane but also the nuclear membrane. On the other hand, control cells did not show any PSAM GlyR or EGFP signal (Figure 33).

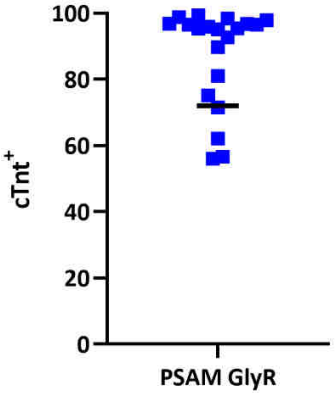

Figure 32: PSAM GlyR differentiation quality. Note that the mean cTnt (70.94%) is adjusted to the number of cardiomyocytes generated in a differentiation run.

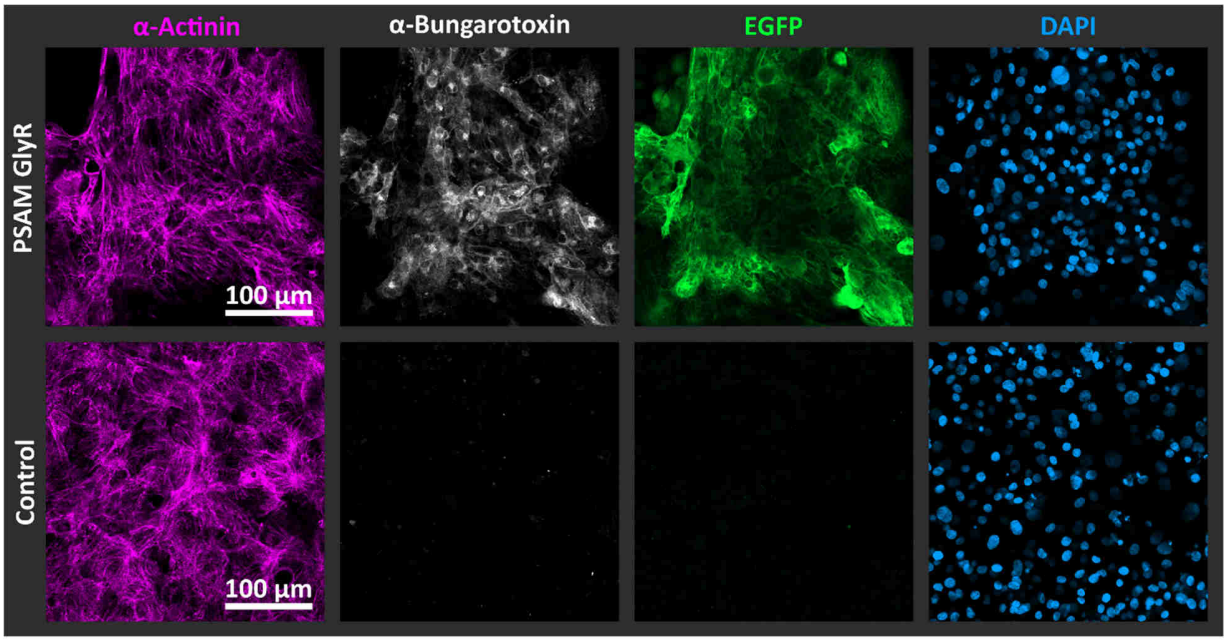

Figure: 33: Microscopic analysis of PSAM GlyR cardiomyocyte structure. Sarcomere structure is comparable between PSAM GlyR and control cardiomyocytes. PSAM GlyR (detected by α-Bungarotoxin) and EGFP were only found in PSAM GlyR cardiomyocytes. Previously published in "Contractile force of transplanted cardiomyocytes contributes to heart function after injury" by Stüdemann et al., BioRxiv, pages 2021.11.23.469715 (2021).

6.3.1 PSAM GlyR EHT Functional Characterization

MD student Christoph Manthey conducted the following characterization of PSAM GlyR EHTs under my supervision. The results relevant to the transplantation study will be shortly summarized in this thesis. PSAM GlyR EHTs developed a force of 0.21±0.03 mN at day 32 compared to 0.24±0.02 mN in control EHTs (not statistically significant (ns), Figure 34). Baseline frequency at day 32 was 26.25±10.32 bpm in PSAM GlyR compared to 31.17±5.01 bpm in control EHTs (Figure 34). However, time to peak -80% (TTP -80%) remained higher in PSAM GlyR EHTs with 0.22±0.05 s compared to control EHTs that exhibited 0.16±0.01 s ($p \leq 0.001$, Figure 34). Similarly, relaxation time 80% (RT 80%) was longer in PSAM-GlyR EHTs with 0.43±0.09 s, compared to control EHTs in which RT 80% was 0.26±0.02 s ($p \leq 0.001$, Figure 34) after 32 days.

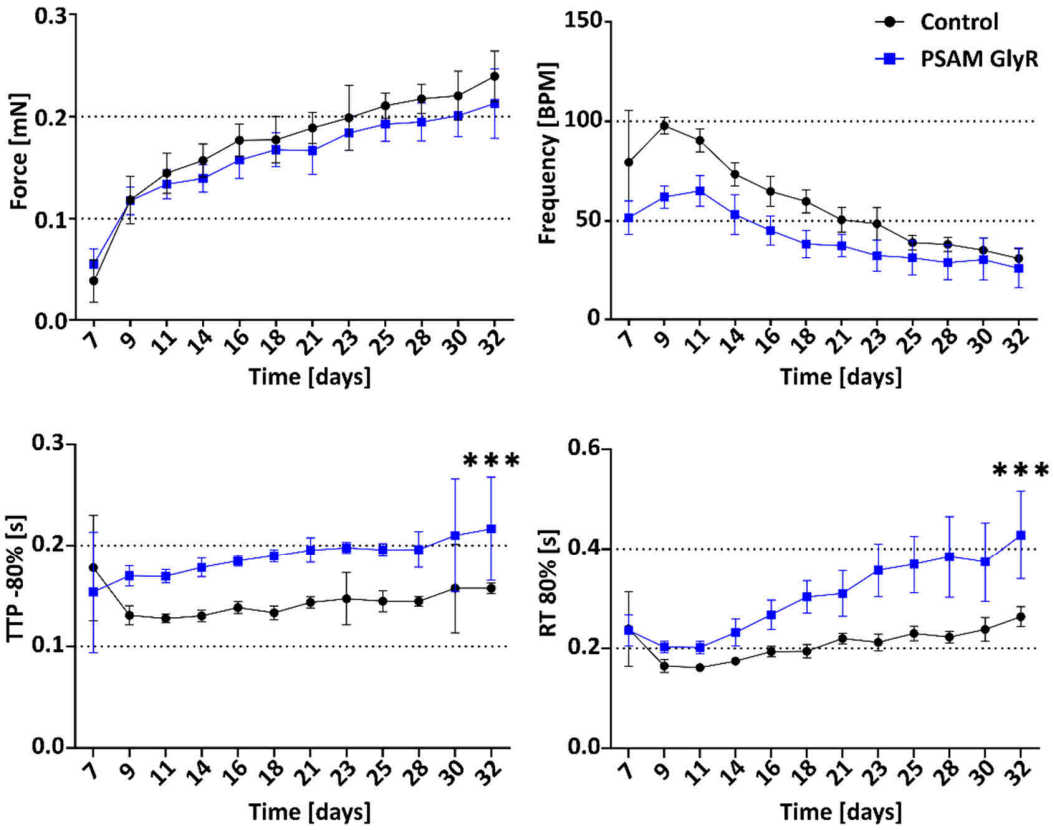

Figure 34: PSAM GlyR EHT characterization. Upper left panel: Force of EHTs steadily increased after onset of beating on day 7. Contraction force was higher on day 32 in control EHTs. Upper right panel: PSAM GlyR EHTs showed similar frequencies to control EHTs. Lower left panel: TTP -80% of PSAM GlyR EHTs was higher on day 32 than in control EHTs. Lower right panel: RT 80% was higher in PSAM GlyR EHTs on day 32. n=18-21 for control and n=24-29 for PSAM GlyR EHTs, mean±SD, nested t test for day 32, ***p≤0.001.

When treated with 100 µM PSEM^{89S}, PSAM GlyR EHTs consistently stopped to contract and could not be paced electrically. This complete block of contractility was reversible after washout. In contrast, control EHTs retained their force and frequency and could still be paced during PSEM^{89S} application (Figure 35).

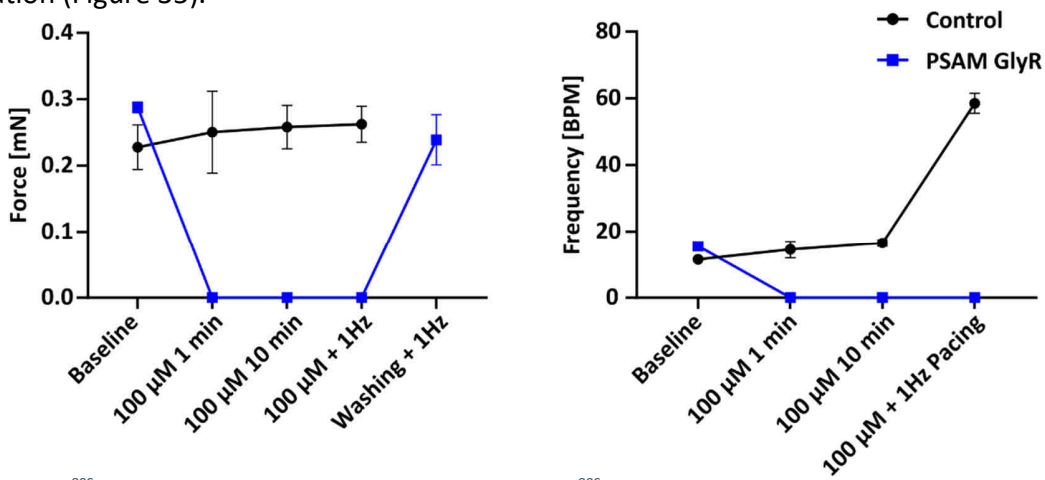

Figure 35: PSEM^{89S} application in PSAM GlyR and control EHTs. PSEM^{89S} caused a stop of contractility. EHTs could not be paced during application, however after wash out this was again possible. Control EHTs were largely unaffected by PSEM^{89S} application, n=4 per group, mean±SD.

However, PSEM^{89S} also affected control EHTs. In particular, RT 80% showed a slight increase under PSEM^{89S} treatment (Figure 36). As the PSAM GlyR LBD originates from a nAChR, we investigated

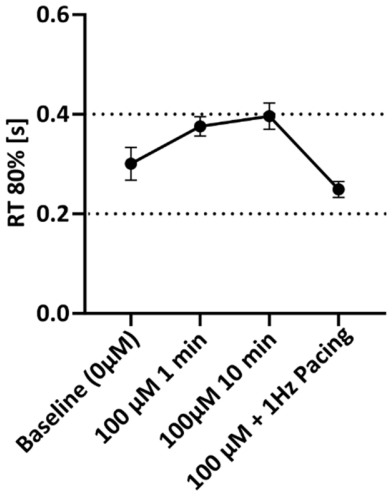

Figure 36: RT 80% of control EHTs upon PSEM^{89S} application. RT 80% slightly increase upon PSEM^{89S} treatment, n=4, mean±SD.

whether ACh could still activate PSAM GlyR cells as this could potentially affect an in vivo application. Physiological ACh concentrations did not affect PSAM GlyR EHTs. Only supraphysiological ACh concentration (3000 µM) caused a reduction in RT 80% ($p \leq 0.05$ and $p \leq 0.01$) and a tendency for reduction in force (Figure 37), indicating very little remaining ACh receptor activity.

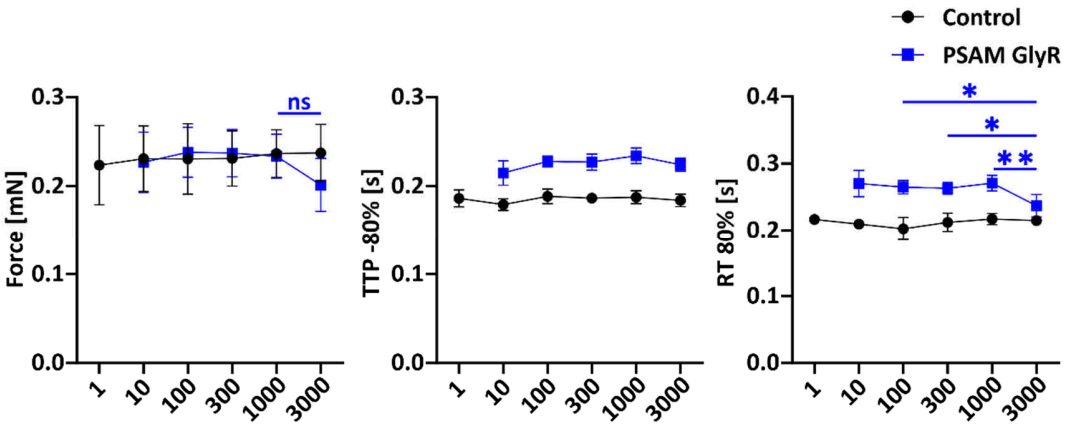

Figure 37: PSAM GlyR and control EHT characteristics during ACh application. Only 3000 µM ACh seemed to have a small effect on force while TTP -80% was unaffected. RT 80% decreased upon 3000 µM application, n=4 for control and n=7 for PSAM GlyR EHTs, mean±SD, Brown-Forsythe and Welch ANOVA with multiple comparisons, *p≤0.05, **p≤0.01.

Electrophysiology of PSAM GlyR and control EHTs was analyzed. For this, action potentials (AP) were measured by sharp microelectrode. APs in PSAM GlyR EHTs showed a resting membrane potential (RMP) of -60 mV in contrast to -80 mV in control EHTs (Figure 38, $p \leq 0.05$). Action potential amplitude (APA) was significantly lower in PSAM GlyR EHTs (Figure 38, $p \leq 0.05$). The maximal change of voltage over time (dV/dt) was higher in control EHTs (Figure 38, $p \leq 0.01$). AP duration 90% (APD90) was similar in both groups (Figure 38).

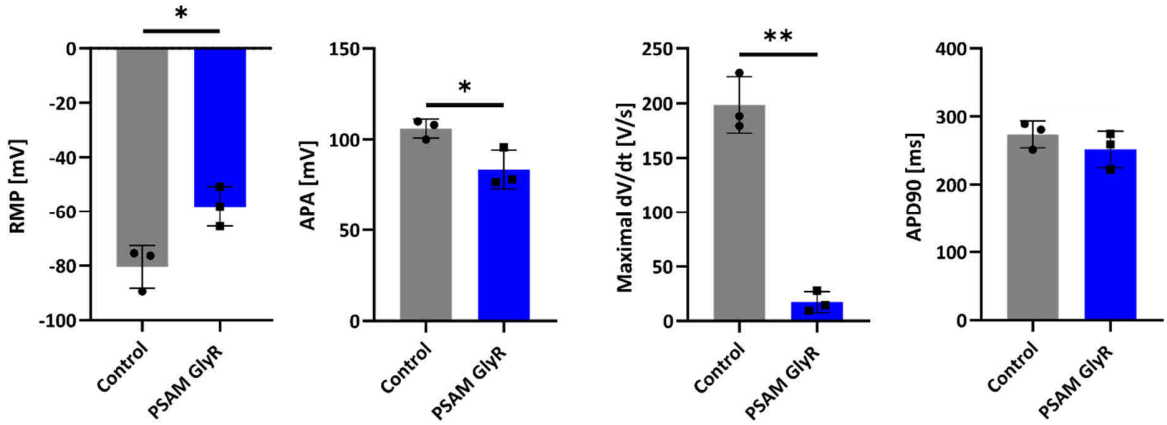

Figure 38: Action potential measurements of control and PSAM GlyR EHTs. RMP was lower in PSAM GlyR EHTs as well as APA. Maximal dV/dt was lower in PSAM GlyR EHTs. APD90 was similar between groups. n=3, mean±SD, unpaired t test with Welch's correction, *p≤0.05, **p≤0.01.

APs were measured prior to and during PSEM^{89S} application. 100 µM PSEM^{89S} was applied to the measurement system. In contrast to the video-optical analysis, PSEM^{89S} concentration steadily increased because the pump system constantly exchanged the measurement solution. Hence, the AP of PSAM GlyR EHTs ceased within 13 minutes. We could observe an increase in RMP during wash-in, while APA decreased until APs completely ceased. Upon washing, EHTs recovered within 15 minutes to their baseline AP (Figure 39).

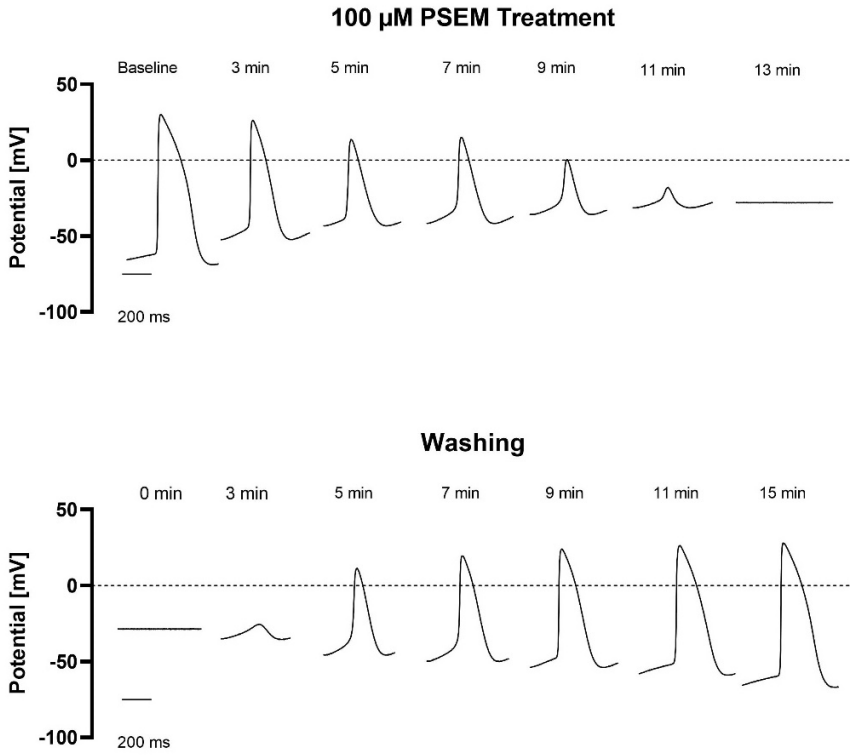

Figure 39: APs during PSEM^{89S} application. During wash in of PSEM^{89S} a depolarization can be observed. In addition, APA decreases until APs fully cease. Wash out reverses these effects.

RMP increased reversibly to -21 mV during PSEM^{89S} application (Figure 40). APA, max dV/dt, and APD90 were completely reversed upon washout of PSEM^{89S} (Figure 40).

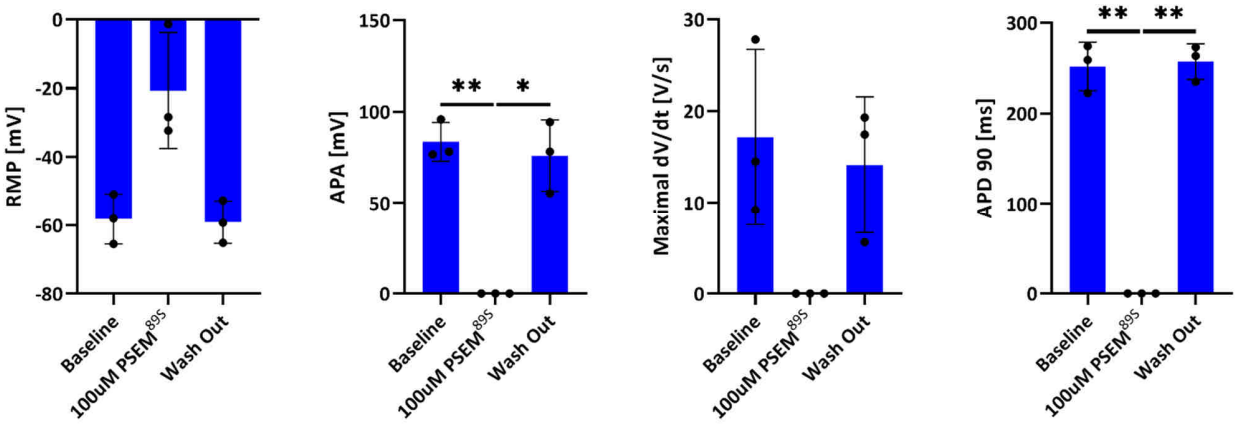

Figure 40: AP characteristics of PSAM GlyR EHTs prior, during and after PSEM^{89S} application. RMP increased to -21 mV during PSEM^{89S} application. Contractions stopped reversibly. All parameters recovered to their baseline values during wash out. n=3 EHTs, mean±SD, repeated measured ANOVA with Geisser-Greenhouse correction and multiple comparisons, *p≤0.05, **p≤0.01.

In control EHTs, PSEM^{89S} led to a tendency of RMP increase and a reduction of max dV/dt(p≤0.05). In addition, there was a tendency for an increase in APD90 and a tendency for a reduction of APA (Figure 41).

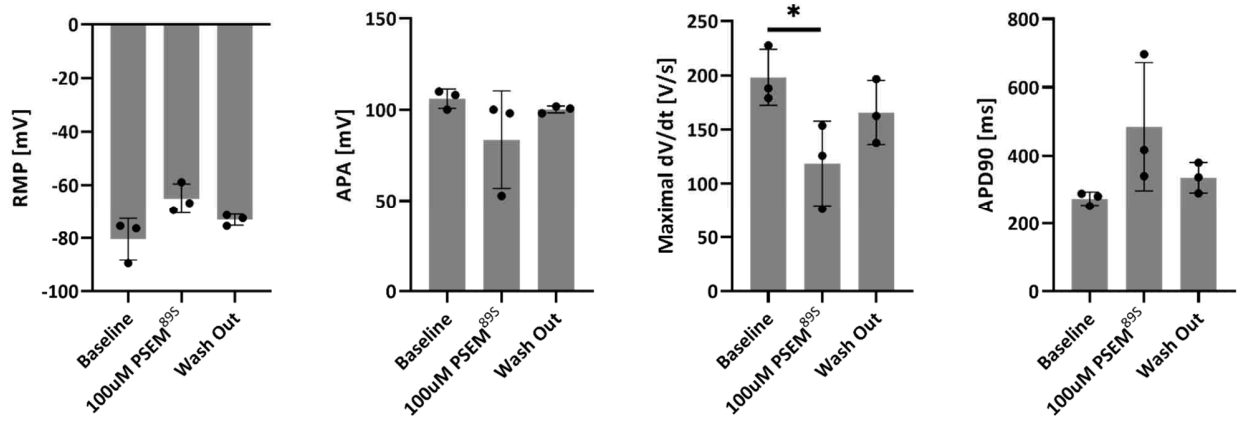

Figure 41: AP characteristics of control EHTs prior, during and after PSEM^{89S} application. RMP seemed to slightly decrease during PSEM^{89S} application. APA showed a tendency for reduction. Maximal dV/dt decreased during PSEM^{89S} application but recovered. APD90 seems to slightly increase during PSEM^{89S} application, n=3, EHTs, mean±SD, repeated measured ANOVA with Geisser-Greenhouse correction and multiple comparisons, *p≤0.05.

6.3.2 Morphological Characterization of PSAM GlyR EHTs

Immunofluorescence imaging of PSAM GlyR EHTs revealed a similar sarcomere structure compared to control EHTs. Native EGFP was observed in all cells, confirming transgene expression (Figure 42). Cardiomyocytes matured in the three-dimensional construct and aligned along the outer surface of the EHT and α-Bungarotoxin stained the cell membrane (Figure 42).

In summary, we found that PSAM GlyR cardiomyocytes can be stopped with PSEM^{89S} in a matter of seconds. Control cardiomyocytes were only slightly affected. PSAM GlyR EHTs showed similar development to control EHTs and similar microscopical structure.

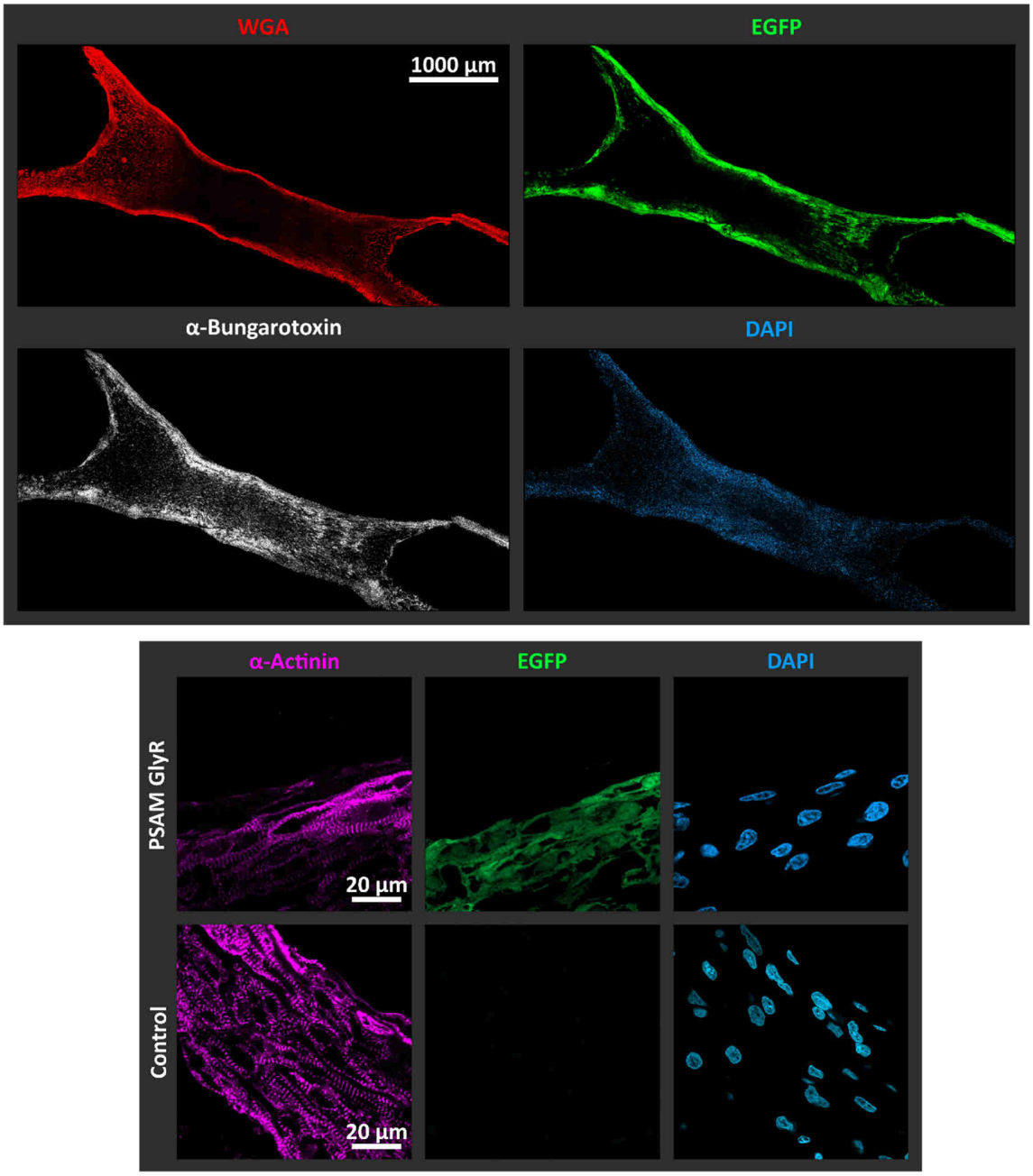

Figure 42: Microscopy of PSAM GlyR EHTs. Upper panel: PSAM GlyR EHTs show comparable sarcomere structure. EGFP is only found in PSAM GlyR EHTs. Lower panel: WGA is used to visualize cell membranes. EGFP and α-Bungarotoxin (PSAM GlyR) signal is found on the outer parts of the EHT. Previously published in "Contractile force of transplanted cardiomyocytes contributes to heart function after injury" by Stüdemann et al., BioRxiv, pages 2021.11.23.469715 (2021).

6.4 Characterization of LMO4 and iLMO4 Cardiomyocytes

Next to a chemogenetic cell line in which contractility could be switched off, we developed combined chemo-/ optogenetic cell lines. The aims remained the same: iPSC-cardiomyocytes in which contractility could reversibly be switched off promptly. However, activation could be achieved either by light (470 nm) or the luciferase substrate CTZ. For in vivo use, it was crucial,

and similar to PSAM/PSEM, that the necessary substrate concentration was appropriate for in vivo use. Alternatively, for in vitro and ex vivo experiments, an external light source could be used.

In a first trial, EHTs were cast from LMO4 and iLMO4 hiPSC-cardiomyocytes. From previous experiments with PSAM 5HT3 and PSAM GlyR, we knew it was more likely that activation of the anion channel (iLMO4) would stop contractility. Hence, we first treated iLMO4 EHTs with CTZ (100 µM). Contractility stopped after ~10 minutes, but even after three times washing, EHTs did not recover (Figure 43).

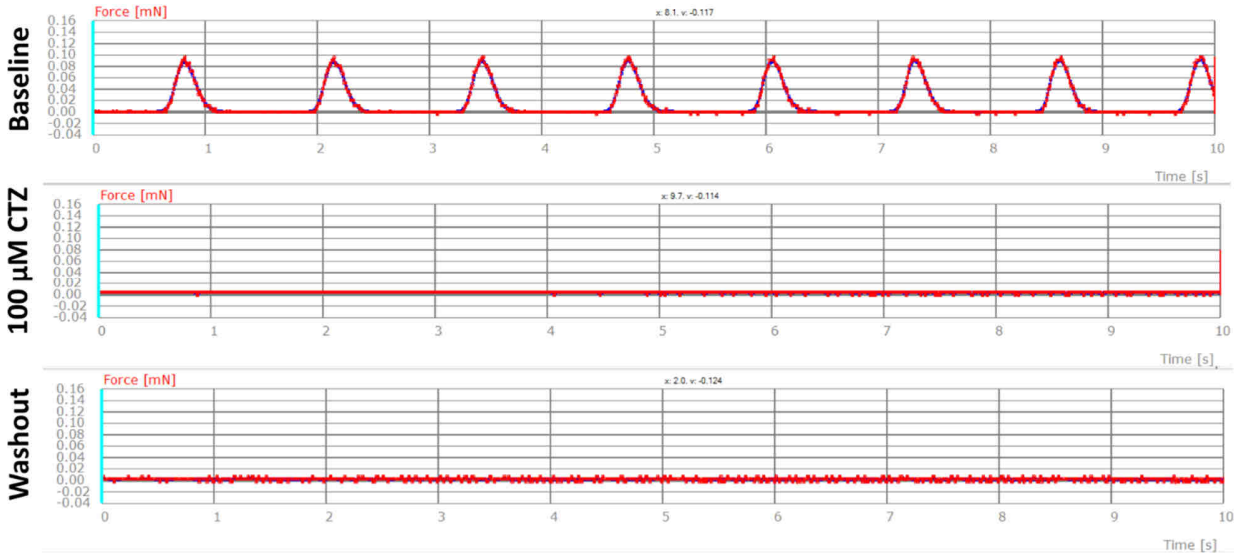

Figure 43: iLMO4 EHT contractility prior during and after CTZ application. A concentration of 100 µM CTZ stopped contractility, however, EHTs did not recover after washout.

Because of the potentially toxic effects of CTZ on cardiomyocytes, we focused on the activation of LMO4 and iLMO4 via light. Blue light (470 nm) was used to alter contraction behavior. Frequencies of 2 Hz up to 5 Hz were used (30 ms, 0.3 mW/mm^2) as we did not have the technical possibility at the time to apply light continuously. However, even then, in iLMO4 EHTs, 2 Hz light pacing was sufficient to stop contractility (Figure 44). In contrast, LMO4 EHTs followed optical pacing frequency up to 5 Hz (Figure 45). We, therefore, chose iLMO4 cardiomyocytes for thorough analysis because of their quick off kinetics and high light sensitivity. iLMO4 cardiomyocytes, in combination with direct photostimulation, fulfilled the criterium of a quick stop of contractility. However, photostimulation of light is nearly impossible in vivo for an application in the thoracic cavity.

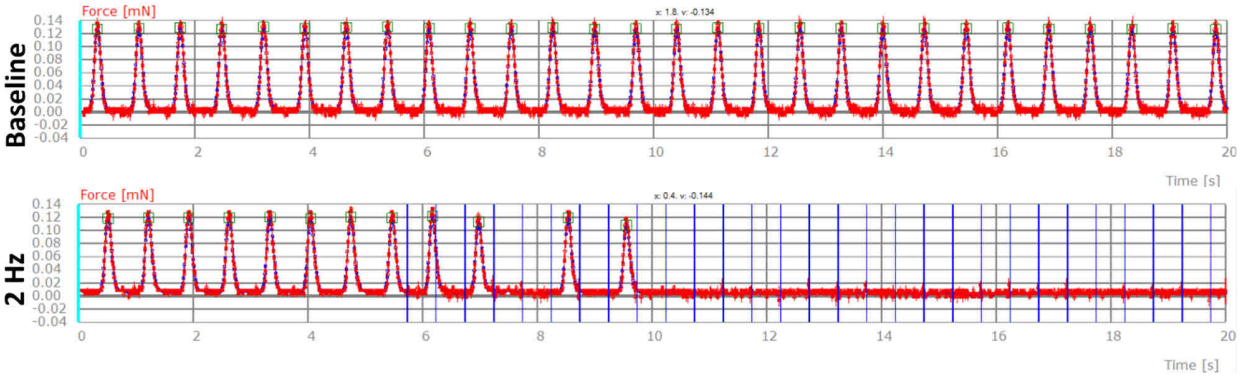

Figure 44: Force measurements in iLMO4 EHTs. Upper panel: Baseline force. Lower panel: upon 2 Hz optical pacing (vertical blue lines) iLMO4 EHTs showed lower force development and eventually stopped contracting.

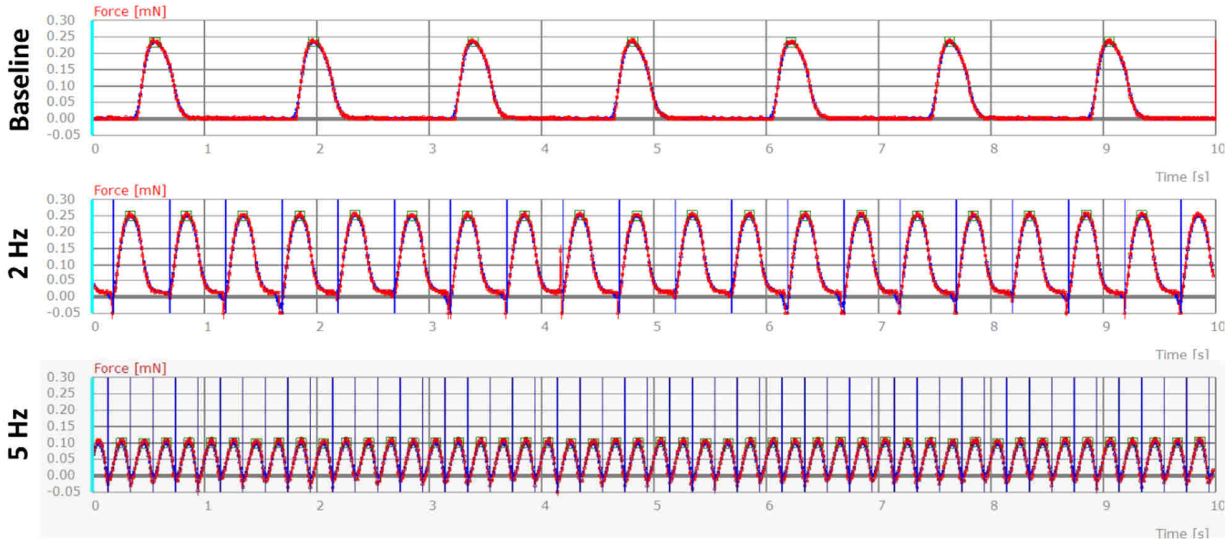

Figure 45: LMO4 EHT force measurements. Upper panel: baseline force. Middle panel: LMO4 EHTs follow optical pacing (vertical blue lines) at 2 Hz. Lower panel: LMO4 EHTs follow optical pacing at 5 Hz.

6.4.1 iLMO4 EHT Functional Characterization

iLMO4 cardiomyocytes were characterized in more detail. MD student Judith Rössinger conducted the following experiments under my supervision. The results relevant for transplantation studies will be shortly summarized in this thesis.

A total of 1.409×10^9 cells was generated for this work by 2D and 3D differentiation methods. Mean $cTnt^+$ was 84.02% (Figure 46).

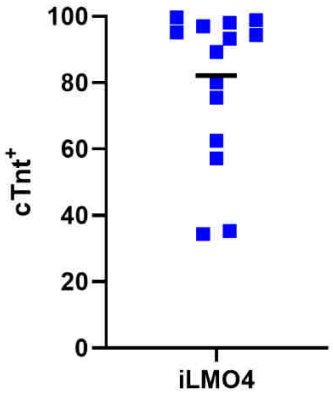

Figure 46: iLMO4 differentiation quality. Note that the mean cTnt (84.02%) is adjusted to the amount of cardiomyocytes generated in a differentiation run.

iLMO4 EHTs were overall heterogeneous in force, frequency, RT 80%, and TTP -80%. We observed a high batch-to-batch variability. We reasoned that these EHTs are highly light-sensitive, even to the remaining ambient light after switching off the room light. Hence, all three batches are depicted separately because we took more and more measures to reduce light contamination over time. Batch 1 and 2 developed lower forces than control EHTs, while a third batch reached similar forces as control EHTs (Figure 47). Especially frequencies were heterogeneous. Batch 2 had higher frequencies, while batch 1 was similar to control EHTs. Batch 3, on the other hand,

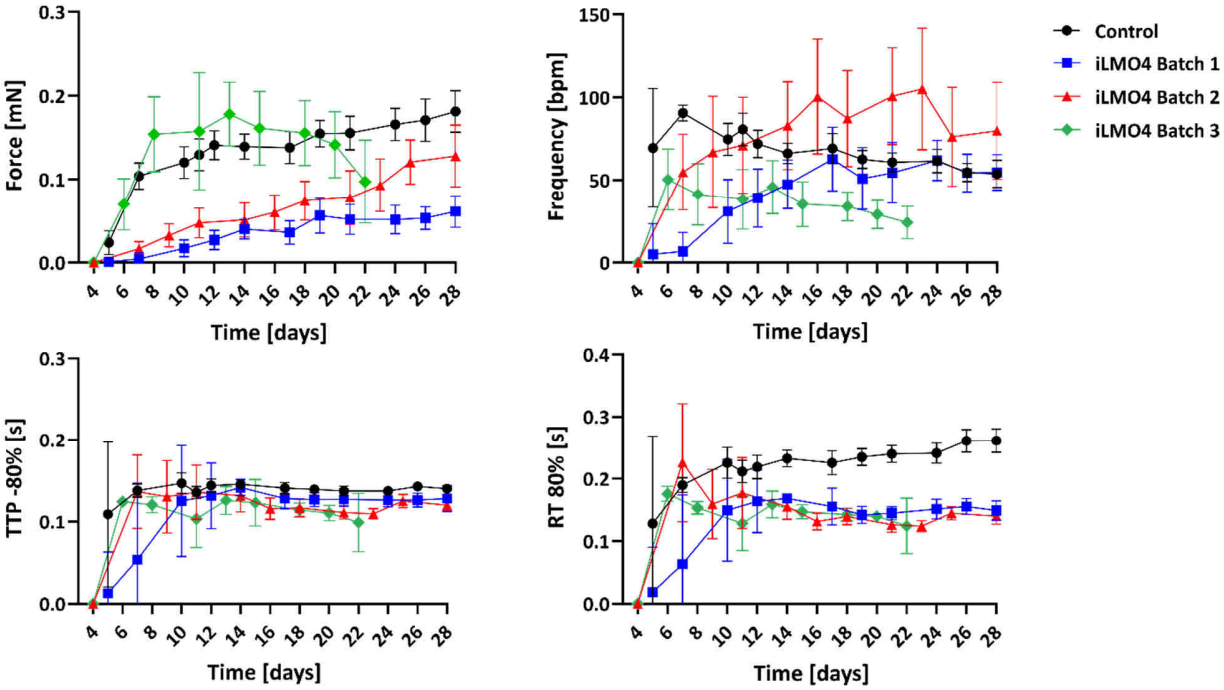

Figure 47: iLMO4 EHT characterization. Upper left panel: Force of EHTs steadily increased after onset of beating on day 5 to 10, depending on the batch. Contraction force was batch-dependent different. Upper right panel: iLMO4 EHTs showed highly heterogenous frequencies compared to control EHTs. Lower left panel: TTP -80% of iLMO4 EHTs was overall lower than in control EHTs. Lower right panel: RT 80% was lower in iLMO4 EHTs, n=41 for control and n=15/23/10 for iLMO4 EHTs, mean±SD.

had lower frequencies (Figure 47). TTP -80% reached similar values in all iLMO4 batches; however, it was still lower than in control EHTs. RT 80% was lower in all three batches than in control EHTs (Figure 47).

To quantify the differences, we analyzed the data for day 21/22. iLMO4 EHTs had a mean force of 0.08±0.04 mN, compared to 0.16±0.02 mN in control EHTs ($p<0.0001$, Figure 48). Control EHTs had a mean frequency of 61±6 bpm, while iLMO4 EHTs had a mean frequency of 72±38 bpm (ns, Figure 48). Frequencies were overall highly heterogeneous in iLMO4 EHTs. TTP -80% was lower in iLMO4 EHTS (0.12±0.01 s) compared to control EHTs (0.14±0.01 s, $p<0.0001$, Figure 48). Moreover, RT 80% was lower in iLMO4 EHTs (0.13±0.01 s) opposed to control EHTs (0.24±0.01 s, $p<0.0001$, Figure 48).

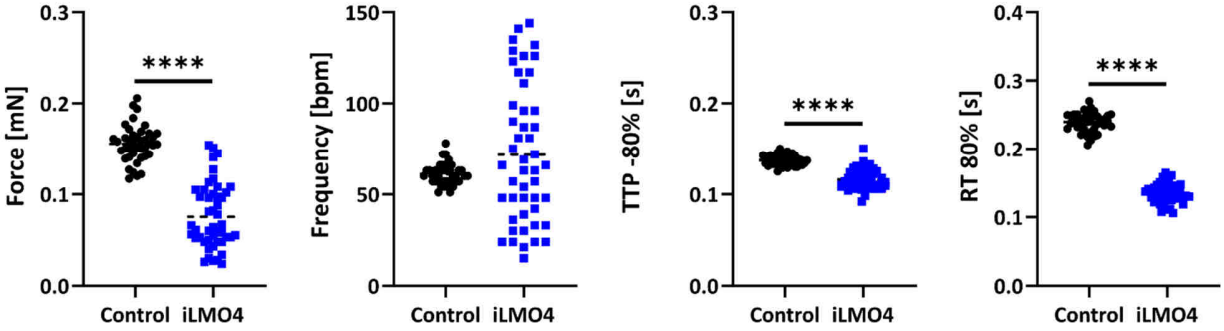

Figure 48: iLMO4 EHT characteristics on day 21/22. Upper left panel: force was significantly lower in iLMO4 EHTs. Upper right panel: frequencies were similar between iLMO4 and control EHTs, however the frequencies of iLMO4 differed greatly. Lower left panel: TTP -80% was significantly lower in iLMO4 EHTs. Lower right panel: RT 80% was significantly lower in iLMO4 EHTs, n=41 for control and n=47 for iLMO4, mean±SD, Welch's t test, ****p≤0.0001. Previously published in "Contractile force of transplanted cardiomyocytes contributes to heart function after injury" by Stüdemann et al., BioRxiv, pages 2021.11.23.469715 (2021).

iLMO4 and control EHTs were paced electrically up to 6 Hz. Control EHTs followed the given pacing frequency (green line, Figure 49) up to 3 Hz, and 3 out of 8 EHTs followed external pacing up to 4 Hz. iLMO4 EHTs, on the other hand, only followed up to 2 Hz. More detailed analysis revealed that the critical pacing frequency of iLMO4 EHTs was 2.5 to 2.75 Hz. Beyond this frequency, most EHTs went into a 1:2 pattern, meaning they followed every second pacing pulse (red line, Figure 49). This is a crucial result for the transplantation of these cardiomyocytes because a guinea pig heart has a frequency of roughly 350 bpm (4.2 Hz) in vivo. This means that not all transplanted cardiomyocytes may follow the given heart frequency, and therefore their contribution to force development might be underestimated.

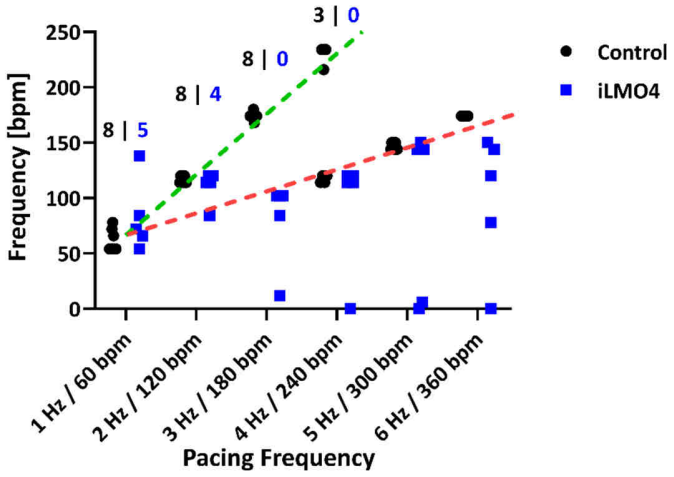

Figure 49: iLMO4 and control EHT pacing. The ordinate indicates the given pacing frequency while on the abscissa the actual measured frequency is plotted. The green dotted line indicates the ideal measured frequency while the red dotted line indicates 1:2 pattern. Numbers above indicate the number of EHTs that followed the electrical pacing frequency below. While control EHTs followed up to 3 Hz and some even to 4 Hz, all iLMO4 EHTs stopped following the pacing frequency above 2 Hz, n=5 for iLMO4 EHTs and n=8 for control EHTs.

Next, we assessed which light intensity was needed to stop EHT contractility. Technically we were able to assess the range of 0.005mW/mm^2 to 0.066mW/mm^2. Eventually, iLMO4 EHTs stopped at all intensities, but at low intensity, there was a gradual decline in contractility, whereas higher light intensities resulted in an immediate stop (Figure 50).

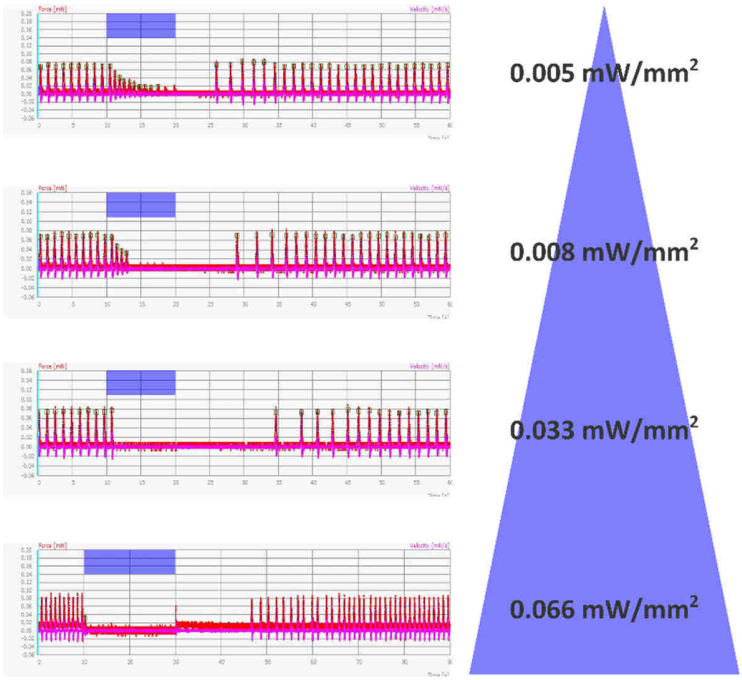

Figure 50: Light intensity needed to stop contractility of iLMO4 EHTs. Left: Force recording of iLMO4 EHTs over time. Blue boxes indicate illumination with the light intensity given on the right. Lowest intensity (0.005mW/mm^2) was enough to stop EHTs, however contractility was fading out. All other intensities were sufficient in stopping EHTs almost immediately. Previously published in "Contractile force of transplanted cardiomyocytes contributes to heart function after injury" by Stüdemann et al., BioRxiv, pages 2021.11.23.469715 (2021).

We then assessed how the control EHTs were affected by photostimulation. iLMO4 EHTs stopped contracting almost immediately after 470 nm light application, as previously described. Additionally, electrical stimulation could evoke no contractions (Figure 51). In contrast, control EHTs were not affected by 470 nm light, and electrical pacing worked as expected (Figure 51).

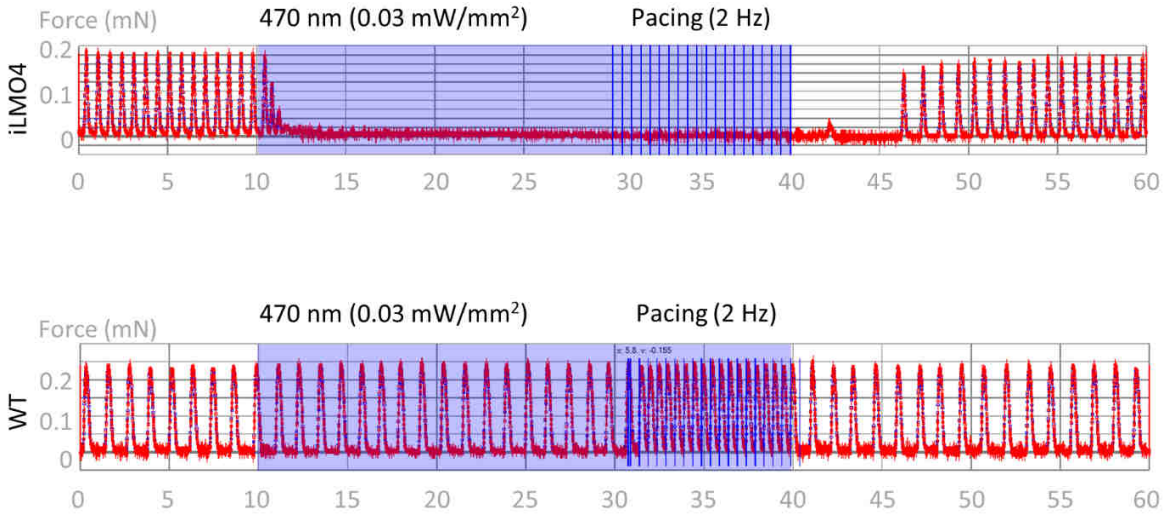

Figure 51: Force measurements in iLMO4 and control EHTs. 470 nm light stops contractility in iLMO4 EHTs but does not affect control EHTs. Electrical pacing does not evoke contractions in iLMO4 EHTs upon light exposure. Previously published in "Contractile force of transplanted cardiomyocytes contributes to heart function after injury" by Stüdemann et al., BioRxiv, pages 2021.11.23.469715 (2021).

Next, we assessed in more detail how CTZ would affect iLMO4 and control EHTs. GLucM23 produces light of 470-490 nm light (Lindberg et al. 2013), which is well in the human eye's visible spectrum. Hence, CTZ treated iLMO4 EHTs generate blue light. Moreover, cells were visualized, and as usually observed in EHTs, most cardiomyocytes aligned in the outer regions of the EHT (Figure 52). We found that CTZ at 100 µM inconsistently decreased contractility in iLMO4 EHTs but did not lead to a full stop of contractility. 300 µM stopped contractility in two EHTs but only

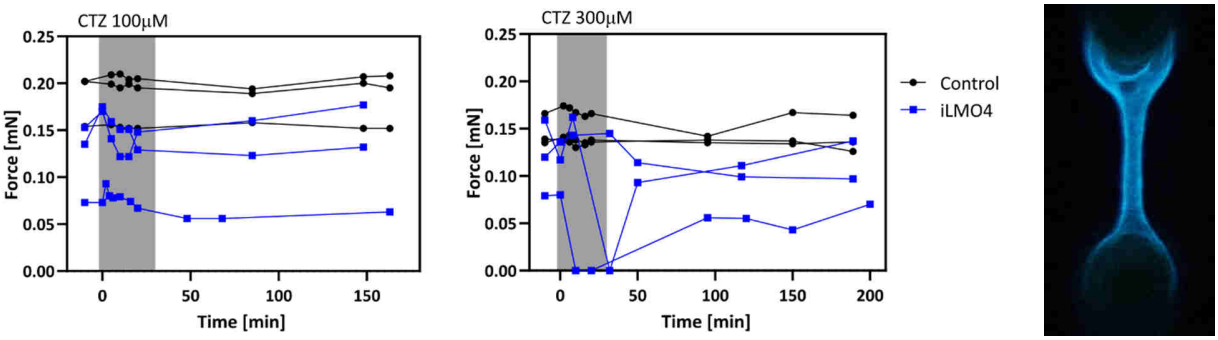

Figure 52: CTZ treatment of iLMO4 and control EHTs. Left: iLMO4 EHTs were only partly affected by 100 µM CTZ and did not stop. Control EHTs were unaffected. Middle: Two out of three iLMO4 EHTS stopped when 300 µM CTZ were applied. Control EHTs did not react to CTZ treatment. All EHTs are plotted individually, n=3 per group. Right: CTZ treated iLMO4 EHT generates blue light. Note the localization of the cells, as usually in the outer regions of the EHT. Previously published in "Contractile force of transplanted cardiomyocytes contributes to heart function after injury" by Stüdemann et al., BioRxiv, pages 2021.11.23.469715 (2021).

weakened contractility in a third one. iLMO4 EHTs only partly recovered from CTZ application (Figure 52). Control EHTs were not affected by CTZ at 100 µM and 300 µM (Figure 52).

6.4.2 Electrophysiology

In analogy to the characterization of PSAM GlyR EHTs, iLMO4 EHTs were analyzed electrophysiologically by sharp microelectrode. AP measurements were very difficult with the very light-sensitive iLMO4 EHTs. The following analysis, therefore, is based on measurements from two EHTs. APs in iLMO4 showed an RMP of -40 mV compared to -72 mV in controls. APA was lower in iLMO4. Maximal voltage over time change (dV/dt) was lower in iLMO4 as well as APD90 (Figure 53). These can also be seen in the exemplary AP in Figure 54.

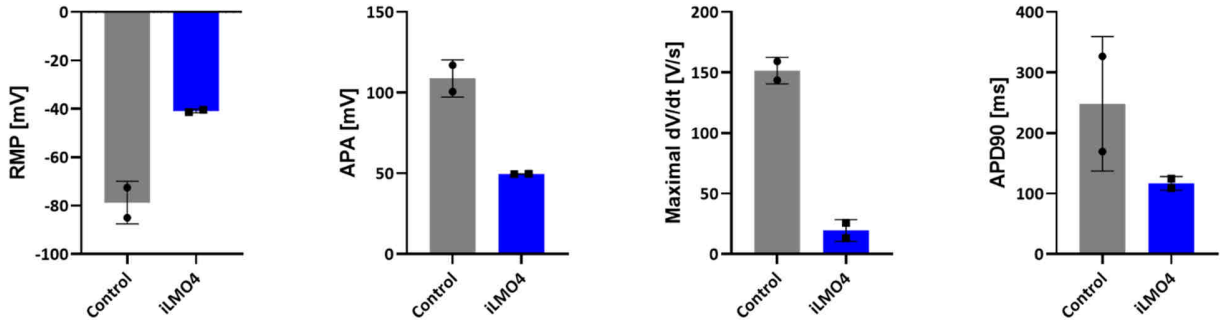

Figure 53: Action potential measurements of control and iLMO4 EHT. RMP in iLMO4 EHTs is at -40.34 mV, in contrast to control EHTs at -72.56 mV. APA, maximal dV/dt and APD90 are all lower in iLMO4 EHTs, mean of 10 APs in n=2 EHTs per group, mean±SD.

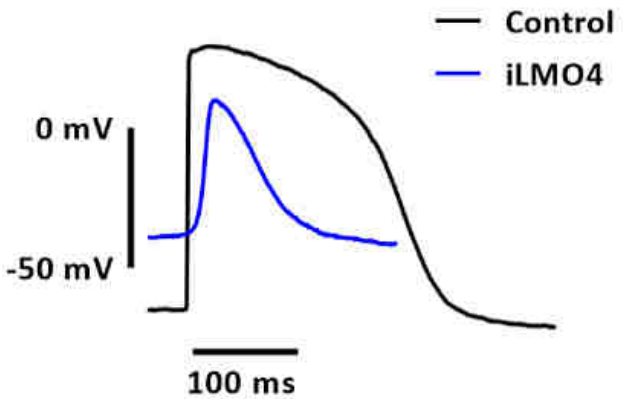

Figure 54: Exemplary AP of a control EHT (black) and an iLMO4 EHT (blue). Note the reduced APA, APD90, max dV/dt and more positive RMP in iLMO4.

Photostimulation in iLMO4 EHTs was technically challenging. Blue light sources created electrical interference and impaired recording quality. Therefore, a flashlight (white light) was used to activate iLMO4. We then analyzed action potential upon light exposure. We observed a decline of APA while the RMP shifted from -38 mV to -30 mV. APs ceased within six contractions (< 1 s). After switching off the light source, APs recovered swiftly. The first contraction occurred roughly 0.5 s after the termination of photostimulation (Figure 55).

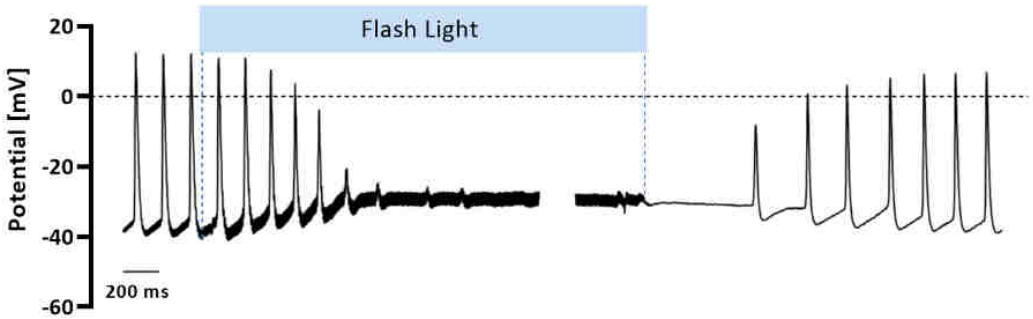

Figure 55: AP measurements prior, during and after light exposure. A flash light was used to illuminate the EHT. Within 0.8 s APs ceased but recovered quickly after ca. 0.5 s. RMP increased during light exposure from -38 mV to -30 mV.

6.4.3 Morphological Characterization of iLMO4 EHTs

Immunofluorescence imaging of iLMO4 cardiomyocytes showed a similar sarcomere structure to control cardiomyocytes. EYFP was localized in the cell membrane. iLMO4 EHTs revealed a similar sarcomere structure compared to control EHTs. Native EYFP was observed in the cell membrane, confirming stable transgene expression after several weeks of culture in a 3D model (Figure 56).

In conclusion, we found that iLMO4 cardiomyocytes could not be stopped with a high micromolar concentration of CTZ in a matter of seconds, making a successful in vivo application unlikely. iLMO4 EHTs could, however, be stopped by photostimulation. Morphologically, iLMO4 EHTs did not deviate from control EHTs, but electrophysiological analysis showed that iLMO4 EHTs differed drastically from control EHTs.

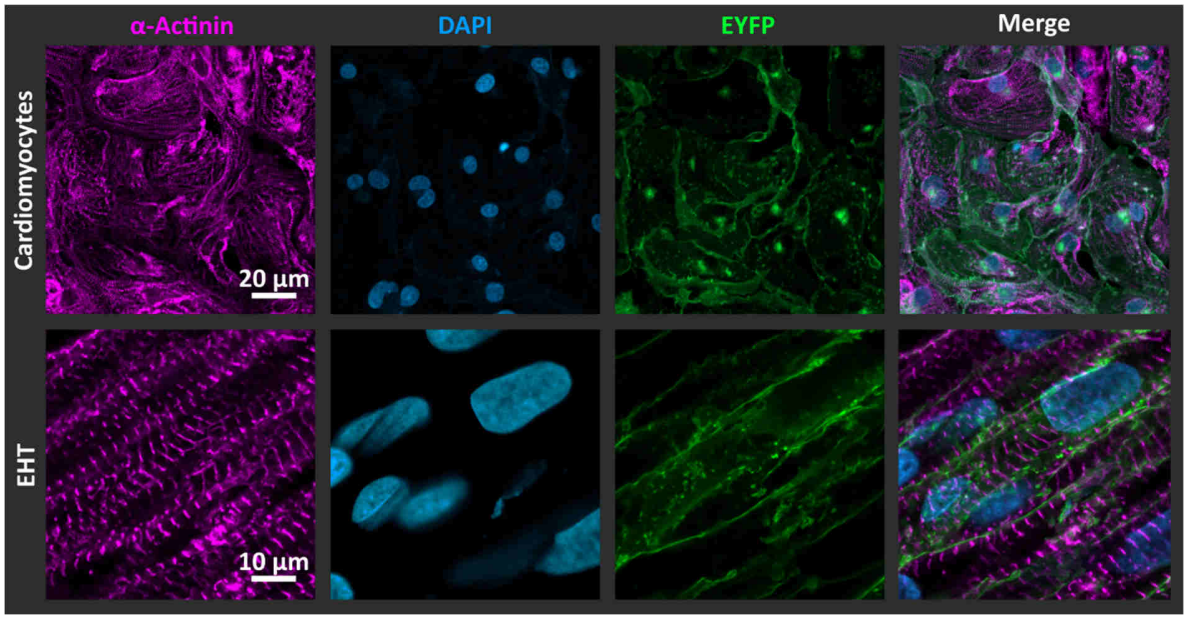

Figure 56: Immunofluorescence imaging of iLMO4 cardiomyocytes in 2D and 3D. Sarcomere structure is similar to control cardiomyocytes. EYFP (iLMO4) is found in the cell membrane of iLMO4 cardiomyocytes. Previously published in "Contractile force of transplanted cardiomyocytes contributes to heart function after injury" by Stüdemann et al., BioRxiv, pages 2021.11.23.469715 (2021).

6.5 Investigation of PSAM GlyR and iLMO4 Contribution In Vivo

We created two cell lines that (partially) demonstrated the required characteristics for further use in transplantation studies. PSAM GlyR could be switched off by applying PSEM^{89S}, while iLMO4 could be switched off using photostimulation (470 nm). Now we aimed to assess the degree of contribution of these cardiomyocytes to left ventricular function in a cryoinjury guinea pig model. At first, we conducted transplantation of PSAM GlyR cardiomyocytes. Prior to our transplantation study, we first conducted a pharmacokinetics study to assess whether an in vivo assessment of PSAM GlyR cardiomyocytes' contribution would be feasible.

6.5.1 PSEM^{89S} Pharmacokinetics

To successfully switch off contractility of PSAM-GlyR cardiomyocytes after transplantation, sufficient (≥30-100 µM) PSAM^{89S} serum concentrations had to be achieved. The original publication of PSAM GlyR reported that intraperitoneal injection in mice resulted in a concentration of 16 µM, indicating that it might be difficult to obtain a sufficient plasma concentration to silence PSAM GlyR cardiomyocytes (Magnus et al. 2011). PSEM^{89S} was injected in guinea pigs intraperitoneally, reaching a maximum concentration of 13.7±2.0 µM after 15 minutes (Figure 57). Intravenous injection in the vena saphena resulted in a maximum concentration of only 13.8±0.5 µM after 15 minutes. The time course of serum concentrations hardly differed from that seen after intraperitoneal injection (Figure 57), indicating that application may not have been purely intravenous. Indeed, intravenous injection in the vena jugularis (much larger than the vena saphena) resulted in 54.3±0.3 µM immediately after injection (Figure 57). Hence, vena jugularis injection was the only route of injection to safely reach a serum concentration above 30 µM, which was necessary to stop contractility in vitro. From the injection via vena jugularis, we derived a half-life time of 49.5 minutes. Overall, the pharmacokinetic study revealed that the PSAM GlyR system had significant limitations for an in vivo application.

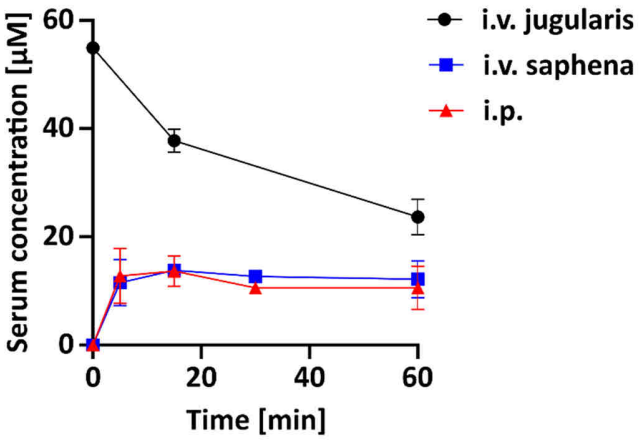

Figure 57: PSEM^{89S} kinetics in guinea pigs. PSEM^{89S} was injected i.p., i.v. via the vena jugularis or vena saphena. Blood was withdrawn at baseline and after 5, 15, 30 and 60 minutes, n=3 animals per group, mean±SD.

6.5.2 Langendorff System

Because of these results, we conducted the transplantation study without an in vivo assessment of cardiac function under PSEM^{89S} application. As an alternative, we assembled a Langendorff apparatus to investigate the contribution of PSAM GlyR cardiomyocytes in an ex vivo setting.

A self-built platform (height 100 cm) was used to produce constant hydrostatic pressure. We used a mouse pressure catheter (Transonic, FTH-1212B-4518) to measure intraventricular pressure before the PSEM^{89S} application. Two tanks with modified KHB were used. One tank contained PSEM^{89S} at a concentration of 100 µM. Switching between both tanks allowed the application of PSEM^{89S}. However, this setup had several limitations and required substantial modifications before we could stably analyze left ventricular function. One problem was that we observed an immediate change in developed pressure when switching between the two tanks, occurring much faster than the wash-in phase of PSEM^{89S} of four minutes (Figure 58).

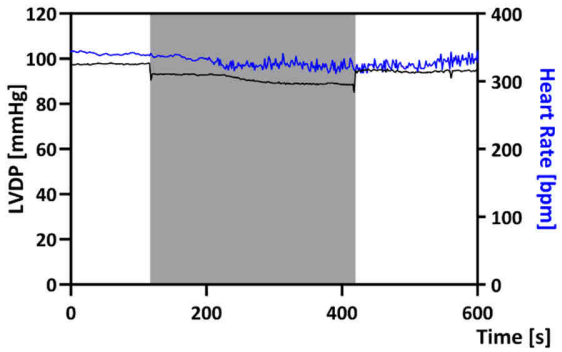

Figure 58: LVDP and heart rate recordings prior and during PSEM^{89S} application. Duration of PSEM^{89S} application is indicated by the grey area. LVDP drops immediately after valve switching, showing that subtle hydrostatic pressure differences rather than PSEM^{89S} are the reason.

Wash-in time was determined by measuring the time it took ink-stained modified KHB to reach the heart. This immediate change occurred because the volume in the two tanks differed since we had to use a small volume PSEM^{89S} tank because of economic reasons. Therefore, the hydrostatic pressure caused by the two different tanks was slightly different but already noticeable in the developed left ventricular pressure. We also realized that by inserting a small catheter designed for in vivo application, meaning for a fully loaded ventricle, we would not measure the likely subtle differences in left ventricular pressure while switching off contractility of the transplanted cells. Therefore, we improved the setup.

- Reduced the height of the platform from 100 cm to 70 cm to reduce the likelihood of incompetent aortic valves (Curtis et al. 1986).

- To avoid pressure changes when switching between tanks, we employed clinical syringe pumps to add the substrate directly to the KHB flow at low speed. Therefore, PSEM^{89S} in high concentration (3 mM) was used, equaling a 30x stock solution diluted in the KHB flow to the heart to 1x. This resulted in 100 µM PSEM^{89S}.

- A self-assembled balloon catheter was used to allow isovolumetric contractions (AD Instruments 2003; Sutherland et al. 2003a, b). This is crucial because the left ventricle is unfilled. Therefore, catheter measurements will be inaccurate (Figure 59). For this, the left atrium was opened, and the balloon was inserted via the mitral valve.

Figure 59: Self-assembled balloon catheter. Left panel: deflated balloon. Right panel: Inflated balloon.

- Electrical pacing via two stainless steel hooks to compensate for the negative chronotropic effect of PSEM^{89S} in the hope of reducing the negative inotropic effect (force-frequency relationship).

- The number of arrhythmic events was high. Hence, we applied lidocaine (170 µM) during the experiment, which abolished almost all arrhythmic events (Vandecasteele et al. 1999).

In summary, I was able to assemble a Langendorff apparatus that reliably measured LVDP and heart frequency over extended periods. In addition, compounds such as PSEM^{89S} could be added without disturbing the measurement and with minimal volume addition. Moreover, hearts could be paced, and lidocaine prevented the frequent arrhythmic events. The final setup is schematically shown in Figure 60.

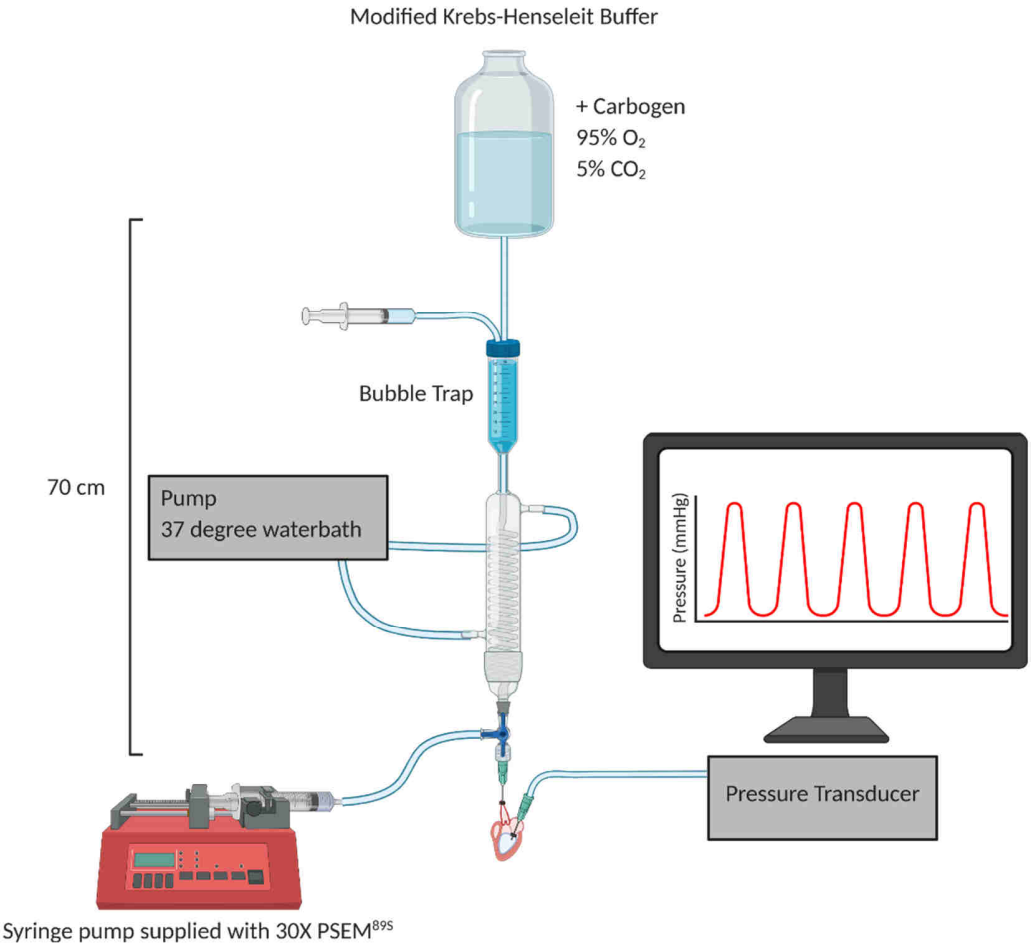

Figure 60: Schematic view of the Langendorff apparatus after modifications. Modified KHB was supplied via a tank placed on a 70 cm high platform. A bubble trap was used to remove air bubbles. A pump and water bath supplied warmth. A syringe pump was used to supply PSEM^{89S}. The balloon catheter placed in the left ventricle was connected to a pressure transducer.

6.5.3 Transplantation Study

We then conducted a transplantation study in guinea pigs. We first performed the PSAM GlyR study, followed by an iLMO4 study. Experimental data from the surgery are summarized for both studies combined. Guinea pigs underwent a first thoracotomy during which a cryoinjury was induced. Cardiomyocyte transplantation was performed seven days after injury. Two days prior to cell transplantation, immunosuppression was started to prevent graft rejection. Across all animals, cyclosporin A concentration was 496±40 µg/L. Next, either wildtype cardiomyocytes (referred to as control), PSAM GlyR, or iLMO4 cardiomyocytes were injected directly into the scar area.

We assessed cardiac function before surgery, after cryoinjury, and four weeks after transplantation. Taking together all animals across all groups, baseline FAC was 43.0±1.2% and dropped to 30.6±1.6% after cryoinjury (Figure 61). In more detail, baseline FAC was 43.6±1.7% (control), 39.8±1.5% (iLMO4) and 50.8±2.4% (PSAM GlyR). Upon cryoinjury, FAC dropped in control animals to 27.7±2.6% ($p \leq 0.01$), 33.5±2.4% in iLMO4 animals (ns), and 29.0±2.8% in PSAM

GlyR animals (p≤0.05; Figure 61). Transplantation of $20x10^6$ cardiomyocytes stabilized FAC; however, there was no significant beneficial increase of FAC caused by cardiomyocytes transplantation of any cell line (Figure 61). FAC stabilized at 30.5±2.2% in control, 33.0±2.3% in iLMO4 and 32.8±3.2% in PSAM GlyR animals.

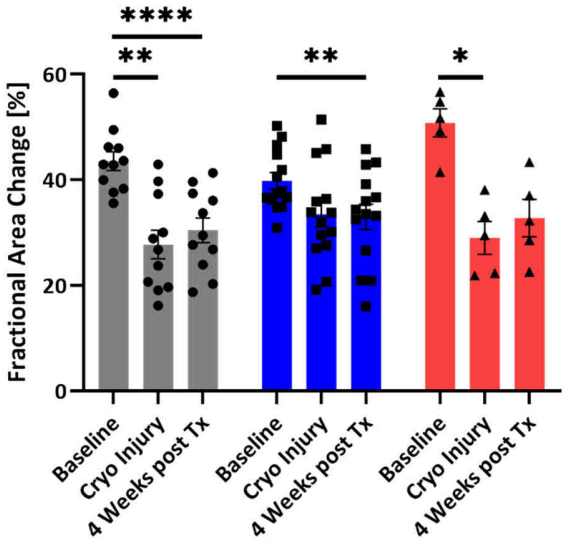

Figure 61: FAC in guinea pigs prior surgery, seven days after cryoinjury and four weeks after transplantation, assessed by echocardiography, n=11 for control, n=14 for iLMO4 and n=5 for PSAM GlyR, mean±SEM, 2way ANOVA with Turkey's multiple comparison test, *p≤0.05, **p≤0.01, ****p≤0.0001. Previously published in "Contractile force of transplanted cardiomyocytes contributes to heart function after injury" by Stüdemann et al., BioRxiv, pages 2021.11.23.469715 (2021).

We assessed fractional shortening (FS) as an alternative measure for cardiac function. FS was 46.2±1.5% at baseline and was reduced by cryoinjury to 33.9±1.5% across all groups (Figure 62). In more detail, control animals had an FS of 46.7±2.0%, iLMO4 animals of 43.9±2.1%, and PSAM GlyR animals showed an FS of 51.6±4.4%. Cryoinjury reduced FS to 33.9±2.8% (p≤0.01) in control animals, 35.1±2.2% (ns) in iLMO4, and 30.5±2.5% (ns) in PSAM GlyR animals (Figure 62).

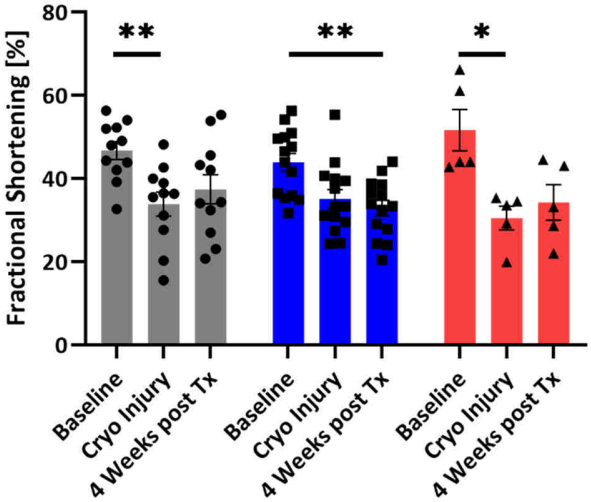

Figure 62: FS in guinea pigs prior surgery, seven days after cryoinjury and four weeks after transplantation, assessed by echocardiography, n=11 for control, n=14 for iLMO4 and n=5 for PSAM GlyR, mean±SEM, 2way ANOVA with Turkey's multiple comparison test, *p≤0.05, **p≤0.01.

Cardiomyocyte transplantation stabilized FS at 37.4±3.3% in control animals, 32.9±1.8% in iLMO4, and 34.3±3.8% in PSAM GlyR animals (Figure 62).

Infarct, scar, and graft size were determined from paraffin sections of four sections per heart after the hearts were harvested. All sections, stained for dystrophin, are found in the Appendix. Immunohistochemistry was performed by Kristin Hartmann (Histology Core Facility, UKE). One example is depicted here (Figure 63).

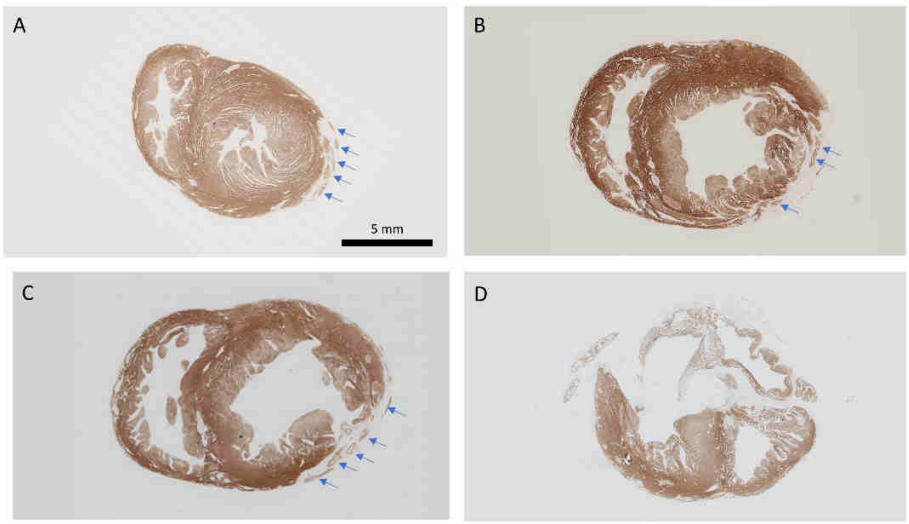

Figure 63: Dystrophin staining of a guinea pig heart. Depicted are four sections from apex (A) to base (D). Blue arrows indicate grafted cardiomyocytes.

Infarct size (length-based) was 27.1±2.0% compared to 21.0±1.5% in iLMO4 and 25.7±4.0% in PSAM GlyR hearts (Figure 64). Similarly, scar size (area-based) was 17.3±1.6% in control, 13.9±0.8% in iLMO4 and 18.9±3.2% in PSAM GlyR (Figure 64). Graft size (area-based) was also similar. In control animals, the graft constituted 9.5±1.8% of the scar area. In iLMO4, we found a graft size of 13.1±2.7%, and in PSAM GlyR animals, a graft size of 11.0±3.2% (Figure 64).

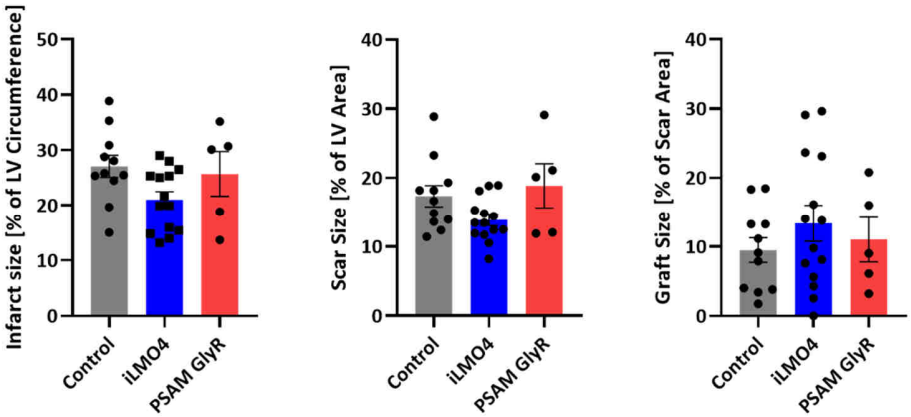

Figure 64: Histological analysis of infarct (length-based), scar (are-based) and graft size (area-based). One mean value per animal was derived by averaging the measurements from four sections (A to D) from the apex to the base of the heart, n=11 for control, n=14 for iLMO4 and n=5 for PSAM GlyR, mean±SEM, Brown-Forsythe and Welch ANOVA test with Dunnett's T3 multiple comparison test. Previously published in "Contractile force of transplanted cardiomyocytes contributes to heart function after injury" by Stüdemann et al., BioRxiv, pages 2021.11.23.469715 (2021).

Grafted cells were identified by EGFP or human Ku80 (Figure 65). This shows that these cells were not only of human origin but also expressed the transgene four weeks after transplantation. In addition, immunostaining of PSAM GlyR hearts revealed that grafted cells expressed α-actinin, meaning they were cardiomyocytes.

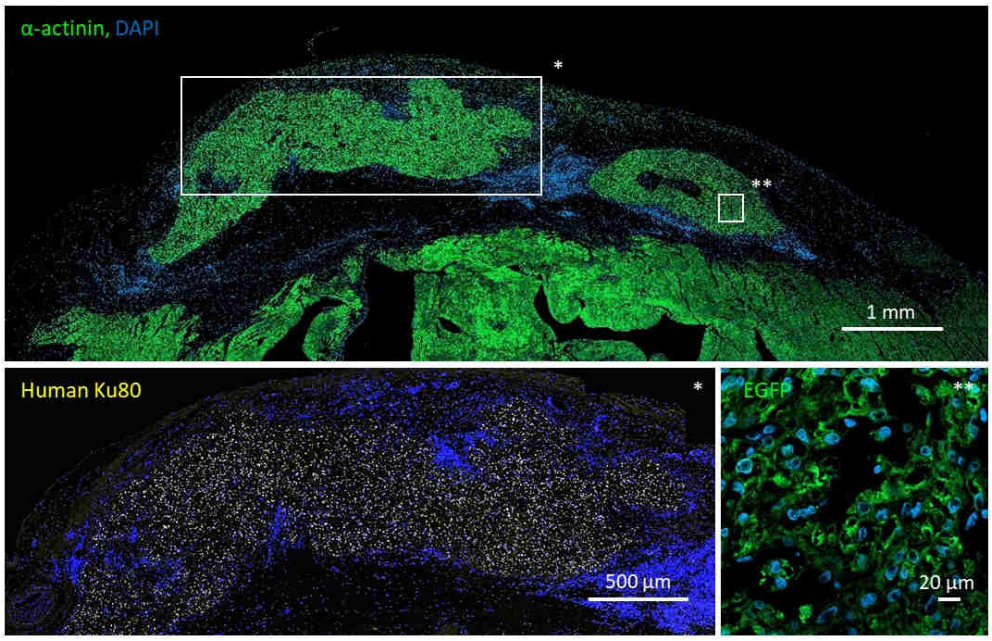

Figure 65: Immunostaining of PSAM GlyR heart. Upper panel: α-actinin positive islands are found in the scar area. Left panel: These islands were identified as Ku80 positive, meaning they are grafted cells of human origin. Right panel: In addition, these cells were EGFP positive, showing again that these cells were grafted cardiomyocytes but also that the transgene was still expressed four weeks after transplantation. Previously published in "Contractile force of transplanted cardiomyocytes contributes to heart function after injury" by Stüdemann et al., BioRxiv, pages 2021.11.23.469715 (2021).

All further immunostainings were performed and acquired by MD student Rajiven Srikantharajah under my supervision. iLMO4 hearts were stained for MLC2v, illustrating cardiomyocytes. Engrafted cardiomyocytes were found in the scar. Figure 66 depicts the varying degree of remuscularization. Direct intramyocardial injection sometimes resulted in large grafts (Figure 66, left and middle) or tiny grafts (Figure 66, right). We aimed for injection in the scarred area in the left ventricle, where most grafted cells are found. However, grafted cells could be found in the septum in some hearts, reaching almost into the right ventricle (Figure 66, left) or in the posterior wall (Figure 66, right).

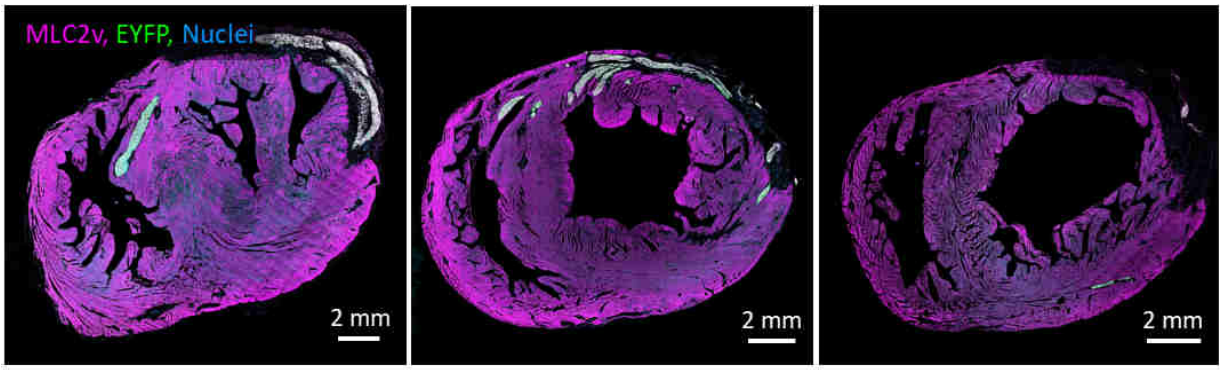

Figure 66: whole heart sections of three iLMO4-injected hearts. Hearts were stained for MLC2v as a cardiomyocyte marker and EYFP, indicating grafted cells. Grafts had a wide variety in size and location. Previously published in "Contractile force of transplanted cardiomyocytes contributes to heart function after injury" by Stüdemann et al., BioRxiv, pages 2021.11.23.469715 (2021).

Grafted cells were in direct contact with the host myocardium (Figure 67, white arrows). Still, there were also regions in which grafted cells were separated from the host myocardium by a fibrous layer (Figure 67, orange arrow).

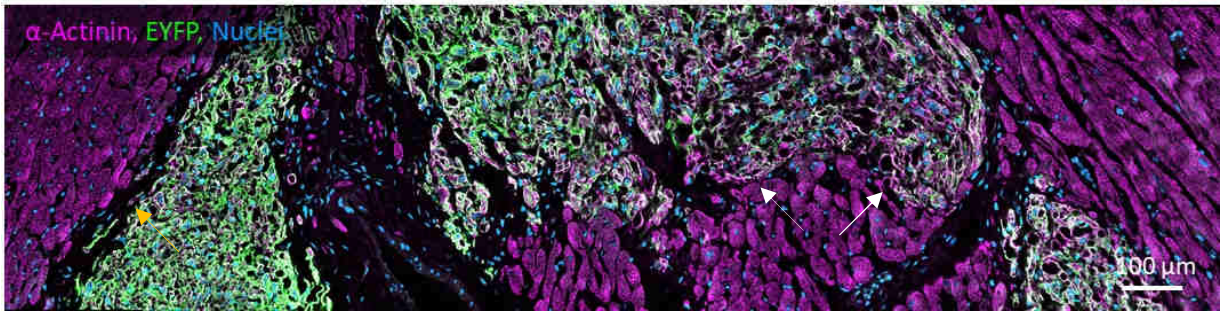

Figure 67: Immunostaining of grafted iLMO4 cells and host myocardium four weeks after transplantation. Some grafted areas directly interacted with host myocardium (white arrows) while in other cases grafted cells were encapsulated by a cell layer (red arrow). Previously published in "Contractile force of transplanted cardiomyocytes contributes to heart function after injury" by Stüdemann et al., BioRxiv, pages 2021.11.23.469715 (2021).

Sarcomere structure in grafted cells was less organized, indicating immaturity (Figure 68). Moreover, grafted cells were smaller and showed additional signs of immaturity, such as peripheral myofibrils. Yet, they also showed signs of further maturation after transplantation and almost exclusively expressed the ventricular myosin light chain isoform (Figure 68, right).

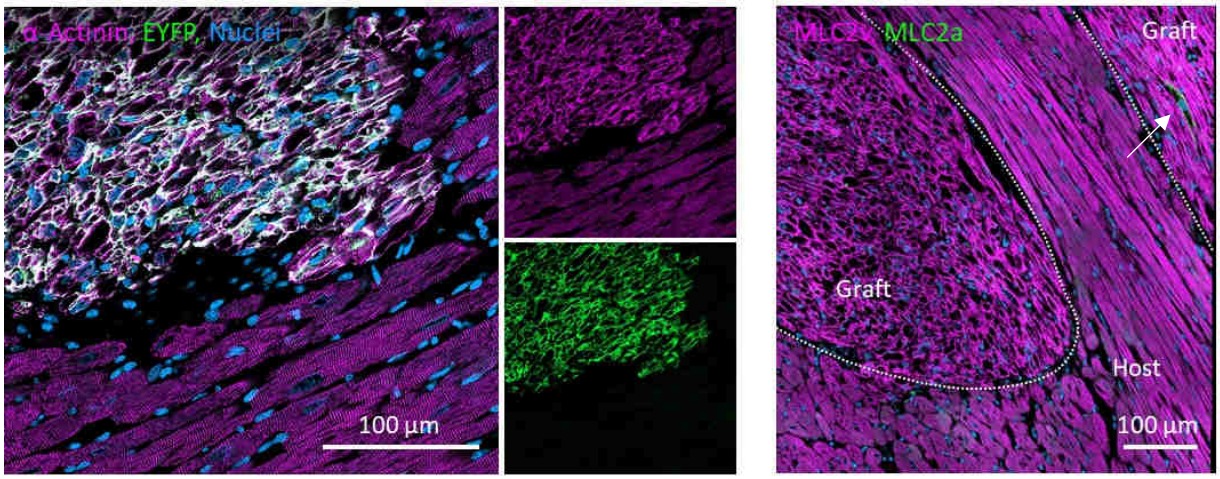

Figure 68: Immunostainings of grafted iLMO4 cells and host myocardium four weeks after transplantation in higher magnification. Left panel: Graft and host cardiomyocytes. Grafted cells were smaller and less organized. Right panel: Grafted cells almost exclusively expressed MLC2v. Only one MLC2a positive cell can be seen here (white arrow). Previously published in "Contractile force of transplanted cardiomyocytes contributes to heart function after injury" by Stüdemann et al., BioRxiv, pages 2021.11.23.469715 (2021).

Interactions between engrafted cardiomyocytes and host tissue were visible on many slides. Graft and host cells showed interactions via connexin43 or cadherin, providing histological evidence for structural integration and coupling. Yet, connexin43 and cadherin expression remained immature four weeks after transplantation (Figure 69). For comparison, connexin43 and cadherin expression pattern at intercalated discs in the host myocardium is shown in the insets (Figure 69, insets).

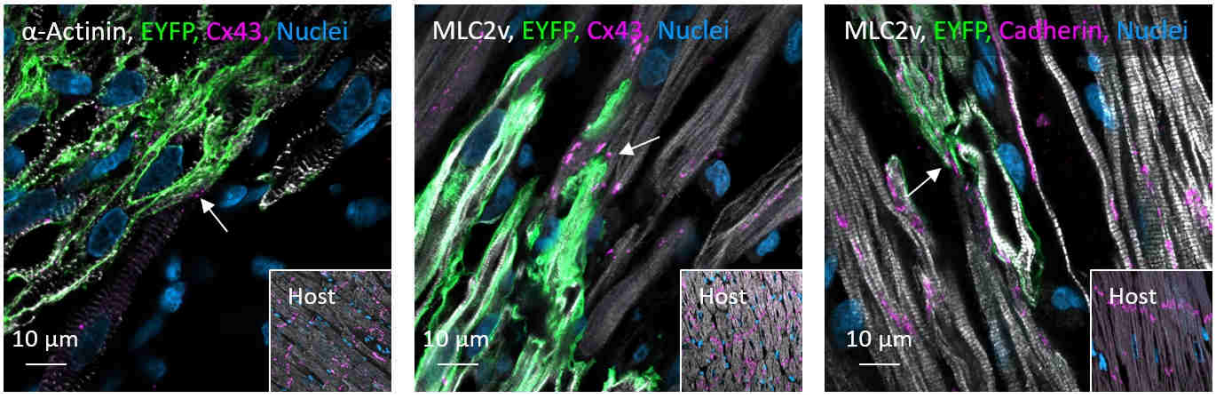

Figure 69: iLMO4 and host cardiomyocyte interactions. Grafted cells interacted via connexin43 or cadherin with host myocardium. Grafted cells appear immature because Connexin43 and cadherin were expressed circumferentially rather than in intercalated disks. Previously published in "Contractile force of transplanted cardiomyocytes contributes to heart function after injury" by Stüdemann et al., BioRxiv, pages 2021.11.23.469715 (2021).

6.5.4 PSAM GlyR Cardiomyocyte Contribution to Left Ventricular Pressure

As neither PSEM^{89S} nor CTZ was suitable for an in vivo application, we assessed cardiac function in the Langendorff apparatus. PSEM^{89S} was administered to achieve a final concentration of 100 µM. Measurement of the flow-through showed concentrations of 53.5±4.0 µM during PSEM^{89S} application, which was reduced during washout to 10.2±3.2 µM (Figure 70, left). Hence, concentration in the eluate was high enough to stop PSAM GlyR cardiomyocytes, considering the in vitro study results. To reduce the potential negative side effects of PSEM^{89S}, we reduced the final concentration. We measured the PSEM^{89S} concentration in the eluate of some hearts after applying 60 µM and found a PSEM^{89S} concentration of 46.0±2.0 µM in the eluate (Figure 70, right). This concentration was also sufficient to stop PSAM GlyR cardiomyocytes' contractility in vitro and was used from then on.

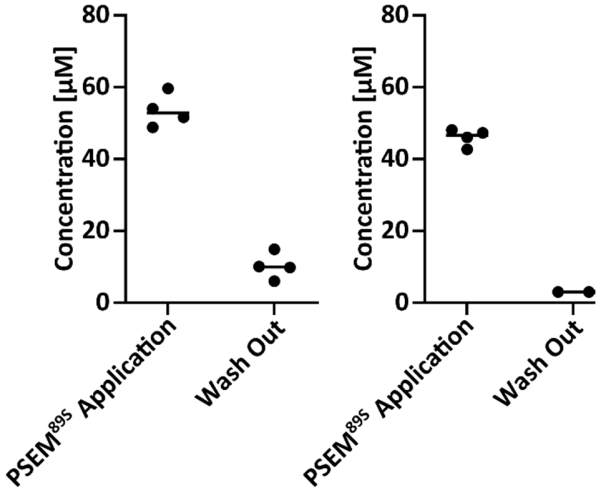

Figure 70: PSEM^{89S} concentration in the Langendorff eluate. Left panel: PSEM^{89S} application of 100 µM led to a concentration in the eluate of 53.5 µM which decreased to 10.2 µM during washing. Right panel: When 60 µM were applied, 46 µM were found in the eluate, n=4 and n=2.

We then conducted transplantation of PSAM GlyR or control cardiomyocytes and assessed left ventricular function in the Langendorff system four weeks after transplantation. Hearts were cannulated and equilibrated for 15 minutes before starting PSEM^{89S} treatment under electrical pacing. LVDP was 64.9±7.9 mmHg in hearts that had received control cardiomyocytes and 63.6±16.2 mmHg PSAM GlyR hearts. PSEM^{89S} application (60 µM) resulted in an LVDP reduction of 7.7±2.4 mmHg (12%) in PSAM GlyR hearts and 8.3±2.1 mmHg (13.09%) in control hearts (Figure 71). There was no significant difference between both groups. During washout, hearts recovered, reaching 66.4±7.0 mmHg (PSAM GlyR) and 63.8±15.0 mmHg in control hearts. (Figure 71).

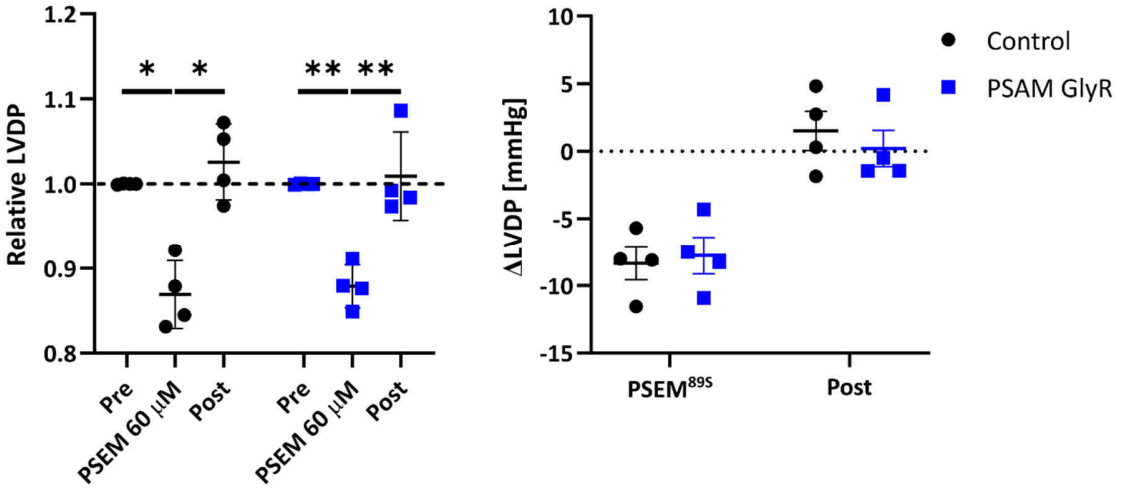

Figure 71: LVDP recordings in guinea pig hearts. Left panel: Relative LVDP in control and PSAM GlyR injected animals. LVDP was normalized to baseline value for each individual animal. PSEM^{89S} leads to a reversible reduction of LVDP in both groups, n=4 per group, Two-way ANOVA with Turkey's multiple comparison, *p≤0.05, **p≤0.01. Right panel: LVDP change relative to baseline LVDP. There was no difference between the LVDP change in control and PSAM GlyR animals, n=4 per group, mean±SD, Welch's t test, *p≤0.05, **p≤0.01. Previously published in "Contractile force of transplanted cardiomyocytes contributes to heart function after injury" by Stüdemann et al., BioRxiv, pages 2021.11.23.469715 (2021).

In conclusion, we found no difference in the drop of LVDP between control and PSAM GlyR hearts. The overall drop caused by PSEM^{89S} was unexpected as we prevented chronotropic effects with pacing. Moreover, we did not observe inotropic or chronotropic effects on control EHTs. Hence, we could not conclude that PSAM GlyR cardiomyocytes actively contribute to left ventricular function.

To further investigate the unexpected negative inotropic and chronotropic PSEM^{89S} effects in control hearts, we assessed PSEM^{89S} application in healthy guinea pig hearts. Application of PSAM^{89S} consistently reduced LVDP (negative inotropic) and heart rate (negative chronotropic) in healthy (Figure 72) guinea pig hearts, demonstrating that the effect was independent of cardiomyocyte transplantation. Furthermore, neither hexamethonium (nicotinergic AChR antagonist), atropine (muscarinergic AChR antagonist), nor pancuronium (nicotinergic AChR antagonist) could inhibit the negative inotropic and negative chronotropic effect. Hence, the

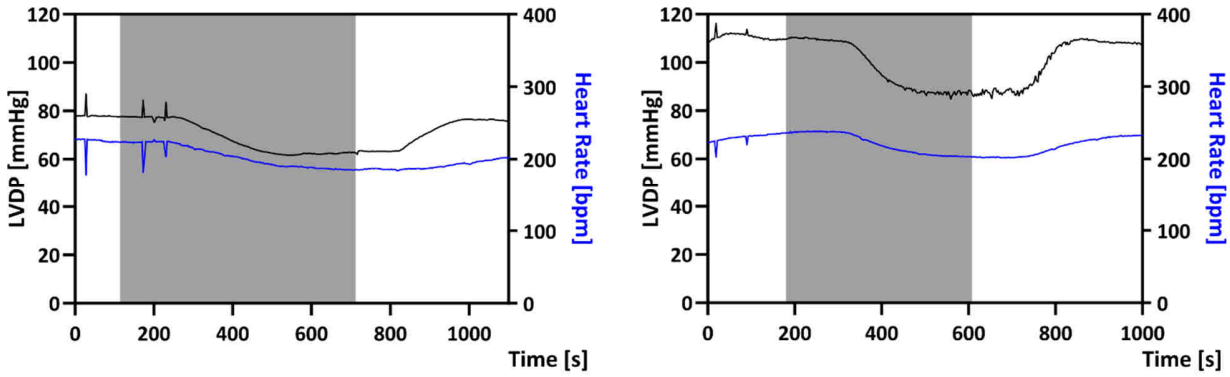

Figure 72: LVDP and heart rate recordings from guinea pig hearts. PSEM^{89S} application (grey box) caused a reversible reduction of LVDP and heart rate in a healthy (left) and control cell transplanted heart (right). Previously published in "Contractile force of transplanted cardiomyocytes contributes to heart function after injury" by Stüdemann et al., BioRxiv, pages 2021.11.23.469715

remaining AChR activity was excluded, but this did not resolve the initial problem of PSEM^{89S} negative inotropy and chronotropy.

6.5.5 iLMO4 Cardiomyocyte Contribution to Left Ventricular Pressure

We then conducted iLMO4 and control cell transplantation in cryoinjured guinea pigs. Four weeks after transplantation, hearts were cannulated and equilibrated for 15 minutes in the Langendorff system. LVDP increased by 15.1±1.8 mmHg during this time. Baseline frequency across all hearts was 162±22 bpm. Absolute LVDP was 60.4±3.8 mmHg in iLMO4 and 59.3±4.2 mmHg in control hearts. We then applied blue (470 nm) and red (660 nm) light to the Langendorff hearts. An example of one heart and the light application is depicted in Figure 73.

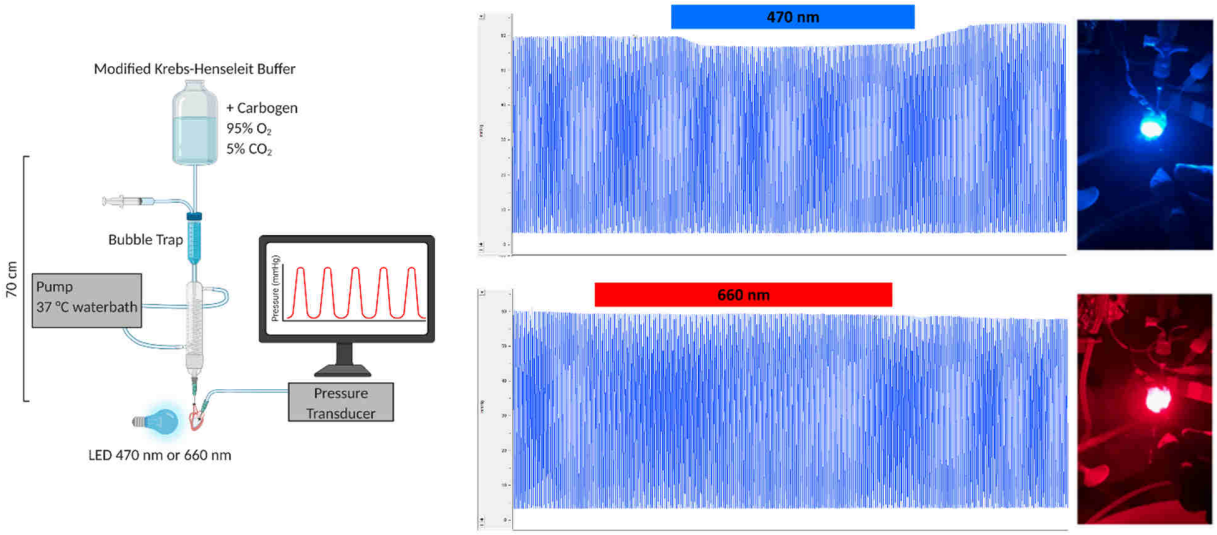

Figure 73: Illumination of guinea pig hearts with a coolLED pE4000 during Langendorff preparation. Left: Schematic view of the Langendorff apparatus. Right: Guinea pig hearts illuminated with 470 nm or 660 nm light during LVDP measurements. Shown is an exemplary original trace of LVDP (y axis) over time (x axis). Previously published in "Contractile force of transplanted cardiomyocytes contributes to heart function after injury" by Stüdemann et al., BioRxiv, pages 2021.11.23.469715 (2021).

Instead of ten averaged contractions, we analyzed individual contractions because the light effect occurs within seconds while PSEM^{89S} caused a reduction of LVDP within minutes.

Upon 470 nm light exposure, we observed an LVDP decline in iLMO4 hearts of 0.52 mmHg (0.75%), while LVDP in control hearts increased by 0.44 mmHg (0.75%; Figure 74, left). Hence, a difference of 1.5% occurs in LVDP upon 470 nm light application between both groups. Next, we analyzed the recovery phase from light. Absolute LVDP was 60.7±3.6 mmHg in iLMO4 and 62.4±3.9 mmHg in control hearts. Upon switching off the 470 nm light, we observed an increase of LVDP in iLMO4 hearts of 0.92 mmHg (1.45%) while LVDP in control hearts decreased by 0.10 mmHg (0.16%; Figure 74, right). Hence, a difference of 1.61% occurs in LVDP upon recovery from 470 nm light application.

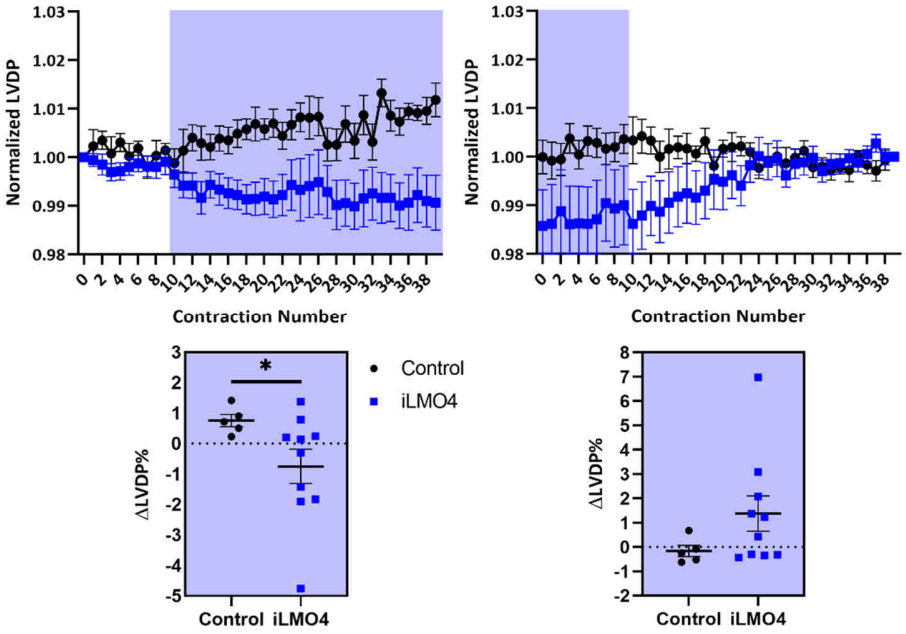

Figure 74: LVDP in Langendorff hearts prior, during and after application of 470 nm light. Left: 10 contractions prior and 30 during light exposure are depicted, normalized to the first contraction. Blue area indicates light application, mean±SEM. The mean of contraction 35 to 40 was analyzed and normalized to the mean of contraction 1 to 5 prior light for each group, n=5 for control and n=10 for iLMO4 hearts, mean±SEM, Welch's t test. Right: 10 contractions during and 30 after light exposure are depicted, normalized to the last contraction. Blue area indicates light application, mean±SEM. The mean of contraction 35 to 40 was analyzed and compared to the mean of contraction 1 to 5 during light for each group, n=5 for control and n=10 for iLMO4 hearts, mean±SEM, Welch's t test. Previously published in "Contractile force of transplanted cardiomyocytes contributes to heart function after injury" by Stüdemann et al., BioRxiv, pages 2021.11.23.469715 (2021).

We then repeated light exposure under electrical pacing. The mean frequency was increased from 162±22 bpm to 203±23 bpm. Baseline LVDP was 68.0±7.3 mmHg in iLMO4 and 60.3±3.6 mmHg in control hearts. Upon 470 nm light application, LVDP increased by 0.17 mmHg (0.38%) in iLMO4 and 0.39 mmHg (0.70%) in control hearts (Figure 75, left). The mean difference was only 0.32% under pacing conditions.

At the end of photostimulation, baseline LVDP was 70.1±7.0 mmHg in iLMO4 and 62.3±3.6mmHg in control hearts. Upon switching off the 470 nm light source, LVDP increased by 0.70 mmHg (1.05%) in iLMO4 and decreased by 0.16 mmHg (0.21%) in control hearts (Figure 75, right). The mean difference was 1.26% between iLMO4 and control hearts under pacing during recovery.

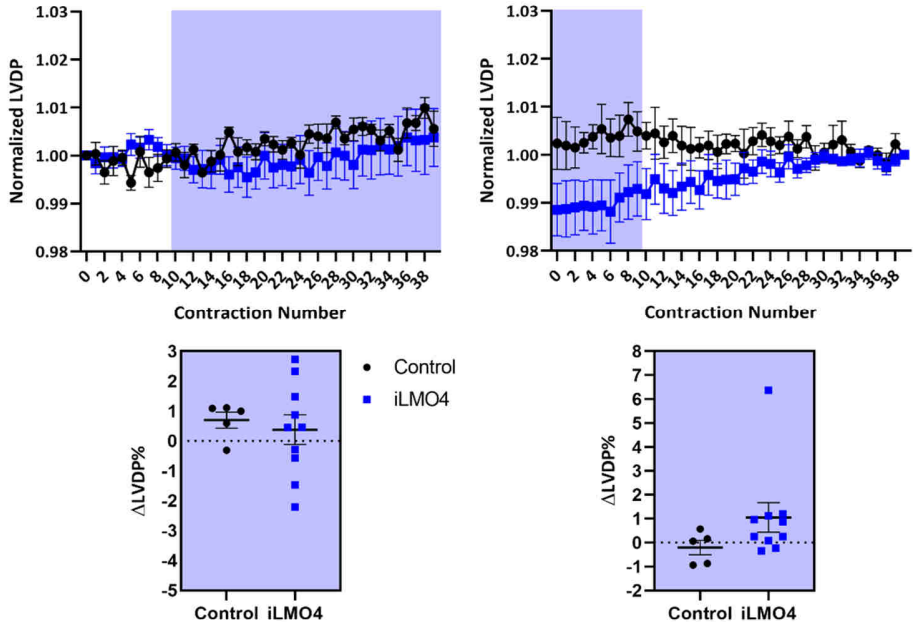

Figure 75: LVDP in Langendorff hearts prior, during and after application of 470 nm light under electrical pacing. Left: 10 contractions prior and 30 during light exposure are depicted, normalized to the first contraction. Blue area indicates light application, mean±SEM. The mean of contraction 35 to 40 was analyzed and normalized to the mean of contraction 1 to 5 prior light for each group, n=5 for control and n=10 for iLMO4 hearts, mean±SEM, Welch's t test. Right: 10 contractions during and 30 after light exposure are depicted, normalized to the last contraction. Blue area indicates light application, mean±SEM. The mean of contraction 35 to 40 was analyzed and compared to the mean of contraction 1 to 5 during light for each group, n=5 for control and n=10 for iLMO4 hearts, mean±SEM, Welch's t test. Previously published in "Contractile force of transplanted cardiomyocytes contributes to heart function after injury" by Stüdemann et al., BioRxiv, pages 2021.11.23.469715 (2021).

Red light (660 nm) was used as an internal control. Upon 660 nm light exposure, LVDP in iLMO4 hearts increased from 62.0±3.8 mmHg by 0.12 mmHg (0.21%). Control hearts had a baseline LVDP of 62.31±3.88 mmHg, which increased by 0.58 mmHg (0.97%; Figure 76, left). Overall, 660 nm light created a difference of 0.76% between groups.

Upon 660 nm light exposure termination, LVDP in iLMO4 hearts increased from 62.50±3.73mmHg by 0.06 mmHg (0.05%). Control hearts had a baseline LVDP of 63.30±3.82 mmHg, which increased by 0.08 mmHg (0.11%; Figure 76, right). Overall, 660 nm light created a difference of 0.05% between groups.

A correlation between graft size and LVDP change from baseline revealed that only hearts with large grafts exhibited a reduction in LVDP. However, one heart (799) which showed the biggest effect, unexplainably had only a graft of 5.61%. Excluding this heart resulted in a good correlation of graft percentage to LVDP change (Figure 77)

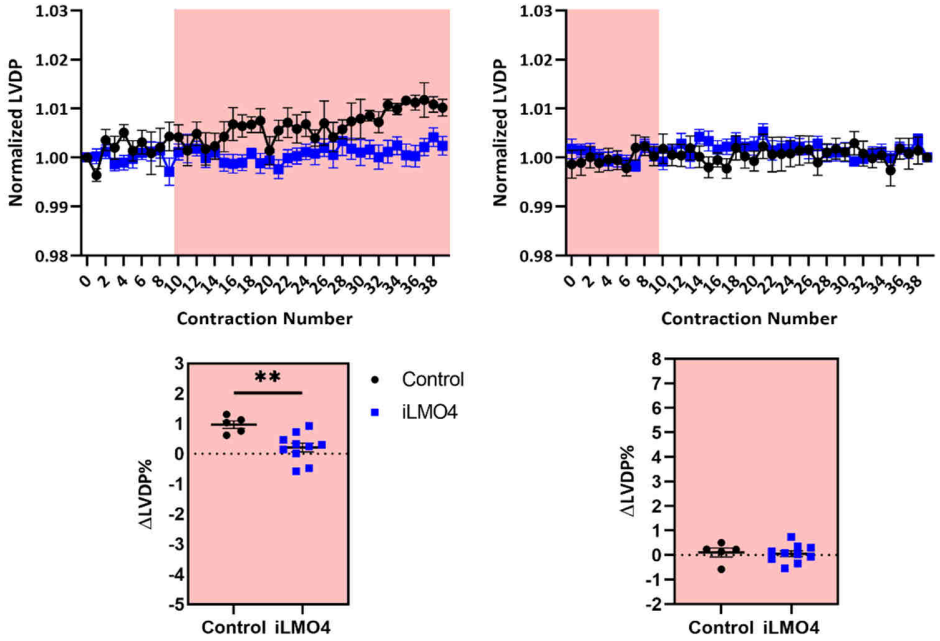

Figure 76: LVDP in Langendorff hearts prior, during and after application of 660 nm light. Left: 10 contractions prior and 30 during light exposure are depicted, normalized to the first contraction. Blue area indicates light application, mean±SEM. The mean of contraction 35 to 40 was analyzed and normalized to the mean of contraction 1 to 5 prior light for each group, n=5 for control and n=10 for iLMO4 hearts, mean±SEM, Welch's t test. Right: 10 contractions during and 30 after light exposure are depicted, normalized to the last contraction. Blue area indicates light application, mean±SEM. The mean of contraction 35 to 40 was analyzed and compared to the mean of contraction 1 to 5 during light for each group, n=5 for control and n=10 for iLMO4 hearts, mean±SEM, Welch's t test. Previously published in "Contractile force of transplanted cardiomyocytes contributes to heart function after injury" by Stüdemann et al., BioRxiv, pages 2021.11.23.469715 (2021).

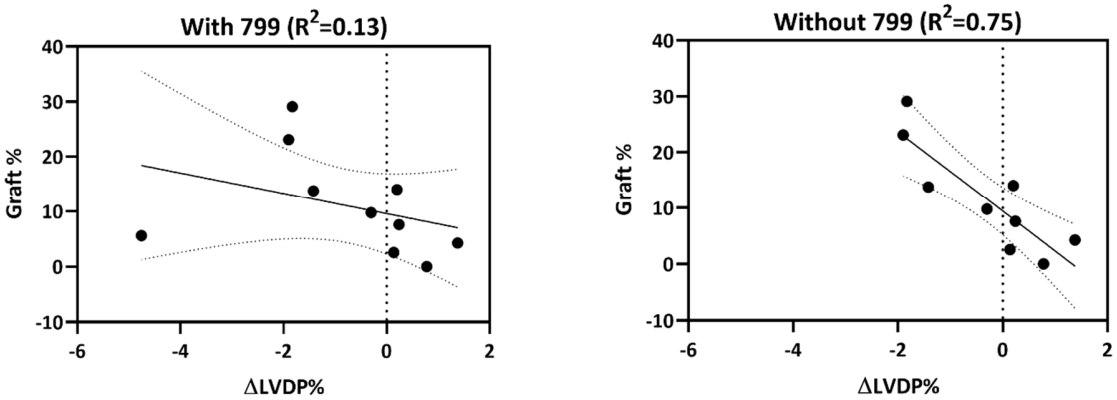

Figure 77: Graft to LVDP change correlation. Left: Correlation with all hearts that received iLMO4 cardiomyocytes. Right: Excluding the data of heart 799 resulted in a better correlation.

As an additional activation mode, we infused CTZ in a subgroup (n=3) as a bolus (calculated concentration of ~300 µM). iLMO4 cardiomyocytes could be illuminated and clearly localized in the scar area (Figure 78). However, CTZ application induced an increase in LVDP (ns, Figure 79). In addition, CTZ application was arrhythmogenic in one heart, although electrical pacing was active (Figure 79, upper right). Hence, CTZ could not be used to assess iLMO4 cardiomyocyte

contribution to heart function. However, it was useful to assess the viability and location of grafted cardiomyocytes and demonstrated that human grafts were functionally vascularized.

Figure 78: CTZ-induced illumination of transplanted iLMO4 cardiomyocytes. Left: Langendorff heart under normal room light. Middle: when darkening the room and infusing CTZ, the iLMO4 cardiomyocytes begin to emit blue light. Right: Upon complete darkness iLMO4 cardiomyocytes can be localized across the whole injury site on the left ventricle. Previously published in "Contractile force of transplanted cardiomyocytes contributes to heart function after injury" by Stüdemann et al., BioRxiv, pages 2021.11.23.469715 (2021).

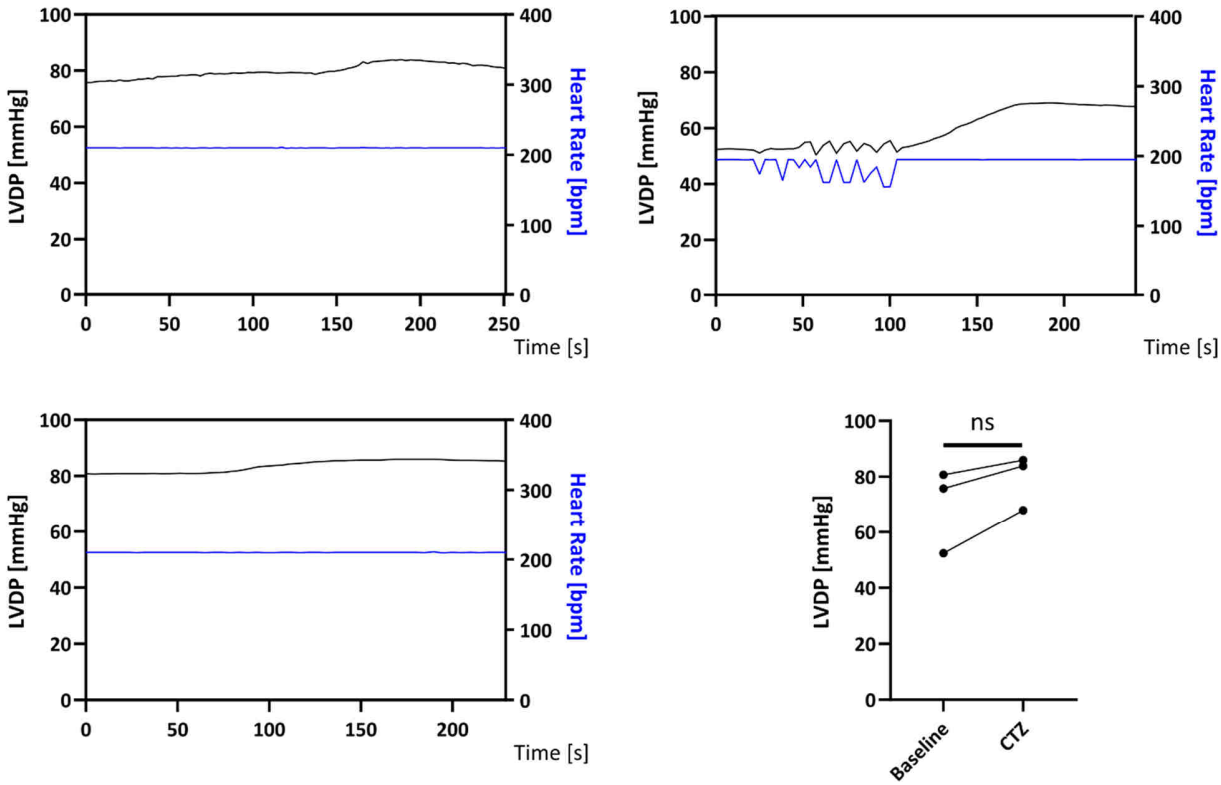

Figure 79: CTZ infusion in iLMO4 transplanted Langendorff hearts. CTZ was infused as a bolus at t=0 in three hearts. When CTZ reached the heart there was a tendency for increase of LVDP (lower right panel), n=3, paired t test.

In conclusion, we found that iLMO4 cardiomyocytes contribute to heart function. However, the contribution occurred only under relatively low spontaneous beating (beating frequency 162 bpm) and was not seen under electrical pacing at a higher rate (beating frequency 203 bpm).

7 DISCUSSION

In this study, we aimed to generate cardiomyocytes with an off-on switch, i.e., cardiomyocytes in which contractility could be switched off with high temporal resolution. Therefore, we generated four novel iPSC lines that expressed a putative chemogenetic or optogenetic off-on switch. All four cell lines could be differentiated into cardiomyocytes. Furthermore, contractility could be inhibited reversibly in two cell lines (PSAM GlyR and iLMO4), both containing an activatable anion channel. PSAM GlyR and iLMO4 cardiomyocytes were characterized in vitro and showed similar functional characteristics as the parental control cell line but also demonstrated physiological differences that will be discussed further below. We conducted a transplantation study to assess whether cardiomyocytes actively contribute to left ventricular function. Here we employed a cryoinjury guinea pig model. PSAM GlyR and iLMO4 cardiomyocytes were directly injected into the injured area one week after injury. Cardiomyocytes from both PSAM GlyR or iLMO4 lines successfully engrafted and partially remuscularized the injured heart. In vivo assessment of the off-on switch proved difficult, which is why an ex vivo Langendorff model was used. We found severe limitations in the PSAM GlyR off-on switch, which hindered the assessment of the active contribution of these cardiomyocytes to heart function. However, with iLMO4 cells, we found that transplanted cardiomyocytes actively contribute to heart function.

7.1 CRISPR/Cas9 Strategy

To express exogenous genes in iPSCs mainly two methods are common. The viral delivery of the transgene, e.g., using AAVs or stable genomic integration by CRISPR/Cas9. Lentiviral transduction, which is also often used, allows for genomic integration but at a random location (Steinbeck et al. 2015; Mattapally et al. 2018; Zhao et al. 2020). This occurs even in non-dividing cells (Naldini et al. 1996). Similarly, iPSC-derived cardiomyocytes can be transduced (Weinberger et al. 2016). Using a multiplicity of infection (MOI) of 0.2, only 25.7±0.6% transduction efficiency was reached in EHTs, which was enough to allow optical pacing (Lemme et al. 2020). In this project, we aimed to avoid virus transduction due to (i) potential safety issues for transplantation studies, (ii) expression/ silencing issues, (iii) packaging issues due to transgene size in AAV (iv), random genomic integration when using Lentivirus and (v) potential inefficient ability to stop contractility due to low transduction efficiency.

Hence, we generated plasmids for CRISPR/Cas9-mediated gene editing, containing a CAG promoter that demonstrated stronger silencing-resistance than EF1α and CMV promoters in hiPSCs (Luo et al. 2014). The ubiquitous expression with the CAG promoter also allows differentiation into other cell types because the promoter is not cell type-specific. Homologous DNA sequences up- and downstream of the transgene enhance editing success (Smithies et al. 1985). These so-called homology arms (HA) can be more than 1 kb each (Deng and Capecchi 1992), but in hiPSCs, HAs of 800 bp to 1000 bp each were reported to be sufficient and are regularly used (Byrne et al. 2015; Oceguera-Yanez et al. 2016; Hong et al. 2017; Yao et al. 2017; Zhang et al. 2017). We employed HAs of roughly 800 bp (Qian et al. 2014). Our plasmids targeted

the AAVS1 locus, a genomic "safe harbor" for transgene knock-in. Disruption of this locus has no deleterious effects on the cell, and expression occurs continuously (Ogata et al. 2003; Smith et al. 2008; Luo et al. 2014; Oceguera-Yanez et al. 2016).

A puromycin resistance was introduced in addition to a fluorescent protein. Puromycin is regularly used to enrich edited cells in CRISPR experiments (Luo et al. 2014; Oceguera-Yanez et al. 2016). EGFP was included next to PSAMs, while EYFP was linked to the LMOs. Fluorescent proteins allowed FACS enrichment. We used both methods for enrichment and did not observe a major limitation of one of the methods. However, eventually only FACS-enriched cells were used in this work.

We employed an RNP-based nucleofection for CRISPR/Cas9 editing. This method is preferred in iPSCs as, in contrast to Cas9 plasmids, the RNP cannot integrate into the genome. In addition, Cas9 plasmid expression persists for days, leading to more off-target effects. Hence RNP delivery is preferred, although rapid degradation can occur (Kim et al. 2014; Liang et al. 2015).

Other research groups reported editing ratios of 0.1-4%, which are in concordance with our results as we found a maximum of 3.13% (Mali et al. 2013; Roberts et al. 2017). To enhance these ratios, we tested two different gRNAs. Previously, this could almost double the editing efficiency from 2.3 to 3.9% (Mali et al. 2013). We also found big differences when testing two different gRNAs, but did not assess this quantitively. Different other methods to enhance editing efficiency were proposed (Lin et al. 2014; Yang et al. 2016; Zhang et al. 2017; Guo et al. 2018; Yiangou et al. 2019). However, in our hands, nocodazole-mediated cell cycle synchronization led to substantial cell death in hiPSCs at 50 ng/ml (Yiangou et al. 2019). As we could enrich scarcely edited cell lines with puromycin or FACS, we used none of these proposed methods to enhance HDR/NHEJ ratio in our experiments.

We chose the AAVS1 "safe harbor" for the transgene knock-in, since the disruption of this locus had no deleterious effects and was constantly expressed in hESCs even after differentiation and transplantation (Ogata et al. 2003; Smith et al. 2008; Luo et al. 2014; Oceguera-Yanez et al. 2016). However, one recent study provided evidence that the AAVS1 locus can be subject to silencing during differentiation (Bhagwan et al. 2020). We observed no silencing and detected EGFP/ EYFP expression during and after cardiac differentiation and four weeks after transplantation.

7.2 iPSC Clone Genotyping

Picked clones were pre-screened with a PCR for the 5' and 3' insertion site and an internal PCR. Oceguera-Yanez et al. found 25% homozygous, 67% heterozygous, and 8.3% aberrant clones with this strategy. In contrast, Haupt et al. found 25% of iPSCs to be precisely edited (not specified if homozygous or heterozygous). Homozygosity and aberrant ratios match our results; however, we found several clones with an unclear genotype that could not be clarified. In these clones, a 5' or 3' band appeared while the respective other one was missing. One possible explanation is the knock-in of only part of the plasmid or parts of the plasmid backbone (Roberts et al. 2017). A

second explanation is that one PCR simply did not work. As there were always options with a clear genotype, we did not analyze these clones further and did not choose any of these clones for our experiments.

We went on to perform long-range PCR to confirm correct insertion further and to sequence these PCR products. Two or three clones per cell line were sequenced, of which two with the correct sequence were chosen for further analysis. PSAM GlyR BF6 was excluded at this stage because the sequencing was incomplete. In all other lines, one clone was chosen at random. In PSAM 5HT3 clones, we found a silent mutation TTC → TTT, at bp 423, amino acid 141 (Phenylalanine). We could trace this back to the donor plasmid pAAVS1-CAG-PSAM-5HT3.

Southern blotting remains the gold standard for genotyping. It can distinguish homozygous from heterozygous clones and, most importantly, detect additional donor vector integrations (Oceguera-Yanez et al. 2016). Our results confirmed seven selected clones as homozygous with correct insertion, as no additional bands could be observed. Only one clone, PSAM 5HT3 BF5, showed a second unintended internal band which hints at additional vector integration. This is why we chose PSAM 5HT3 BF4 for further experiments, although Sanger sequencing confirmed the correct sequence in both clones. Of note, clone LMO AF10 is homozygous according to Southern blotting, although with PCR we found an "unedited" band, meaning it could have been heterozygous. As there were other options, I did not follow up on this but used LMO AP1 as an undoubtedly homozygous clone.

7.3 iPSC characterization

We created a master and working cell bank for the two confirmed clones per cell line and characterized those for $SSEA3^+$ and $EYFP^+/EGFP^+$. $SSEA3^+$ is a commonly used surface antigen for pluripotency. All cell lines demonstrated $SSEA3^+$ positivity. At this point, we also measured the expression of the transgenes by the EYFP/EGFP signal. PSAM GlyR, iLMO4, and LMO4 exhibited EYFP/EGFP positivity above 96%. Only both PSAM 5HT3 clones exhibited a ratio of <96%. These cell banks could be contaminated by unedited cells, creating mosaicism. As both clones have very similar ratios of $EGFP^+$ (95.8% vs. 95.4%), it is more likely that this specific transgene is simply expressed to a lesser degree than PSAM GlyR, which is highly similar in terms of its promoter and size.

We performed karyotype analysis by Nanostring. This method allows detecting missing or additional chromosomal parts by probe detection. These probes are spread across all chromosomes and cover the genome with a relatively high resolution. Two other methods could be used for karyotyping. First, Giemsa-banding is used to stain condensed chromosomes. Changes in staining intensity can then detect genomic aberrations. The limitation of Giemsa-banding is the resolution, limited to about five megabases (Mb) (Shaffer and Bejjani 2004). Alternatively, a PCR-based kit can be used (#07550, Stem Cell Technologies). Only nine specific, commonly mutated

genetic loci are tested with this kit. Although this method is precise, it does not give an overview of the whole genome as the Nanostring panel.

Eventually, a bioluminescence signal was detected, confirming the luciferase's expression and functionality in LMO4 and iLMO4.

7.4 Functional Characterization of iPSCs and iPSC-Cardiomyocytes

7.4.1 PSAM 5HT3 and PSAM GlyR

In a pilot trial, we generated a small amount of EHTs to test if the substrate PSEM^{89S} would stop the contractility of PSAM 5HT3 and PSAM GlyR cardiomyocytes. The requirements for this were:

- Reversibility of the off switch (off-on switch)
- Quick off-on kinetics
- Adequate substrate concentration for an in vivo use

In ex vivo experiments, PSEM^{89S} at 10 µM activated neuronal activity in PSAM 5HT3 neuronal slices, and the same concentration was enough to inhibit activity in PSAM GlyR neurons (Magnus et al. 2011). Hence, we tested different concentrations of PSEM^{89S}, starting at 1 µM going up to 100 µM. None of the concentrations could alter contraction force or frequency as desired in PSAM 5HT3 EHTs. We originally hypothesized that constant activation of PSAM 5HT3 would lead to depolarization block in our cardiac model. These results stand in contrast to neurons in which PSAM 5HT3 activation led to depolarization and neuronal firing (Magnus et al. 2011). One potential explanation is the ion flux of PSAM 5HT3 in cardiomyocytes might be insufficient. Another option might be that even higher concentrations might be necessary to activate PSAM 5HT3. As switching off cardiomyocyte contractility with this system was impossible, I did not follow up on it.

PSAM GlyR EHTs, on the other hand, could be stopped with PSEM^{89S}. Yet, the required concentrations were slightly higher than reported for neurons (30 - 100 µM). Nevertheless, 30 µM was sufficient to switch off contractility after several minutes. Dilution in the culture well and diffusion into the EHTs matrix could explain this delay. 100 µM, on the other hand, stopped contractility almost immediately.

The combination of PSAM GlyR/ PSEM^{89S} fulfilled all the requirements above of stopping contractility in cardiomyocytes with high temporal resolution. Therefore, we decided to characterize PSAM GlyR cardiomyocytes in more detail and generate more cardiomyocytes for these experiments.

Cardiomyocyte differentiation efficiency was low in PSAM GlyR iPSCs. Typically, differentiation of the parental line UKEi001-A shows efficiencies of 0.75 to 1, meaning that from every iPSC, 0.75 to 1 cardiomyocyte is produced in the 3D protocol. However, PSAM GlyR differentiation showed efficiencies of 0.22, indicating that the transgene knock-in limits differentiation efficiency.

In 2D cardiomyocytes, expression of PSAM GlyR was confirmed by α-bungarotoxin staining, demonstrating that the transgene under a CAG promoter is not subject to silencing in the AAVS1 locus after differentiation (Luo et al. 2014; Bhagwan et al. 2020). Additionally, cytosolic EGFP was observed. PSAM GlyR was found in the cell membrane and surprisingly in the nuclear membrane. Sarcomere structure (assessed by α-actinin staining) was similar to control cells. Comparable results were obtained in EHTs. PSAM GlyR cardiomyocytes matured over time and aligned along the force lines like control cardiomyocytes. PSAM GlyR was also localized in the cell membrane after several weeks of cultivation in a three-dimensional format.

Although there were no major structural differences, PSAM GlyR EHTs exhibited higher TTP and RT and lower force than controls after 32 days in culture. In addition, electrophysiological parameters were altered, such as a more positive RMP and reduced APA and dV/dt. These observations are best explained by a leakiness of the PSAM GlyR channel combined with its high expression level. Background PSAM GlyR leakiness could explain the overall slower contraction kinetics and the lower developed force because it would result in a higher RMP, thereby partially inactivating sodium channels. Eventually, this will result in slower contraction kinetics. Therefore, we did analyze whether there was a constant leakiness. However, the electrophysiological analysis (discussed below) supports this hypothesis.

We did not observe a major effect of ACh on PSAM GlyR EHT contractility. Only 3000 µM ACh decreased RT in these EHTs. This is in concordance with the original publication, stating that after modifications, EC_{50} for ACh increased from 26 to 570 µM. Hence, as observed, ACh is unlikely to have affected our results (Magnus et al. 2011).

Upon treatment with $PSEM^{89S}$, PSAM GlyR EHTs stopped contractility. In theory, the continuous activation of an anion channel could have three consequences: hyperpolarization, depolarization, or shunting. Hyperpolarization regularly occurs when employing ACRs in neurons. Photostimulation leads to a cease of AP firing and additional RMP reduction (Steinbeck et al. 2015). However, hyperpolarization in the EHT model might explain a stop in contractility but cannot explain that electrical pacing was impossible. Similar findings were reported for other anion channels systems (Kopton et al. 2018). Alternatively, shunting inhibition could play a role that has been shown to be the mechanism behind ChloC-mediated neuronal silencing. The equilibrium potential of Cl^- and the membrane potential are similar. Hence, during ChloC activation, a depolarizing current will allow Cl^- to flow in either direction, locally equalizing depolarizing currents (Wietek et al. 2014). The mechanism underlies Ohm's law, saying that the voltage equals the current difference times resistance (V = IxR). Opening more Cl^--conducting channels enhances Cl^- conductance, thereby reducing the cell's resistance. This results in a reduced voltage change upon a depolarizing current and hence shunting of the current.

However, it has been shown that in cardiomyocytes, the ubiquitous opening of anion channels leads to a net outward flow of Cl^- against the concentration gradient along the electrical gradient (Kopton et al. 2018) and resulted in depolarization.

AP measurements revealed that $PSEM^{89S}$ increased (i.e., depolarized) the resting membrane potential, resulting in a complete stop of electrical activity. This speaks for depolarization as observed in iLMO4 EHTs. Hence, depolarization is a main driver for inhibiting contractility, but shunting could also contribute. Further research is needed to clarify how depolarization and shunting work in cardiomyocytes. Regardless of the mechanism, PSAM GlyR cardiomyocytes fulfilled all requirements for the subsequent transplantation study. The off-switch worked reversibly in a matter of seconds, and 30 µM to 100 µM are adequate concentrations for in vivo use.

Interestingly, $PSEM^{89S}$ also affected control EHTs. It slightly prolonged APD and RT 80% while TTP -80% and dV/dt were slightly reduced. Previously, an effect on control neurons was not observed (Magnus et al. 2011). These results fit well to an I_{Kr} block, which is not unlikely, given that most drugs show an I_{Kr} block at high concentrations, and this is the main reason for drug withdrawal from the market (Piccini et al. 2009). Moreover, the EHT system is highly sensitive regarding the I_{Kr} block (Lemoine et al. 2018).

7.4.2 LMO4 and iLMO4

In search of an off-on switch for cardiomyocytes, we tested next to the chemogenetic an optogenetic approach. I generated a small amount of EHTs to test if 470 nm photostimulation would be able to stop the contractility of LMO4 and iLMO4 cardiomyocyte contractility. The requirements for this strategy were similar to those of the chemogenetic approach:

- Reversibility of the off switch (off-on switch)
- Quick off-on kinetics
- Adequate substrate concentration for in vivo use in the case of CTZ.

We generated LMO4 and iLMO4 EHTs. We first aimed to silence iLMO4 EHTs by applying CTZ. However, although the CTZ application caused EHTs to stop, contractility did not resume, even after several washing steps. We, therefore, focused on the light activation of iLMO4.

LMO4 EHTs could be optically paced up to 5 Hz but did not stop contracting. On the other hand, iLMO4 EHTs stopped contracting almost immediately after exposure to light. Hence, we chose this cell line for further analysis because the mechanism fulfilled all the criteria mentioned above.

LMO4 contains VChR1 as the light-responsive component, while iLMO4 contains iChloC. VChR1 is considered a slow channelrhodopsin with an off-rate of >90 ms (Lin 2011). However, this is still enough to be used for the electrical pacing of cardiomyocytes. On the other hand, iChloC has an off-rate of seconds, meaning that it cannot be used for pacing but is optimal for silencing studies

(Wietek et al. 2015; Wiegert et al. 2017). We could observe this in our EHT experiments. When 470 nm light exposure was terminated, it took around 5 seconds until EHTs started to contract again. Electrical pacing could not evoke contractions during light application. Like PSAM GlyR, we assume that iChloC activation depolarizes the cell via depolarization and possibly shunting.

Cardiomyocyte differentiation efficiency was low in iLMO4 iPSCs. PSAM GlyR differentiation showed a mean efficiency of 0.32 compared to 0.75-1 in control cells. Therefore, the transgene knock-in seems to limit differentiation efficiency.

Also, the development of iLMO4 EHTs was impaired. EHTs developed lower force than control EHTs and had reduced TTP and RT 80%. Over time we realized that the remaining room light affected force in iLMO4 EHTs. From there on, experiments were conducted with as little light contamination as possible. Measures included switching off the room light, covering EHT plates in the incubator with optically opaque lids to reduce light contamination during incubator door opening/ closing, and covering the white box with optically opaque curtains. Diminishing background light exposure could partially reverse the effect on force. Only in batch 3 (green), light contamination was fully avoided, and force development over the first weeks matched control EHTs. Nevertheless, the inherent leakiness of the iLMO4 channel (similar to PSAM GlyR) could explain the reduced force and variable frequencies.

RT and TTP were lower in iLMO4 than in control EHTs. Yet, given the lower force, contraction and relaxation velocity were still lower than in WT EHTs. We found a potential explanation for these effects when measuring the action potentials of these EHTs. iLMO4 EHTs exhibited APs that resemble those of the sinus node. These APs have a slow upstroke, driven by I_f and LTCCs rather than I_{Na}. In addition, the take-off potential was significantly increased in iLMO4 EHTs. The leakiness of iLMO4 could explain this. The reversal potential (E_{rev}) of endogenous chloride-conducting channels is around -33 to -40 mV, similar to the take-off potential of our iLMO4 EHTs (Clemo et al. 1999; Baumgarten et al. 2005). Moreover, this would explain the reduced kinetics and sinus node-like AP shape: At -40 mV, all voltage-gated sodium channels are permanently closed. Hence, the upstroke is slower than in control EHTs, because it is mediated via LTCCs. Whether these findings were due to leakiness of the channel was not analyzed, but the findings clearly indicate leakiness.

iLMO4 EHTs could follow electrical pacing only up to 2.75 Hz, whereas control EHTs usually follow up to 4 Hz. This finding further supports the leakiness of iLMO4. Furthermore, the incapability to be paced reliably above 2.75 Hz has consequences for the ex vivo results discussed later.

iLMO4 EHTs were highly light sensitive. Even 30 ms pulses (during the pilot trial) or light intensity of 0.005 mW/mm^2 under continuous application were enough to stop contractility. In comparison, 0.1 mW/mm^2 was used for GtACR1, and 10 ms pulses were used for pacing (Kopton et al. 2018). In an in vivo study, 0.1 mW/mm^2 was used for the photostimulation of iChloC (Wietek et al. 2015). Most likely, these differences can be explained by the expression level that is likely

higher in our study. We used a consecutively active CAG promoter with a genomically encoded construct, while others used viral transduction.

We later tested the CTZ application more thoroughly. iLMO4 EHTs stopped when CTZ was applied in high concentration (300 µM). However, the effect was inconsistent. Out of three EHTs, only two stopped but only partially regained their baseline force. On the other hand, control EHTs were unaffected by CTZ. Therefore, we hypothesize that CTZ treatment causes a hypoxic state in iLMO4 EHTs because the bioluminescence reaction of luciferase utilizes O_2. Thus, hypoxia may be induced during the light reaction, causing cardiomyocyte death. However, further experiments are necessary to investigate if this holds.

7.5 In Vivo Experiments

After finding two strategies to stop iPSC-derived cardiomyocyte contractility, we aimed to assess their contribution to heart function in vivo. We used a guinea pig model previously established in the Institute of Experimental Pharmacology and Toxicology. Guinea pigs are a preferable animal model for cardiomyocyte transplantation studies because their cardiac physiology more closely resembles humans than any other small animal model. Following previous studies, we injured the left ventricular wall with a liquid N_2-cooled stamp because the high level of collateralization of the coronary arteries hinders ligation (Maxwell et al. 1987; Weinberger et al. 2016; Stüdemann and Weinberger 2021; Querdel et al. 2021). We aimed for a subacute injury model. Hence, seven days after cryoinjury, cells were transplanted, and experiments were finalized four weeks after transplantation (Weinberger et al. 2016; Querdel et al. 2021).

Histologically, we observed comparable scar sizes in all groups and a graft size of 11% across all animals. This is highly similar to recent studies of our group with EHT patches of similar cell dose, which discovered graft sizes of 12% after EHT transplantation, containing $12x10^6$ cardiomyocytes (Breckwoldt et al. 2017; Querdel et al. 2021). Another guinea pig study found only 8.4% remuscularization of the scar area while using five times more cells (Shiba et al. 2012).

We observed a significant reduction of FAC and FS as measures for cardiac function in control and PSAM GlyR animals after injury. Overall, cell transplantation did not result in a functional improvement. Shiba et al. similarly reported stabilization but no improvement of cardiac function by injecting hESC-cardiomyocytes (Shiba et al. 2012). However, the authors used $100x10^6$ cells, five times more than in our approach. In earlier studies of our group, transplantation of an EHT, containing roughly $12x10^6$ cells, led to functional improvement (Weinberger et al. 2016; Querdel et al. 2021). These results hint at more efficient remuscularization of EHTs versus direct cell injection. This seems plausible, considering cell retention in a contracting heart is low when applying a suspension of cells intramyocardially.

Nevertheless, assessment of functional improvement was not the primary goal of this study. Hence, we did not include a control group with cell-free injections or a group where EHTs of the

same cell lines were transplanted. A direct comparison of both routes of transplantation would be desirable in the future.

To assess the contribution of transplanted cardiomyocytes to left ventricular function in vivo, we aimed to stop cardiomyocyte contractility while performing echocardiography. However, as the required PSEM^{89S} concentration to stop cardiomyocytes in vitro was higher than the maximal concentration in mice (Magnus et al. 2011), we first performed a pharmacokinetic study.

7.6 PSEM^{89S} Pharmacokinetics

Intraperitoneal and intravenous injection via the vena saphena resulted in insufficient serum concentrations (c_{max}: 13.8±0.5 µM). Vena jugularis injection, however, resulted in sufficient serum concentrations (in 54.3±0.3 µM). The differences between the vena saphena and jugularis are most likely explained by technical issues. Intravenous injection in guinea pigs is difficult, and we often observed extravasation while injecting into the vena saphena. This can explain the lower concentrations in comparison to vena jugularis injection. Therefore, even though injection in the vena jugularis resulted in sufficient plasma concentrations to stop cardiomyocyte contractility, we decided against an in vivo analysis. This was because the risk of technical failure to reach sufficient serum concentration seemed too high.

Moreover, in vivo assessment of PSAM GlyR cardiomyocyte contribution would be challenging as we could not ensure sufficient PSEM^{89S} concentrations and needed high amounts of the expensive compound PSEM^{89S}. Moreover, echocardiography has high variability. For example, in healthy rats, FS can have a standard deviation of ca. 10% (Zacchigna et al. 2021), meaning that the expected contribution of transplanted cardiomyocytes, which is likely to be smaller than 10%, could be disguised. In addition, echocardiography after two thoracotomies becomes even more challenging and likely has an even higher variability. The combination of these factors led to the decision against an in vivo application.

7.7 Langendorff Assembly

After deciding that in vivo assessment of cardiac function would be very challenging and most likely unsuccessful, we needed another method to assess cardiac function. For this, we used the method of Langendorff heart preparation. Here, the heart is perfused via a cannula in the aorta. Of note, the aortic perfusion is retrograde. However, the coronary arteries are perfused anterograde. There are two variants of the Langendorff perfusion: the constant flow and constant pressure mode. Constant flow mode is advisable for testing vasoactive compounds but less suited for investigating inotropy or chronotropy because the system cannot adapt to changes in the energy demand of the myocardium (Dhein 2005). Hence, as used in our study, the constant pressure mode is best-suited for investigations of the contribution of transplanted cells. The simplest approach uses hydrostatic pressure, created by positioning a tank with the perfusate on a platform above the cannulated heart. We started our experiments with 100 cm (74 mmHg) but lowered the pressure to 70 cm (51 mmHg) to avoid aortic valve incompetence (Curtis et al. 1986;

Dhein 2005). To limit PSEM^{89S} consumption, we used a second smaller tank to supply the hearts with the substrate. However, we observed pressure changes while switching between tanks, caused by the different volumes and, therefore, slightly different heights of the two tanks. This result highlights the sensitivity of the system. Hence, we switched to syringe pumps which allowed us to inject high concentrations of PSEM^{89S} in the perfusate flow above the heart. Here, we were concerned about i) disturbing the system by adding pressure, ii) disturbing the temperature because the syringe pumps cannot be heated, and iii) lower oxygenation because syringes cannot be gassed with Carbogen. Hence, we used a 30x concentration (3 mM, later 1.8 mM) in the syringe pump. This way, we could adjust the flow rate to each heart and minimize disturbing influences because the unheated, unoxygenated solution was diluted to 1/30th of the perfusate flow (3.3%).

Next, we switched from a mouse catheter, typically used for in situ hemodynamic measurements, to a self-built balloon catheter. Since ventricular loading does not occur in the Langendorff heart, isovolumetric contractions are necessary to assess cardiac force development properly. Frequently latex balloons are used, however using non-elastic cling film has several advantages: i) higher conformity to the lumen of the ventricle, ii) higher compliance, and iii) higher flexibility. In addition, cling film balloons can be assembled in various sizes and selected according to the heart size on the spot (Sutherland et al. 2003b).

We observed high rates of ventricular arrhythmia in the isolated guinea pig hearts. Hence, we used lidocaine (170 µM), a well-established sodium-channel blocker, employed as an anti-arrhythmic drug in the clinic and experimentally for muscle preparations (Collinsworth et al. 1974; Vandecasteele et al. 1999). As expected, the use of lidocaine abolished almost all arrhythmic events.

7.8 PSAM GlyR Langendorff

To assess the contribution of PSAM GlyR cardiomyocytes to heart function, we employed the optimized Langendorff system. PSEM^{89S} reduced LVDP and frequency in guinea pig hearts, regardless of injury or cell transplantation. We hypothesized that the negative inotropic effects resulted from the negative chronotropic effects of PSEM^{89S} (force-frequency relationship). The developed force at 5 Hz is halved in guinea pig papillary muscle when reducing frequency to 2 Hz (Wang et al. 1988). We, therefore, electrically paced the hearts. However, the PSEM^{89S} application still exerted a negative inotropic effect. Our second hypothesis was that PSEM^{89S} acts as an agonist on muscarinergic Ach receptors, but atropine (10 µM) could not block the negative inotropic response. Similarly, pancuronium (nAChR antagonist) and hexamethonium 50 µM (nAChR antagonist in ganglia) could not prevent the negative inotropism, excluding these signaling pathways as potential off-targets of PSEM^{89S}.

Considering our in vitro results, where we found an increase in APD upon PSEM^{89S} application, a human E*ther-à-go-go*-Related Gene (hERG) block seemed likely when applying PSEM^{89S} in high

concentration. hERG mediates the inward rectifying rapid component of $I_{Kr,}$ which is responsible for repolarization at the plateau phase of the action potential. A blockade of hERG causes prolongation of the plateau phase, which can cause ventricular arrhythmia (torsades de pointes), potentially leading to syncope, ventricular fibrillation, and sudden cardiac death (Recanatini et al. 2005). Nonspecific hERG blockade has been the leading cause for drug withdrawal from the market in the US (Piccini et al. 2009). In the EHT system, we obtained results fitting this hypothesis, but these will be discussed in the dissertation of Christoph Manthey. Nevertheless, the EHT system is highly sensitive and in vitro results could lead to a different conclusion than results obtained from the Langendorff system. We did not find an increase in relaxation time during $PSEM^{89S}$ application in guinea pig hearts, typical for an I_{Kr} block. However, previous results in guinea pigs show that blocking Ca^{2+} with verapamil or nifedipine can reduce left ventricular pressure and heart rate, which fits our observations (Hauser et al. 2005). Regardless of the mechanism, we could not resolve why $PSEM^{89S}$ evoked a negative inotropic and chronotropic response.

This effect of $PSEM^{89S}$ was unexpected because potential effects on the heart have not been observed in any study so far. Yet, all studies were conducted in the neuroscience field and did not assess heart function. As the potential active contribution of transplanted PSAM GlyR cardiomyocytes to left ventricular function would be heavily confounded by this unexpected $PSEM^{89S}$ effect, we abandoned this strategy and focused on the optogenetic strategy.

7.9 iLMO4 Langendorff

We assessed the left ventricular pressure of iLMO4 and control hearts in the Langendorff system, similar to the PSAM GlyR chemogenetic study. Instead of a chemical substrate, a pE-4000 (coolLED) was used to illuminate the injured left ventricular wall. We found that 470 nm light during spontaneous contractions reduced LVDP by 0.52 mmHg (0.75%) across all iLMO4 animals. In control animals a slight increase of 0.44 mmHg (0.75%) occurred. Looking at individual animals, five out of ten hearts showed a decrease in LVDP, while five remained similar to control hearts.

Interestingly, all hearts that showed a functional reduction demonstrated rather large grafts in the histological analysis. We correlated graft size to the decrease in function and did not find a clear correlation. One explanation might be the number of hearts in this analysis. Even though ten animals are a large number for advanced physiological studies, one outlier (large effect with rather small graft, 5.61%) was sufficient to change an otherwise rather clear correlation. Additionally, other factors such as graft localization (in the scar versus intramyocardial), the degree of connectivity to the host myocardium, and the anatomical localization are factors that most likely will define the degree of functional contribution.

The effect size seems small but realistic. Considering that the left ventricular mass is roughly 60% of the average heart mass (in this study 2.3 g), left ventricular mass equals 1.5 g. With an average scar size of 20%, of which 13% were remuscularized by iLMO4 cardiomyocytes, one can calculate

a graft mass of 40 mg. This accounts for ~3% of the left ventricle mass. Since iPSC-cardiomyocytes are immature, generated force is most likely smaller than host guinea pig cardiomyocytes, potentially impacting the contribution. We also observed swelling of the scar area upon prolonged perfusion, as previously described (Liao et al. 2012). This factor could have negatively impacted engrafted cardiomyocytes, possibly leading to an underestimation of the contribution of grafted cells. Moreover, differences in the cardiac physiology between human and guinea pig cardiomyocytes could influence the results.

No reproducible decline in LVDP was observed upon electrical pacing, and only four hearts dropped in their left ventricular pressure, resulting in an overall not significant effect. But even the slight response in some hearts was weaker than under spontaneous conditions. Electrical pacing was conducted at higher frequencies than the hearts' spontaneous frequency (162±22 bpm vs. 203±23 bpm). Hence, the light effect seems to be frequency-specific. This hypothesis is underlined by our in vitro results showing that iLMO4 EHTs cannot consistently be paced above 2.75 Hz. Therefore, we assume that iLMO4 cardiomyocytes' contribution to LVDP is frequency-dependent and cannot occur at a frequency above the maximal iLMO4 pacing frequency.

No decline of left ventricular pressure was observed during photostimulation with 660 nm light under spontaneous conditions. Application of 660 nm light served as a negative control. None of the hearts showed a decline of LVDP, showing that hearts do not react to light exposure per se. Additionally, iLMO4 cardiomyocyte inactivation is wavelength-specific, as shown in our in vitro experiments.

Upon switching off 470 nm light under spontaneous conditions, we observed recovery by 1.76%. A smaller difference was observed under pacing (1.21%). Upon 660 nm light, a difference of 0.34% was observed. Therefore, also during recovery, the effect of blue light was diminished under pacing. However, hearts recovered from 470 nm to higher LVDP than before light exposure. These results are in concordance with our in vitro results. Here we observed iLMO4 EHT develop higher forces upon recovery from 470 nm light exposure.

We also assessed whether CTZ could be used in the Langendorff system. CTZ application resulted in bright bioluminescence, but unexpectedly we observed a small positive inotropic effect upon CTZ application. This has not been reported in the literature and was not observed in EHTs. Hence, a species-specific effect seems possible. However, as CTZ was not advantageous over direct light application in the Langendorff system, we did not follow up. Nevertheless, CTZ was highly useful to locate iLMO4 cardiomyocytes after grafting in the heart.

7.10 Conclusion and Future Perspectives

In conclusion, I generated four novel iPSC lines employing CRISPR/Cas9 with the aim to differentiate cardiomyocytes with an off-on switch to assess the contribution of transplanted cardiomyocytes to heart function after injury. All four cell lines could be differentiated into

cardiomyocytes. Furthermore, in two of the four cell lines, both expressing an anion channel (PSAM GlyR and iLMO4), contractility could reversibly be stopped either by chemogenetic or optogenetic means. However, the chemogenetic system had substantial limitations for an in vivo and an ex vivo application. In contrast, iLMO4 cardiomyocytes could successfully assess the contribution to left ventricular function after injury in a Langendorff system. With this system, we found for the first time that engrafted cardiomyocytes contribute to cardiac function.

To reach a full understanding of the contribution of hiPSC-cardiomyocytes to heart function, in vivo results are desirable. Unfortunately, unexpected limitations of the two substrates $PSEM^{89S}$ and CTZ, prevented us from obtaining these results by echocardiography. In the future, the primary aim is to acquire in vivo evidence for the direct contribution of hiPSC-cardiomyocytes to cardiac function. To do so, two strategies could be pursued: i) an improved chemogenetic cell line or ii) light application in vivo. Recently, an optimized PSAM GlyR version for in vivo applications has been described: $PSAM^4$ GlyR. Here, the substrate can activate the receptor in nanomolar rather than in micromolar concentrations. Moreover, the substrate for $PSAM^4$ GlyR is varenicline, a clinically approved drug, more likely not to exhibit off-target effects. One could also think of a light application in vivo. Here, open-chest catheterization would allow for light application. Often results obtained in small animal models could not be verified in larger species. Therefore, regardless of the cell lines used, it could be useful to translate these findings to larger animals such as pigs or primates in the future, ultimately aiming to improve the efficacy of this novel therapeutic option for heart failure patients. Overall, the small animal model guinea pig enabled us to mechanistically understand that transplanted cardiomyocytes can contribute to left ventricular function.

8 REFERENCES

AD Instruments (2003) Intraventricular Pressure Measurement in a Langendorff Preparation

Aktories K, Förstermann U, Hofmann F, Starke K (2013) Pharmakologie und Toxikologie, 11th Editi

Alkass K, Panula J, Westman M, et al (2015) No Evidence for Cardiomyocyte Number Expansion in Preadolescent Mice. Cell 163:1026–1036. https://doi.org/10.1016/j.cell.2015.10.035

Anker SD, Coats AJS, Cristian G, et al (2015) A prospective comparison of alginate-hydrogel with standard medical therapy to determine impact on functional capacity and clinical outcomes in patients with advanced heart failure (AUGMENT-HF trial). Eur Heart J 36:2297–2309. https://doi.org/10.1093/eurheartj/ehv259

Arrenberg AB, Stainier DYR, Baier H, Huisken J (2010) Optogenetic control of cardiac function. Science (80-) 330:971–974. https://doi.org/10.1126/science.1195929

Bader D, Oberpriller JO (1978) Repair and reorganization of minced cardiac muscle in the adult newt (Notophthalmus viridescens). J Morphol 155:349–357. https://doi.org/10.1002/jmor.1051550307

Bargehr J, Ong LP, Colzani M, et al (2019) Epicardial cells derived from human embryonic stem cells augment cardiomyocyte-driven heart regeneration. Nat Biotechnol 37:895–906. https://doi.org/10.1038/s41587-019-0197-9

Baumgarten CM, Browe DM, Ren Z (2005) Swelling- and Stretch-activated Chloride Channels in the Heart: Regulation and Function. In: Kamkin A, Kiseleva I (eds) Mechanosensitivity in Cells and Tissues. Moscow: Academia

Bedada FB, Chan SSK, Metzger SK, et al (2014) Acquisition of a quantitative, stoichiometrically conserved ratiometric marker of maturation status in stem cell-derived cardiac myocytes. Stem Cell Reports 3:594–605. https://doi.org/10.1016/j.stemcr.2014.07.012

Berglund K, Birkner E, Augustine GJ, Hochgeschwender U (2013) Light-Emitting Channelrhodopsins for Combined Optogenetic and Chemical-Genetic Control of Neurons. PLoS One 8:e59759. https://doi.org/10.1371/journal.pone.0059759

Bergmann O, Bhardwaj RDD, Bernard S, et al (2009) Evidence for cardiomyocyte renewal in humans. Science 324:98–102. https://doi.org/10.1126/science.1164680

Bergmann O, Zdunek S, Felker A, et al (2015) Dynamics of Cell Generation and Turnover in the Human Heart. Cell 161:1566–1575. https://doi.org/https://doi.org/10.1016/j.cell.2015.05.026

Bhagwan JR, Denning C, Collins E, et al (2020) Variable expression and silencing of CRISPR-Cas9 targeted transgenes identifies the AAVS1 locus as not an entirely safe harbour. F1000Research 8:1911. https://doi.org/10.12688/f1000research.19894.2

Breckwoldt K, Letuffe-Brenière D, Mannhardt I, et al (2017) Differentiation of cardiomyocytes and generation of human engineered heart tissue. Nat Protoc 12:1177–1197.

https://doi.org/10.1038/nprot.2017.033

Bruegmann T, Malan D, Hesse M, et al (2010) Optogenetic control of heart muscle in vitro and in vivo. Nat Methods 7:897–900. https://doi.org/10.1038/nmeth.1512

Bui AL, Horwich TB, Fonarow GC (2011) Epidemiology and risk profile of heart failure. Nat Rev Cardiol 8:30–41. https://doi.org/10.1038/nrcardio.2010.165

Buja LM (2005) Myocardial ischemia and reperfusion injury. Cardiovasc Pathol 14:170–175. https://doi.org/10.1016/J.CARPATH.2005.03.006

Burke AP, Virmani R (2007) Pathophysiology of Acute Myocardial Infarction. Med. Clin. North Am. 91:553–572

Burns SS, Kapur R (2020) Putative Mechanisms Underlying Cardiovascular Disease Associated with Clonal Hematopoiesis of Indeterminate Potential. Stem Cell Reports 15:292–306. https://doi.org/10.1016/j.stemcr.2020.06.021

Burridge PW, Keller G, Gold JD, Wu JC (2012) Production of de novo cardiomyocytes: Human pluripotent stem cell differentiation and direct reprogramming. Cell Stem Cell 10:16–28. https://doi.org/10.1016/j.stem.2011.12.013

Byrne SM, Ortiz L, Mali P, et al (2015) Multi-kilobase homozygous targeted gene replacement in human induced pluripotent stem cells. Nucleic Acids Res 43:e21. https://doi.org/10.1093/NAR/GKU1246

Castro L, Geertz B, Reinsch M, et al (2019) Implantation of hiPSC-derived Cardiac-muscle Patches after Myocardial Injury in a Guinea Pig Model. J Vis Exp. https://doi.org/10.3791/58810

Ceto S, Sekiguchi KJ, Takashima Y, et al (2020) Neural Stem Cell Grafts Form Extensive Synaptic Networks that Integrate with Host Circuits after Spinal Cord Injury. Cell Stem Cell 27:430-440.e5. https://doi.org/10.1016/J.STEM.2020.07.007

Chong JJH, Yang X, Don CW, et al (2014) Human embryonic-stem-cell-derived cardiomyocytes regenerate non-human primate hearts. Nature 510:273–277. https://doi.org/10.1038/nature13233

Christman KL, Vardanian AJ, Fang Q, et al (2004) Injectable fibrin scaffold improves cell transplant survival, reduces infarct expansion, and induces neovasculature formation in ischemic myocardium. J Am Coll Cardiol 44:654–660. https://doi.org/10.1016/j.jacc.2004.04.040

Clauss S, Bleyer C, Schüttler D, et al (2019) Animal models of arrhythmia: classic electrophysiology to genetically modified large animals. Nat Rev Cardiol 16:457–475. https://doi.org/10.1038/s41569-019-0179-0

Clemo HF, Stambler BS, Baumgarten CM (1999) Swelling-activated chloride current is persistently activated in ventricular myocytes from dogs with tachycardia-induced congestive heart failure. Circ Res 84:157–165. https://doi.org/10.1161/01.RES.84.2.157

Collet J-P, Thiele H, Barbato E, et al (2020) 2020 ESC Guidelines for the management of acute coronary syndromes in patients presenting without persistent ST-segment elevation. Eur Heart J. https://doi.org/10.1093/eurheartj/ehaa575

Collinsworth KA, Kalman SM, Harrison DC (1974) The clinical pharmacology of lidocaine as an antiarrhythmic drug. Circulation 50:1217–1230

Curtis MJ, Macleod BA, Tabrizchi R, Walker MJA (1986) An improved perfusion apparatus for small animal hearts. J Pharmacol Methods 15:87–94. https://doi.org/10.1016/0160-5402(86)90008-2

Daadi MM, Klausner JQ, Bajar B, et al (2016) Optogenetic stimulation of neural grafts enhances neurotransmission and downregulates the inflammatory response in experimental stroke model. Cell Transplant 25:1371–1380. https://doi.org/10.3727/096368915X688533

Dai DF, Danoviz ME, Wiczer B, et al (2017) Mitochondrial maturation in human pluripotent stem cell derived cardiomyocytes. Stem Cells Int 2017:. https://doi.org/10.1155/2017/5153625

Dasagrandhi D, R ASK, Muthuswamy A, et al (2018) Ischemia/reperfusion injury in male guinea pigs: An efficient model to investigate myocardial damage in cardiovascular complications. Biomed Pharmacother 99:469–479. https://doi.org/10.1016/j.biopha.2018.01.087

De Silva M, Mihailovic A, Baron Toaldo M (2020) Two-dimensional, M-mode, and Doppler echocardiography in 22 conscious and apparently healthy pet guinea pigs. J Vet Cardiol 27:54–61. https://doi.org/10.1016/j.jvc.2020.01.004

Dell'Anno MT, Caiazzo M, Leo D, et al (2014) Remote control of induced dopaminergic neurons in parkinsonian rats. J Clin Invest 124:3215–3229. https://doi.org/10.1172/JCI74664

Deng C, Capecchi MR (1992) Reexamination of Gene Targeting Frequency as a Function of the Extent of Homology between the Targeting Vector and the Target Locus. Mol Cell Biol 12:3365–3371

Denning C, Borgdorff V, Crutchley J, et al (2016) Cardiomyocytes from human pluripotent stem cells: From laboratory curiosity to industrial biomedical platform. Biochim Biophys Acta - Mol Cell Res 1863:1728–1748. https://doi.org/10.1016/j.bbamcr.2015.10.014

Deutsche Stiftung Organtransplantation (2021) Jahresbericht Organspende und Transplantation in Deutschland 2020

DeWood MA, Spores J, Notske R, et al (1980) Prevalence of total coronary occlusion during the early hours of transmural myocardial infarction. N Engl J Med 303:897–902. https://doi.org/10.1056/NEJM198010163031601

Dhein S (2005) The langendorff heart. In: Practical Methods in Cardiovascular Research. pp 155–172

Dobaczewski M, Gonzalez-Quesada C, Frangogiannis NG (2010) The extracellular matrix as a modulator of the inflammatory and reparative response following myocardial infarction. J Mol Cell Cardiol 48:504–511. https://doi.org/10.1016/J.YJMCC.2009.07.015

Docherty KF, Vaduganathan M, Solomon SD, McMurray JJV (2020) Sacubitril/Valsartan: Neprilysin Inhibition 5 Years After PARADIGM-HF. JACC Hear Fail 8:800–810. https://doi.org/10.1016/J.JCHF.2020.06.020

Doudna JA, Charpentier E (2014) The new frontier of genome engineering with CRISPR-Cas9. Science (80-) 346:. https://doi.org/10.1126/SCIENCE.1258096

Eschenhagen T, Bolli R, Braun T, et al (2017) Cardiomyocyte regeneration: A consensus statement. Circulation 136:680–686. https://doi.org/10.1161/CIRCULATIONAHA.117.029343

Eschenhagen T, Didié M, Münzel F, et al (2002) 3D engineered heart tissue for replacement therapy. Basic Res Cardiol Suppl 97:. https://doi.org/10.1016/s1053-2498(01)00732-x

Eschenhagen T, Fink C, Remmers U, et al (1997) Three-dimensional reconstitution of embryonic cardiomyocytes in a collagen matrix: a new heart muscle model system. FASEB J 11:683–94. https://doi.org/10.1096/fasebj.11.8.9240969

Fan C, Fast VG, Tang Y, et al (2019) Cardiomyocytes from CCND2-overexpressing human induced-pluripotent stem cells repopulate the myocardial scar in mice: A 6-month study. J Mol Cell Cardiol 137:25–33. https://doi.org/10.1016/j.yjmcc.2019.09.011

Fan C, Tang Y, Zhao M, et al (2020) CHIR99021 and fibroblast growth factor 1 enhance the regenerative potency of human cardiac muscle patch after myocardial infarction in mice. J Mol Cell Cardiol 141:1–10. https://doi.org/10.1016/j.yjmcc.2020.03.003

Fenske S, Hennis K, Rötzer RD, et al (2020) cAMP-dependent regulation of HCN4 controls the tonic entrainment process in sinoatrial node pacemaker cells. Nat Commun 11:5555. https://doi.org/10.1038/s41467-020-19304-9

Fu X, Khalil H, Kanisicak O, et al (2018) Specialized fibroblast differentiated states underlie scar formation in the infarcted mouse heart. J Clin Invest 128:2127–2143. https://doi.org/10.1172/JCI98215

Fuchs M, Schibilsky D, Zeh W, et al (2019) Does the heart transplant have a future? Eur J Cardio-thoracic Surg 55:I38–I48. https://doi.org/10.1093/ejcts/ezz107

Fusaki N, Ban H, Nishiyama A, et al (2009) Efficient induction of transgene-free human pluripotent stem cells using a vector based on Sendai virus, an RNA virus that does not integrate into the host genome. Proc Japan Acad Ser B Phys Biol Sci 85:348–362. https://doi.org/10.2183/pjab.85.348

Gerbin KA, Mitzelfelt KA, Guan X, et al (2020) Delta-1 Functionalized Hydrogel Promotes hESC-Cardiomyocyte Graft Proliferation and Maintains Heart Function Post-Injury. Mol Ther - Methods Clin Dev 17:986–998. https://doi.org/10.1016/j.omtm.2020.04.011

Gerbin KA, Yang X, Murry CE, Coulombe KLK (2015) Enhanced Electrical Integration of Engineered Human Myocardium via Intramyocardial versus Epicardial Delivery in Infarcted Rat Hearts. PLoS One 10:e0131446. https://doi.org/10.1371/journal.pone.0131446

Ginks WR, Sybers HD, Maroko PR, et al (1972) Coronary Artery Reperfusion: II. Reduction of

Myocardial Infarct Siz at 1 Week After the Coronary Occlusion. J Clin Invest 51:2717–2723. https://doi.org/10.1172/JCI107091

Govorunova EG, Cunha SR, Sineshchekov OA, Spudich JL (2016) Anion channelrhodopsins for inhibitory cardiac optogenetics. Sci Reports 2016 61 6:1–7. https://doi.org/10.1038/srep33530

Govorunova EG, Sineshchekov OA, Janz R, et al (2015) Natural light-gated anion channels: A family of microbial rhodopsins for advanced optogenetics. Science (80-) 349:647–650. https://doi.org/10.1126/science.aaa7484

Grant AO (2009) Cardiac ion channels. Circ. Arrhythmia Electrophysiol. 2:185–194

Guo Q, Ma-Edmonds M, Mintier G, et al (2018) 'Cold shock' increases the frequency of homology directed repair gene editing in induced pluripotent stem cells. Sci Rep 8:1–11. https://doi.org/10.1038/s41598-018-20358-5

Hansen A, Eder A, Bönstrup M, et al (2010) Development of a drug screening platform based on engineered heart tissue. Circ Res 107:35–44. https://doi.org/10.1161/CIRCRESAHA.109.211458

Harris DA, Das AM (1991) Control of mitochondrial ATP synthesis in the heart. Biochem J 280:561. https://doi.org/10.1042/BJ2800561

Haubner BJ, Schneider J, Schweigmann U, et al (2016) Functional Recovery of a Human Neonatal Heart after Severe Myocardial Infarction. Circ Res 118:216–221. https://doi.org/10.1161/CIRCRESAHA.115.307017

Hauser DS, Stade M, Schmidt A, Hanauer G (2005) Cardiovascular parameters in anaesthetized guinea pigs: A safety pharmacology screening model. J Pharmacol Toxicol Methods 52:106–114. https://doi.org/10.1016/j.vascn.2005.03.003

He L, Han M, Zhang Z, et al (2019) Reassessment of c-Kit+ Cells for Cardiomyocyte Contribution in Adult Heart. Circulation 140:164–166. https://doi.org/10.1161/CIRCULATIONAHA.119.039909

Heatley JJ (2009) Cardiovascular Anatomy, Physiology, and Disease of Rodents and Small Exotic Mammals. Vet Clin North Am Exot Anim Pract 12:99–113. https://doi.org/10.1016/j.cvex.2008.08.006

Heidenreich PA, Albert NM, Allen LA, et al (2013) Forecasting the impact of heart failure in the united states a policy statement from the american heart association. Circ Hear Fail 6:606–619. https://doi.org/10.1161/HHF.0b013e318291329a

Herron TJ, Rocha AM Da, Campbell KF, et al (2016) Extracellular Matrix-Mediated Maturation of Human Pluripotent Stem Cell-Derived Cardiac Monolayer Structure and Electrophysiological Function. Circ Arrhythm Electrophysiol 9:e003638. https://doi.org/10.1161/CIRCEP.113.003638

Heusch G (2019) Myocardial ischemia: Lack of coronary blood flow, myocardial oxygen supply-demand imbalance, or what? Am J Physiol - Hear Circ Physiol 316:H1439–H1446.

https://doi.org/10.1152/ajpheart.00139.2019

Himmel HM, Bussek A, Hoffmann M, et al (2012) Field and action potential recordings in heart slices: correlation with established in vitro and in vivo models. 276 Br J Pharmacol 166:276–296. https://doi.org/10.1111/j.1476-5381.2011.01775.x

Hockemeyer D, Wang H, Kiani S, et al (2011) Genetic engineering of human pluripotent cells using TALE nucleases. Nat Biotechnol 2011 298 29:731–734. https://doi.org/10.1038/nbt.1927

Hong SG, Yada RC, Choi K, et al (2017) Rhesus iPSC Safe Harbor Gene-Editing Platform for Stable Expression of Transgenes in Differentiated Cells of All Germ Layers. Mol Ther 25:44–53. https://doi.org/10.1016/j.ymthe.2016.10.007

Horikoshi Y, Yan Y, Terashvili M, et al (2019) Fatty Acid-Treated Induced Pluripotent Stem Cell-Derived Human Cardiomyocytes Exhibit Adult Cardiomyocyte-Like Energy Metabolism Phenotypes. Cells 8:1095. https://doi.org/10.3390/cells8091095

Hume JR, Ueharat A (1985) Ionic basis of the different action potential configurations of single guinea-pig atrial and ventricular myocytes

Hwang HS, Kryshtal DO, Feaster TK, et al (2015) Comparable calcium handling of human iPSC-derived cardiomyocytes generated by multiple laboratories. J Mol Cell Cardiol 85:79–88. https://doi.org/10.1016/J.YJMCC.2015.05.003

Ibáñez B, Heusch G, Ovize M, Van De Werf F (2015) Evolving therapies for myocardial ischemia/reperfusion injury. J Am Coll Cardiol 65:1454–1471. https://doi.org/10.1016/j.jacc.2015.02.032

Ibanez B, James S, Agewall S, et al (2018) 2017 ESC Guidelines for the management of acute myocardial infarction in patients presenting with ST-segment elevation. Eur. Heart J. 39:119–177

Iorga B, Schwanke K, Weber N, et al (2018) Differences in contractile function of myofibrils within human embryonic stem cell-derived cardiomyocytes vs. Adult ventricular myofibrils are related to distinct sarcomeric protein isoforms. Front Physiol 8:. https://doi.org/10.3389/fphys.2017.01111

Ishizuka T, Masaaki K, Araki R, Yawo H (2006) Kinetic evaluation of photosensitivity in genetically engineered neurons expressing green algae light-gated channels. Neurosci Res 54:85–94. https://doi.org/10.1016/j.neures.2005.10.009

Jaiswal S, Natarajan P, Silver AJ, et al (2017) Clonal Hematopoiesis and Risk of Atherosclerotic Cardiovascular Disease. N Engl J Med 377:111–121. https://doi.org/10.1056/nejmoa1701719

Jennings RB (2013) Historical perspective on the pathology of myocardial ischemia/reperfusion injury. Circ Res 113:428–438. https://doi.org/10.1161/CIRCRESAHA.113.300987

Ji B, Kaneko H, Minamimoto T, et al (2016) Multimodal imaging for DREADD-expressing neurons in living brain and their application to implantation of iPSC-derived neural progenitors. J

Neurosci 36:11544–11558. https://doi.org/10.1523/JNEUROSCI.1279-16.2016

Jolly SR, Kane WJ, Hook BG, et al (1986) Reduction of myocardial infarct size by neutrophil depletion: Effect of duration of occlusion. Am Heart J 112:682–690. https://doi.org/10.1016/0002-8703(86)90461-8

Kääb S, Näbauer M (2001) Diversity of ion channel expression in health and disease. Eur Hear Journal, Suppl 3:31–40. https://doi.org/10.1016/S1520-765X(01)90004-5

Kågström J, Sjögren EL, Ericson AC (2007) Evaluation of the guinea pig monophasic action potential (MAP) assay in predicting drug-induced delay of ventricular repolarisation using 12 clinically documented drugs. J Pharmacol Toxicol Methods 56:186–193. https://doi.org/10.1016/j.vascn.2007.03.003

Kallas A, Pook M, Maimets M, et al (2011) Nocodazole treatment decreases expression of pluripotency markers nanog and Oct4 in human embryonic stem cells. PLoS One 6:e19114. https://doi.org/10.1371/journal.pone.0019114

Kamakura T, Makiyama T, Sasaki K, et al (2013) Ultrastructural maturation of human-induced pluripotent stem cell-derived cardiomyocytes in a long-term culture. Circ J 77:1307–1314. https://doi.org/10.1253/circj.CJ-12-0987

Karbassi E, Fenix A, Marchiano S, et al (2020) Cardiomyocyte maturation: advances in knowledge and implications for regenerative medicine. Nat Rev Cardiol 17:341–359. https://doi.org/10.1038/s41569-019-0331-x

Kehat I, Kenyagin-Karsenti D, Snir M, et al (2001) Human embryonic stem cells can differentiate into myocytes with structural and functional properties of cardiomyocytes. J Clin Invest 108:407–414. https://doi.org/10.1172/JCI12131

Kim S, Kim D, Cho SW, et al (2014) Highly efficient RNA-guided genome editing in human cells via delivery of purified Cas9 ribonucleoproteins. Genome Res 24:1012–1019. https://doi.org/10.1101/gr.171322.113

Kimura W, Xiao F, Canseco DC, et al (2015) Hypoxia fate mapping identifies cycling cardiomyocytes in the adult heart. Nature 523:226–230. https://doi.org/10.1038/nature14582

Kopton RA, Baillie JS, Rafferty SA, et al (2018) Cardiac Electrophysiological Effects of Light-Activated Chloride Channels. Front Physiol 9:1806. https://doi.org/10.3389/fphys.2018.01806

Kotin RM, Linden RM, Berns KI (1992) Characterization of a preferred site on human chromosome 19q for integration of adeno-associated virus DNA by non-homologous recombination. EMBO J 11:5071–5078. https://doi.org/10.1002/j.1460-2075.1992.tb05614.x

Krause T (2021) Repolarisation of human induced pluripotent stem cell cardiomyocytes in engineered heart tissue. A systematic comparison to human adult cardiac tissue.

Laflamme MA, Chen KY, Naumova A V, et al (2007) Cardiomyocytes derived from human

embryonic stem cells in pro-survival factors enhance function of infarcted rat hearts. Nat Biotechnol 25:1015–1024. https://doi.org/10.1038/nbt1327

Laflamme MA, Gold J, Xu C, et al (2005) Formation of human myocardium in the rat heart from human embryonic stem cells. Am J Pathol 167:663–671. https://doi.org/10.1016/S0002-9440(10)62041-X

Lancaster JJ, Sanchez P, Repetti GG, et al (2019) Human Induced Pluripotent Stem Cell–Derived Cardiomyocyte Patch in Rats With Heart Failure. Ann Thorac Surg 108:1169–1177. https://doi.org/10.1016/j.athoracsur.2019.03.099

Lemme M, Braren I, Prondzynski M, et al (2020) Chronic intermittent tachypacing by an optogenetic approach induces arrhythmia vulnerability in human engineered heart tissue. Cardiovasc Res 116:1487–1499. https://doi.org/10.1093/cvr/cvz245

Lemoine MD, Krause T, Koivumäki JT, et al (2018) Human Induced Pluripotent Stem Cell-Derived Engineered Heart Tissue as a Sensitive Test System for QT Prolongation and Arrhythmic Triggers. Circ Arrhythmia Electrophysiol 11:. https://doi.org/10.1161/CIRCEP.117.006035

Lemoine MD, Mannhardt I, Breckwoldt K, et al (2017) Human iPSC-derived cardiomyocytes cultured in 3D engineered heart tissue show physiological upstroke velocity and sodium current density. Sci Rep 7:. https://doi.org/10.1038/s41598-017-05600-w

Levy D, Kannel WB (1988) Cardiovascular risks: New insights from Framingham. Am Heart J 116:266–272. https://doi.org/10.1016/0002-8703(88)90099-3

Levy WC, Mozaffarian D, Linker DT, et al (2006) The Seattle Heart Failure Model: Prediction of survival in heart failure. Circulation 113:1424–1433. https://doi.org/10.1161/CIRCULATIONAHA.105.584102

Li RK, Mickle DAG, Weisel RD, et al (1996) Human pediatric and adult ventricular cardiomyocytes in culture: Assessment of phenotypic changes with passaging. Cardiovasc Res 32:362–373. https://doi.org/10.1016/0008-6363(96)00079-X

Liang X, Potter J, Kumar S, et al (2015) Rapid and highly efficient mammalian cell engineering via Cas9 protein transfection. J Biotechnol 208:44–53. https://doi.org/10.1016/J.JBIOTEC.2015.04.024

Liao R, Podesser BK, Lim CC (2012) The continuing evolution of the Langendorff and ejecting murine heart: new advances in cardiac phenotyping. Am J Physiol Heart Circ Physiol 303:H156-67. https://doi.org/10.1152/ajpheart.00333.2012

Libby P, Bonow RO, Mann DL, Zipes DP (2008) Braunwald´s Heart Disease, 8th Editio. Saunders Elsevier

Liehn EA, Merx MW, Postea O, et al (2008) Ccr1 deficiency reduces inflammatory remodelling and preserves left ventricular function after myocardial infarction. J Cell Mol Med 12:496–506. https://doi.org/10.1111/J.1582-4934.2007.00194.X

Liehn EA, Postea O, Curaj A, Marx N (2011) Repair After Myocardial Infarction, Between Fantasy and Reality: The Role of Chemokines. J Am Coll Cardiol 58:2357–2362.

https://doi.org/10.1016/J.JACC.2011.08.034

Lin JY (2011) A user's guide to channelrhodopsin variants: Features, limitations and future developments. Exp Physiol 96:19–25. https://doi.org/10.1113/expphysiol.2009.051961

Lin JY, Lin MZ, Steinbach P, Tsien RY (2009) Characterization of Engineered Channelrhodopsin Variants with Improved Properties and Kinetics. Biophys J 96:1803–1814. https://doi.org/10.1016/J.BPJ.2008.11.034

Lin S, Staahl BT, Alla RK, Doudna JA (2014) Enhanced homology-directed human genome engineering by controlled timing of CRISPR/Cas9 delivery. Elife 3:e04766. https://doi.org/10.7554/eLife.04766

Lindberg E, Mizukami S, Ibata K, et al (2013) Development of luminescent coelenterazine derivatives activatable by β-galactosidase for monitoring dual gene expression. Chem - A Eur J 19:14970–14976. https://doi.org/10.1002/chem.201302002

Lindsey ML, Bolli R, Canty JM, et al (2018) Guidelines for experimental models of myocardial ischemia and infarction. Am J Physiol - Hear Circ Physiol 314:H812–H838. https://doi.org/10.1152/ajpheart.00335.2017

Linke WA (2018) Titin Gene and Protein Functions in Passive and Active Muscle. Annu Rev Physiol 80:389–411. https://doi.org/10.1146/annurev-physiol-021317-121234

Liu C, Zhang L, Liu H, Cheng K (2017) Delivery strategies of the CRISPR-Cas9 gene-editing system for therapeutic applications. J Control Release 266:17–26. https://doi.org/10.1016/j.jconrel.2017.09.012

Liu YW, Chen B, Yang X, et al (2018) Human embryonic stem cell–derived cardiomyocytes restore function in infarcted hearts of non-human primates. Nat Biotechnol 36:597–605. https://doi.org/10.1038/nbt.4162

Lopaschuk GD, Jaswal JS (2010) Energy metabolic phenotype of the cardiomyocyte during development, differentiation, and postnatal maturation. J Cardiovasc Pharmacol 56:130–140. https://doi.org/10.1097/FJC.0b013e3181e74a14

Lopaschuk GD, Spafford MA, Marsh DR (1991) Glycolysis is predominant source of myocardial ATP production immediately after birth. Am J Physiol - Hear Circ Physiol 261:. https://doi.org/10.1152/ajpheart.1991.261.6.h1698

Louch WE, Koivumäki JT, Tavi P (2015) Calcium signalling in developing cardiomyocytes: implications for model systems and disease. J Physiol 593:1047–1063. https://doi.org/10.1113/JPHYSIOL.2014.274712

Lund LH, Edwards LB, Kucheryavaya AY, et al (2015) The Registry of the International Society for Heart and Lung Transplantation: Thirty-second Official Adult Heart Transplantation Report - 2015; Focus Theme: Early Graft Failure. J Hear Lung Transplant 34:1244–1254. https://doi.org/10.1016/j.healun.2015.08.003

Lundy SD, Zhu WZ, Regnier M, Laflamme MA (2013) Structural and functional maturation of cardiomyocytes derived from human pluripotent stem cells. Stem Cells Dev 22:1991–2002.

https://doi.org/10.1089/scd.2012.0490

Luo Y, Liu C, Cerbini T, et al (2014) Stable Enhanced Green Fluorescent Protein Expression After Differentiation and Transplantation of Reporter Human Induced Pluripotent Stem Cells Generated by AAVS1 Transcription Activator-Like Effector Nucleases. Stem Cells Transl Med 3:821–835. https://doi.org/10.5966/sctm.2013-0212

Ma J, Guo L, Fiene SJ, et al (2011) High purity human-induced pluripotent stem cell-derived cardiomyocytes: electrophysiological properties of action potentials and ionic currents. Am J Physiol Hear Circ Physiol 301:H2006. https://doi.org/doi:10.1152/ajpheart.00694.2011

Magnus CJ, Lee PH, Atasoy D, et al (2011) Chemical and genetic engineering of selective ion channel-ligand interactions. Science (80-) 333:1292–1296. https://doi.org/10.1126/science.1206606

Magnus CJ, Lee PH, Bonaventura J, et al (2019) Ultrapotent chemogenetics for research and potential clinical applications. Science eaav5282. https://doi.org/10.1126/science.aav5282

Mali P, Yang L, Esvelt KM, et al (2013) RNA-guided human genome engineering via Cas9. Science 339:823–6. https://doi.org/10.1126/science.1232033

Mann DL, Felker GM (1999) Mechanisms and Models in Heart Failure: A Translational Approach. Circ Res 100:999–10:1435–1450. https://doi.org/10.1161/CIRCRESAHA.121.318158

Mannhardt I, Breckwoldt K, Letuffe-Brenière D, et al (2016) Human Engineered Heart Tissue: Analysis of Contractile Force. Stem Cell Reports 7:29–42. https://doi.org/10.1016/j.stemcr.2016.04.011

Mannhardt I, Saleem U, Mosqueira D, et al (2020) Comparison of 10 Control hPSC Lines for Drug Screening in an Engineered Heart Tissue Format. Stem Cell Reports 15:983–998. https://doi.org/10.1016/j.stemcr.2020.09.002

Marks L, Borland S, Philp K, et al (2012) The role of the anaesthetised guinea-pig in the preclinical cardiac safety evaluation of drug candidate compounds. Toxicol Appl Pharmacol 263:171–183. https://doi.org/10.1016/j.taap.2012.06.007

Mattapally S, Zhu W, Fast VG, et al (2018) Spheroids of cardiomyocytes derived from human-induced pluripotent stem cells improve recovery from myocardial injury in mice. Am J Physiol Hear Circ Physiol 315:327–339. https://doi.org/10.1152/ajpheart.00688.2017.-The

Maxwell MP, Hearse DJ, Yellon DM (1987) Species variation in the coronary collateral circulation during regional myocardial ischaemia: A critical determinant of the rate of evolution and extent of myocardial infarction. Cardiovasc Res 21:737–746. https://doi.org/10.1093/cvr/21.10.737

McCain ML, Parker KK (2011) Mechanotransduction: the role of mechanical stress, myocyte shape, and cytoskeletal architecture on cardiac function. Pflügers Arch - Eur J Physiol 2011 4621 462:89–104. https://doi.org/10.1007/S00424-011-0951-4

Miragoli M, Gaudesius G, Rohr S (2006) Electrotonic modulation of cardiac impulse conduction by myofibroblasts. Circ Res 98:801–810.

https://doi.org/10.1161/01.RES.0000214537.44195.a3

Mishra V, Fiane AE, Winsnes BA, et al (2017) Cardiac replacement therapies: outcomes and costs for heart transplantation versus circulatory assist. Scand Cardiovasc J 51:1–7. https://doi.org/10.1080/14017431.2016.1196826

Miura T, Yellon DM, Hearse DJ, Downey JM (1987) Determinants of infarct size during permanent occlusion of a coronary artery in the closed chest dog. J Am Coll Cardiol 9:647–654. https://doi.org/10.1016/S0735-1097(87)80060-8

Mollova M, Bersell K, Walsh S, et al (2013) Cardiomyocyte proliferation contributes to heart growth in young humans. Proc Natl Acad Sci U S A 110:1446–1451. https://doi.org/10.1073/pnas.1214608110

Morgan JA, Nemeh HW, Paone G (2014) Should Left Ventricular Assist Devices be Implanted in Patients Seventy Years of Age and Older: A Comparative Analysis. Heart Surg Forum 17:182. https://doi.org/10.1532/HSF98.2014386

Mummery C, Oostwaard DW, Doevendans P, et al (2003) Differentiation of Human Embryonic Stem Cells to Cardiomyocytes. Circulation 107:2733–2740. https://doi.org/10.1161/01.CIR.0000068356.38592.68

Munarin F, Kant RJ, Rupert CE, et al (2020) Engineered human myocardium with local release of angiogenic proteins improves vascularization and cardiac function in injured rat hearts. Biomaterials 251:120033. https://doi.org/10.1016/j.biomaterials.2020.120033

Musunuru K, Sheikh F, Gupta RM, et al (2018) Induced Pluripotent Stem Cells for Cardiovascular Disease Modeling and Precision Medicine: A Scientific Statement From the American Heart Association. Circ Genomic Precis Med 11:e000043. https://doi.org/10.1161/HCG.0000000000000043

Nagel G, Brauner M, Liewald JF, et al (2005) Light activation of Channelrhodopsin-2 in excitable cells of caenorhabditis elegans triggers rapid behavioral responses. Curr Biol 15:2279–2284. https://doi.org/10.1016/j.cub.2005.11.032

Nagel G, Ollig D, Fuhrmann M, et al (2002) Channelrhodopsin-1: A light-gated proton channel in green algae. Science (80-) 296:2395–2398. https://doi.org/10.1126/science.1072068

Nagel G, Szellas T, Huhn W, et al (2003) Channelrhodopsin-2, a directly light-gated cation-selective membrane channel. Proc Natl Acad Sci U S A 100:13940–13945. https://doi.org/10.1073/pnas.1936192100

Nakamura M, Sadoshima J (2018) Mechanisms of physiological and pathological cardiac hypertrophy. Nat Rev Cardiol 15:387–407. https://doi.org/10.1038/s41569-018-0007-y

Naldini L, Blömer U, Gallay P, et al (1996) In vivo gene delivery and stable transduction of nondividing cells by a lentiviral vector. Science (80-) 272:263–267. https://doi.org/10.1126/SCIENCE.272.5259.263

NIH (2021) pubmed.ncbi.nlm.nih.gov. https://pubmed.ncbi.nlm.nih.gov/?term=iPSC differentiation protocol&sort=date&ac=yes

Oceguera-Yanez F, Kim S Il, Matsumoto T, et al (2016) Engineering the AAVS1 locus for consistent and scalable transgene expression in human iPSCs and their differentiated derivatives. Methods 101:43–55. https://doi.org/10.1016/j.ymeth.2015.12.012

Ogata T, Kozuka T, Kanda T (2003) Identification of an Insulator in AAVS1, a Preferred Region for Integration of Adeno-Associated Virus DNA. J Virol 77:9000. https://doi.org/10.1128/JVI.77.16.9000-9007.2003

Packer M, Anker SD, Butler J, et al (2020) Cardiovascular and Renal Outcomes with Empagliflozin in Heart Failure. N Engl J Med 383:1413–1424. https://doi.org/10.1056/nejmoa2022190

Page DL, Caulfield JB, Kastor JA, et al (1971) Myocardial Changes Associated with Cardiogenic Shock. N Engl J Med 285:133–137. https://doi.org/10.1056/nejm197107152850301

Park SY, Song S-H, Palmateer B, et al (2017) Novel luciferase-opsin combinations for improved luminopsins. J Neurosci Res. https://doi.org/10.1002/jnr.24152

Pecha S, Yorgan K, Röhl M, et al (2019) Human iPS cell-derived engineered heart tissue does not affect ventricular arrhythmias in a guinea pig cryo-injury model. Sci Rep 9:9831. https://doi.org/10.1038/s41598-019-46409-z

Piccini JP, Whellan DJ, Berridge BR, et al (2009) Current challenges in the evaluation of cardiac safety during drug development: Translational medicine meets the Critical Path Initiative. Am Heart J 158:317–326. https://doi.org/10.1016/j.ahj.2009.06.007

Piquereau J, Caffin F, Novotova M, et al (2013) Mitochondrial dynamics in the adult cardiomyocytes: Which roles for a highly specialized cell? Front Physiol 4:102. https://doi.org/10.3389/fphys.2013.00102

Ponikowski P, Anker SD, AlHabib KF, et al (2014) Heart failure: preventing disease and death worldwide. ESC Hear Fail 1:4–25. https://doi.org/10.1002/ehf2.12005

Ponikowski P, Voors AA, Anker SD, et al (2016) 2016 ESC Guidelines for the diagnosis and treatment of acute and chronic heart failure: The Task Force for the diagnosis and treatment of acute and chronic heart failure of the European Society of Cardiology (ESC)Developed with the special contribution of. Eur Heart J 37:2129–2200. https://doi.org/10.1093/eurheartj/ehw128

Porrello ER, Mahmoud AI, Simpson E, et al (2011) Transient regenerative potential of the neonatal mouse heart. Science (80-) 331:1078–1080. https://doi.org/10.1126/science.1200708

Prondzynski M, Lemoine MD, Zech AT, et al (2019) Disease modeling of a mutation in α-actinin 2 guides clinical therapy in hypertrophic cardiomyopathy. EMBO Mol Med 11:. https://doi.org/10.15252/emmm.201911115

Qian K, Huang CL, Chen H, et al (2014) A simple and efficient system for regulating gene expression in human pluripotent stem cells and derivatives. Stem Cells 32:1230–1238. https://doi.org/10.1002/stem.1653

Querdel E, Reinsch M, Castro L, et al (2021) Human Engineered Heart Tissue Patches

Remuscularize the Injured Heart in a Dose-Dependent Manner. Circulation 143:1991–2006. https://doi.org/10.1161/CIRCULATIONAHA.120.047904

Rajamohan D, Matsa E, Kalra S, et al (2013) Current status of drug screening and disease modelling in human pluripotent stem cells. BioEssays 35:281–298. https://doi.org/10.1002/bies.201200053

Ran FA, Hsu PD, Wright J, et al (2013) Genome engineering using the CRISPR-Cas9 system. Nat Protoc 8:2281. https://doi.org/10.1038/NPROT.2013.143

Recanatini M, Poluzzi E, Masetti M, et al (2005) QT prolongation through hERG K+ channel blockade: Current knowledge and strategies for the early prediction during drug development. Med Res Rev 25:133–166. https://doi.org/10.1002/med.20019

Reed GW, Rossi JE, Cannon CP (2017) Acute myocardial infarction. Lancet 389:197–210. https://doi.org/10.1016/S0140-6736(16)30677-8

Reimer KA, Jennings RB (1979) The "wavefront phenomenon" of myocardial ischemic cell death. II. Transmural progression of necrosis within the framework of ischemic bed size (myocardium at risk) and collateral flow. Lab Investig 40:633–644

Reimer KA, Lowe JE, Rasmussen MM, Jennings RB (1977) The wavefront phenomenon of ischemic cell death. 1. Myocardial infarct size vs duration of coronary occlusion in dogs. Circulation 56:786–794. https://doi.org/10.1161/01.CIR.56.5.786

Ribeiro MC, Tertoolen LG, Guadix JA, et al (2015) Functional maturation of human pluripotent stem cell derived cardiomyocytes in vitro – Correlation between contraction force and electrophysiology. Biomaterials 51:138–150. https://doi.org/10.1016/J.BIOMATERIALS.2015.01.067

Riegler J, Tiburcy M, Ebert A, et al (2015) Human Engineered Heart Muscles Engraft and Survive Long Term in a Rodent Myocardial Infarction Model. Circ Res 117:720–730. https://doi.org/10.1161/CIRCRESAHA.115.306985

Roberts B, Haupt A, Tucker A, et al (2017) Systematic gene tagging using CRISPR/Cas9 in human stem cells to illuminate cell organization. Mol Biol Cell 28:2854–2874. https://doi.org/10.1091/mbc.E17-03-0209

Rockey DC, Bell PD, Hill JA (2015) Fibrosis — A Common Pathway to Organ Injury and Failure. N Engl J Med 372:1138–1149. https://doi.org/10.1056/NEJMra1300575

Romagnuolo R, Masoudpour H, Porta-Sánchez A, et al (2019) Human Embryonic Stem Cell-Derived Cardiomyocytes Regenerate the Infarcted Pig Heart but Induce Ventricular Tachyarrhythmias. Stem Cell Reports 12:967–981

Ronaldson-Bouchard K, Ma SP, Yeager K, et al (2018) Advanced maturation of human cardiac tissue grown from pluripotent stem cells. Nature 556:239–243. https://doi.org/10.1038/s41586-018-0016-3

Roth GAA, Mensah GAA, Johnson COO, et al (2020) Global Burden of Cardiovascular Diseases and Risk Factors, 1990-2019: Update From the GBD 2019 Study. J Am Coll Cardiol 76:2982–

3021. https://doi.org/10.1016/j.jacc.2020.11.010

Sabbah HN, Wang M, Gupta RC, et al (2013) Augmentation of left ventricular wall thickness with alginate hydrogel implants improves left ventricular function and prevents progressive remodeling in dogs with chronic heart failure. JACC Hear Fail 1:252–258. https://doi.org/10.1016/j.jchf.2013.02.006

Salameh A, Wustmann A, Karl S, et al (2010) Cyclic Mechanical Stretch Induces Cardiomyocyte Orientation and Polarization of the Gap Junction Protein Connexin43. Circ Res 106:1592–1602. https://doi.org/10.1161/CIRCRESAHA.109.214429

Saleem U, Meer BJV, Katili PA, et al (2020) Blinded, Multicenter Evaluation of Drug-induced Changes in Contractility Using Human-induced Pluripotent Stem Cell-derived Cardiomyocytes. Toxicol Sci 176:103–123. https://doi.org/10.1093/toxsci/kfaa058

Satin J, Itzhaki I, Rapoport S, et al (2008) Calcium Handling in Human Embryonic Stem Cell-Derived Cardiomyocytes. Stem Cells 26:1961–1972. https://doi.org/10.1634/stemcells.2007-0591

Satin J, Kehat I, Caspi O, et al (2004) Mechanism of spontaneous excitability in human embryonic stem cell derived cardiomyocytes. J Physiol 559:479–496. https://doi.org/10.1113/jphysiol.2004.068213

Schaaf S, Eder A, Vollert I, et al (2014) Generation of strip-format fibrin-based engineered heart tissue (EHT). Methods Mol Biol 1181:121–129. https://doi.org/10.1007/978-1-4939-1047-2_11

Schaaf S, Shibamiya A, Mewe M, et al (2011) Human Engineered Heart Tissue as a Versatile Tool in Basic Research and Preclinical Toxicology. PLoS One 6:e26397. https://doi.org/10.1371/journal.pone.0026397

Schotten U, Verheule S, Kirchhof P, Goette A (2011) Pathophysiological mechanisms of atrial fibrillation: A translational appraisal. Physiol Rev 91:265–325. https://doi.org/10.1152/physrev.00031.2009

Scuderi GJ, Butcher J (2017) Naturally Engineered Maturation of Cardiomyocytes. Front cell Dev Biol 5:. https://doi.org/10.3389/FCELL.2017.00050

Senyo SE, Steinhauser ML, Pizzimenti CL, et al (2013) Mammalian heart renewal by pre-existing cardiomyocytes. Nature 493:433–6. https://doi.org/10.1038/nature11682

Shadrin IY, Allen BW, Qian Y, et al (2017) Cardiopatch platform enables maturation and scale-up of human pluripotent stem cell-derived engineered heart tissues. Nat Commun 8:1825. https://doi.org/10.1038/s41467-017-01946-x

Shaffer LG, Bejjani BA (2004) A cytogeneticist's perspective on genomic microarrays. Hum Reprod Update 10:221–226. https://doi.org/10.1093/humupd/dmh022

Shiba Y, Fernandes S, Zhu W-Z, et al (2012) Human ES-cell-derived cardiomyocytes electrically couple and suppress arrhythmias in injured hearts. Nature 489:322–325. https://doi.org/10.1038/nature11317

Shiba Y, Filice D, Fernandes S, et al (2014) Electrical integration of human embryonic stem cell-derived cardiomyocytes in a guinea pig chronic infarct model. J Cardiovasc Pharmacol Ther 19:368–381. https://doi.org/10.1177/1074248413520344

Shiba Y, Gomibuchi T, Seto T, et al (2016) Allogeneic transplantation of iPS cell-derived cardiomyocytes regenerates primate hearts. Nature 538:388–391. https://doi.org/10.1038/nature19815

Shibamiya A, Schulze E, Krauß D, et al (2020) Cell Banking of hiPSCs: A Practical Guide to Cryopreservation and Quality Control in Basic Research. Curr Protoc Stem Cell Biol 55:e127. https://doi.org/10.1002/CPSC.127

Shiotani M, Harada T, Abe J, et al (2007) Methodological validation of an existing telemetry system for QT evaluation in conscious guinea pigs. J Pharmacol Toxicol Methods 55:27–34. https://doi.org/10.1016/j.vascn.2006.04.008

Siedner S, Krüger M, Schroeter M, et al (2003) Developmental changes in contractility and sarcomeric proteins from the early embryonic to the adult stage in the mouse heart. J Physiol 548:493–505. https://doi.org/10.1113/jphysiol.2002.036509

Smith JR, Maguire S, Davis LA, et al (2008) Robust, Persistent Transgene Expression in Human Embryonic Stem Cells Is Achieved with AAVS1-Targeted Integration. Stem Cells 26:496–504. https://doi.org/10.1634/stemcells.2007-0039

Smithies O, Gregg RG, Boggs SS, et al (1985) Insertion of DNA sequences into the human chromosomal β-globin locus by homologous recombination. Nature 317:230–234. https://doi.org/10.1038/317230a0

Snir M, Kehat I, Gepstein A, et al (2003) Assessment of the ultrastructural and proliferative properties of human embryonic stem cell-derived cardiomyocytes. Am J Physiol - Hear Circ Physiol 285:. https://doi.org/10.1152/ajpheart.00020.2003

Söderlund C, Rådegran G (2015) Immunosuppressive therapies after heart transplantation — The balance between under- and over-immunosuppression. Transplant Rev 29:181–189. https://doi.org/10.1016/j.trre.2015.02.005

Soonpaa MH, Field LJ (1997) Assessment of cardiomyocyte DNA synthesis in normal and injured adult mouse hearts. Am J Physiol - Hear Circ Physiol 272:. https://doi.org/10.1152/ajpheart.1997.272.1.h220

Soonpaa MH, Koh GY, Klug MG, Field LJ (1994) Formation of nascent intercalated disks between grafted fetal cardiomyocytes and host myocardium. Science (80-) 264:98–101. https://doi.org/10.1126/science.8140423

Sorrentino A, Steinhorn B, Troncone L, et al (2019) Reversal of heart failure in a chemogenetic model of persistent cardiac redox stress. Am J Physiol - Hear Circ Physiol 317:H617–H626. https://doi.org/10.1152/AJPHEART.00177.2019

Statistisches Bundesamt (2021) Sterbefälle (absolut, Sterbeziffer, Ränge, Anteile) für die 10/20/50/100 häufigsten Todesursachen (ab 1998). Gliederungsmerkmale: Jahre, Region,

Alter, Geschlecht, ICD-10. https://www.gbe-bund.de/gbe/pkg_isgbe5.prc_menu_olap?p_uid=gast&p_aid=71304904&p_sprache=D&p_help=0&p_indnr=516&p_indsp=&p_ityp=H&p_fid=#SOURCES)

Steinbeck JA, Choi SJ, Mrejeru A, et al (2015) Optogenetics enables functional analysis of human embryonic stem cell-derived grafts in a Parkinson's disease model. Nat Biotechnol 33:204–209. https://doi.org/10.1038/nbt.3124

Steinhorn B, Sorrentino A, Badole S, et al (2018) Chemogenetic generation of hydrogen peroxide in the heart induces severe cardiac dysfunction. Nat Commun 9:1–10. https://doi.org/10.1038/s41467-018-06533-2

Stockmann C, Hersh AL, Sherwin CMT, Spigarelli MG (2014) Alignment of United States funding for cardiovascular disease research with deaths, years of life lost, and hospitalizations. Int J Cardiol 172:e19–e21. https://doi.org/10.1016/j.ijcard.2013.12.095

Stüdemann T, Weinberger F (2021) The guinea pig model in cardiac regeneration research; Current tissue engineering approaches and future directions. In: Zhang J, Serpooshan V (eds) Advanced Technologies in Cardiovascular Bioengineering, 1st edn. Springer International Publishing, p 440

Sun X, Wu J, Qiang B, et al (2020) Transplanted microvessels improve pluripotent stem cell-derived cardiomyocyte engraftment and cardiac function after infarction in rats. Sci Transl Med 12:1–12. https://doi.org/10.1126/scitranslmed.aax2992

Sutherland FJ, Baker KE, Shattock MJ, Hearse DJ (2003a) Responses to ischaemia and reperfusion in the mouse isolated perfused heart and the phenomenon of "contractile cycling." Clin Exp Pharmacol Physiol 30:879–884. https://doi.org/10.1046/j.1440-1681.2003.03926.x

Sutherland FJ, Shattock MJ, Baker KE, Hearse DJ (2003b) Mouse isolated perfused heart: Characteristics and cautions. Clin Exp Pharmacol Physiol 30:867–878. https://doi.org/10.1046/j.1440-1681.2003.03925.x

Tachibana A, Santoso MR, Mahmoudi M, et al (2017) Paracrine effects of the pluripotent stem cell-derived cardiac myocytes salvage the injured myocardium. Circ Res 121:e22–e36. https://doi.org/10.1161/CIRCRESAHA.117.310803

Takahara A, Sasaki R, Nakamura M, et al (2009) Clobutinol delays ventricular repolarization in the guinea pig heart: Comparison with cardiac effects of hERG K+ channel inhibitor E-4031. J Cardiovasc Pharmacol 54:552–559. https://doi.org/10.1097/FJC.0b013e3181bfb17c

Takahashi K, Tanabe K, Ohnuki M, et al (2007) Induction of Pluripotent Stem Cells from Adult Human Fibroblasts by Defined Factors. Cell 131:861–872. https://doi.org/https://doi.org/10.1016/j.cell.2007.11.019

Takahashi K, Yamanaka S (2016) A decade of transcription factor-mediated reprogramming to pluripotency. Nat Rev Mol Cell Biol 17:183–193. https://doi.org/10.1038/nrm.2016.8

Tewary M, Shakiba N, Zandstra PW (2018) Stem cell bioengineering: building from stem cell

biology. Nat Rev Genet 2018 1910 19:595–614. https://doi.org/10.1038/s41576-018-0040-z

Thomson JA, Itskovitz-Eldor J, Shapiro SS, et al (1998) Embryonic Stem Cell Lines Derived from Human Blastocysts. Science (80-) 282:1145 LP – 1147. https://doi.org/10.1126/science.282.5391.1145

Thygesen K, Alpert JSS, Jaffe ASS, et al (2019) Fourth universal definition of myocardial infarction (2018). Eur Heart J 40:237–269. https://doi.org/10.1093/eurheartj/ehy462

Tiburcy M, Hudson JE, Balfanz P, et al (2017) Defined Engineered Human Myocardium With Advanced Maturation for Applications in Heart Failure Modeling and Repair. Circulation 135:1832–1847. https://doi.org/10.1161/CIRCULATIONAHA.116.024145

Tønnesen J, Parish CL, Sørensen AT, et al (2011) Functional Integration of Grafted Neural Stem Cell-Derived Dopaminergic Neurons Monitored by Optogenetics in an In Vitro Parkinson Model. PLoS One 6:e17560. https://doi.org/10.1371/JOURNAL.PONE.0017560

Ulmer BM, Stoehr A, Schulze ML, et al (2018) Contractile Work Contributes to Maturation of Energy Metabolism in hiPSC-Derived Cardiomyocytes. Stem Cell Reports 10:834–847. https://doi.org/10.1016/j.stemcr.2018.01.039

Van Berlo JH, Kanisicak O, Maillet M, et al (2014) C-kit+ cells minimally contribute cardiomyocytes to the heart. Nature 509:337–341. https://doi.org/10.1038/nature13309

Van De Werf F (2014) The history of coronary reperfusion. Eur Heart J 35:2510–2515. https://doi.org/10.1093/eurheartj/ehu268

Van Den Bos EJ, Mees BME, De Waard MC, et al (2005) A novel model of cryoinjury-induced myocardial infarction in the mouse: A comparison with coronary artery ligation. Am J Physiol - Hear Circ Physiol 289:H1291-300. https://doi.org/10.1152/ajpheart.00111.2005

Vandecasteele G, Eschenhagen T, Scholz H, et al (1999) Muscarinic and β-adrenergic regulation of heart rate, force of contraction and calcium current is preserved in mice lacking endothelial nitric oxide synthase. Nat Med 5:331–334. https://doi.org/10.1038/6553

Varró A, Lathrop DA, Hester SB, et al (1993) Ionic currents and action potentials in rabbit, rat, and guinea pig ventricular myocytes. Basic Res Cardiol 88:93–102. https://doi.org/10.1007/BF00798257

Velagaleti RS, Pencina MJ, Murabito JM, et al (2008) Long-term trends in the incidence of heart failure after myocardial infarction. Circulation 118:2057–62. https://doi.org/10.1161/CIRCULATIONAHA.108.784215

Vogel U (2020) Deutscher Herzbericht 2020

Vreeker A, Stuijvenberg L van, Hund TJ, et al (2014) Assembly of the Cardiac Intercalated Disk during Pre- and Postnatal Development of the Human Heart. PLoS One 9:e94722. https://doi.org/10.1371/JOURNAL.PONE.0094722

Wang DY, Chae SW, Gong QY, Lee CO (1988) Role of a(Na)(i) in positive force-frequency

staircase in guinea pig papillary muscle. Am J Physiol - Cell Physiol 255:. https://doi.org/10.1152/ajpcell.1988.255.6.c798

Weber N, Schwanke K, Greten S, et al (2016) Stiff matrix induces switch to pure β-cardiac myosin heavy chain expression in human ESC-derived cardiomyocytes. 111:1–16. https://doi.org/10.1007/s00395-016-0587-9

Weinberger F, Breckwoldt K, Pecha S, et al (2016) Cardiac repair in guinea pigs with human engineered heart tissue from induced pluripotent stem cells. Sci Transl Med 8:363ra148. https://doi.org/10.1126/scitranslmed.aaf8781

Wiegert JS, Mahn M, Prigge M, et al (2017) Silencing Neurons: Tools, Applications, and Experimental Constraints. Neuron 95:504–529. https://doi.org/10.1016/j.neuron.2017.06.050

Wietek J, Beltramo R, Scanziani M, et al (2015) An Imporved Chloride-Conducting Channelrhodopsin for Light-Induced Inhibition of Neuronal Activity In Vivo. Sci Rep 5:14807. https://doi.org/10.1038/srep14807

Wietek J, Wiegert JS, Adeishvili N, et al (2014) Conversion of Channelrhodopsin into a Light-Gated Chloride Channel. Science (80-) 344:409–412. https://doi.org/10.1126/science.1249375

Wu KC, Weiss RG, Thiemann DR, et al (2008) Late Gadolinium Enhancement by Cardiovascular Magnetic Resonance Heralds an Adverse Prognosis in Nonischemic Cardiomyopathy. J Am Coll Cardiol 51:2414–2421. https://doi.org/10.1016/j.jacc.2008.03.018

Yang D, Scavuzzo MA, Chmielowiec J, et al (2016) Enrichment of G2/M cell cycle phase in human pluripotent stem cells enhances HDR-mediated gene repair with customizable endonucleases. Sci Rep 6:21264. https://doi.org/10.1038/srep21264

Yang X, Rodriguez M, Pabon L, et al (2014) Tri-iodo-l-thyronine promotes the maturation of human cardiomyocytes-derived from induced pluripotent stem cells. J Mol Cell Cardiol 72:296–304. https://doi.org/10.1016/j.yjmcc.2014.04.005

Yang X, Rodriguez ML, Leonard A, et al (2019) Fatty Acids Enhance the Maturation of Cardiomyocytes Derived from Human Pluripotent Stem Cells. Stem Cell Reports 13:657–668. https://doi.org/10.1016/j.stemcr.2019.08.013

Yao X, Wang X, Hu X, et al (2017) Homology-mediated end joining-based targeted integration using CRISPR/Cas9. Cell Res 27:801–814. https://doi.org/10.1038/cr.2017.76

Ye L, D'Agostino G, Loo SJ, et al (2018) Early Regenerative Capacity in the Porcine Heart. Circulation 138:2798–2808. https://doi.org/10.1161/CIRCULATIONAHA.117.031542

Yechikov S, Copaciu R, Gluck JM, et al (2016) Same-Single-Cell Analysis of Pacemaker-Specific Markers in Human Induced Pluripotent Stem Cell-Derived Cardiomyocyte Subtypes Classified by Electrophysiology. Stem Cells 34:2670–2680. https://doi.org/10.1002/STEM.2466

Yiangou L, Grandy RA, Morell CM, et al (2019) Method to Synchronize Cell Cycle of Human

Pluripotent Stem Cells without Affecting Their Fundamental Characteristics. Stem Cell Reports 12:165–179. https://doi.org/10.1016/j.stemcr.2018.11.020

Yu SP, Tung JK, Wei ZZ, et al (2019) Optochemogenetic stimulation of transplanted ips-NPCs enhances neuronal repair and functional recovery after ischemic stroke. J Neurosci 39:6571–6594. https://doi.org/10.1523/JNEUROSCI.2010-18.2019

Zacchigna S, Paldino A, Falcão-Pires I, et al (2021) Towards standardization of echocardiography for the evaluation of left ventricular function in adult rodents: A position paper of the ESC Working Group on Myocardial Function. Cardiovasc Res 117:43–59. https://doi.org/10.1093/cvr/cvaa110

Zannad F, Ferreira JP, Pocock SJ, et al (2020) SGLT2 inhibitors in patients with heart failure with reduced ejection fraction: a meta-analysis of the EMPEROR-Reduced and DAPA-HF trials. Lancet 396:819–829. https://doi.org/10.1016/S0140-6736(20)31824-9

Zenchak JR, Palmateer B, Dorka N, et al (2020) Bioluminescence-driven optogenetic activation of transplanted neural precursor cells improves motor deficits in a Parkinson's disease mouse model. J Neurosci Res 98:458–468. https://doi.org/10.1002/jnr.24237

Zhang J, Wilson GF, Soerens AG, et al (2009) Functional cardiomyocytes derived from human induced pluripotent stem cells. Circ Res 104:e30. https://doi.org/10.1161/CIRCRESAHA.108.192237

Zhang JP, Li XL, Li GH, et al (2017) Efficient precise knockin with a double cut HDR donor after CRISPR/Cas9-mediated double-stranded DNA cleavage. Genome Biol 18:35. https://doi.org/10.1186/s13059-017-1164-8

Zhao M, Nakada Y, Wei Y, et al (2020) Cyclin d2 overexpression enhances the efficacy of human induced pluripotent stem cell-derived cardiomyocytes for myocardial repair in a swine model of myocardial infarction. Circulation 144:210–228. https://doi.org/10.1161/CIRCULATIONAHA.120.049497

Zhu W, Zhao M, Mattapally S, et al (2018) CCND2 Overexpression Enhances the Regenerative Potency of Human Induced Pluripotent Stem Cell-Derived Cardiomyocytes: Remuscularization of Injured Ventricle. Circ Res 122:88–96. https://doi.org/10.1161/CIRCRESAHA.117.311504

Zimmermann WH, Didié M, Wasmeier GH, et al (2002a) Cardiac grafting of engineered heart tissue in syngenic rats. Circulation 106:. https://doi.org/10.1161/01.cir.0000032876.55215.10

Zimmermann WH, Melnychenko I, Wasmeier G, et al (2006) Engineered heart tissue grafts improve systolic and diastolic function in infarcted rat hearts. Nat Med 12:452–458. https://doi.org/10.1038/nm1394

Zimmermann WH, Schneiderbanger K, Schubert P, et al (2002b) Tissue Engineering of a Differentiated Cardiac Muscle Construct. Circ Res 90:223–230. https://doi.org/10.1161/hh0202.103644

9 APPENDIX

9.1 Supplementary Data

9.1.1 Primer List

Supplementary Table 1: Primer list

Name	Sequence
3' integration for	CTGGGGTGCCTAATGAGTGA
CAG seq for	GCTCTAGAGCCTCTGCTAACCATG
EYFP for	CGTGACCACCTTCGGCTAC
EYFP rev	CGGACACGCTGAACTTGTGG
Fragment for	CAAAGAATTCGTCGACACCATGGGAGTCAAAGTTCTGT
Fragment rev	GAATTCACGCGTGATATCTTACTTGTACAGCTCGTCCATGCC
Gaussia for	AACGCTGCGCGACCTTTG
GFP EcoRV rev	GAATTCACGCGTGATATCTTACTTGTACAGCTCGTCCATGCCG
GFP for	GCTGCTGCCCGACAACCACTACCTGAGCAC
GFP rev	CGGCGGTCACGAACTCCAGCAGGACCATGT
GFP SalI for	CAAAGAATTCGTCGACATGGTGAGCAAGGGCGAG
HA-L insert for	TCGACCTACTCTCTTCCGCA
HA-L insert rev	GTACTCGGTCATCTCGAGCC
HA-R for	AGAAAAGCCCCATCCTTAGGC
HA-R genomic rev	ACAGTGACCAACCATCCCTG
HA-R insert rev	GGCTCCATCGTAAGCAAACC
iLMO4 for	CACCGGATACGTCAAGGTCA
EGFP intern for	CTACCCCGACCACATGAAGC
NHEJ for	CCTGGCTTTAGCCACCTCTC
PSAM 2A rev	CAGCGCATGCTAGCCGGTGCAGG
PSAM 2A for	GGCTAGCATGCGCTGTTCTCCAGGCG
PSAM 5HT3 for	CACCTGCAACCTTTCAAGCC
PSAM GlyR for	GCCTATGGTATGGGACCTGC
PSAM rev	CCTGCACCTGAGGAGTGAAT
PSAM SalI for	CAAAGAATTCGTCGACCACCATGCGCTGTTCTCCA
PSAM seq for	TATCGACGTCCGCTGGTTTC
Venus for	GTGCTGCTGCCCGACAACC

9.1.2 Southern Blotting Probe Sequences

5' probe

GCTGGACTCCACCAACGCCGACGGTATCAGCGCCCTGCACCAGGTCAGCGCCCCCCGCCCGGCGTCTCCC
GGGGCCAGGTCCACCCTCTGCTGCGCCACCTGGGGCATCCTCCTTCCCCGTTGCCAGTCTCGATCCGCCC
CGTCGTTCCTGGCCCTGGGCTTTGCCACCCTATGCTGACACCCCGTCCCAGTCCCCCTTACCATTCCCCTTC
GACCACCCCACTTCCGAATTGGAGCCGCTTCAACTGGCCCTGGGCTTAGCCACTCTGTGCTGACCACTCT
GCCCCAGGCCTCCTTACCATTCCCCTTCGACCTACTCTCTTCCGCATTGGAGTCGCTTTAACTGGCCCTGGC
TTTGGCAGCCTGTGCTGACCCATGCAGTCCTCCTTACCATCCCTCCCTCGACTTCCCCTCTTCCGATGTTGA
GCCCCTCCAGCCGGTCCTGGACTTTGTCTCCTTCCCTGCCCTGCCCTCTCCTGAACCTGAGCCAGCTCCCAT
AGCTCAGTCTGGTCTATCTGCCTGGCCCTGGCCATTGTCACTTTGCGCTGCCCTCCTCTCGCCCCCGAGTG
CCCTTGCTGTGCCGCCGGAACTCTGCCCTCTAACGCTGCCGTCTCTCTCCTGAGTCCGGACCACTTTGAGC
TCTACTGGCTTCTGCGCCGCCTCTGGCCCACTGTTTCCCCTTCCCAGGCAGGTCC

Internal probe

AAGCTTAGTACTGTCGATCCGCTGGCACGACAGGTTTCCCGACTGGAAAGCGGGCAGTGAGCGCAACGC
AATTAATGTGAGTTAGCTCACTCATTAGGCACCCCAGGCTTTACACTTTATGCTTCCGGCTCGTATGTTGT
GTGGAATTGTGAGCGGATAACAATTTCACACAGGAAACAGCTATGACCATGATTACGCCAAGCTTGGGC
TGCAGGTCGAGGGATCTCCATAAGAGAAGAGGGACAGCTATGACTGGGAGTAGTCAGGAGAGGAGGA
AAAATCTGGCTAGTAAAACATGTAAGGAAAATTTTAGGGATGTTAAAGAAAAAAATAACACAAAACAAA
ATATAAAAAAAAATCTAACCTCAAGTCAAGGCTTTTCTATGGAATAAGGAATGGACAGCAGGGGGCTGTT
TCATATACTGATGACCTCTTTATAGCCAACCTTTGTTCATGGCAGCCAGCATATGGGCATATGTTGCCAAA
CTCTAAACCAAATACTCATTCTGATGTTTTAAATGATTTGCCCTCCCATATGTCCTTCCGAGTGAGAGACA
CAAAAAATTCCAACACACTATTGCAATGAAAATAAATTTCCTTTATTAGCCAGAAGTCAGATGCTCAAGG
GGCTTCATGATGTCCCCATAATTTTTGGCAGAGGGAAAAAGATCTCAGTGGTATTTGTGAGCCAG

9.1.3 crRNA Design

crRNA1 sequence: GTCACCAATCCTGTCCCTAG (green box)

crRNA2 sequence: GGGGCCACTAGGGACAGGAT (orange box)

Position/ Strand	Guide Sequence + *PAM* + Restriction Enzymes + Variants Only G- Only GG- Only A-	MIT Specificity Score	CFD Spec. score	Predicted Efficiency Show all scores Doench '16	Mor.-Mateos	Outcome Out-of-Frame	Lindel	Off-targets for 0-1-2-3-4 mismatches + next to PAM	Genome Browser links to matches sorted by CFD off-target score exons only chr19 only
28 / rev	GTCCCTAGTGGCCCCACTGT *GGG* Enzymes: *BsII, HpyCH4III, TspRI* Cloning / PCR primers	80	89	36	48	75	78	0 - 0 - 0 - 9 - 86 0 - 0 - 0 - 2 - 2	4:exon:RP11-281A20.2 3:intron:SNAP47 4:intron:HGD show all...
40 / rev	GTCACCAATCCTGTCCCTAG *TGG* Enzymes: *BshFI, NlaIV, PspPI, MaeI* Cloning / PCR primers	80	88	61	37	56	75	0 - 0 - 0 - 9 - 102 0 - 0 - 0 - 2 - 3 111 off-targets	4:intergenic:LL22NC03-121E8.3-MIR3201 4:intergenic:RP11-1299A16.1-BTF3P13 4:intron:TTN show all...
46 / fw	ACCCCACAGTGGGGCCACTA *GGG* Enzymes: *BsiFI, MaeI* Cloning / PCR primers	79	89	53	66	62	73	0 - 0 - 1 - 14 - 130 0 - 0 - 0 - 0 - 1 145 off-targets	4:intergenic:TNFAIP8-RN7SL174P 4:intergenic:RP3-378P9.2-KLHL13 4:intron:ULK4 show all...
51 / fw	ACAGTGGGGCCACTAGGGAC *AGG* Enzymes: *BsiFI* Cloning / PCR primers	76	88	55	69	58	72	0 - 0 - 1 - 5 - 151 0 - 0 - 1 - 0 - 9 157 off-targets	4:intron:KIAA1644 2:intergenic:CTD-2337A12.1-PCSK1 3:exon:ZNF710/RP11-61FZ3.1 show all...
27 / rev	TCCCTAGTGGCCCCACTGTG *GGG* Enzymes: *BsII, HpyCH4III, TspRI* Cloning / PCR primers	70	81	55	65	75	91	0 - 0 - 3 - 17 - 154 0 - 0 - 1 - 6 - 6 174 off-targets	4:intergenic:AC104088.1-ITGA6 4:intron:GSG1 4:intron:BIK show all...
29 / rev	TGTCCCTAGTGGCCCCACTG *TGG* Enzymes: *BsII, HpyCH4III, TspRI* Cloning / PCR primers	68	86	55	57	79	82	0 - 0 - 2 - 24 - 138 0 - 0 - 1 - 5 - 5	4:intron:AGMO 4:intron:HYDIN 4:intergenic:RN7SKP183-RNU6-133P show all...
56 / fw	GGGGCCACTAGGGACAGGAT *TGG* Enzymes: *AsuHPI, MaeIII, Tsp45I* Cloning / PCR primers	61	82	54	54	68	78	0 - 0 - 2 - 27 - 218 0 - 0 - 0 - 4 - 5 247 off-targets	3:intron:CPNE5 4:intron:RAP1GAP 3:intergenic:SNORA25-AL603632.1 show all...
80 / fw	GACAGAAAAGCCCCATCCTT *AGG* Inefficient Enzymes: *BstDEI, Bse21I, BsII* Cloning / PCR primers	60	81	49	47	74	83	0 - 0 - 3 - 28 - 225 0 - 0 - 0 - 2 - 5 256 off-targets	3:intron:RGP1 3:intergenic:C9orf3-MIR227B 3:intergenic:CST5-CSTP1 show all...

Supplementary Figure 1: crRNA Design with CRISPOR Tool (http://crispor.tefor.net/)

9.1.4 Plasmid Maps

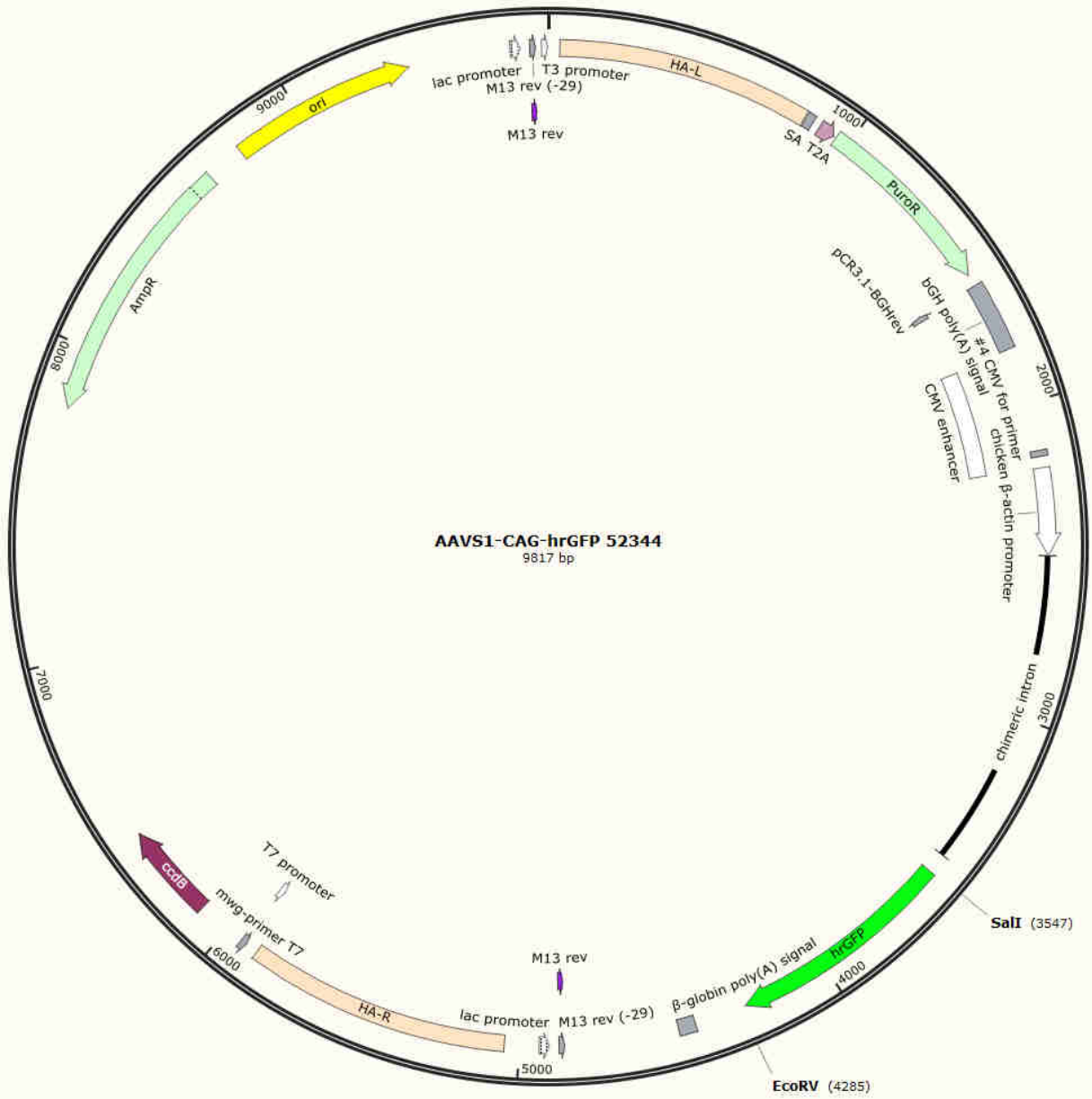

Supplementary Figure 2: Plasmid map of AAVS1-CAG-hrGFP (Addgene, #52344)

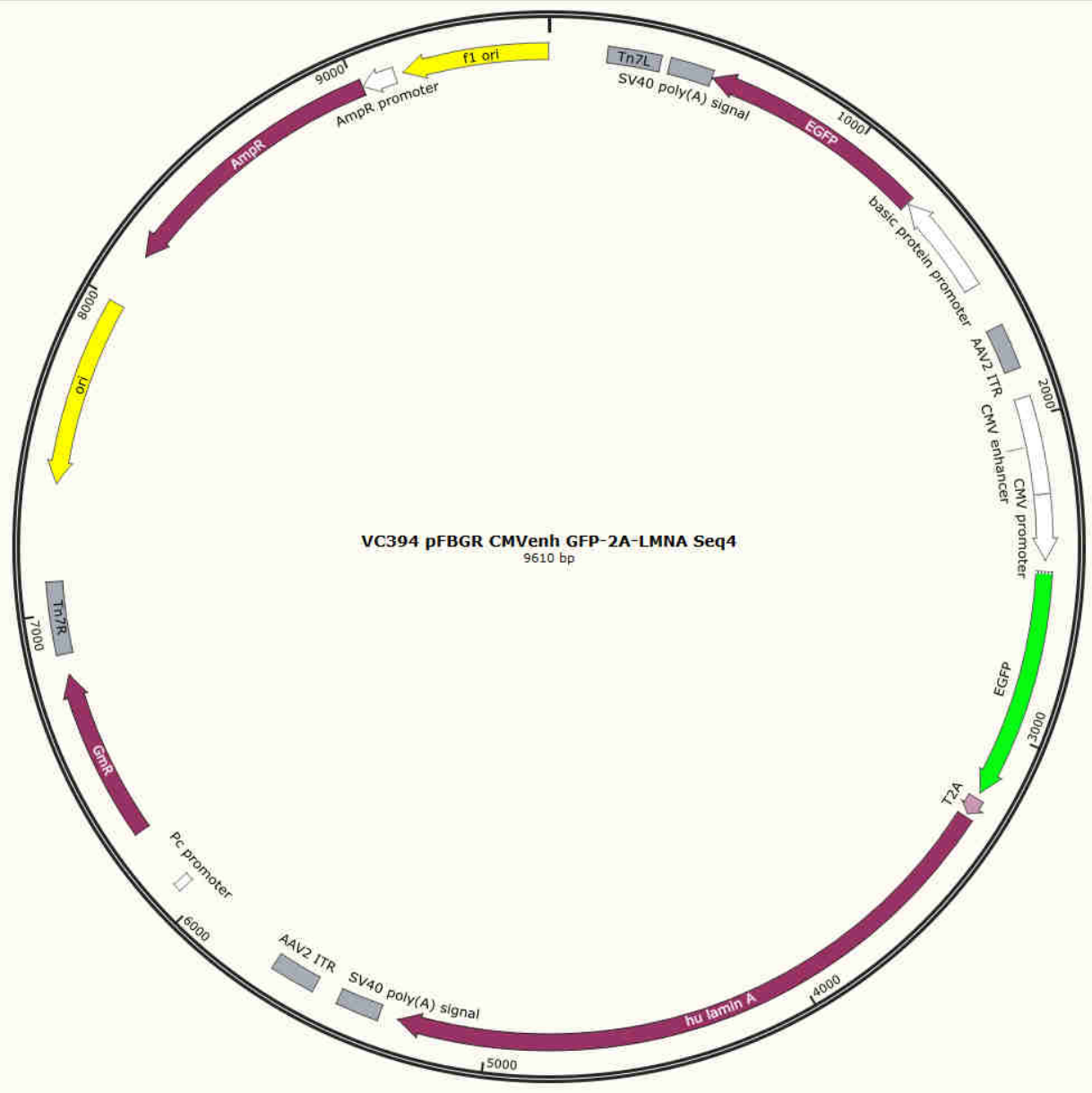

Supplementary Figure 3: Plasmid map of pFBGR CMVenh GFP-2A-LMNA

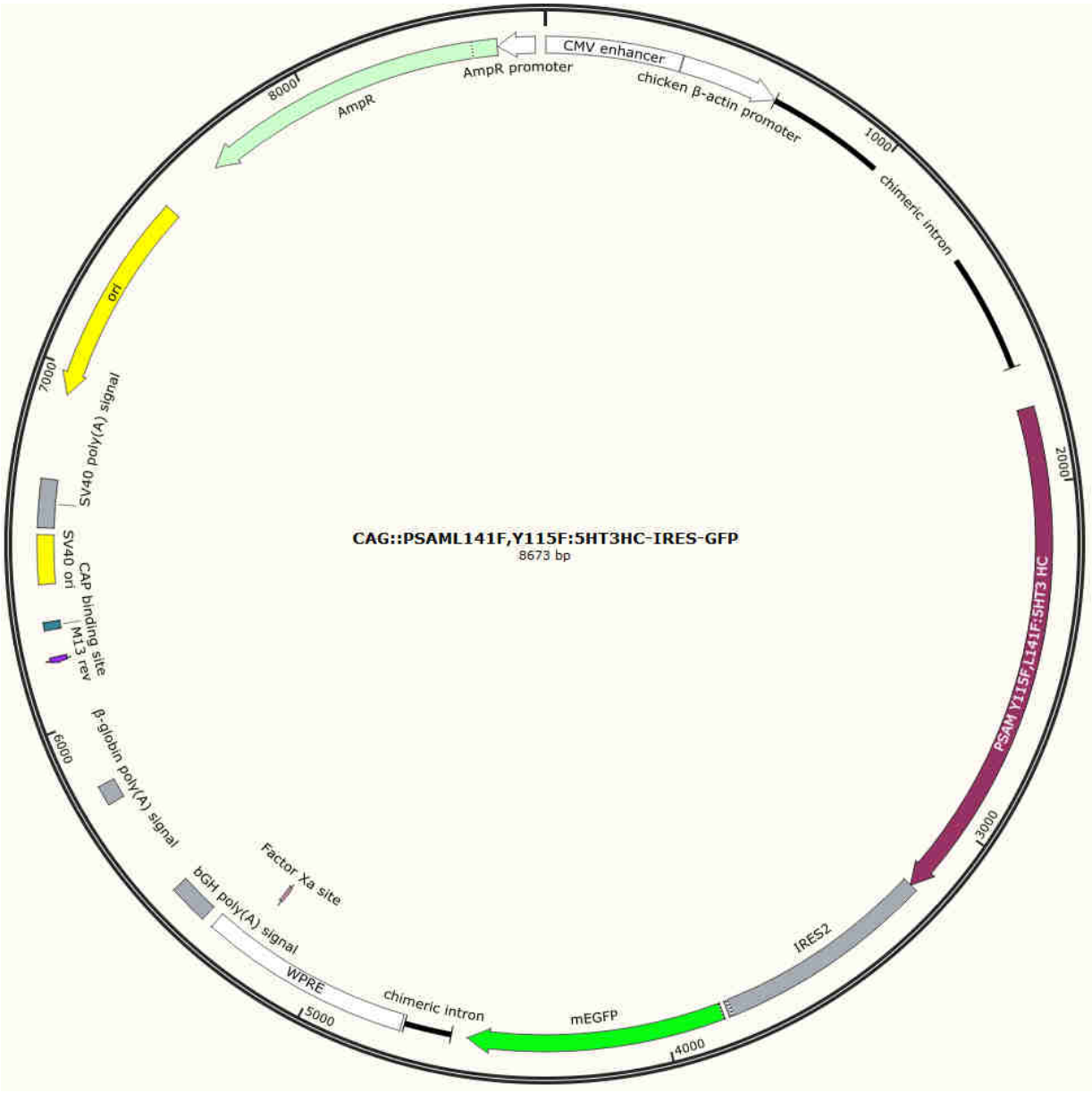

Supplementary Figure 4: Plasmid map of CAG::PSAML141F,Y115F: 5HT3HC-IRES-GFP (Addgene, #32476)

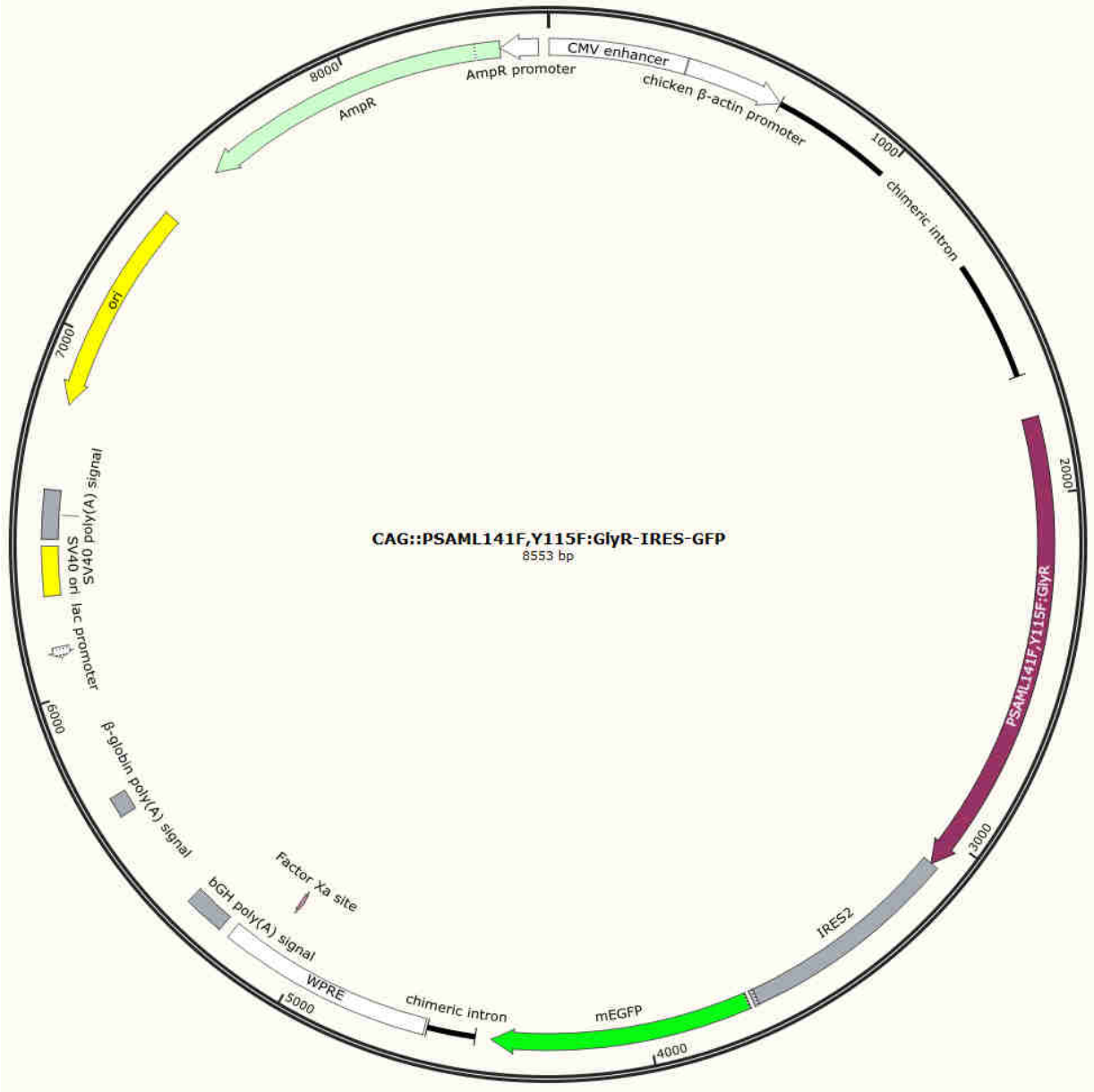

Supplementary Figure 5: Plasmid map of CAG::PSAML141F,Y115F:GlyR-IRES-GFP (Addgene, #32480)

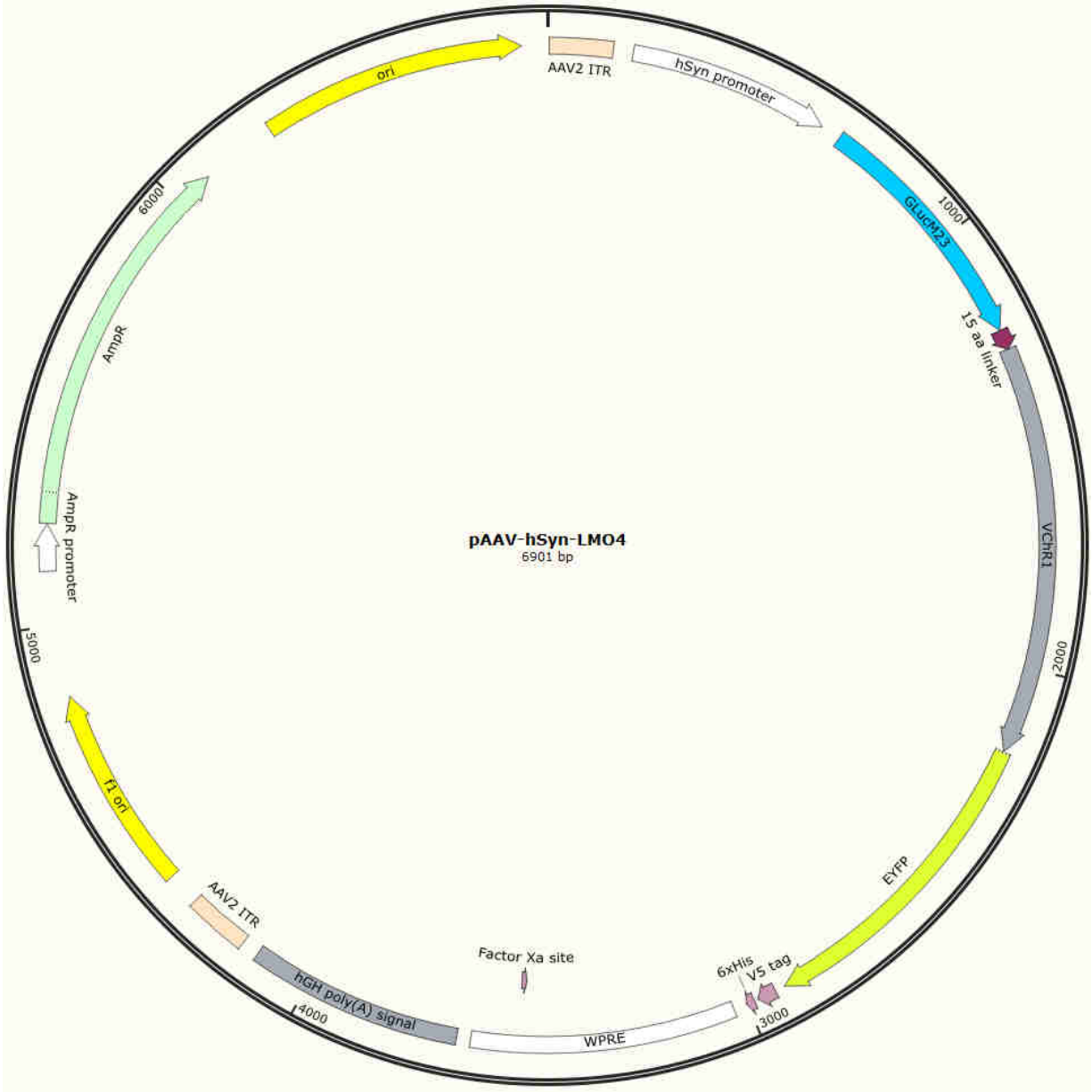

Supplementary Figure 6: Plasmid map of pAAV-hSyn-LMO4

Supplementary Figure 7: Plasmid map of pcDNA-CAG-iLMO4

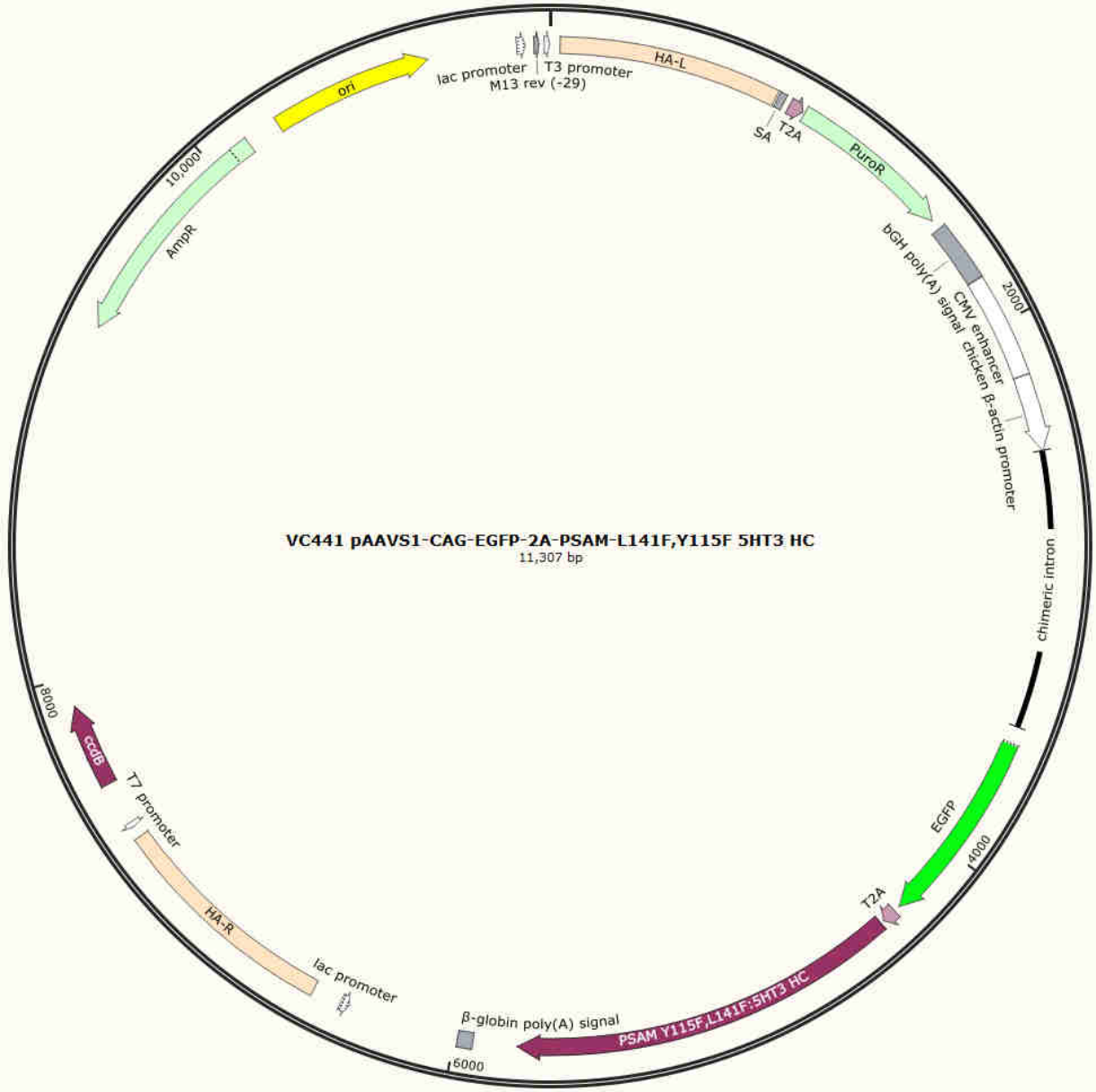

Supplementary Figure 8: Plasmid map of pAAVS1-CAG-EGFP-2A-PSAM-L141F,Y115F 5HT3 HC

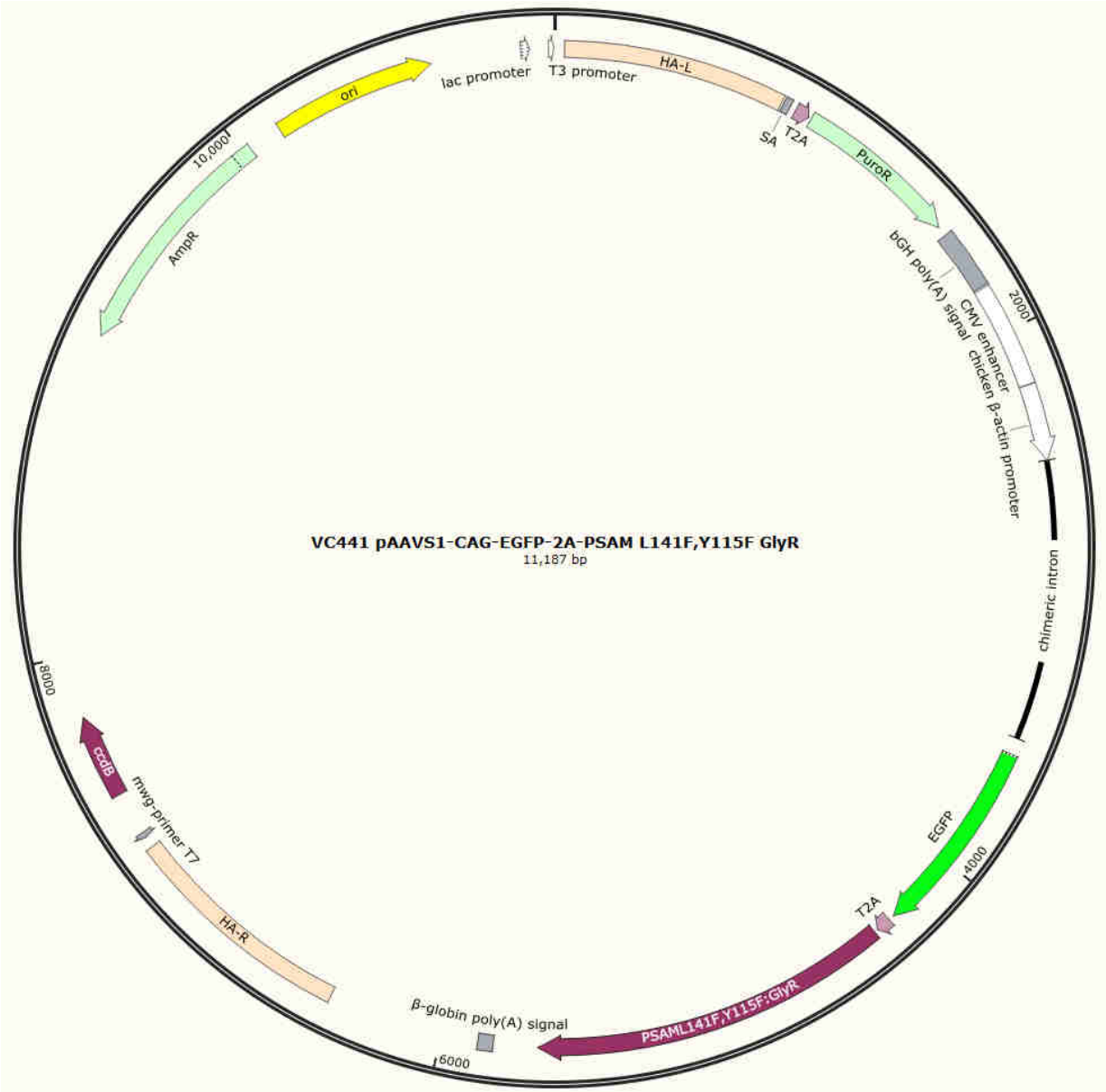

Supplementary Figure 9: Plasmid map of pAAVS1-CAG-EGFP-2A-PSAM-L141F,Y115F GlyR

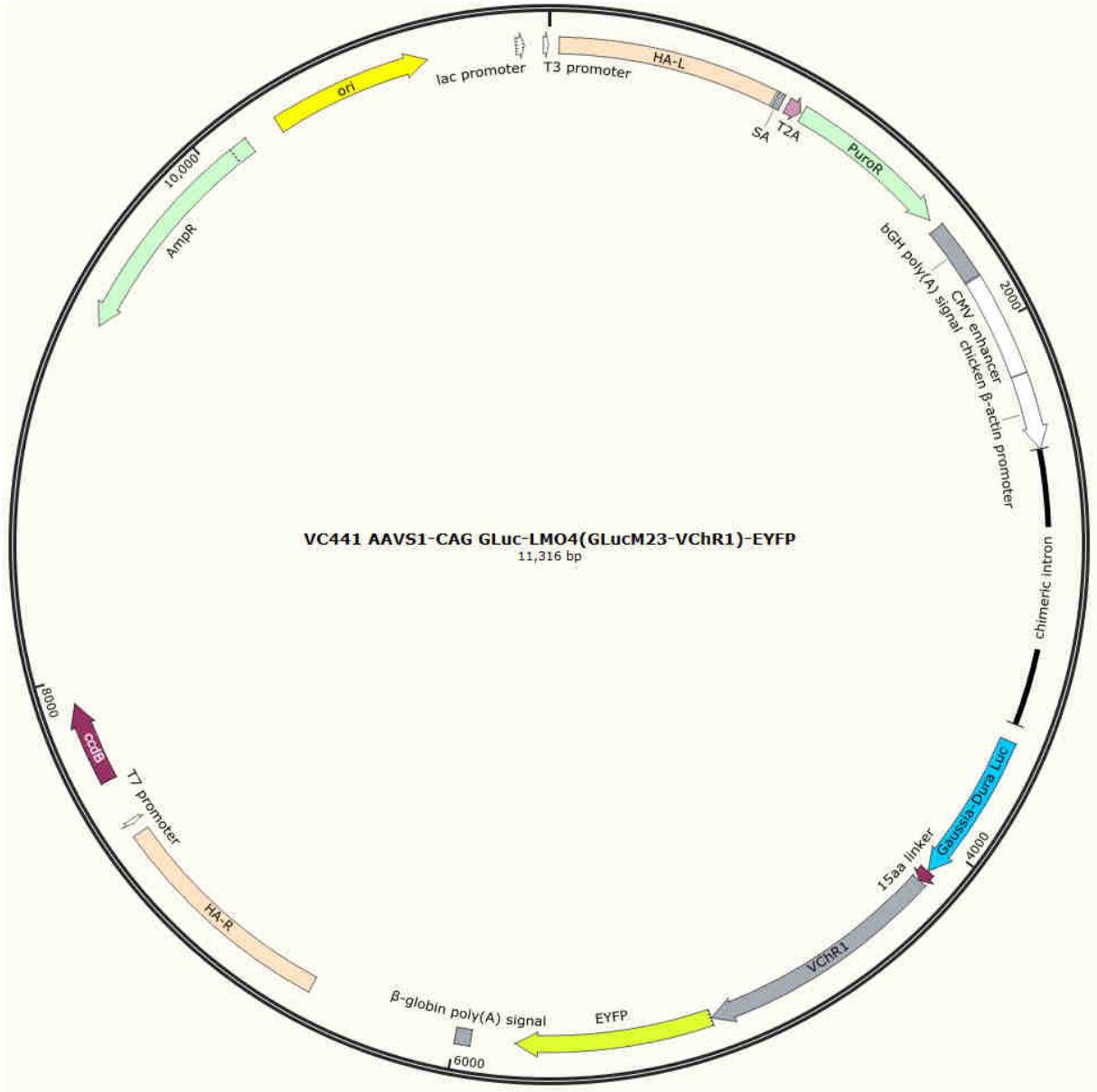

Supplementary Figure 10: Plasmid map of pAAVS1-CAG LMO4(GLucM23-VChR1)-EYFP

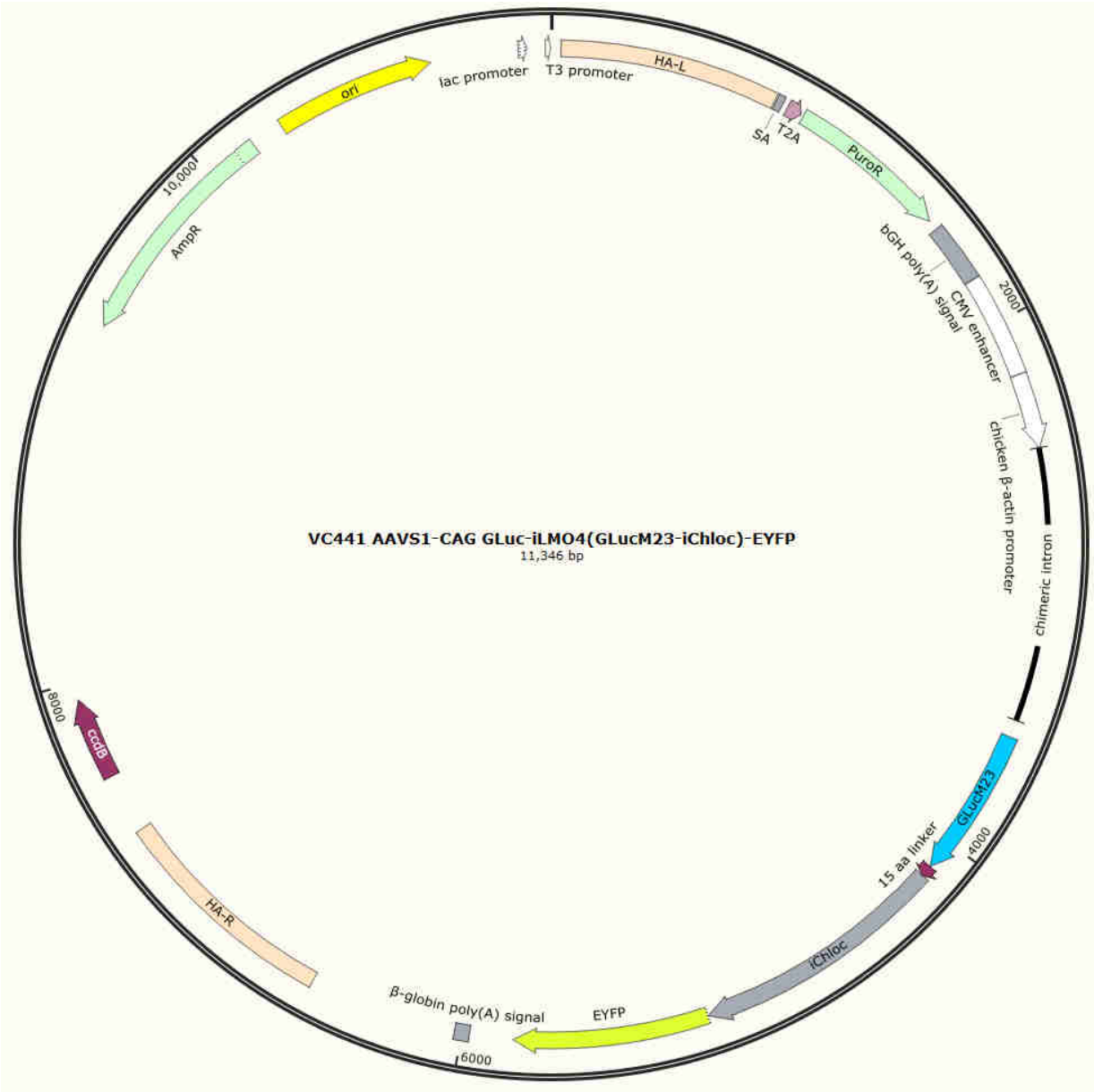

Supplementary Figure 11: Plasmid map of pAAVS1-CAG iLMO4(GLucM23-iChloC)-EYFP

9.1.5 Genotype Screening

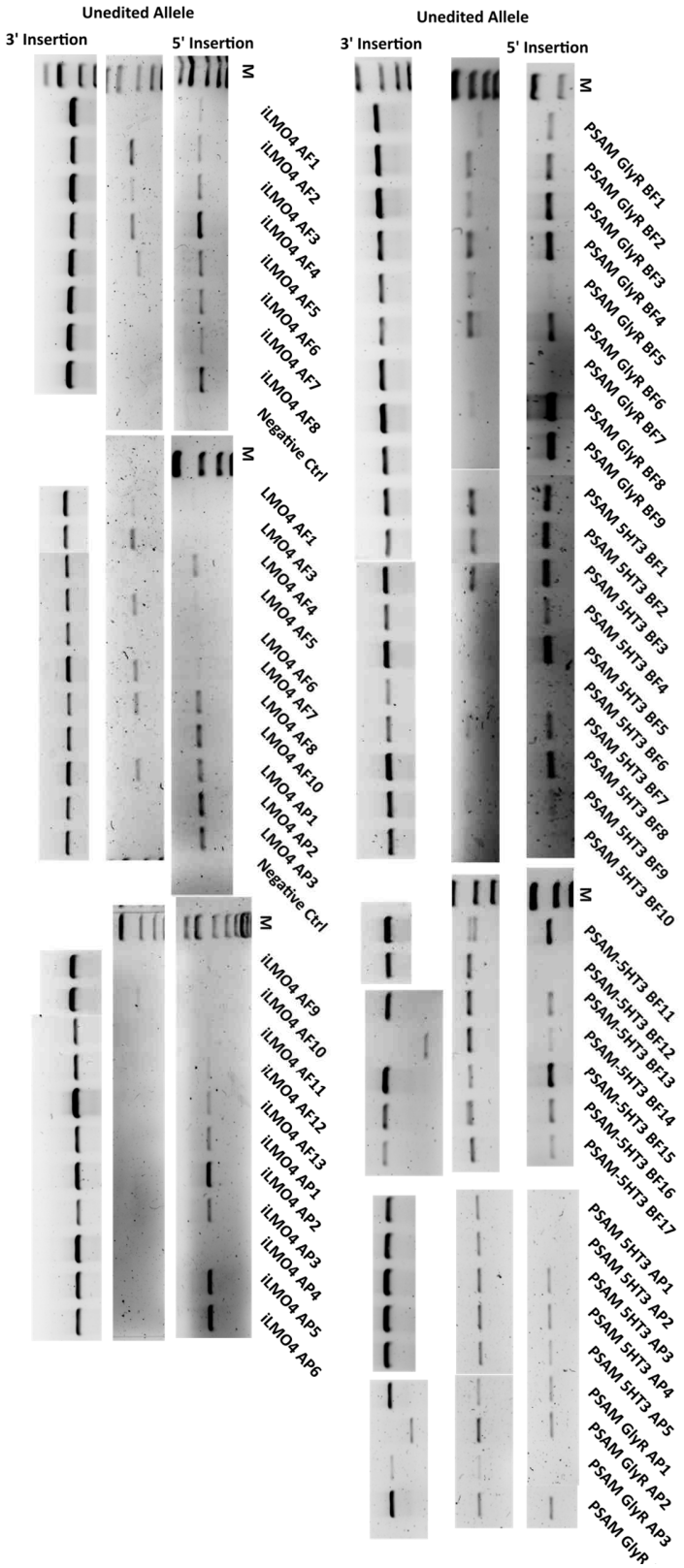

Supplementary Figure 12: Gel pictures of genotype screening

9.1.6 Dystrophin Stainings of Guinea Pig Hearts

PSAM GlyR Transplantation

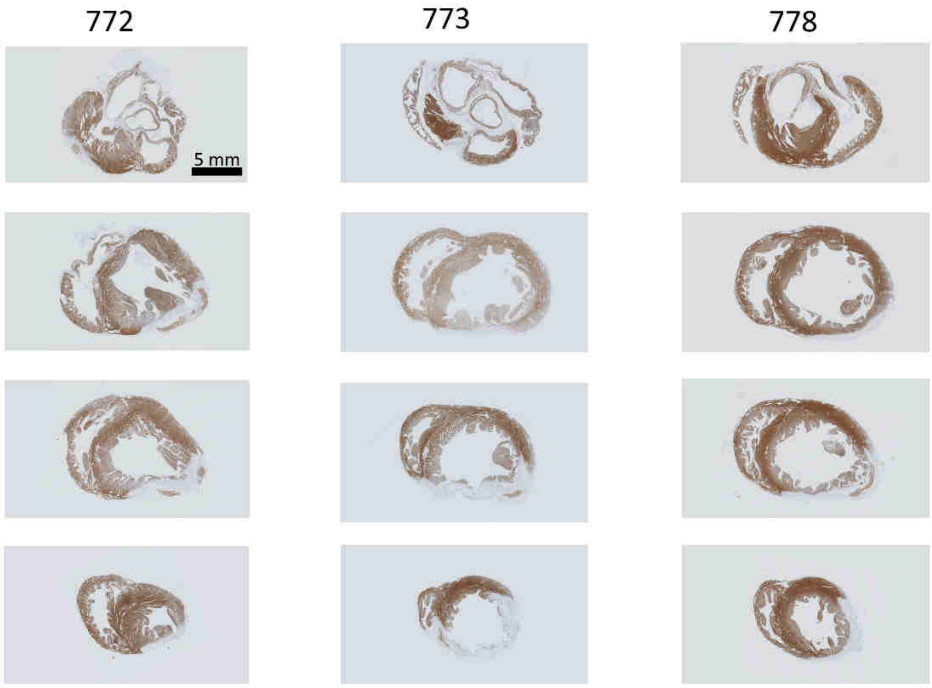

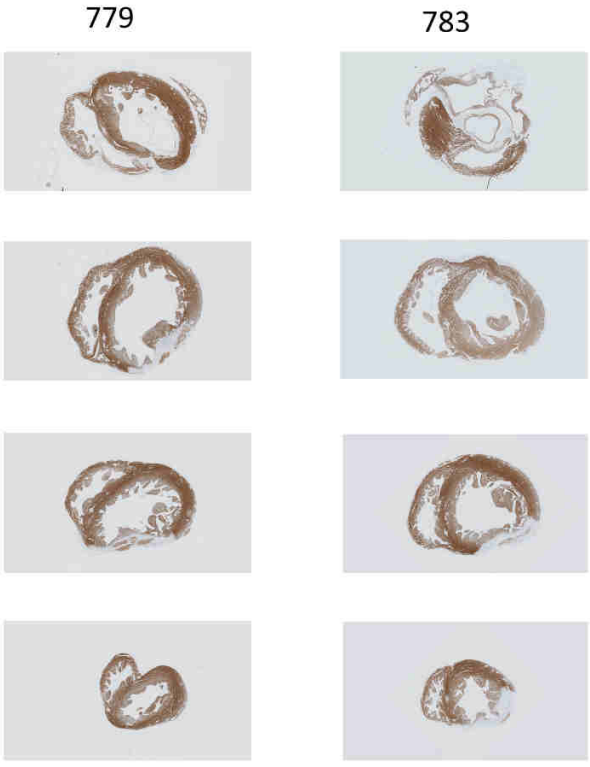

Control Transplantation

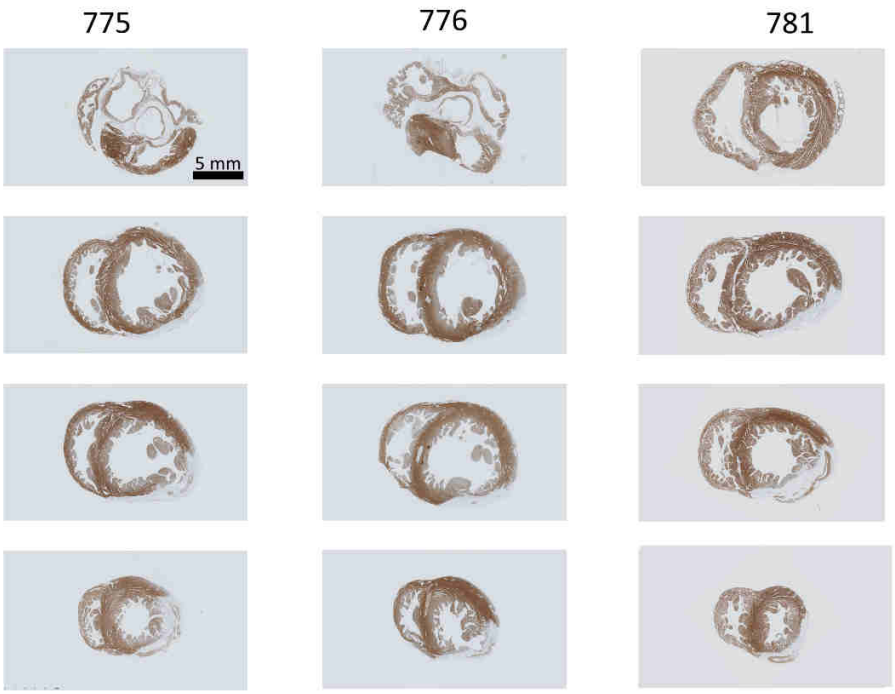

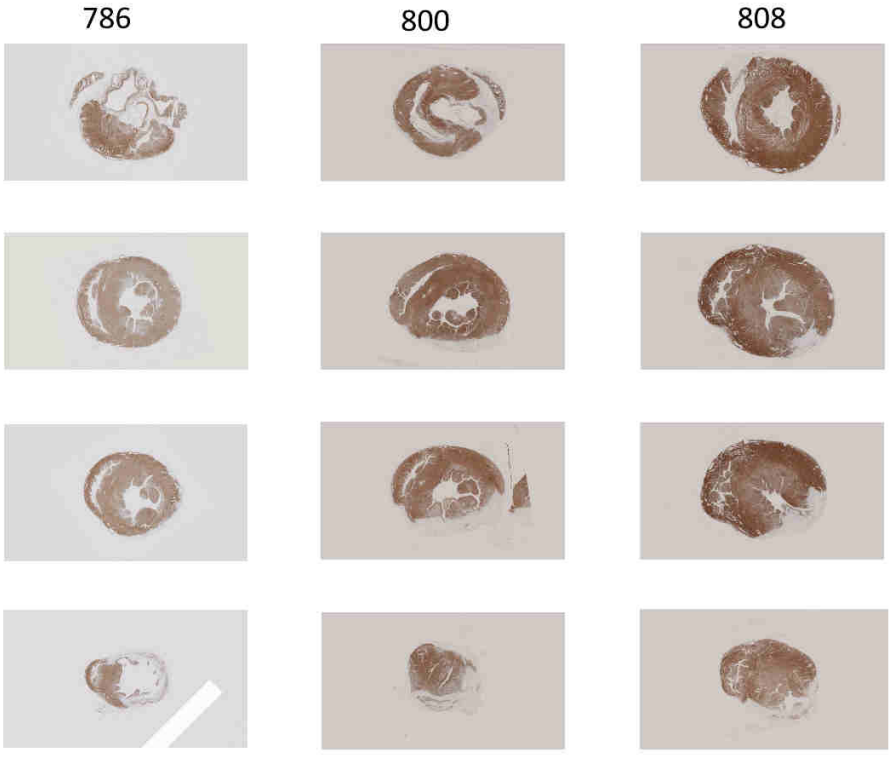

810

817

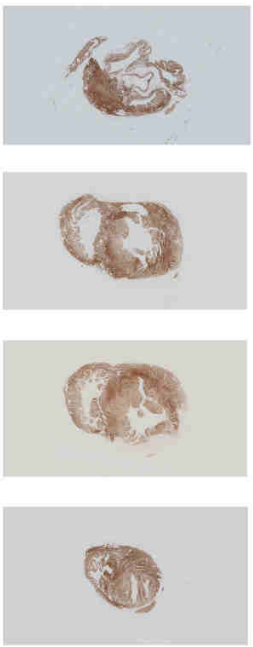

819

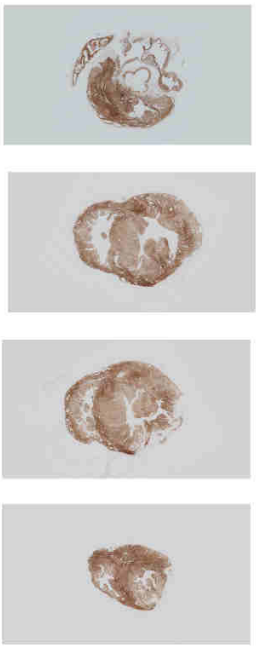

821

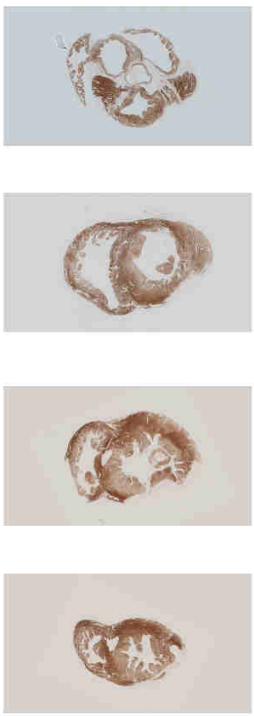

822

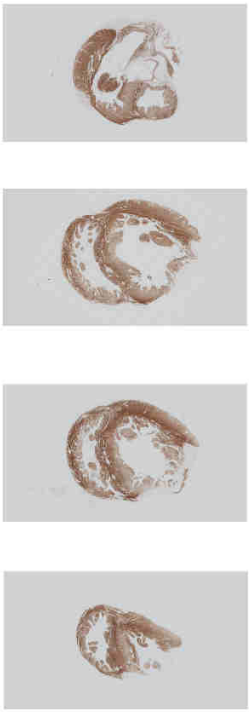

iLMO4 Transplantation

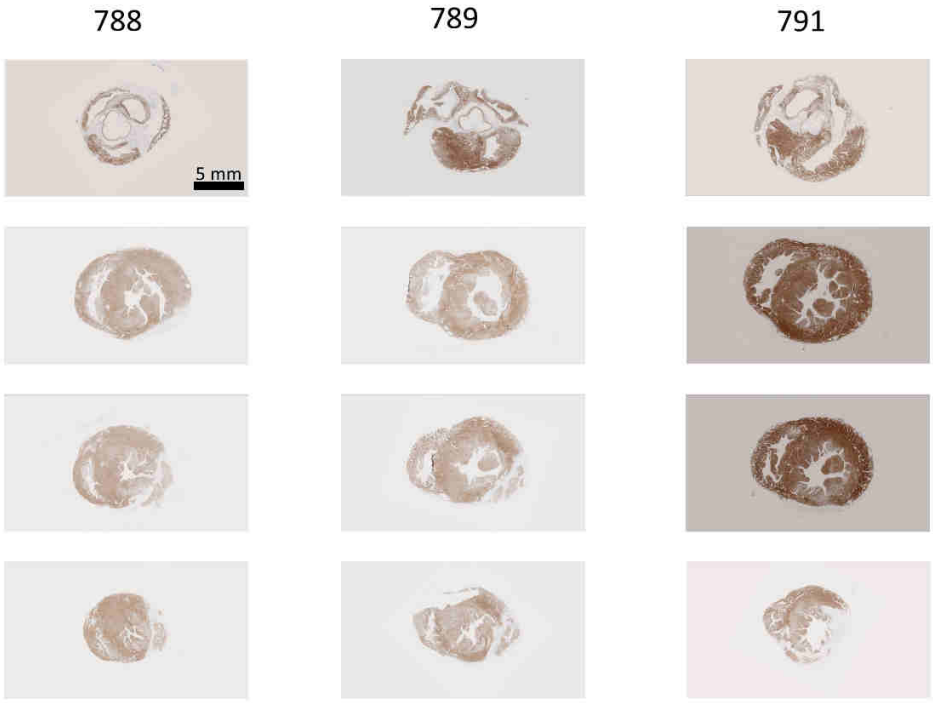

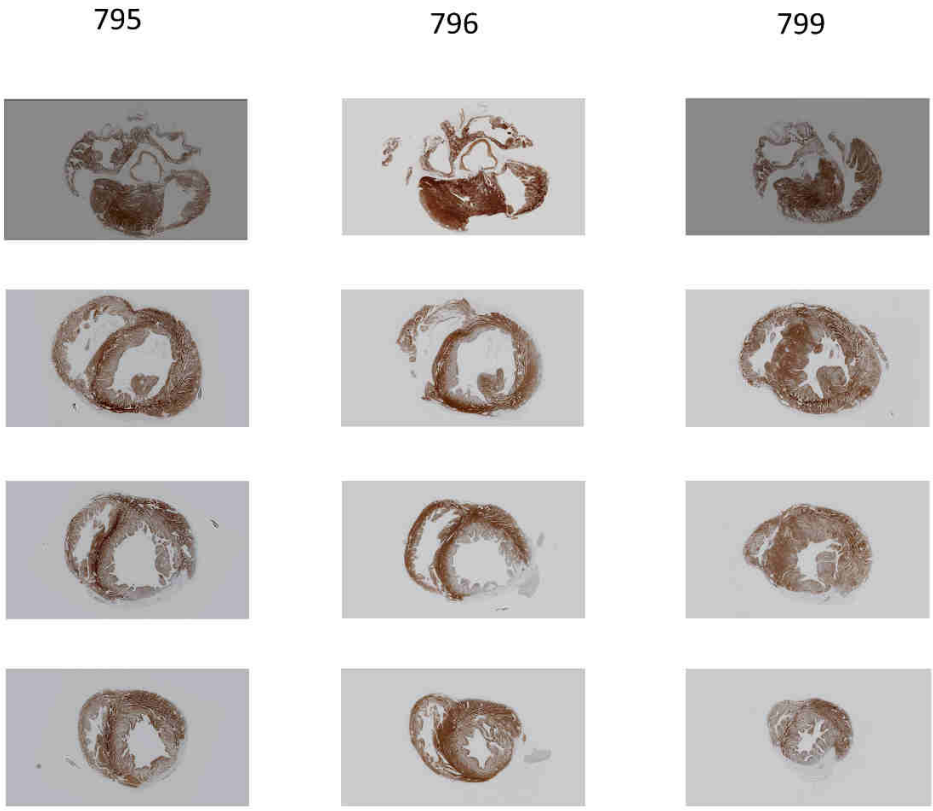

805

814

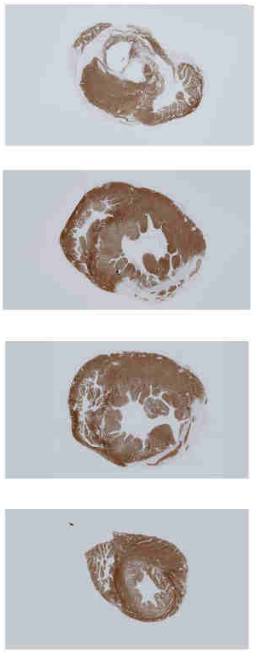

815

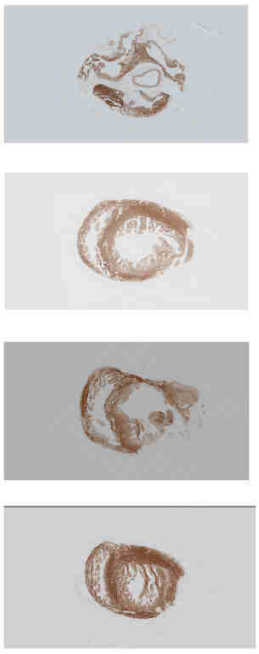

816

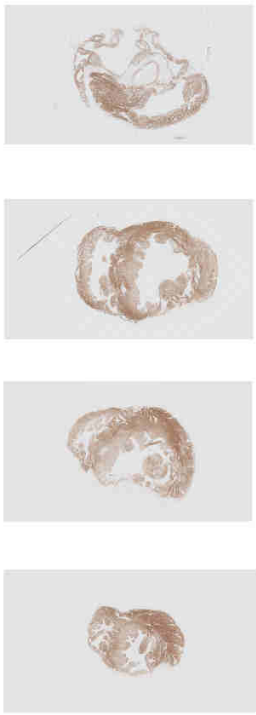

823

824

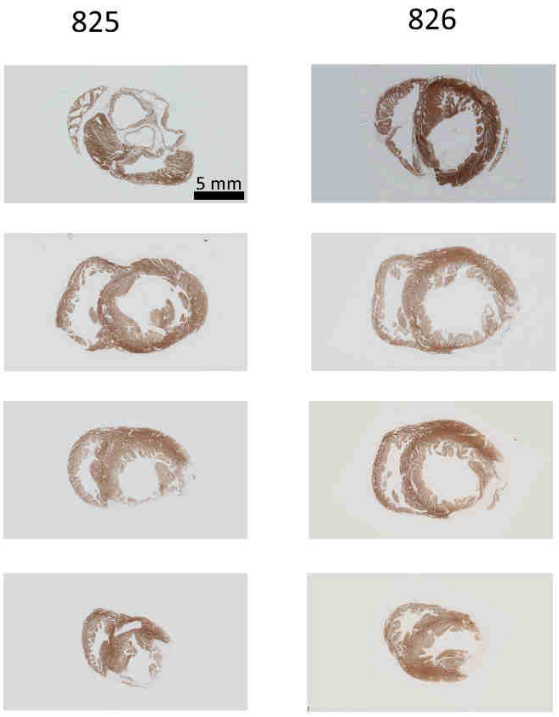

Supplementary Figure 13: Dystrophin stainings of all heart sections (A to D) analyzed in this study.

9.1.7 Langendorff Original Recordings of iLMO4 and Control Hearts

795 (iLMO4)

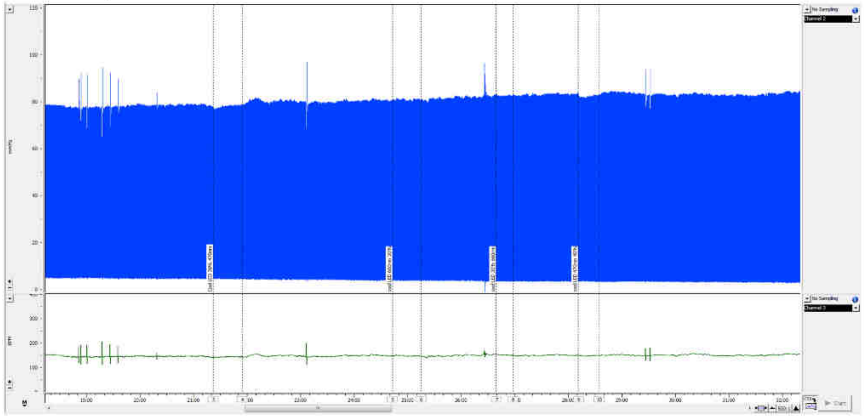

796 (iLMO4)

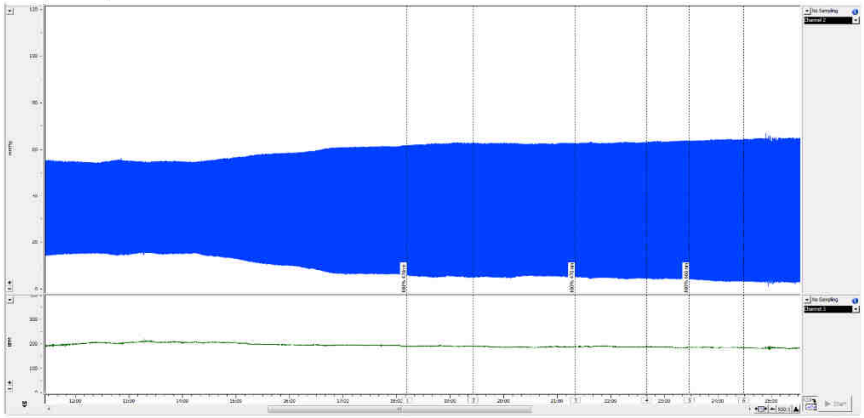

799 (iLMO4)

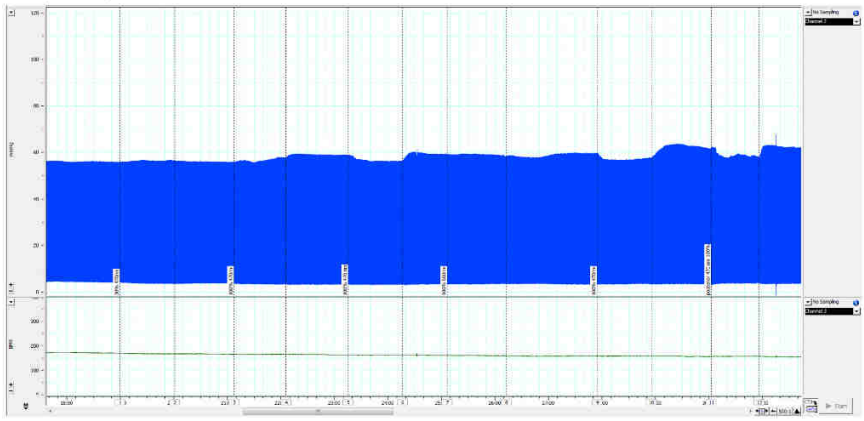

805 (iLMO4)

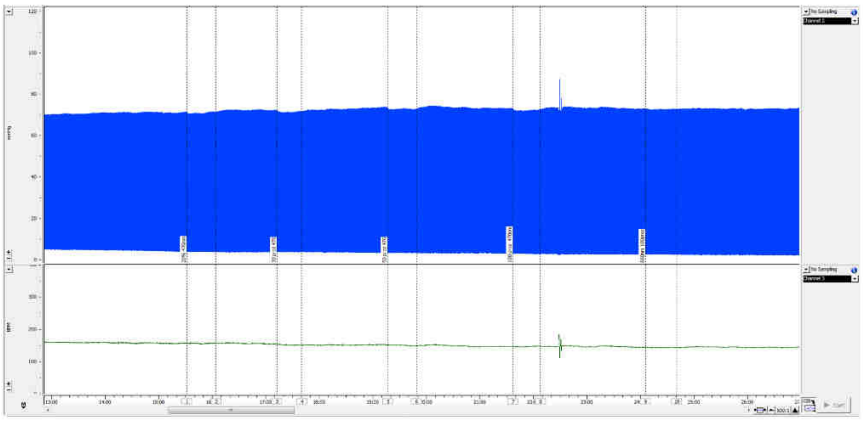

815 (iLMO4)

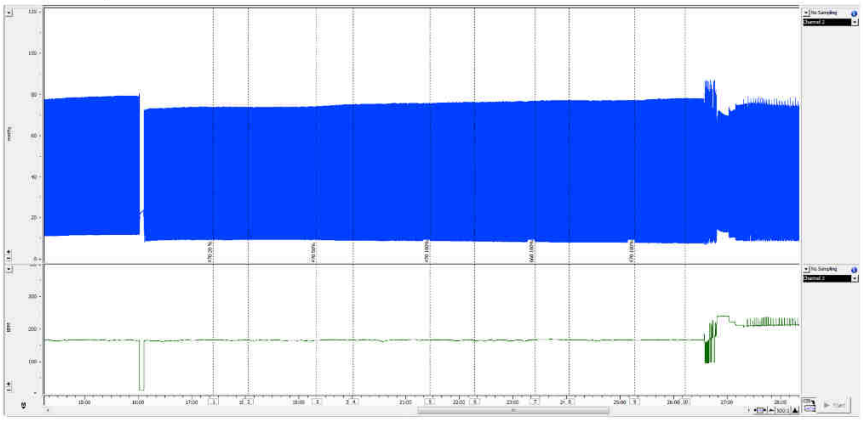

823 (iLMO4)

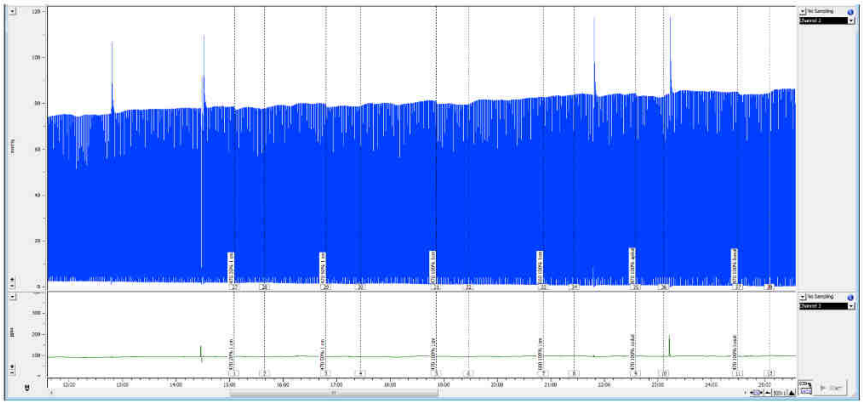

824 (iLMO4)

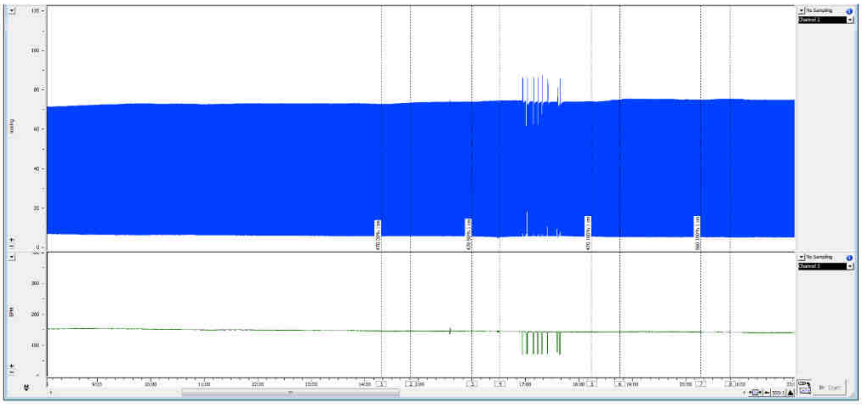

825 (iLMO4)

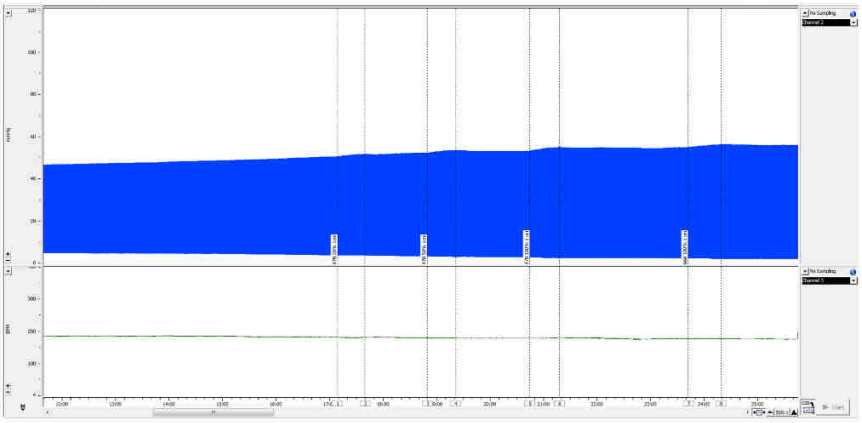

826 (iLMO4)

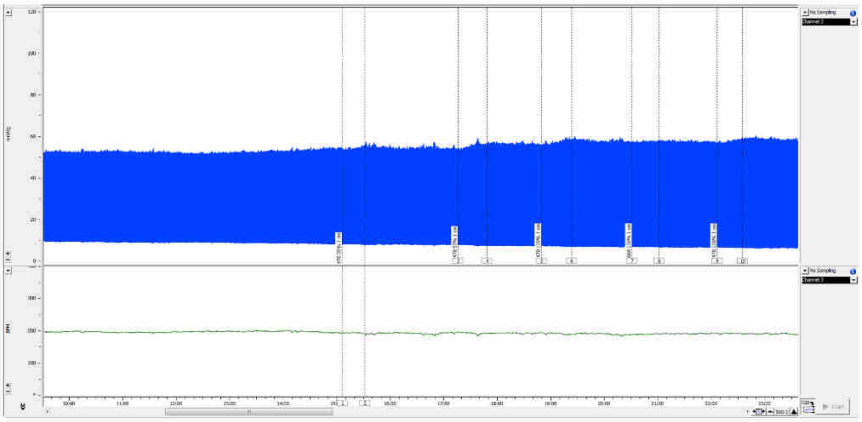

800 (Control)

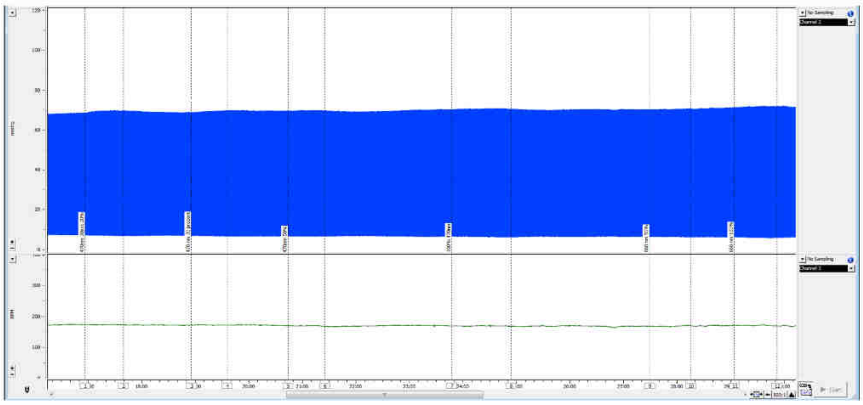

817 (Control)

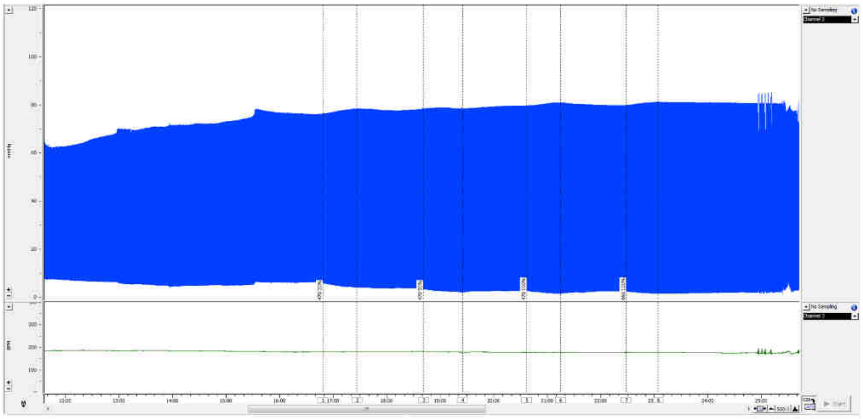

819 (Control)

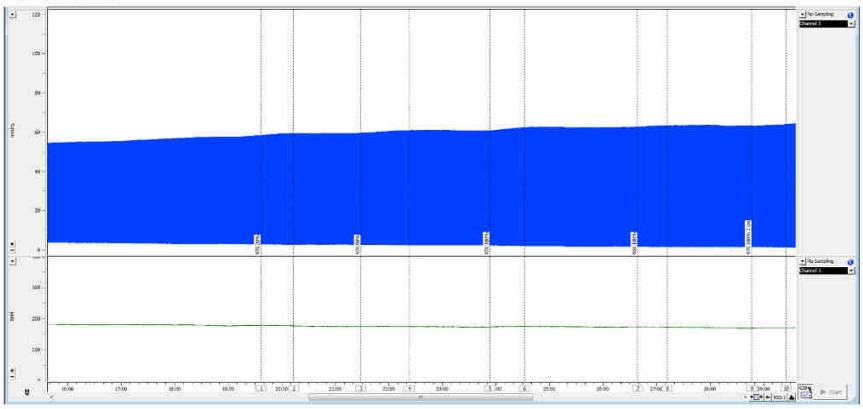

821 (Control)

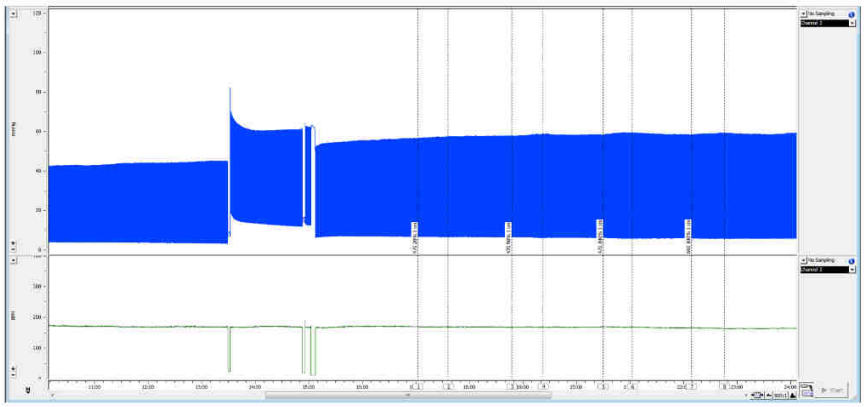

822 (Control)

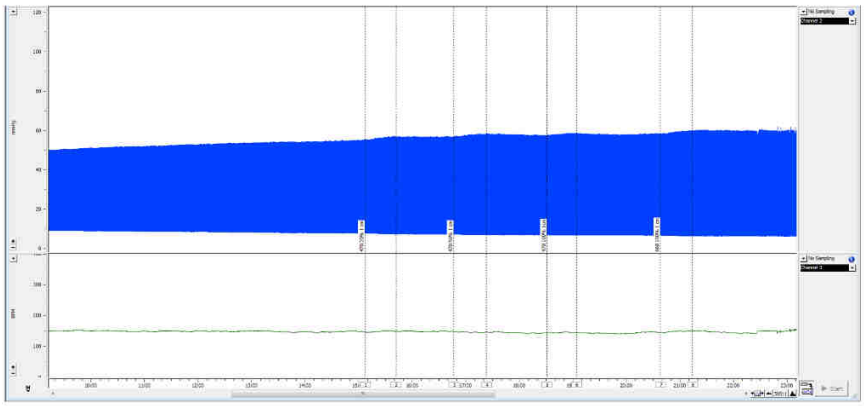

Supplementary Figure 14: Original Langendorff recordings of all hearts. Previously published in "Contractile force of transplanted cardiomyocytes contributes to heart function after injury" by Stüdemann et al., BioRxiv, pages 2021.11.23.469715 (2021).

9.2 Devices, Materials and Substances

9.2.1 Devices

4D-Nucleofector™ Core Unit	Lonza
4D-Nucleofector™ X Unit	Lonza
AbiPrism7900HT cycler	Applied Biosystems
Accu-jetR pro	Brand
A-D converter	ADInstruments, ML 826 Powerlab 2/26
Amplifier	npi electronic, BA 1S/BA-01X
Analytic scale Genius	Sartorius AG
AriaFusion FACS sorter	BD Biosciences
Bio-Rad ChemiDoc™ Touch Imaging System	Bio-Rad Laboratories
Brückenmessverstärker	FMI GmbH, MIO 0501
Catheter FTH-1212B-4518	Transonic Scisense
CASY Cell Counter	Schärfe System

Centrifuges

5415 R	Eppendorf
5424 R	Eppendorf
5810 R	Eppendorf
Avanti JXN-26	Beckmann-Coulter
J-6B	Beckmann
Labofuge 400R	Heraeus
Multifuge X3R	Heraeus
Rotanta/RP	Hettich
Universal 30 RF	Hettich

ChemiDoc™ Touch Imaging system	Bio-Rad Laboratories
Combispin FVL-2400N with vortex function	PeqLab
Custom made LED plate 24-well format (blue and red)	Custom made at UKE, Hamburg
Custom made trigger box	Custom made at UKE, Hamburg
DSLR with tripod	Nikon, D3100
EF600 Cell Freezer	Asymptote
Electrode puller	Zeitz DMZ
FACS Canto II Flow Cytometer	BD Biosciences
Faraday cage	Custom made at UKE, Hamburg
Fluid Aspiration system BVC control	Vacuubrand
Heating system	Lohmann Research Equipment, LTR-2 P.I.D.
Impalement Micromanipulator	Narishige group, MMO-203

Incubators for cell culture

CB 220	Binder

HERAcell 150i	Thermo Fisher Scientific
HERAcell 240	Thermo Fisher Scientific
Innova 4000	New Brunswick Scientific
MCO-19M	Sanyo
MCO-20AIC	Sanyo
Lamp KL-1500	Schott
Magnet plate Variomag/ Cimarec Biosystem 4 Direct	Thermo Scientific
Magnet plate Variomag/ Cimarec Biosystem Direct	Thermo Scientific
Magnet/heating plate IKA Combimag RET	Janke & Kunkel GmbH& Co KG

Microscopes

Axioskop 2 with AxioCam color camera	Zeiss
BSB 4A	Gelaire
EVOS FL Cell Imaging System	Advanced Microscopy Group
LSM 800 Airyscan	Zeiss
SZ61 SZ-STB1	Olympus
T1-SM Nikon Eclipse TS100	Nikon
NanoZoomer	Hamamatsu
nCounter SPRINT™ Profiler	NanoString
pE4000	coolLED
Perfusor compact	Braun
Perfusor-fm	Braun
pH meter, digital	Mettler Toledo
Pipette 10/100/1000 µL	Eppendorf, Peqlab
Pipetus	Hirschmann
Position Micromanipulator	Narishige group, MM-3
Power supply	peqlab, EV243
Powermeter + Sensor	Thor Labs, PM400 + S130C
Pre-amp headstage	npi electronic
Pressure Transducer	FMI GmbH, TBD-1222
Pressure-volume box	Transonic Scisense, FY097B
Rolling pump	Ismatec
S2020 1.8	Thermo Fisher Scientific
S88X dual output square pulse stimulator	Grass
Scale EK-4000H	AND
Scale Ohaus Precision Advanced	Ohaus
Silicone bath	Lohmann Research Equipment
Soldering bolt LS-99, modified	Daytools
Spectrophotometer NanoDrop ND-1000	Thermo Fisher Scientific
Stimulator	Biotronik, UHS20

Stimulator	Grass, SD9
Stimulator C Type 224	Hugo Sachs Elektronik

Sterile working benches

BSB 41	Gelaire
HeraSafe	Heraeus
Security working hood HERAsafeR	Thermo Fisher Scientific

Thermoblock Thermostat 5320	Eppendorf

Thermocyclers

2720 Thermal Cycler	Applied Biosystems
GeneAmp® PCR System 9700	Applied Biosystems
Primus 25 advanced	peqlab
vapo.protect	Eppendorf

Thermoshaker	Schutron
Ventana® BenchMark® XT	Roche
Vevo3100	VisualSonics
Video-optical force analysis system ("white box")	EHT technologies GmbH, Hamburg, A0001
Vortex Reax 2000	Heidolph
Vortex VF2	Janke & Kunkel GmbH& Co KG
Warming Cabinett 37 °C	Custom made at UKE, Hamburg
Water bath	GFL
Water bath 2590	Medax

9.2.2 Software

AxioVision Rel. 4.8.2	Zeiss
BioRender	BioRender
Chart5.5.6™	AD Instruments
Excel	Microsoft
FACSDiva	BD Biosciences
FlowJo V10	BD Biosciences
Image Lab	Bio-Rad Laboratories
ImageJ	NIH
Inkscape	Inkscape Community
Labscribe2	Transonic Scisense
nCounter CNV Collector Tool	Nanostring
NDP.view2	Hamamatsu Photonics
Prism 8.0	GraphPad Software
SDS 2.4.1	Applied Biosystem
SnapGene® 3.3.4	GSL Biotech LLC
VevoLab	VisualSonics
ZEN 2012	Zeiss

9.2.3 Materials and Equipment

10 mL Wide Tip Stripette	Corning, 4492
12-well plates	Thermo Fisher Scientific, 150628
15 mL tubes	GreinerBio-one, 188271
15 mL tubes red cap	Sarstedt, 62.554.502
2.0mm stainless steel needle	Acufirm, 14080220
24-well plates	Thermo Fisher Scientific, 142475
250 ml Vacuum Filtration "rapid"-Filtermax	TPP, 99250
4-0 suture PROLENE™	Ethicon, 662SLH
48-well plates	Thermo Fisher Scientific, 150687
50 mL tubes	GreinerBio-One, 227261
5-0 suture PROLENE™	Ethicon, 8710H
500 ml Vacuum Filtration "rapid"-Filtermax	TPP, 99500
6-well plates	Greiner
6-well plates	Thermo Fisher Scientific, 140675
8-0 suture PROLENE™	Ethicon, 8841H
96-well plates	Thermo Fisher Scientific, 167008
Adhesive tape	3M Health Care
Aquasonic 100	Parker, 01-08
Aspiration pipette 2 mL	Sarstedt, 86.1252.011
Cannulae (22-27G)	Braun
Catheter BD Venflon™ Pro Safety 20G	BD
Cell culture tube 12mL, round bottom (for EHT generation)	GreinerBio One, 163160,
Comb 10 well 0.75 mm	Bio-Rad Laboratories, 165-3354
Comb 10 well 1.0 mm	Bio-Rad Laboratories, 165-3359
Cotton swabs	Meditrade, 1260
Cryovial CryoPure tube 1.6 mL	Sarstedt, 72.379
Depilatory cream	Veet
EHT electrode	EHT Technologies GmbH, P0001
EHT pacing adapter/cable	EHT Technologies GmbH, P0002
EHT PDMS net	Self-build
EHT PDMS rack (24-well format)	EHT Technologies GmbH, C0001
EHT PTFE spacer 24-well	EHT Technologies GmbH, C0002
Falcon tube, graduated, 15 mL	Sarstedt, 62.554.502
Falcon® 225mL PP Centrifuge Tube	Corning, 352075
Filtropur BT50 500ml	Sarstedt, 83.3941.101
Flow Cytometry tubes	Sarstedt, 55.1579
Gel casting chamber	
Gel electrophoresis chamber	
Glass Bottom Culture Dishes	MatTek Corporation, P35G-1.0-14-C
Glass coverslips (24x24 mm)	VWR

Glass electrodes	Hilgenberg, HILG1103227
Hot Plate A3	Labotect
Injectomat Line	Fresenius Kabi AG, 9004132
Micro-Fine™+ U-100 Insulin	BD
Nalgene Mr. Frosty® Cryo 1°C Freezing Container	Thermo Fischer Scientific
Neubauer counting chamber	Karl-Hecht KG
Nunc™ EasYFlask™ Cell Culture Flasks 175cm^2 Nunclon Delta Surface	Thermo Fisher Scientific, 156340
Nunc™ EasYFlask™ Cell Culture Flasks 75cm^2 Nunclon Delta Surface	Thermo Fisher Scientific, 156499
Omnican® 50 30G	Braun
Peripheral venous catheter 20G	Braun
Pipette tips	Sarstedt, 70.762, 70.760.002
Pipette tips with filter Biosphere®	Sarstedt, 70.1130.210, 70.1116.210 70.760.212, 70.762.211
RoVent® Jr.	Kent Scientific
SafeSeal tube 1.5 mL	Sarstedt, 72.706
Scalpel Blade	Bayha GmbH
Serological pipette 10 mL	Sarstedt, 86.1254.001
Serological pipette 25 mL	Sarstedt, 86.1685.001
Serological pipette 2 mL	Sarstedt, 86.1252.001
Serological pipette 50 mL	Sarstedt, 86.1256.001
Serological pipette 5 mL	Sarstedt, 86.1253.001
Signal gel	Parker, 15-60
Spinner flask, 1000 ml	Integra, 182 101
Spinner flask, 500 ml	Integra, 182 051
Stamp for cryoinjury	Self-assembled
Sterican® cannulae 28G-24G	Braun
Surcigal tools	various suppliers
Syringes 1 ml	Braun
T175 suspension cell culture flask	Sarstedt, 83.3912.502
Teflon spacer for patches	Self-built
Teflon spacers (dimensions: length 12 mm, width 3 mm, height 13.5 mm)	EHT technologies GmbH, C0002
Vaporizer	Visualsonics
VetFlo™	Kent Scientific
V-shaped sedimentation rack	Custom made at UKE Hamburg

9.2.4 Media and Serum

Basal Medium (Neurobasal)	Thermo Fisher Scientific, 21103-049
DMEM	Life Technologies, A14430-01
DMEM	Biochrom, F0415
DMEM, (no Phenol Red)	Life Technologies, 21063045

DMEM/F-12 without Glutamine	Life Technologies, 21331-046
Fetal Bovine Serum superior (FBS)	Biochrom, S0615
Goat serum	
Horse serum	Life Technologies, 26050-088
Human serum albumin	Biological Industries, 05-720-1B
mTeSR Plus	StemCell Technologies, 05825
RPMI 1640	Life Technologies, 21875-034
StemPro™-34 SFM	Life Technologies, 10639011

9.2.5 Reagents and Enzymes

1-Thioglycerol (MTG)	Sigma-Aldrich, M6145
2-Propanol	Roth, 9866.6
2x DMEM	Gibco, 52100-021
Accutase® Cell Dissociation Reagent	Sigma-Aldrich, A6964-100mL
Acetic acid, glacial	Roth, 6755.1
Agarose	Thermo Fisher Scientific, 15510-027
Alt-R® Cas9 Electroporation Enhancer	IDT, 1075916
Alt-R® CRISPR-Cas9 crRNA	IDT, self-designed
Alt-R® CRISPR-Cas9 tracrRNA	IDT, 1072532
Alt-R® S.p. Cas9 Nuclease V3	IDT, 1081059
Aqua	B. Braun
Biotin	Sigma-Aldrich, B4639-100MG
$CaCl_2$ x $2H_2O$	Merck, 1.02382
Catalase	Sigma-Aldrich, C40-100MG
CloneR 10x Cloning Supplement	StemCell Technologies, 0588
Collagenase II	Worthington, LS004176
Corticosterone	Sigma-Aldrich, C2505-500MG
D(+) Glucose	PanReac AppliChem, A3666,1000
D(+)-Galactose	Sigma-Aldrich, G0625-100G
D(+)-Glucose anhydrous	Roth, X997.2
DAPI	Biochemica, A1001 0025
DB3.1 Competent *E. coli*	Invitrogen, 11782-018
Dimethyl sulfoxide (DMSO) for cell culture	Sigma-Aldrich, D4540
DL-alpha tocophercol acetate	Sigma-Aldrich, T3001-10G
DL-alpha tocopherol	Sigma-Aldrich, T3251-5G
DNA loading dye, 6x	Thermo Fisher Scientific, R0611
DNase II, type V (from bovine spleen)	Sigma-Aldrich, D8764
dNTP mix	Qiagen, 160037931
DPBS	Gibco, 14190250
EDTA	Roth, X986.2
Ethanol 99%	Chemsolute, 2212.5000
Ethanol, 96%	Roth, T171.4 and Chemsolute 2209.5000
Ethanolamine	Sigma-Aldrich, E9508-100ML

FastDigest EcoRV	Thermo Fisher Scientific, FD0304
FastDigest Green Buffer (10X)	Thermo Fisher scientific, B64
FastDigest PstI	Thermo Fisher Scientific, FD0614
FastDigest SalI	Thermo Fisher Scientific, FD0644
Fluka Yeast Extract	Sigma Aldrich, 9182
Geltrex®	Gibco, A14133-02
GeneRuler 1 kb DNA Ladder	Thermo Fisher Scientific, SM0313
GeneRuler 100 bp DNA Ladder	Thermo Fisher Scientific, SM0241
GlutaMAX™ Supplement	Gibco, 35050061
Glutathione	Sigma-Aldrich, G6013-5G
Glycerol	Roth, 3783.1
Glycerol	Merck 1.04092
HBSS minus Ca^{2+}/Mg^{2+}	Gibco, 14175-053
HEPES	Sigma-Aldrich, 9105.4
HotStarTaq DNA Polymerase	Qiagen, 203207
L-Carnitine	Sigma-Aldrich, C0283-1G
L-Glutamine	Gibco, 25030-081/ - 024
Linoleic acid	Sigma-Aldrich, L1012-100MG
Linolenic acid	Sigma-Aldrich, L2376-500MG
Lipid Mix (1000x)	Sigma-Aldrich, L5146
Luria-Agar	Sigma Aldrich, l3147-250g
Magnesium chloride ($MgCl_2$)	Sigma Aldrich, M0250
Magnesium sulphate heptahydrate ($MgSO_4$ x $7H_2O$)	Merck, 1.05886
Matrigel® Basement Membrane Matrix (for Cheese Differentiation	Corning, 354234
Matrigel® Growth Factor Reduced (GFR) Basement Membrane Matrix (for hiPSC culture)	Corning, 354230
Medical Oxygen	TMG
MEM Non-Essential Amino Acids Solution (100X)	Life Technologies, 11140050
$MgCl_2$	Qiagen, 163050234
Midori Green	Nippon Genetics Europe, M604
Mowiol® 4-88	Roth, 0718
MyTaq™ DNA Polymerase	Bioline, BIO-21106
NanoFuel Solvent	Nanolight, #399
NEBNext® High-Fidelity 2X PCR Master Mix	New England Biolabs, M0541S
Nitrogen, liquid (N2)	TMG
Non-essential amino acids (NEAA)	Gibco, 11140
Nuclease-free water	ThermoFisher Scientific, R0581
octenisept®	Schulke
Oleic acid	Sigma-Aldrich, O1383-1G
Paraformaldehyde	Merck, 1.04005
PBS Tablets	Gibco, 18912014
PCR Buffer 10x	Qiagen, 163045984

PEI MAX Hydrochloride Transfection Grade Linear 40,000 mw	Polysciences Europe GmbH, 24765-1
Peptone from meat, enzymatic digest	Sigma Aldrich, 82962-1KG
Phosphoascorbate (2-Phospho-L-ascorbic acid trisodium salt)	Sigma-Aldrich, 49752
Pluronic® F-127	Sigma-Aldrich, P2443-250G
Polyvinyl alcohol	Sigma-Aldrich, P8136
Potassium chloride (KCl)	Merck, 1.04936
Potassium di-hydrogen phosphate (KH2PO4)	Merck, 4873
PrimeSTAR® GXL DNA Polymerase	Takara, R050B
Proteinase K	Qiagen,19133
Putrescine	Sigma-Aldrich, P5780-5G
Q-solution	Qiagen, 160016150
Retinyl acetate	Sigma-Aldrich, R7882-1G
Roti®-GelStain	Roth, 3865.1
Roti®-Histofix 4%	Roth, P087.3
Saponin	Sigma-Aldrich, 47036 or Merck, 558255
SapphireAmp® Fast PCR Master Mix	Takara, RR350A
Sodium azide	Sigma-Aldrich, 71290
Sodium citrate dihydrate	Sigma-Aldrich, W302600
Sodium chloride (NaCl)	Roth, 3957.1 or JT Baker, 7647-14-5
Sodium chloride (NaCl) solution (0.9%)	B. Braun, 3570210
Sodium hydrogen carbonate ($NaHCO_3$)	Merck, 1.06329
Sodium hydrogenphosphate (Na_2HPO_4)	Sigma Aldrich, S0876
Sodium pyruvate	Sigma, P5280
Sodium Selenite	Sigma-Aldrich, S9133-1MG
Sterofundin® ISO 1/1 E ISO	Braun
T3	Sigma-Aldrich, T6397-100MG
TBS	Sigma-Aldrich, T6664
trans-4-(Aminomethyl)cyclohexanecarboxylic acid	Sigma, 857653
TRIS-hydrochloride	Roth, 9090.2
Triton X®-100	Roth, 3051.3
Trypan blue	Sigma, T8154
Xylene	JT Baker, 8080.2500

9.2.6 Proteins

Activin A	R&D Systems, 338-AC
Aprotinin	Genaxxon bioscience M6361.1010
Aprotinin	Sigma-Aldrich, A1163-10G
Bcl-xL BH4 4-23	Sigma-Aldrich, 197217
BMP-4	R&D Systems, 314-BP
BSA Fraction V IgG free, FA-poor	Fisher Scientific, 30036578

Dorsomorphin dihydrochloride	Tocris, 3093
FGF2 (human recombinant basic FGF)	Peprotech, #100-18B or Milentyi Biotec, 130-104-923
Fibrinogen	Sigma-Aldrich, F8630
Human Holo-Transferrin	Sigma-Aldrich, T0665-500MG
Human serum albumin	Biological Industries, 05-720-1B
IGF-1	Peprotech, 100-11R3
Insulin, human	Sigma-Aldrich, I9278
Progesterone	Sigma-Aldrich, P8783-1G
TGF-β1	Peprotech, 100-21C
Thrombin	Sigma, 605157 or Biopur, BP11-10-1104
Transferrin human	Sigma-Aldrich, T8158
Wheat germ agglutinin	Thermo-Fisher Scientific, W21404
α-Bungarotoxin	Thermo-Fisher Scientific, B35451

9.2.7 Small Molecules and Drugs

Ampicillin trihydrate	Serva, 13397.01
Atropine sulfate	Braun
BTS (N-Benzyl-p-Toluenesulfonamide)	TCI, B3082-25G
Buprenorphine	Eumedica
Coelenterazin	Nanolight, #303, #3031
Dormicum (Midazolam)	Chepla Pharm
Dormitor (Medetomidin)	Orion Pharma
Dorsomorphin	Tocris, 3093
Enro 2.5 (Enrofloxazin 2,5%)	WDT
Fentanyl	Janssen
Forene® (Isofluran)	Abbvie, B506
Heparin-Natrium	LEO
Hexamethonium bromide	Sigma-Aldrich, H0879
Isoprenaline	Sigma-Aldrich, I6504
KY021111	R&D Systems, #4731
Lidocaine	L7757-25G
Nocodazole	Calbiochem, 487928
Pancuronium-Actavis	Actavis
Penicillin/streptomycin	Gibco, 15140-122
Pinacidil monohydrate	Sigma- Aldrich, P154
PSEM^{89S}	Tocris, 6426
Puromycin	Invivogen, QLL-38-04B
Rimadyl® (Carprofen)	Zoetis
Sandimmun (Cyclosporin A)	Novartis
Urbason (Methylprednisolon)	Sanofi

XAV-939	Tocris, 3748
Y-27632 2 HCl	Biorbyt, orb154626 or orb60104

9.2.8 Kits

Amaxa™ P3 Primary Cell 4D-Nucleofector X Kit L	Lonza, V4XP-3024
NucleoBond® Xtra Maxi	Macherey-Nagel, 740414
NucleoSpin® Plasmid	Macherey-Nagel, 740588
NEBNext® High-Fidelity 2X PCR Master Mix	NewEngland BioLabs, M0541
QIAquick PCR Purification Kit	Qiagen, 28106
DNeasy® Blood & Tissue Kit	Qiagen, 69506
In-Fusion® HD Cloning Kit	Takara Bio, Pt5162-1
SapphireAmp® Fast PCR 2X Master Mix	Takara Bio, RR350A
GeneJET PCR Purification Kit	Thermo Fisher Scientific, K0701

9.2.9 Antibody List

Supplementary Table 2: Antibody list

Antigen	Supplier	Antigen Retrieval	Titer
MLC2a	BD Pharmingen, clone S58-205, Cat. 565496	Citrate buffer	1:500
MLC2v	Proteintech, pAb, Cat.10906-1-AP	Citrate buffer	1:250
Alpha-Actinin	Sigma-Aldrich, clone EA-53 Cat. A7811	Proteinase K	1:600
Dystrophin	Millipore, clone 1808, Cat. MAB1645	EDTA	1:150
Ku80	Cell Signaling Technology, clone C48E7, Cat. CST-2180	Citrate buffer	1:800
Connexin 43	BD Transduction Laboratories, clone 2/Connexin-43, Cat. 610062	Citrate buffer	1:400
Connexin 43	Abcam, pAb, Cat. ab11370	Citrate buffer/Proteinase K	1:400
N-Cadherin	Sigma-Aldrich, clone CH19, Cat. C1821	Citrate buffer	1:400
GFP	Abcam, clone 3H9, Cat. ab252881	Citrate buffer/Proteinase K	1:500
GFP	Abcam, pAb, Cat. ab6556	Proteinase K	1:500
SSEA3 (AlexaFluor® 647)	BD Pharmingen, Clone MC-63, Cat. 561145	n/a	1:50
Isotype SSEA3	BD Pharmingen, clone MOPC/21, Cat. 557714	n/a	1:50
Cardiac troponin T (APC)	Miltenyi Biotec, clone REA400, Cat. 130-120-403	n/a	1:50
Isotype cardiac troponin T	Miltenyi Biotec, clone REA293, Cat. 130-120-709	n/a	1:50
Goat anti-mouse Alexa Fluor 546	Invitrogen, A-11003	n/a	1:100
Goat anti-rabbit Alexa Fluor 546	Invitrogen, A-11035	n/a	1:100
Goat anti-mouse Alexa Fluor 647	Invitrogen, A-21236	n/a	1:100

9.3 Security information

The experiments were all performed in certified security standard S1 and S2 laboratories. All chemicals, buffers, and solutions were handled and disposed of according to their security data sheets in appropriate containers. Cell-containing or contaminated material was autoclaved before disposal. All surfaces that have been possibly contaminated with genetically modified organisms were cleaned with 70% ethanol.

Supplementary Table 3: List of hazardous substances used according to GHS

Substance	CAS #	H-statements	P-statements
1-Thioglycerol	96-27-5	H: 302-311-315-319-335	P: 261-280-305+351+338+312
2-Propanol	67-63-0	H: 225, 319, 336	P: 210, 261, 305+351+338
A2 Buffer	1310-73-2d, 151-21-3	H: 315, 319	
A3 Buffer	50-01-1,	H: 302, 319	
Acetic acid	64-19-7	H: 226-290-314	P: 210-280-301+330+331-305+351+338-308+310
AL-T/M Buffer	50-01-1, 110-16-7	H: 315, 317, 319	P: 280, 333+313, 362, 501
Ampicillin sodium salt	69-52-3	H: 317, 334	P: 261, 280, 342+311
Ampicillin trihydrate	7177-48-2	H: 317-334	P: 280-285, 302+352-304+341-333+313-342+311
Atropine sulfate	5908-99-6	H: 300+330	P: 301+310+330, 304+340+310
AW Buffer	50-01-1, 67-63-0	H: 226, 302, 319, 336	
AW1 Buffer	50-01-1	H: 302, 332, 315, 319	P: 280, 362, 501
Binding Buffer		H: 302, 314, 412	P: 273, 264, 280, 270
Buprenorphine	52485-79-7	H: 302-361	P: 281
Calcium chloride dihydrate	10035-04-8	H: 319	P: 305+351+388
Carprofen	53716-49-7	H: 301	P: 301+310
Catalase	9001-05-2	H334	P: 261, 284, 304+340+312, 501

Cyclosporin A	59865-13-3	H: 302-350-360	P: 201-308+313
DAB	91-95-2	H: 302, 319, 341, 350	P201, 301+312+330, 305+351+338, 308+313
Dorsomorphin	866405-64-3	H: 302, 312, 332	P: 301+312, 304+340, 302+352, 261, 280, 264, 270, 271, 330, 501, 363
EDTA	6381-92-6	H: 332, 373	P: 260, 314
ELU Buffer	67-63-0, 7447-40-7,	H: 226, 319	P 210, 280sh
Enrofloxacin	93106-60-6	H: 361f, 372, 410	P: 201, 264, 273, 280, 308+313, 391
Ethanol, absolute	64-17-5	H: 225, 319	P: 210, 240, 305+351+338, 403+233
Fentanyl	437-38-7	H: 300+310+330, 336	P: 260, 262, 264, 280, 302+352+310, 304+340+310
Formaldehyde	50-00-0	H: 351-331-311-301-314-317	P: 301+310-303+361+353-305+351+338, 320-361-405-501
Hydrochloric acid	7647-01-0	H: 314-335	P: 260-301+330+331-303+361+353-305+351+338-405-501
Isoflurane	26675-46-7	H: 336	P: 304+340-312-403+233-405-501
Lidocaine	137-58-6	H: 302	P: 264, 270, 301+312, 330, 501
Lipid mix	64-17-5	H: 225, 319	P210, 280, 305+351+338, 337+313, 403+235
LYS Buffer	1310-73-2d, 151-21-3,	H: 315, 319	P: 280h
MEM non-essential amino acid solution	n/a	H: 315, 319	P: 280,264, 302+352, 305+351+338, 332+313, 337+313
Methylprednisolone	83-43-2	H: 360, 372	P: 260, 264, 280, 308+313, 405, 501
Midazolam	5946-70-8	H: 302+312+332	P: 261, 280, 321, 330, 362+364, 501

Midori Green	n/a		P: 261, 280
Nitrogen, liquid (N_2)	7727-37-9	H: 281	P: 282, 336+315, 403
N-benzyl-p-toluenesulfonamide	1576-37-0	H: 315, 319, 335	P: 302+352, 337+313, 304+340, 312, 280, 332+313
Nocodazole	31430-18-9	H: 341, 361d	P: 201, 202, 280, 308+313, 405, 501
Pancuronium bromide	15500-66-0	H: 301	P: 301+310
PB Buffer	50-01-1, 67-63-0	H: 225, 315, 319, 336	P: 210, 280, 403
PEI MAX® - Transfection Grade Linear PEI Hydrochloride	49553-93-7	H: 302+312, 315+320	P: 280A, 302+352, 305B, 313, 351, 501
Penicillin	61-33-6	H: 317	P: 280
Pinacidil monohydrate	85371-64-8	H: 302, 315, 319, 335	P: 261, 305+351+338
Potassium di-hydrogen Phosphate	7778-77-0	--	P: 260
Proteinase K	39450-01-6	H: 334	P: 304+340, 261, 342+311, 284
Puromycin	58-58-2	H:302	
Putrescine	110-60-1	H: 302, 311, 314, 330	P: 260, 280, 301 + 312, P303 + P361 + P353, P304 + P340 + P310, P305 + P351 + P338
Retinyl acetate	127-47-9	H: 360D, 413	P: 202, 273, 280, 308+313, 405, 501
RNase A	9001-99-4	H: 334	P: 261sh, 342+311
Roti®-Histofix 4%	50-00-0 67-56-1	H: 302, 317, 341, 350	P: 261, 280, 302+352, 308+313
Saponin	8047-15-2	H: 319, 335	P 261, 305+351+338
Sodium azide	26628-22-8	H: 300-400-410	P: 273–309-310
Sodium hydroxide	1310-73-2	H: 314	P: 280–301+330+331–309–310-305+351+338
Sodium selenite	10102-18-8	H: 300+330, 315, 317, 319, 411	P: 260, 273, 280, 301+330+331+310, 302+ 352,

			304+340+310, 305+351+338, 403+233
Streptomycin	57-92-1	H: 302	
Thrombin	9002-04-4	H: 315, 319, 334, 335	P: 261, 305+351+338, 342+311
trans-4-(Aminomethyl)cyclohexanecarboxylic acid	1197-18-8	H: 315, 319, 335	P261, 305+351+338
TRIS-Hydrochloride (Tris-HCl)	1185-53-1	H: 315, 319, 335	P: 280, 302+352, 305+351+338
Triton X-100	9002-93-1	H: 302-318-411	P: 273-280-305+351+338
Trypan blue	72-57-1	H: 350	P: 201-308+313
WASH Buffer	64-17-5d, 7447-40-7	H: 226	P: 210
Xylene	1330-20-7	H: 226, 304, 312 + 332, 315, 319, 335, 373	P: 210, 260, 280, 301+310, 303+361+353, 305+351+338
Y-27632	331752-47-7	H: 302-312-332	P: 280

10 ACKNOWLEDGEMENTS

This work would not have been possible without the help of countless people that supported me in a professional or personal manner but often in both.

I want to thank you, Prof. Dr. Thomas Eschenhagen, for giving me the opportunity to work in your institute on this exciting and ambitious project. Your valuable advice and willingness to share your extensive knowledge greatly contributed to the success of this project. Moreover, your guidance shaped my first steps in my scientific career.

I would also like to thank Prof. Dr. Elke Oetjen for your interest in my project, the supervision of my thesis on behalf of the Department of Chemistry, the evaluation of my thesis, and presiding the disputation committee of my thesis.

I am extremely grateful to you, Dr. Florian Weinberger. You exceeded my expectations for a PhD supervisor. In the past three years you trusted me in all scientific endeavors but never hesitated to be hands-on during critical experiments, sharing all your experience and knowledge, keeping me going. This goes hand in hand with the environment you created in our lab group, one of openness, critical thinking and taking care of each other (birthday and project celebrations included). Many thanks to all current and past members of the group who greatly contributed to this environment.

Along with Florian, here I want to especially thank Birgit Geertz and Constantin von Bibra who spent countless hours with me in the operation room, performing Langendorff experiments or taking care of our guinea pigs at night or on weekends.

Moreover, I am grateful to Aya Shibamiya and Maria Köhne, because without you the sheer number of cardiomyocytes (around four billion!) that were generated for this project would not exist. Countless stressful months of cardiomyocyte differentiations would have been way harder to endure alone and nearly impossible.

I had the privilege to work with Judith Rössinger, Christoph Manthey and Rajiven Srikantharajah. Thank you for your huge contribution to this project and for giving me an opportunity to teach and supervise, although I think you taught me more than I could return. Moreover, thanks for countless (more or less productive) coffee breaks, late night sessions in the lab and keeping me sane.

I very much appreciate the help of J. Simon Wiegert for optogenetic advice and sharing equipment, the animal staff of the UKE for taking very good care of our animals, Kristin Hartman for top-notch quality tissue sections and stainings, Ingke Braren for invaluable teaching of molecular biology, Irm Hermans-Borgmeyer for Southern Blotting, Christiane Pahrmann for bioluminescence measurements, Elisabeth Krämer for karyotyping, Sandra Laufer for providing the UKEi-001a line, the FACS Core facility for technical support.

Many more people of the IEPT would need to be thanked here namely; even in crazy times during a global pandemic you created an enjoyable, productive and pleasant work environment.

Last but not least, I am deeply grateful to my family. Your “of course you can do that” attitude and unwavering support got me where I am now.

11 DECLARATION OF ACADEMIC HONESTY – EIDESSTATTLICHE ERKLÄRUNG

I hereby declare that my thesis entitled

“Active contribution of transplanted induced pluripotent stem cell-derived cardiomyocytes to left ventricular function in a guinea pig model “

carried out at the Institute of Experimental Pharmacology and Toxicology, UKE Hamburg in the laboratory of Prof. Dr. Thomas Eschenhagen, with the support of Dr. Florian Weinberger and the supervision of Prof. Dr. Elke Oetjen for the Department of Chemistry, was written independently by myself. No other sources or aids than those indicated were used. The submitted written form of the thesis complies with the electronic version. This thesis was not handed in in any other form for another examination procedure.

Hamburg, 14.12.2021  Tim Niklas Stüdemann

---

Hiermit versichere ich an Eides statt, die vorliegende Dissertation mit dem Titel

“Active contribution of transplanted induced pluripotent stem cell-derived cardiomyocytes to left ventricular function in a guinea pig model “

durgeführt am Institut für Experimentelle Pharmakologie und Toxikologie des Universitätsklinikums Hamburg-Eppendorf unter der Leitung von Herrn Prof. Dr. Thomas Eschenhagen, der Unterstützung von Herrn Dr. Florian Weinberger und der Betreuung durch Frau Prof. Dr. Elke Oetjen für den Fachbereich Chemie selbst verfasst und keine anderen als die angegebenen Hilfsmittel benutzt zu haben. Die eingereichte schriftliche Fassung entspricht der auf dem elektronischen Speichermedium. Ich versichere, dass diese Dissertation nicht in einem früheren Promotionsverfahren eingereicht wurde.“

Hamburg, den 14.12.2021  Tim Niklas Stüdemann